ISSN 0366-5542
CODEN: CCHHAQ

地質調査所報告　第278号

地質リモートセンシングに関する研究

地　質　調　査　所

平成4年3月

地 質 調 査 所 報 告　第 278 号

所 長　小 川 克 郎

Report No. 278

Geological survey of Japan

Katsuro OGAWA, Director

地質リモートセンシングに関する研究

Research on geologic remote sensing system

編 集

津　宏 治

Edited by

Hiroji TSU

地 質 調 査 所

平成 4 年 3 月

Geological survey of Japan

March, 1992

巻 頭 言

我が国の陸域観測衛星の第１号として地球資源衛星１号(JERS-1)の開発が宇宙開発委員会で承認され、通商産業省がミッション機器の光学センサ（OPS）と合成開口レーダー（SAR）の開発を担当し、宇宙開発事業団が打ち上げロケットと衛星バスの開発を担当する共同開発体制の下、鋭意その開発が進められてきた。この間、通商産業省ではこれらミッション機器開発の効果的な推進のために昭和59年度から工業技術院大型プロジェクト「資源探査用観測システム」が開始された。同大型プロジェクトには多くの民間企業が参画するとともに、工業技術院傘下の研究機関も加わった。地質調査所では昭和59年度から上記の大型プロジェクトの一環としての「地質リモートセンシングに関する研究」を通じて、その推進に参画してきた。本研究では昭和59年度から同大型プロジェクトの終了までの昭和63年度までの５年間に２編の中間成果報告書およびデータカタログ集を１編作成してきた。これらの中間成果報告には本研究過程で様々な研究課題を通じて得られた多くの貴重な研究成果が盛り込まれている。またその一部は学会等を通じて公表もされてきた。しかしながら、これらの中間報告書はその性格から内部資料となっていて広く公開されてはいない。また、地球資源衛星１号は現在順調に試験を終え、打ち上げが平成４年２月頃と計画されていて、平成4年度には本格的に光学センサや合成開口レーダーのデータが広く利用できる段階になっている。このような点を考慮すると、地質調査所におけるこれらの地質応用分野での研究成果を取り纏めておくことは意義のあるものであろう。本報告はこれまでの研究成果を取り纏めたもので、ここに報告する次第である。

平成４年３月

地質調査所地殻物理部長

津　宏治

総　目　次

CONTENTS

地質調査所報告第278号，p.1-10, 1992
Rept. Geol. Surv. Japan, No.278

岩石・鉱物のスペクトル・データベース・システム

浦井　稔*・佐藤　功*・二宮芳樹*・津　宏治**

A spectral data base system for rocks and minerals

By

Minoru URAI, Isao SATO, Yoshiki NINOMIYA and Hiroji TSU

Abstract: A spectral data base system is developed for spectral studies of rocks and minerals. Relational Data Model is adopted for the data base because of its flexible retrieval. The data base consists of tables corresponding to spectral values, sample description, results of chemical analysis and results of X-ray diffraction. Using the data base, these datas can be stored, retrieved and displayed efficiently and flexibly.

要　旨

岩石・鉱物のスペクトルの研究を行なうために，岩石・鉱物のスペクトル・データベースを作成した．岩石・鉱物のスペクトル・データを構築するにあたり，データ・モデルとしてデータ利用の柔軟性が最も高いリレーショナル型を採用した．岩石・鉱物のスペクトル・データベースによって，多数の試料に対するスペクトル値および試料収集時の記載や化学分析値等属性データを整理し，効率良く格納・検索することができた．

1. まえがき

岩石・鉱物のスペクトル・データはリモートセンシングによって得られたデータから地表の岩石・鉱物を識別・同定を行うために不可欠である．岩石・鉱物のスペクトルの研究においては，岩石・鉱物のスペクトルを測定するとともに化学分析や鉱物の同定等を実施し，これらのデータを解析することによってスペクトルがどのような要因によって変化するかを調べ，スペクトルが何を意味するかを研究している．このため，これらのデータを整理し効率良く格納・検索するための岩石・鉱物のスペクトル・データベースが必要となった．スペクトル・データベースの研究は Kahle *et al.* (1981) や Purdue 大学 (Silva, 1979) で行われているが，これらのデータベースはスペクトル値のデータベース化のみで十分な属性情報を含んだ総合的なデータベースとはなっていない．本報告ではスペクトル値と試料収集時の記載や化学分析値等の属性情報を効率良く格納・検索および表示するための岩石・鉱物のスペクトル・データベース・システムについて，浦井ほか (1992) のスペクトル研究をモデルにして考察した結果を報告する．

*地殻物理部，**企画室

Keywords: data base, relational data model, spectrum, sample description, chemical analysis, X-ray diffraction analysis

2. 岩石・鉱物のスペクトル研究の概要

岩石・鉱物のスペクトル・データベースを構築するにあたり，実際の岩石・鉱物のスペクトル研究について，浦井ほか (1992) を例として概観した．第1図にスペクトル測定の概要を示す．

浦井らが使用した試料は，主に秋田県 (八幡平)・岩手県 (八幡平)・宮城県 (鬼首)・大分県 (豊肥) の地熱地域で採集された粘土試料，茨城県 (日立)・熊本県・鹿児島県の金属鉱床地域で採集された粘土試料，米国 Clay Minerals Society が提供する標準粘土試料，および，茨城県・福岡県 (平尾台) の石灰石鉱山で採集された炭酸塩岩試料であり，その他に，国内の代表的粘土鉱山や北鹿の黒鉱鉱床周辺の試料および中国の粘土試料も若干含まれる．試料数は，粘土試料が約80個，炭酸塩岩試料が約30個である．試料の形状は，Clay Minerals Society の標準粘土試料は粉末，その他の粘土試料は室内乾燥した直径数 mm-数 cm の土塊状，炭酸塩岩試料は直径 10cm-20cm の塊状である．これらの試料は，資源探査で重要な鉱物である粘土鉱物や炭酸塩鉱物を含む．

試料の採取時の記載として，試料番号，採取年月日，変質の程度等が記載された．

反射スペクトルの測定には，GER (Geophysical Environmental Research) 社 IRIS (InfraRed Intelligent Spectroradiometer) スペクトロラジオメータが使用され，光源にはタングステンランプを，標準反射板には Kodak 社の $BaSO_4$ 塗料 (Kodak white reflectance coating 6080) を高粘度スプレー (Kodak Laboratory Sprayer 13270) でアクリル板に吹き付けたものが使用された．IRIS スペクトロラジオメータは対象物と標準反射板からの反射強度を測定し，これをGER社が提供するソフトウェアでゲイン・暗電流等を補正して標準反射板に対する二方向性反射係数 (Bidirectional Reflection factor) が計算された．反射スペクトルのデータは，約800組の波長と反射係数，および，測定条件等の記載である．

化学分析は試料の一部を粉末化してカナダ Chemex Labs 社に依頼して誘導結合高周波プラズマ分光分析法 (ICP) 等によって行われた．化学分析データは SiO_2 や TiO_2 等の化学分析値および測定条件

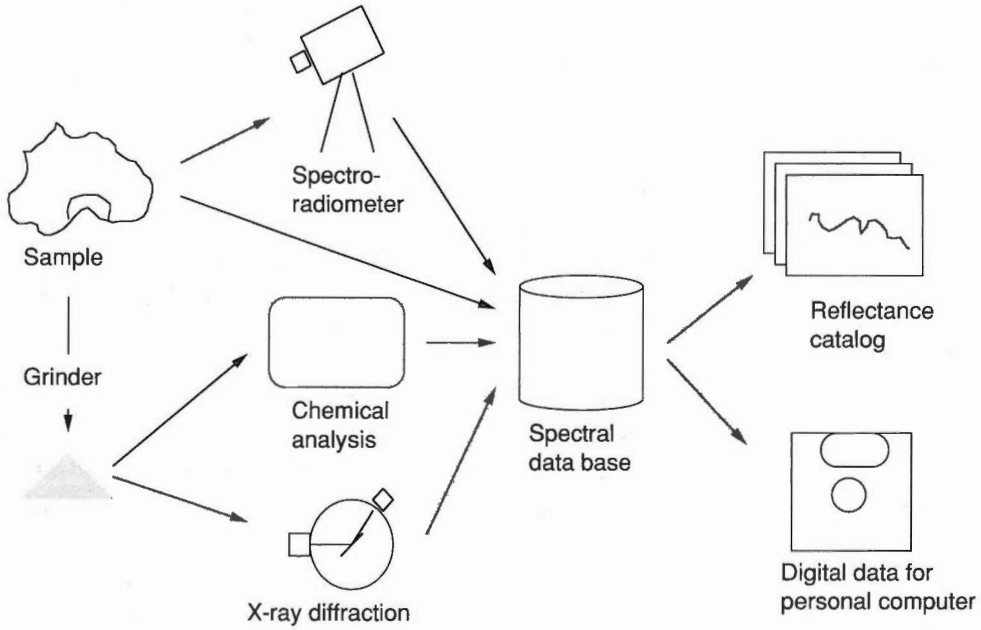

第 1 図　スペクトル測定の概要 (浦井ほか, 1992)

Fig. 1　The outline of spectrum measurements (Urai *et. al.*, 1992)

等の記載である．化学分析値から五十嵐(1984)の方法を使用して粘土ノルム値が計算された．五十嵐の方法は，曹長石以下の30鉱物を対象に行われる．粘土ノルム値データは曹長石以下の30鉱物の含有量および粘土ノルム計算における条件等である．

X線回折は，化学分析のために粉末化したサンプルを理学電機（株）製のX線回折装置(RAD-rA)を使用して不定方位で行われた．X線チャートの解析はあらかじめ用意した数種類の標準X線チャートと重ね合わせることによって同定する機械的作業にとどめ詳細な解析は行われていない．X線回折は2θが70°～2°におけるカウント値，X線回折によって同定された鉱物名および測定条件等の記載である．

3. 岩石・鉱物のスペクトル・データベース・システムの構築

3.1　データベース・システムの設計

岩石・鉱物のスペクトルの研究で必要となるデータは，試料収集時の記載，スペクトル値，化学組成や鉱物組成の同定や定量に必要なデータである．試料収集時の記載には試料番号，収集場所，色や形状に関するデータ等が含まれる．スペクトル値は，数10から数1,000点の波長における反射率，二方向性反射係数，放射率等の数値と測定機器，光源等の測定にかかわるパラメタから構成される．化学組成や鉱物組成の同定や定量に必要なデータは，化学分析やX線回折等の測定から得られるデータであり，様々な測定データが考えられる．

一方，データを利用してスペクトル研究を行う立場からデータベース・システムが具備すべき機能として以下の機能が考えられる．

1)あらかじめデータ検索条件を限定することなく，柔軟なデータ検索が可能であること
2)データの登録・追加・削除が簡単に行えること
3)新たな測定項目の追加・変更等が簡単に行えること
4)端末からデータ検索を行えるだけでなく，プログラムからもデータ検索が可能であること
5)数値データの多様な図形表示が可能であること

第1表　岩石・鉱物のスペクトル・データベースに格納すべき項目
Table 1　Items to be stored in the spectral data base of rocks and minerals

試料収集時の記載に関する項目	化学分析に関する項目
試料番号	化学分析番号
試料名	測定番号
色	測定年月日
収集年月日	測定装置
収集地点	測定のパラメタ
試料の形状	試料の処置
変質の程度	化学分析値
反射スペクトル測定に関する項目	鉱物組成値(ノルム値)*
測定番号	注釈
測定年月日	X線回折測定に関する項目
測定装置	測定番号
測定のパラメタ	測定年月日
試料の処置	測定装置
光源	測定のパラメタ
反射スペクトルから推定される鉱物名*	試料の処置
二方向性反射係数*	X線回折測定から推定される鉱物名*

＊印は繰り返し集団を示す。
Asterisk (*) indicating the repeating group.

3.2 データモデルの選定

データベースにおけるデータ・モデルには，リレーショナル型，ネットワーク型，ツリー型等があるが，岩石・鉱物のスペクトル・データベースではデータ利用の柔軟性が最も高いリレーショナル型を採用した．これは，研究用のデータベースにおいては，検索条件を限定しない柔軟な検索が要求されるためである．リレーショナル型データベース管理システムの下では，各データは表形式の「テーブル」によって管理される．テーブルは論理的にまとまったフィールドの集合である．フィールドはデータ格納および検索の最小単位であり，項目に相当する．例えば，試料番号や試料名はフィールドにあたり，その集合である「試料収集時の記載に関する項目」や「反射スペクトル測定に関する項目」は各々テーブルを構成する．

まず，浦井ほか (1992) のスペクトルの研究をモデルにして岩石・鉱物のスペクトル・データベースに格納すべき項目を選定した．浦井ほかの研究で記述・測定されたデータは第1表に示すとおり

1)試料採取時の記載に関する項目
2)反射スペクトル測定に関する項目
3)化学分析に関する項目
4)X線回折測定に関する項目

である．

次に，これをリレーショナル型データベース管理システムのテーブルに展開した．この時，試料採取時の記載に関する項目を試料テーブル，反射スペクトル測定に関する項目を反射スペクトル測定テーブル，化学分析に関する項目を化学分析テーブルおよびX線回折測定に関する項目をX線回折テーブルに，それぞれグループ化した．

リレーショナル型データベースを構築するに当たって全てのテーブルは第1正規形になければならない．すべての繰り返し集団が除去されている場合，テーブルは第1正規形にある．例えば，X線回折測定に関する項目をテーブルに展開する場合，X線回折測定から推定される鉱物名を格納するフィールドとして鉱物名1，鉱物名2・・・鉱物名 n を定義したと仮定する．この時，X線回折測定から推定される鉱物の種類が n を越えると，全ての鉱物名をテーブルに格納することができない．鉱物名1，鉱物名2・・・鉱物名 n は繰り返し集団にあたり，テーブルを分割することによって排除されなければなら

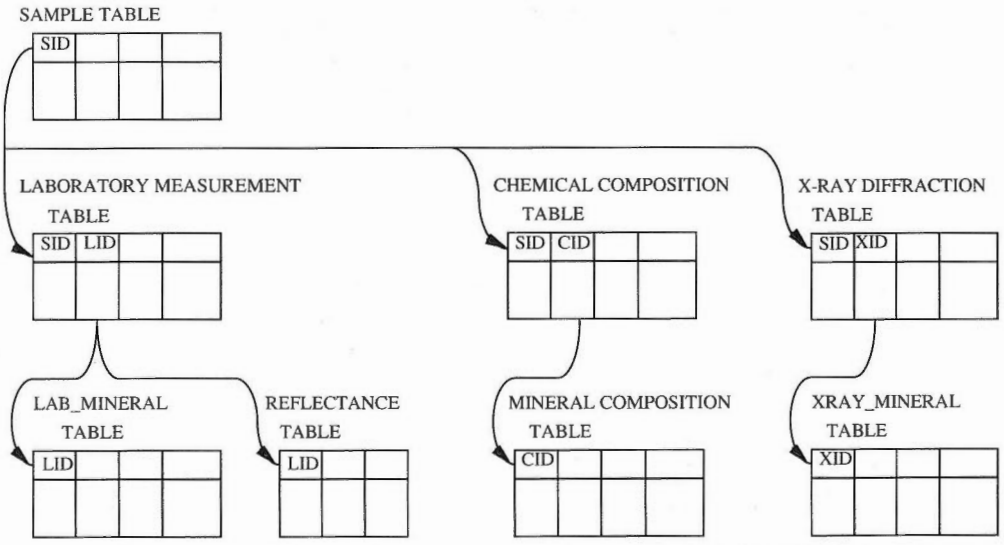

第 2 図　岩石・鉱物のスペクトル・データベースの連系図，矢印は明示的参照関係を表す
Fig. 2　The table connection for the spectral data base of rocks and minerals

第 2 表　岩石・鉱物のスペクトル・データベースのテーブルおよびフィールド
Table 2　Tables and fields for the spectral data base of rocks and minerals

テーブル／フィールド	参照	タイプ	長さ	ロング名
sam				Sample_table
*sid		STRING	20	Sample_ID
name		STRING	30	Sample_name
color		STRING	20	Color
sdate		DATE		Sampling_date
nation		STRING	20	Nation
pref		STRING	20	Prefecture
site		STRING	20	Site
latd		NUMERIC	2	Latitude_degree
latm		FLOAT	52	Latitude_minute
lond		NUMERIC	3	Longitude_degree
lonm		FLOAT	52	Longitude_minute
shape		STRING	12	Sample_shape
alt		STRING	12	Alternation
lab				Laboratory_meas.
*lid		STRING	12	Measurement_ID
lsid	sid	STRING	20	Sample_ID
ldat		DATE		Measurement_date
lequ		STRING	12	Equipment
lref		STRING	12	Reference
lprm		STRING	12	Parameter
ltre		STRING	12	Treatment
lamp		STRING	12	Lamp
labm				Lab_mineral
llid	lid	STRING	12	Measurement_ID
lmin		STRING	20	Detected_mineral
xray				Xray
*xid		STRING	12	Measurement_ID
xsid	sid	STRING	20	Sample_ID
xdate		DATE		Date
xequ		STRING	12	Equipment
xprm		STRING	12	Parameter
xtre		STRING	12	Treatment
xraym				Xray_mineral
xxid	xid	STRING	12	Measurement_ID
xmin		STRING	20	Detected_mineral
chem				Chemical_comp.
*cid		STRING	12	Measurement_ID
csid	sid	STRING	20	Sample_ID
cdate		DATE		Date
cequ		STRING	12	Equipment
cprm		STRING	12	Parameter
sio2		FLOAT	62	SiO2
tio2		FLOAT	62	TiO2
al2o3		FLOAT	62	Al2O3

＊はそのフィールドが1次キーであることを示す。参照の欄に書かれたフィールドはテーブル／フィールド欄に書かれたフィールドと明示的リレーションシップにあることを示す。タイプが STRING, NUMERIC または TEXT の場合、長さの欄はフィールドの長さをバイト単位で示す。タイプが FLOAT の場合、長さの欄の10の位はフィールドの長さをバイト単位で示し、1の位は小数点以下の桁数を示す。

Asterisk (*) indicating the primary key. The field in the REF and the field in the TABLE/FIELD are in a clearly statement relationship. When the TYPE is STRING, NUMERIC or TEXT, the LEN means the field length in byte. When the TYPE is FLOAT, the tens and units in the LEN mean field length in byte and number of fraction in the field.

第 2 表 (続き)
Table 2 (continued)

テーブル／フィールド	参照	タイプ	長さ	ロング名
fe2o3		FLOAT	62	Fe2O3
feo		FLOAT	62	FeO
mno		FLOAT	62	MnO
mgo		FLOAT	62	MgO
cao		FLOAT	62	CaO
na2o		FLOAT	62	Na2O
k2o		FLOAT	62	K2O
p2o5		FLOAT	62	P2O5
s		FLOAT	62	S
C		FLOAT	62	C
zro2		FLOAT	62	ZrO2
h2op		FLOAT	62	H2Op
h2om		FLOAT	62	H2Om
co2		FLOAT	62	CO2
so3		FLOAT	62	SO3
loi		FLOAT	62	LOI
bao		FLOAT	62	BaO
norm				Norm
nsid		STRING	20	Sample_ID
ncid		STRING	12	Chemical_comp_ID
ab		FLOAT	62	Albite
ad		FLOAT	62	Andalusite
al		FLOAT	62	Alunite
an		FLOAT	62	Anorthite
ap		FLOAT	62	Apatite
c		FLOAT	62	Corumdum
cc		FLOAT	62	Calcite
ch		FLOAT	62	Chlorite
cm		FLOAT	62	Chromite
dp		FLOAT	62	Diaspore
en		FLOAT	62	Enstatite
fr		FLOAT	62	Fluorite
gi		FLOAT	62	Gibbsite
he		FLOAT	62	Hematite
hl		FLOAT	62	Halite
il		FLOAT	62	Ilmenite
ka		FLOAT	62	Kaolinite
li		FLOAT	62	Limonite
mg		FLOAT	62	Magnesite
mi		FLOAT	62	Microcline
mo		FLOAT	62	Montmorillonite
mt		FLOAT	62	Magnetite
pp		FLOAT	62	Pyrophyllite
pr		FLOAT	62	Pyrite
q		FLOAT	62	Quartz
ru		FLOAT	62	Rutile
sd		FLOAT	62	Siderite
se		FLOAT	62	Sericite
th		FLOAT	62	Thernardite
z		FLOAT	62	Zircon
ot		FLOAT	62	Others
cond		TEXT	12	Condition
com		TEXT	20	Comment
ref				Reflectance
rsid		STRING	20	Sample_ID
rid		STRING	12	Measurement_ID
wavel		FLOAT	103	Wave_length
rref		FLOAT	62	Reflectance

ない．テーブルを第１正規形に保つため反射スペクトル測定テーブル，化学分析テーブルおよびX線回折テーブルを分割した．第１表の＊印は繰り返し集団を示す．

最終的に浦井ほかのデータを試料テーブル，反射スペクトル測定テーブル，反射スペクトル値テーブル，反射スペクトル検出鉱物テーブル，化学分析テーブル，鉱物組成テーブル，X線測定テーブル およびX線検出鉱物テーブルの８つのグループに分けた．第２図に設計した岩石・鉱物のスペクトル・データベースの連系図を示す．また，第２表に設計した岩石・鉱物のスペクトル・データベースのテーブルおよびフィールドを示す．新たに測定項目を追加する場合は，その測定項目に関するテーブルを作成し，このデータベースに追加すればよい．

3.3 データベース・システムの実現

データベース・システムを実現するために，データベース・システムの設計でデータベース・システムが具備すべき機能を満足する市販のデータベース管理システムを調査した．この結果，データベース・システムが具備すべき機能の内，1)～4) を満足するデータベース管理システムは存在するが，5) の「数値データの多様な図形表示が可能であること」を満足するものはなかった．このため，データベース・システムが具備すべき機能の内，1)～4) を満足するデータベース管理システムの一つである UNIFY を採用し，さらに，数値データの多様な図形表示を可能とする専用のプログラムを開発し，データベース・システムを実現した．

実現したデータベース・システムでは，データ検索言語の一つである SQL でデータを検索することができる．第３表に，X線回折によってカオリナイトが検出された試料を検索し，カオリナイトの含有量が多い順に試料番号，採取地点，反射スペクトルの測定番号，カオリナイトの含有量を表示するため

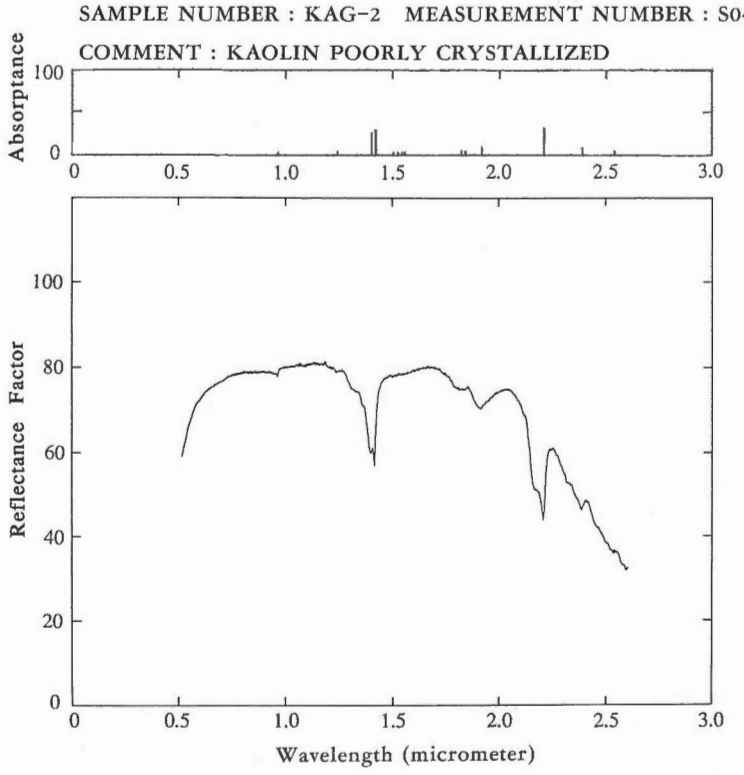

Absorption

NO.	WVL.	ABS.
1	2.212	31.8
2	1.419	29.4
3	1.402	25.9
4	1.916	8.4
5	2.391	8.4
6	2.542	5.7
7	1.822	4.5
8	1.841	4.0
9	1.503	3.5
10	1.524	3.2
11	0.969	2.9
12	1.244	2.8
13	1.558	2.8
14	1.544	2.8

第 3 図　単一の反射スペクトルの表示例
Fig. 3　An example of single spectrum display

のコマンド，および，その検索結果を示す．

データの登録・追加・削除については，データベース管理システムの機能を使用することによって，記述・測定されたデータ毎にメニューが表示され，簡単に行うことができる．

新たな測定項目の追加・変更等データベース管理システムの機能を使用することによって，簡単に行うことができる．

プログラムからのデータ検索については，端末からのデータ検索と同様に HLI 関数を使用して行うことができる．

数値データの多様な図形表示については，現在のところ，2種類のプログラムを開発した．その一つは，第3図に示すように測定番号に対応する反射スペクトル値および吸収帯の位置と吸収量を図示し，吸収帯の位置を吸収量の多いものから表示することができる．これらの吸収帯の位置と吸収量は Yamaguchi and Lyon (1986) の方法で計算したものである．もう一つのプログラムは，第4図に示すようにいくつかの測定番号に対応する複数の反射スペクトル値を同一の波長軸上に重なり合わないよう上

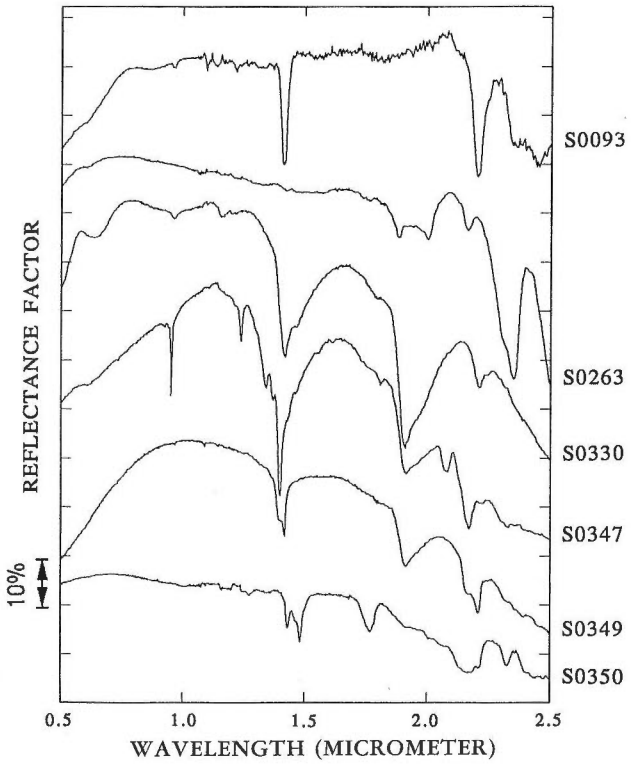

Sample-ID	Spectrum No.	Mineralogy,locality	Reflectance at 1.0um	1.7um (%)
860312-15:57	S0093	Sericite,Ibaraki	83.6	84.4
870218-S10	S0263	Calcite,Fukuoka	72.1	66.8
KINBARA-4	S0330	Montomollironite,Niigata	67.6	55.7
SUDO-5	S0347	Pyrophyllite,Nagano	60.1	51.4
SUDO-7	S0349	Kaolinite,Aichi	47.7	38.4
SUDO-8	S0350	Alunite,Hyogo	24.7	22.4

第 4 図　複数の反射スペクトルの表示例
Fig. 4　An example of multi spectral display

第 3 表　カオリナイトを多く含む試料の検索および検索結果例 (a) 検索コマンド例 (b) 検索結果例
Table 3　An example of retrieval commands and the results for samples containing kaolinite

```
select unique sam.Sample_ID,sam.Site,lab.Measurement_ID,Kaolinite
from sam,chem,norm,xray,xraym,lab
where sam.Sample_ID = lab.Sample_ID and norm.Sample_ID = sam.Sample_ID and
 xray.Sample_ID = sam.Sample_ID and xray.Measurement_ID = xraym.Measurement_ID
 and xraym.Detected_mineral = 'kaolinite'
order by norm.Kaolinite desc/
```

(a)

sam. Sample_ID	!sam. Site	!lab. Measurement_ID!	norm. Kaolinite
KGa-1	!Washington County	!S0431 !	90.92000
KGa-2	!Warren County	!S0433 !	90.58000
860819F2	!Goshogake	!S0178 !	71.25000
860819F1	!Fukenoyu	!S0177 !	70.59000
851021-T1	!Goshogake	!S0061 !	64.00000
870216-S5	!Komatsu-jigoku	!S0236 !	62.46000

(b)

下にずらして表示することができる．複数の反射スペクトル値を上下にずらして表示したため，この図からは反射スペクトルの絶対値を読み取ることができない．このため，比較的反射スペクトルの平坦な波長を選んでその絶対値を数値で表示した．

4. 考察

テーブルをリレーショナル型データベースの第 1 正規形に保つため，岩石・鉱物のスペクトル・データを 8 個のテーブルにグループ分けした．このために，測定の種類毎にデータがグループ化され，今後予想される新しい測定方法によるデータにも柔軟に対応できると考えられる．一方，テーブル数が多くなったためデータベースを検索する際，テーブルの結合を頻繁に行う必要があり，検索が煩雑となった．これに対して，第 3 表 (a) のように，頻繁に行われる検索の手続きを登録することによって検索の煩雑さを軽減した．

今回は，X線回折においてX線強度がデジタル値で得られなかったため，X線強度を岩石・鉱物のスペクトル・データベースに格納することができなかった．X線強度をデータベースに格納することができれば，X線強度による鉱物の自動判定および鉱物量の推定が可能となると考えられる．

5. まとめ

岩石・鉱物のスペクトルの研究を行うために，岩石・鉱物のスペクトル・データベース・システムを構築した．岩石・鉱物のスペクトル・データベース・システムを構築することによって，柔軟な検索条件で岩石・鉱物のスペクトル・データを検索・表示することが可能となり，岩石・鉱物のスペクトルと化学分析値や鉱物の含有量の関係を考察するのに役立った．

岩石・鉱物のスペクトル・データベース・システムを構築するにあたり，データ・モデルとしてデータ利用の柔軟性が最も高いリレーショナル型を採用した．岩石・鉱物のスペクトル・データベース・システムによって，多数の試料に対するスペクトル値および試料収集時の記載や化学分析値等属性データを整理し，効率良く格納・検索することができた．

文 献

五十嵐俊雄 (1984) 粘土質試料のノルム計算．地質ニュース，vol.353, p.37-47.

Kahle, A. B., Goetz, A. F. H., Paley, H. N., Alley, R. E. and Abbott, E. A. (1981) A data base of geologic field spectra. *Proceedings of the Fifteenth International Symposium on Remote Sensing of Environment*, p.329-337.

Silva, L. F. (1979) Spectral Data Systems. *Remote Sensing The Quantitative Approach*, McGRAW-HILL, New York, p.63-76.

浦井 稔・佐藤 功・二宮芳樹・古宇田亮一・宮崎芳徳・山口 靖(1989) 可視～短波長赤外域における岩石・鉱物の反射スペクトル・カタログ．工業技術院地質調査所

――・――・――・――・――・――(1992) 可視～短波長赤外域における粘土・炭酸塩岩の反射スペクトルとその特徴．地調報告，no.278, p.11-26

Yamaguchi, Y. and Lyon, R. J. P. (1986) Identification of clay minerals by feature cording of near-infrared spectra. *Proceedings of the International Symposium on Remote Sensing of Environment Fifth Thematic Conference*, p.627-636.

地質調査所報告第278号，p.11-26, 1992
Rept. Geol. Surv. Japan, No.278

可視～短波長赤外域における粘土・炭酸塩岩の反射スペクトルとその特徴

浦井　稔*・佐藤　功*・二宮芳樹*・古宇田亮一**・宮崎芳徳***・山口　靖***

Visible to short-wave infrared spectra and spectral features of clay and carbonate samples

By

Minoru URAI, Isao SATO, Yoshiki NINOMIYA, Ryoichi KOUDA,
Yoshinori MIYAZAKI and Yasushi YAMAGUCHI

Abstract: Bidirectional Reflection factor in visible to short-wave infrared (0.5 μm–2.5 μm) were measured in natural surface of clay samples and carbonates. X-ray diffraction analysis and chemical analysis were done to confirm the detected mineral with spectral measurements. Most of clay samples were collected in some geothermal areas, metal mining areas and clay mines in Japan. Carbonate rocks were collected in carbonate mines in Japan. The observed spectral minima of natural surfaces according to OH, H_2O and CO_3 absorption were corresponding to published spectral minima of powdered samples. In the moist samples, level of reflection was decreased and spectral features of mineral were covered with water absorption especially near 1.4 and 1.9 μm. It was found that the spectral features near 2.2 μm were more detectable than ones near 1.4 and 1.9 μm in the moist samples.

要　旨

リモートセンシングによる資源探査の基礎資料として，可視～短波長赤外域 (0.5-2.5 μm) における粘土・炭酸塩岩の反射スペクトルを測定し，さらに，化学分析やX線回折法による鉱物の同定を行なった．これを基にして，可視～短波長赤外域における粘土・炭酸塩岩と反射スペクトルの特徴について考察した．この結果，吸収帯の位置は既存の結果と一致したが，試料に含まれる水分が多い場合は全体の反射係数が低下し，1.4 μm および 1.9 μm 付近においては鉱物本来の反射スペクトルの特徴を覆い隠すことがわかった．しかし，水分が多い場合でも 2.2 μm 帯の反射スペクトルの特徴は検出可能であることがわかった．

1. まえがき

岩石・鉱物の反射スペクトルはリモートセンシングによる資源探査の基礎資料として不可欠である．特に，可視～短波長赤外域 (0.5-2.5 μm) は，太陽の放射エネルギーが極大となること，大気の窓の一つにあたること，粘土・炭酸塩岩が特徴的な反射スペクトルを示すことなどから，注目されている．Hunt and Salisbury (1970) などによって，粘土・炭酸塩岩を含む多数の岩石・鉱物の反射スペクトルが明らかにさ

*地殻物理部，**鉱物資源部，***地殻熱部

Keyword: reflectance, visible, short-wave infrared, clay, carbonate

れたが，これらの測定には粉砕された試料が使用されているためリモートセンシングで観測される反射スペクトルとは異なると考えられる．このため，試料を加工することなく粘土・炭酸塩岩の反射スペクトルの測定を行い，さらに，化学分析やX線回折法による鉱物の同定を行い，これをデータベースに蓄積してきた（第1図）．その成果の一つとして反射スペクトル・カタログ（浦井ほか，1989）を出版し，さらに，反射スペクトル・データを公開（浦井，1989）した．本報告では，これを基にして可視～短波長赤外域における粘土・炭酸塩岩の反射スペクトルとその特徴について考察した．

2. 実　　験

2.1 試料の準備

ここで使用した試料は，主に秋田県（八幡平）・岩手県（八幡平）・宮城県（鬼首）・大分県（豊肥）の地熱地域で採集された粘土試料，茨城県（日立）・熊本県・鹿児島県の金属鉱床地域で採集された粘土試料，米国 Clay Minerals Society が提供する標準粘土試料，および，茨城県・福岡県（平尾台）の石灰石鉱山で採集された炭酸塩岩試料であり，その他に，国内の代表的粘土鉱山や北鹿の黒鉱鉱床周辺の試料および中国の粘土鉱山の試料も若干含まれる．試料数は，粘土試料が約80個，炭酸塩岩試料が約30個である．試料の形状は，Clay Minerals Society の標準粘土試料は粉末，その他の粘土試料は室内乾燥した直径数mm ～ 数cmの土塊状，炭酸塩岩試料は直径10cm ～20cmの塊状である．これらの試料は，資源探査で重要な鉱物である粘土鉱物や炭酸塩鉱物を含む．

2.2 反射スペクトルの測定

物体の反射特性を表す量には，反射率 ρ_λ，二方向性反射率 $d\rho_\lambda(\theta, \phi ; \theta', \phi')$ および二方向性反射係数 $R_\lambda(\theta, \phi ; \theta', \phi')$ 等がある．これらの量は，いずれも，波長 λ の関数である．

反射率 ρ_λ は入射放射束を Φ_λ，反射放射束を Φ'_λ とすれば

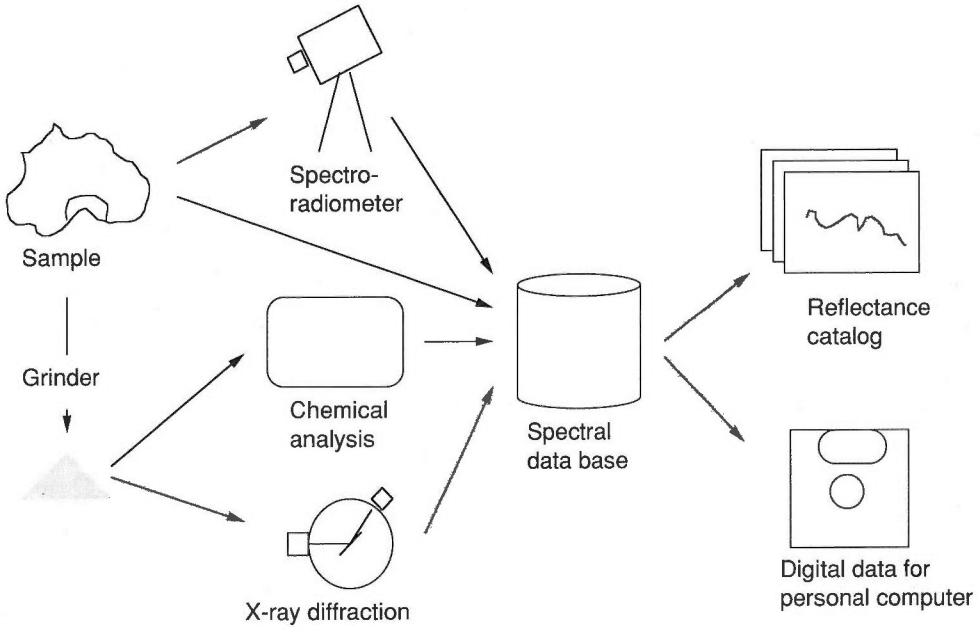

第 1 図　反射スペクトル測定の概要
Fig. 1　The outline of spectrum measurements.

$$\rho_\lambda = \frac{\Phi'_\lambda}{\Phi_\lambda} \tag{1}$$

で表される．反射率 ρ_λ を求めるためには，面に入射する全ての放射束および反射する放射束を測定する必要がある．

二方向性反射率 $d\rho_\lambda(\theta, \phi\ ;\ \theta', \phi')$ は，θ, ϕ 方向からの入射放射束を $d\Phi_\lambda(\theta, \phi)$ とし，θ', ϕ' 方向に反射する反射放射束を $d\Phi'_\lambda(\theta', \phi')$ とすれば

$$d\rho_\lambda(\theta, \phi\ ;\ \theta', \phi') = \frac{d\Phi'_\lambda(\theta', \phi')}{d\Phi_\lambda(\theta, \phi)} \tag{2}$$

で表される．一方，θ, ϕ 方向からの放射照度 $E_\lambda(\theta, \phi)$ および θ', ϕ' 方向に反射する放射輝度 $L_\lambda'(\theta', \phi')$ は，反射面の微小面積を dA，微小立体角を $d\Omega'$とすれば

$$E_\lambda(\theta, \phi) = \frac{d\Phi_\lambda(\theta, \phi)}{dA}, \qquad L_\lambda'(\theta', \phi') = \frac{d\Phi'_\lambda(\theta', \phi')}{dA \cdot d\Omega' \cdot \cos\theta'} \tag{3}$$

で表される．従って，二方向性反射率 $d\rho_\lambda(\theta, \phi\ ;\ \theta', \phi')$ は

$$d\rho_\lambda(\theta, \phi\ ;\ \theta', \phi') = \frac{L_\lambda'(\theta', \phi') \cdot d\Omega' \cdot \cos\theta'}{E_\lambda(\theta, \phi)} \tag{4}$$

で表される．

二方向性反射係数 $R_\lambda(\theta, \phi\ ;\ \theta', \phi')$ は，完全拡散反射体の二方向性反射率を $d\rho_{r\lambda}(\theta, \phi\ ;\ \theta', \phi')$，試料の二方向性反射率を $d\rho_{t\lambda}(\theta, \phi\ ;\ \theta', \phi')$ とすれば

$$R_\lambda(\theta, \phi\ ;\ \theta', \phi') = \frac{d\rho_{t\lambda}(\theta, \phi\ ;\ \theta', \phi')}{d\rho_{r\lambda}(\theta, \phi\ ;\ \theta', \phi')} \tag{5}$$

で表される．この時，両者の放射照度が同一の条件で測定を行った場合，二方向性反射係数 $R_\lambda(\theta, \phi\ ;\ \theta', \phi')$ は，完全拡散反射体の放射照度を $L_{r\lambda}'(\theta', \phi')$，試料の放射照度を $L_{t\lambda}'(\theta', \phi')$ とすれば

$$R_\lambda(\theta, \phi\ ;\ \theta', \phi') = \frac{L_{t\lambda}'(\theta', \phi')}{L_{r\lambda}'(\theta', \phi')} \tag{6}$$

で表される．従って，二方向性反射係数 $R_\lambda(\theta, \phi\ ;\ \theta', \phi')$ は完全拡散反射体と対象物の放射輝度を測定することによって得られる．

本報告では，測定機の都合上，標準反射板を完全拡散反射体とした二方向性反射係数 $R_\lambda(\theta, \phi\ ;\ \theta', \phi')$ を測定した．なお，本論文では，二方向性反射係数 $R_\lambda(\theta, \phi\ ;\ \theta', \phi')$ を反射スペクトルと称する．

反射スペクトルの測定には，GER (Geophysical Environmental Research) 社 IRIS (InfraRed Intelligent Spectroradiometer) スペクトロラジオメータを使用し，光源にはタングステンランプを，標準反射板には Kodak 社の $BaSO_4$ 塗料 (Kodak white reflectance coating 6080) を高粘度スプレー (Kodak Laboratory Sprayer 13270) でアクリル板に吹き付けたものを使用した．第2図にスペクトロラジオメータの概要を示す．以下に IRIS の概要を示す．

Spectral Bandwidth:	2nm in 350nm to 1.0 μm region,4nm in the 1.0 to 3.0 μm region.
Spectral Range:	350nm to 3.0 μm.
Field of View:	3×6 degrees.
Scan Time:	1.5 minutes to longer than 10 minutes.

試料および標準反射板をならべて床に置き，約 60cm の高さに両者を均等に照らす様に光源を設置し，

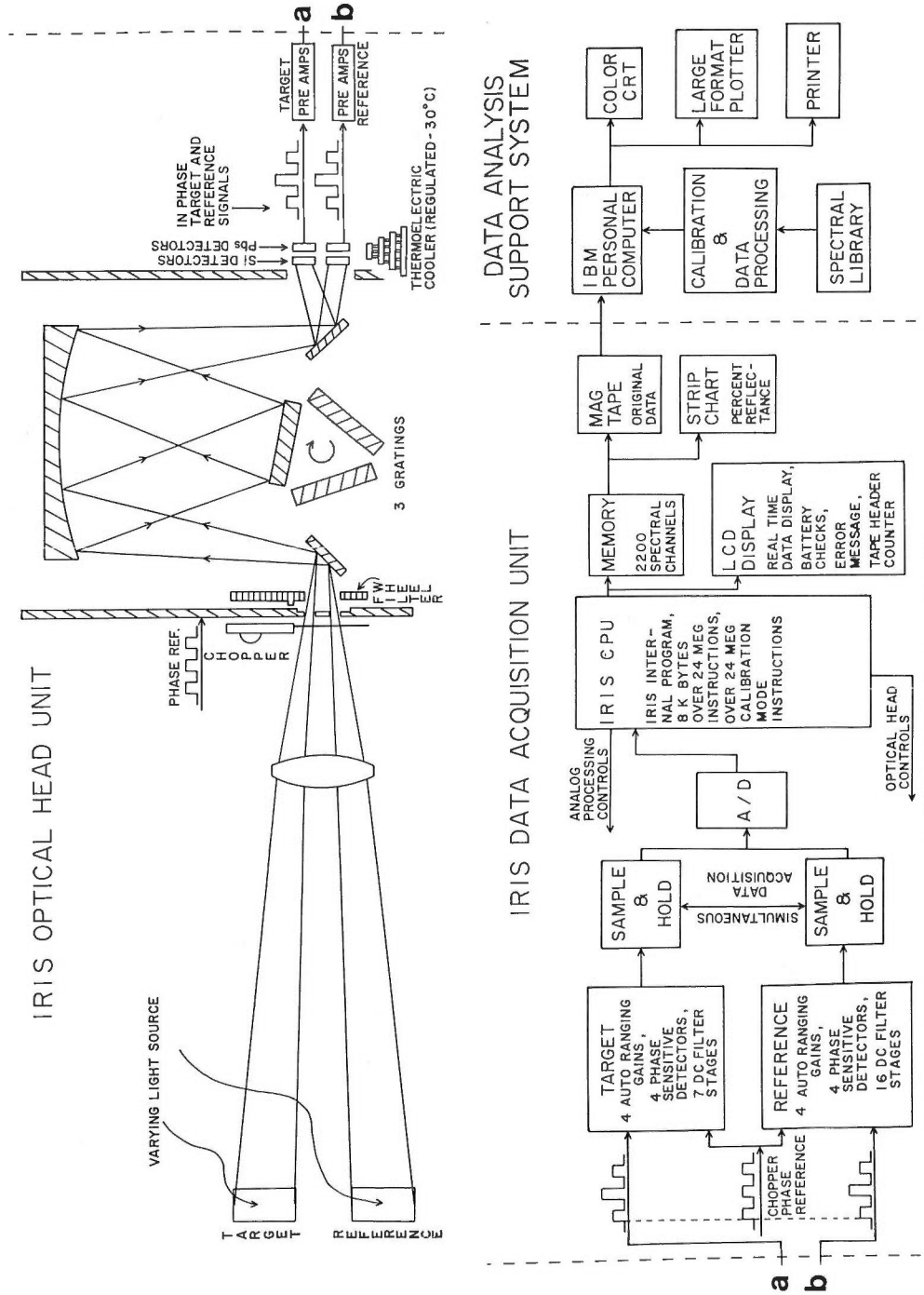

第 2 図　スペクトロラジオメータの概要
Fig. 2　The outline of spectroradiometer.

第 1 表　化学分析値の比較
(a) Haydn (Van Olphen and Fripiat, 1979) の結果と今回の Chemex Labs の結果
(b) H_2O+, H_2O-, -550 および 550-1000 の値を除外して正規化した場合

Table 1　Comparison of chemical analysis.
(a) Comparison with Haydn (Van Olphen and Fripiat, 1979) and Chemex Labs in this study.
(b) Normalized without H_2O+, H_2O-, -550 and 550-1000

(a)

	KGa-1		KGa-2		SWy-1		STx-1		SAz-1		Syn-1		PFl-1	
	MH	CH	MH	CH	MH	CH	MH	CH	MH	CH	MH	CH	MH	CH
SiO_2	44.20	44.15	43.90	43.57	62.90	57.68	70.10	62.11	60.40	51.75	49.70	47.05	60.90	55.46
TiO_2	1.39	1.51	2.08	2.11	0.090	0.10	0.22	0.20	0.24	0.19	0.023	0.01	0.49	0.43
Al_2O_3	39.70	38.71	38.50	37.72	19.60	17.86	16.00	13.84	17.60	15.40	38.20	35.92	10.40	9.44
Fe_2O_3	0.13	0.25	0.98	1.11	3.35	3.67	0.65	0.73	1.42	1.39	0.02	0.06	2.98	3.13
FeO	0.08	0.01	0.15	0.02	0.32	0.20	0.15	0.02	0.08	0.02		0.01	0.40	0.17
MnO	0.002				0.006	0.01	0.009	0.01	0.099	0.08			0.058	0.03
MgO	0.03	0.03	0.03	0.05	3.05	2.49	3.69	3.20	6.46	5.37	0.014	0.22	10.20	8.95
CaO		0.07		0.05	1.68	1.54	1.59	1.55	2.82	3.12		0.11	1.98	1.79
Na_2O	0.013	0.14		0.11	1.53	1.60	0.27	0.43	0.063	0.23	0.26	0.46	0.058	0.20
K_2O	0.050	0.25	0.065	0.18	0.53	0.77	0.078	0.47	0.19	0.30		0.40	0.80	0.89
Li_2O											0.25			
P_2O_5	0.034	0.05	0.045	0.06	0.049	0.06	0.026	0.04	0.020	0.04	0.001	0.02	0.80	0.66
CO_2						0.62								
S			0.02		0.05		0.04				0.10		0.11	
F(§)									(0.287)					
F(*)											(0.76)			
Sub total	85.63	85.17	85.77	84.98	93.16	86.60	92.82	82.60	89.39	77.89	88.57	84.26	89.18	81.15
H_2O+		16.73		16.72		6.06		5.91		0.59		12.65		6.63
H_2O-		0.30		0.67		9.22		15.83		18.98		6.53		11.94
-550	12.60		12.60		1.59		3.32		7.54		8.75		8.66	
550-1000	1.18		1.17		4.47		3.22		2.37		2.40		1.65	
Total	99.41	102.20	99.54	102.37	99.22	101.88	99.36	104.34	99.30	97.46	99.72	103.44	99.49	99.72

MH : Haydn(Van Olphen and Fripiat, 1979)　CH : Chemex Labs in this study
F(§) : fluor by Thomas, not included in total ; F(*) : fluor included in ignition loss.

(b)

	KGa-1		KGa-2		SWy-1		STx-1		SAz-1		Syn-1		PFl-1	
	MH	CH	MH	CH	MH	CH	MH	CH	MH	CH	MH	CH	MH	CH
SiO_2	51.62	51.84	51.18	51.27	67.52	66.61	75.52	75.19	67.57	66.44	56.12	55.84	68.29	68.34
TiO_2	1.62	1.77	2.43	2.48	0.10	0.12	0.24	0.24	0.27	0.24	0.03	0.01	0.55	0.53
Al_2O_3	46.36	45.45	44.89	44.39	21.04	20.62	17.24	16.76	19.69	19.77	43.13	42.63	11.66	11.63
Fe_2O_3	0.15	0.29	1.14	1.31	3.60	4.24	0.70	0.88	1.59	1.78	0.02	0.07	3.34	3.86
FeO	0.09	0.01	0.17	0.02	0.34	0.23	0.16	0.02	0.09	0.03		0.01	0.45	0.21
MnO	0.00				0.01	0.01	0.01	0.01	0.11	0.10			0.07	0.04
MgO	0.04	0.04	0.03	0.06	3.27	2.88	3.98	3.87	7.23	6.89	0.02	0.26	11.44	11.03
CaO		0.08		0.06	1.80	1.78	1.71	1.88	3.15	4.01		0.13	2.22	2.21
Na_2O	0.02	0.16		0.13	1.64	1.85	0.29	0.52	0.07	0.30	0.29	0.55	0.07	0.25
K_2O	0.06	0.29	0.08	0.21	0.57	0.89	0.08	0.57	0.21	0.39		0.47	0.90	1.10
Li_2O											0.28			
P_2O_5	0.04	0.06	0.05	0.07	0.05	0.07	0.03	0.05	0.02	0.05	0.00	0.02	0.90	0.81
CO_2						0.72								
S			0.02		0.05		0.04				0.11		0.12	
Total	100.00	100.00	100.00	100.00	100.00	100.00	100.00	100.00	100.00	100.00	100.00	100.00	100.00	100.00

MH : Haydn(Van Olphen and Fripiat, 1979)　CH : Chemex Labs in this study

約60cmの高さにスペクトロラジオメータを設置して測定を実施した．この時，光源の方向 θ, ϕ およびスペクトロラジオメータの方向 θ', ϕ' は測定しなかった．スペクトルを測定する面積は，スペクトロラジオメータを60cmの高さに設置した場合，約3×6cmである．測定した反射強度を GER 社が提供するソフトウェアでゲイン・暗電流等を補正し標準反射板に対する二方向性反射係数 (Bidirectional Reflection factor) を計算した．

2.3 化学分析

すでに，化学分析が実施された試料 (16個) を除く試料について，試料の一部を粉末化してカナダ Chemex Labs 社に依頼して誘導結合高周波プラズマ分光分析法 (ICP) 等によって化学分析を行った．

第 2 表　粘土ノルム計算の対象となる鉱物 (五十嵐, 1984)
Table 2　Minerals for Norm calculation (Igarashi, 1984)

Symbol	Name of mineral	Chemical composition
ab	Albite	$Na_2O \cdot Al_2O_3 \cdot 6SiO_2$
ad	Andalusite	$Al_2O_3 \cdot SiO_2$
al	Alunite	$K_2O \cdot 3Al_2O_3 \cdot 4SO_3 \cdot 2H_2O$
an	Anorthite	$CaO \cdot Al_2O_3 \cdot 2SiO_2$
ap	Apatite	$10CaO \cdot 3P_2O_5 \cdot H_2O$
C	Corumdum	Al_2O_3
cc	Calcite	$CaO \cdot CO_3$
ch	Chlorite	$5MgO \cdot Al_2O_3 \cdot 3SiO_2 \cdot 4H_2O$
cm	Chromite	$FeO \cdot Cr_2O_3$
dp	Diaspore	$Al_2O_3 \cdot H_2O$
en	Enstatite	$MgO \cdot SiO_2$
fr	Fluorite	CaF_2
gi	Gibbsite(Boemite)	$Al_2O_3 \cdot 3H_2O$
he	Hematite	Fe_2O_3
hl	Halite	NaCl
il	Ilmenite	$FeO \cdot TiO_2$
ka	Kaolinite	$Al_2O_3 \cdot 2SiO_2 \cdot 2H_2O$
li	Limonite	$Fe_2O_3 \cdot H_2O$
mg	Magnesite	$MgO \cdot CO_3$
mi	Microcline	$K_2O \cdot Al_2O_3 \cdot 6SiO_2$
mo	Montmorillonite	$Na_{.33} \cdot MgO \cdot Al_2O_3 \cdot 4SiO_2 \cdot 4H_2O$
mt	Magnetite	$FeO \cdot Fe_2O_3$
pp	Pyrophyllite	$Al_2O_3 \cdot 4SiO_2 \cdot H_2O$
pr	Pyrite	FeS_2
Q	Quartz	SiO_2
ru	Rutile	TiO_2
sd	Siderite	$FeO \cdot CO_3$
se	Sericite	$K_2O \cdot 3Al_2O_3 \cdot 6SiO_2 \cdot 2H_2O$
th	Thernardite	$Na_2O \cdot SO_3$
Z	Zircon	$ZrO_2 \cdot SiO_2$

第 3 表　X線回折実験時の測定パラメタ
Table 3　Parameter for X-ray diffraction measurements.

Target,Filter	Cu,Ni
Voltage,Current	40kV,100～140mA
Full Scale Count	4000cps
Time Constant	0.2sec
Scanning Speed	8° 2θ/min
Chart Speed	80mm/min
Angle Range	70～2° 2θ
Divergence Slit	1°
Scatter Slit	1°
Receiving Slit	0.3

今回の分析の精度を検討するために，Clay Minerals Society が提供するサンプルについて，今回の分析値とすでに公表された結果 (Van Olphen and Fripiat, 1979) を比較した（第 1 表 (a)). KGa-1, KGa-2 については両者の分析値は H_2O+ および H_2O- の値を除いて 1%以内に一致している．Syn-1 については，3%以内に一致している．SWy-1, STx-1, SAz-1, および，PF1-1 については，Van Olphen and Fripiat (1979) の分析値に比較して今回の分析値は，SiO_2 が 5%-9%, Al_2O_3 が 1%-3%少なく，H_2O+ と H_2O- を加えた値は-550 と 550-1000 を加えた値に比較して 7%-10%多い．これは，他の比較した全ての試料についても同様の傾向が見られることや，試料が粉末試料であることから，試料が保管中に 8%～15%の水分を吸収したものと考えられる．水分量を補正すれば，両者の分析値は± 2 %以内に一致する（第 1 表 (b)).

化学分析値から五十嵐 (1984) の方法を使用して粘土ノルム値を計算した．五十嵐の方法は，第 2 表に示す曹長石 (ab) 以下の 30 鉱物を対象に行われる．このため，試料中にこれら以外の鉱物が含まれている場合は，この 30 種の鉱物のどれかに誤認される場合があるので注意を要する．

2.4 X線回折

すでにX線回折が実施された試料 (8 個) を除く試料についてX線回折を実施した．X線回折は，化学分析のために粉末化したサンプルを理学電機 (株) 製のX線回折装置 (RAD-rA) を使用して不定方位で行った．X線チャートの解析はあらかじめ用意した数種類の標準X線チャートと重ね合わせることによって同定する機械的作業にとどめ詳細な解析は行っていない．第 3 表にX線回折データ測定時のパラメタを示す．

第 4 表　X線回折で検出された鉱物と反射スペクトルから検出された鉱物の比較
Table 4　Minerals detected with X-ray diffraction and minerals detected with spectra.

	mo	ka	pp	se	al	ca
X	13	25	6	16	7	28
R	19	18	6	15	1	27
X&R	7	16	6	11	1	27
X/(X&R) (%)	54	64	100	69	14	96
R/(X&R) (%)	37	89	100	73	100	100

X: numbers of samples detected with Xray diffraction
R: numbers of samples detected with reflectance factor
X&R: numbers of sample detected both with Xray diffraction and reflectance factor
mo: montmorillonite, ka: kaolinite, pp: pyrophyllite, se: sericite, ca: calcite

3. 粘土・炭酸塩岩の反射スペクトルの特徴

粘土鉱物は，結晶構造内に OH 基および H_2O を含むために短波長赤外域に特徴的な吸収を示す (Hunt, 1979)．また，炭酸塩岩は，結晶構造内に CO_3 基を含むために同様の波長域に特徴的な吸収を示す (Hunt and Salisbury, 1971)．筆者らの測定においてもこれらの特徴的吸収を検知することができた．以下に，各鉱物の反射スペクトルの特徴を述べる．

3.1 モンモリロナイト (montmorillonite: $R^+(Al, Mg)_4Si_8O_{20}(OH)_4 \cdot nH_2O$)

モンモリロナイトの反射スペクトルは，1.91 μm，1.42 μm，2.21 μm 付近に顕著な吸収が見られる．第3図はモンモリロナイトを含む試料の反射スペクトルである．試料が水分を含む場合は，水の特徴である幅の広い吸収帯が 1.9 μm 付近および 1.4 μm 付近に見られ，これがモンモリロナイトの吸収帯と重

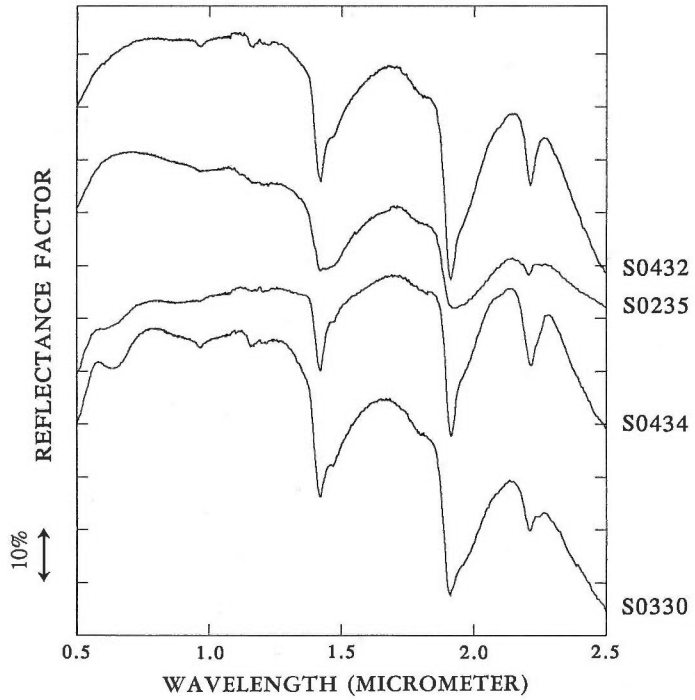

Sample-ID	Spectrum No.	Locality	Montmorillonite contents (%)	Reflectance at 1.0μm	Reflectance at 1.7μm (%)	H_2O+ (%)
STx-1	S0432	Gonzales county, Texas, USA	38	79.5	74.4	5.91
870216-S4	S0235	Yutsubu, Oita, Japan	34	30.8	23.7	10.30
SWy-1	S0434	Crook county, Wyoming, USA	29	65.2	69.0	6.06
KINBARA-4	S0330	Odo, Niigata, Japan	28	64.7	55.7	4.96

第 3 図　モンモリロナイトの反射スペクトル
各反射スペクトルは重なり合わないよう上下にシフトした．鉱物の含有量は五十嵐(1984) で計算した．

Fig. 3　Spectra of montmorillonites.
The spectra are displaced vertically. The mineral contents are calculated with Igarashi (1984)

なる．比較的多くの水分を含む 870216-S4 の試料についてこの影響が顕著である．

3.2 カオリナイト (kaolinite: $Al_4Si_4O_{10}(OH)_8$)

カオリナイトの反射スペクトル（第 4 図）は 1.4 μm 付近 2.2 μm 付近に特徴的な吸収ダブレットが見られる．さらに 0.95 μm 付近に小さな吸収ダブレットが見られる．試料が水分を含んでいる場合は，1.4 μm および 1.9 μm に水による幅の広い吸収が見られ，カオリナイトによる 1.4 μm のダブレットは検知できなくなるが，2.2 μm のダブレットは検知可能である．

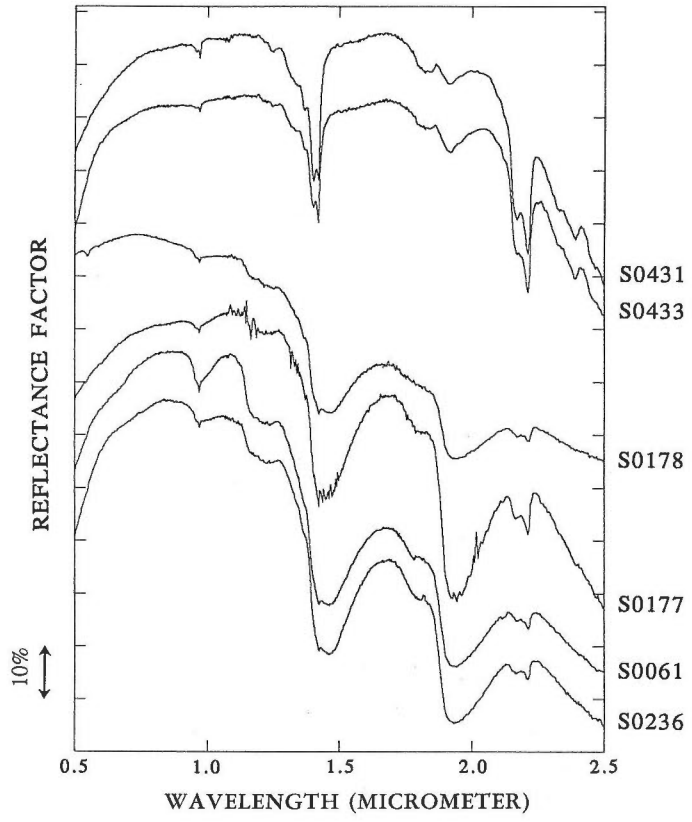

Sample-ID	Spectrum No.	Locality	Kaolinite contents (%)	Reflectance at 1.0μm	Reflectance at 1.7μm (%)	H_2O+ (%)
KGa-1	S0431	Washington county, Georgia, USA	91	86.6	87.3	16.73
KGa-2	S0433	Warren county, Georgia, USA	91	80.0	79.7	16.72
860819F2	S0178	Goshogake, Akita, Japan	71	43.1	22.9	12.09
860819F1	S0177	Goshogake, Akita, Japan	71	74.1	60.4	10.58
851021-T1	S0061	Goshogake, Akita, Japan	64	64.8	35.6	10.60
870216-S5	S0236	Komatsujigoku, Oita, Japan	62	64.1	37.3	10.46

第 4 図　カオリナイトの反射スペクトル
各反射スペクトルは重なり合わないよう上下にシフトした．鉱物の含有量は五十嵐(1984) で計算した．

Fig. 4　Spectra of kaolinites.
The spectra are displaced vertically. The mineral contents are calculated with Igarashi (1984)

3.3 葉ロウ石 (pyrophyllite: $Al_2Si_4O_{10}(OH)_2$)

1.40 μm 付近に非常に鋭く強い吸収が見られる．その他に，2.17 μm，1.92 μm，2.09 μm および 0.953 μm 付近に吸収が見られる（第5図）．試料に含まれる水分量が少ないためか，水による 1.4 μm および 1.9 μm における幅の広い吸収の影響は顕著でない．

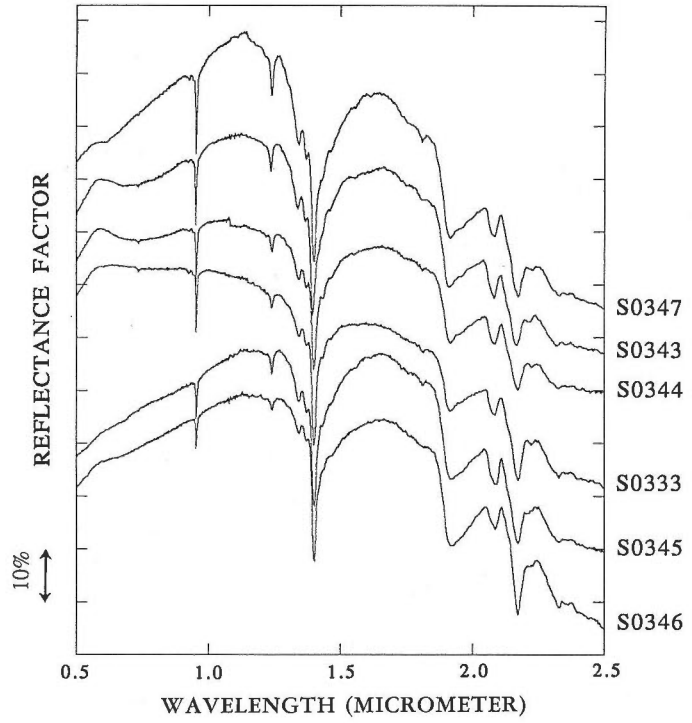

Sample-ID	Spectrum No.	Locality	Pyrophyllite contents (%)	Reflectance at 1.0μm	Reflectance at 1.7μm (%)	H_2O+ (%)
SUDO-5	S0347	Shinyo, Nagano, Japan	94	60.1	51.4	5.04
SUDO-1	S0343	China	94	45.3	40.1	5.24
SUDO-2	S0344	China	94	39.2	33.9	5.28
KINBARA-7	S0333	Mitsuishi, Okayama, Japan	76	49.4	37.7	4.10
SUDO-3	S0345	China	48	45.0	47.0	2.60
SUDO-4	S0346	China	43	54.2	51.2	2.61

第 5 図　葉ロウ石反射スペクトル
各反射スペクトルは重なり合わないよう上下にシフトした．鉱物の含有量は五十嵐(1984)で計算した．

Fig. 5　Spectra of pyrophyllites.
The spectra are displaced vertically. The mineral contents are calculated with Igarashi (1984)

3.4 絹雲母 (sericite: K_2 (Al, Fe^{3+}, Fe^{2+}, Mg) $_4$ (Si, Al) $_8O_{20}$ (OH, F) $_4$)

2.20 μm および 1.41 μm 付近にやや鋭い吸収が見られる．水分を含む場合は，1.4 μm および 1.9 μm 付近に幅の広い吸収が見られる（第 6 図）．

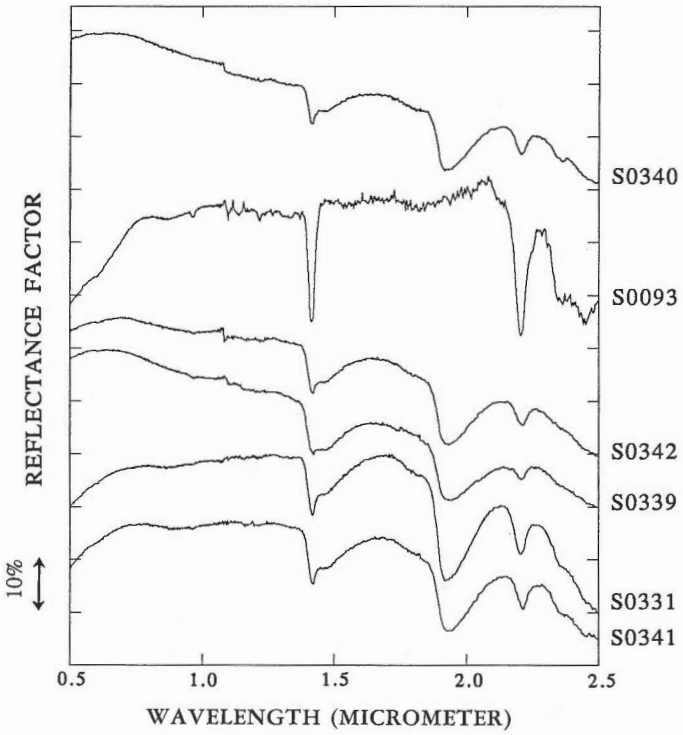

Sample-ID	Spectrum No.	Locality	Sericite contents (%)	Reflectance at 1.0μm	Reflectance at 1.7μm (%)	H_2O+ (%)
M86101113	S0340	Abeki, Aomori, Japan	38	42.7	35.7	2.72
860312-15:57	S0093	Hitachi, Ibaraki, Japan	37	83.6	84.4	2.58
M86101114	S0342	Abeki, Aomori, Japan	35	39.2	33.9	2.76
M86101115	S0339	Abeki, Aomori, Japan	35	33.6	24.3	3.47
KINBARA-5	S0331	Murakami, Niigata, Japan	32	62.3	63.2	2.52
M86101206	S0341	Hokuroku, Akita, Japan	31	49.5	46.9	2.34

第 6 図　絹雲母の反射スペクトル
各反射スペクトルは重なり合わないよう上下にシフトした．鉱物の含有量は五十嵐(1984) で計算した．

Fig. 6　Spectra of sericites.
The spectra are displaced vertically. The mineral contents are calculated with Igarashi (1984)

3.5 明ばん石 (alunite: $KAl_3(SO_4)_2(OH)_6$)

1.4 μm -1.5 μm にかけてやや幅の広いダブレットが見られる. その他に, 2.17 μm, 2.33 μm, 1.77 μm 付近に吸収が見られる (第 7 図). KINBARA-3 は明ばん石とカオリナイトを含む試料である. 水による 1.4 μm および 1.9 μm における幅の広い吸収の影響は顕著でない.

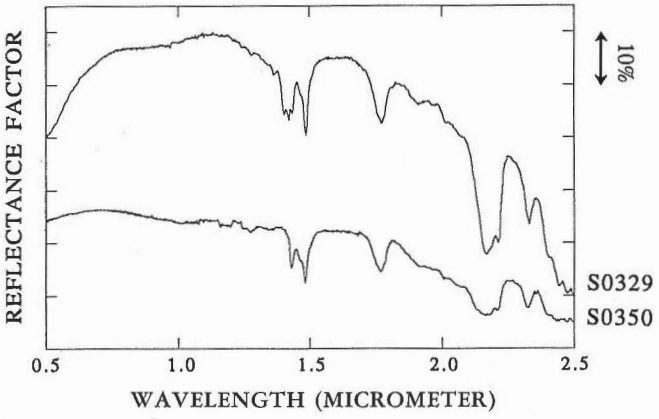

Sample-ID	Spectrum No.	Locality	Alunite contents (%)	Reflectance at 1.0μm	Reflectance at 1.7μm (%)	H_2O+ (%)
KINBARA-3	S0329	Kampaku, Tochigi, Japan	53	82.5	77.2	14.96
SUDO-8	S0350	Tochibara, Hyogo, Japan	47	24.7	22.4	6.40

第 7 図 明ばん石の反射スペクトル
各反射スペクトルは重なり合わないよう上下にシフトした. 鉱物の含有量は五十嵐(1984) で計算した.

Fig. 7 Spectra of alunites.
The spectra are displaced vertically. The mineral contents are calculated with Igarashi (1984)

3.6 方解石 (calcite: $CaCO_3$)

方解石は 2.35 μm 付近に CO_3 による強い吸収が見られる．その他に 2.55 μm, 2.17 μm, 2.0 μm, 1.88 μm に吸収が見られる（第 8 図）．試料に含まれる水分量が少ないためか，水による 1.4 μm および 1.9 μm における幅の広い吸収の影響は顕著でない．

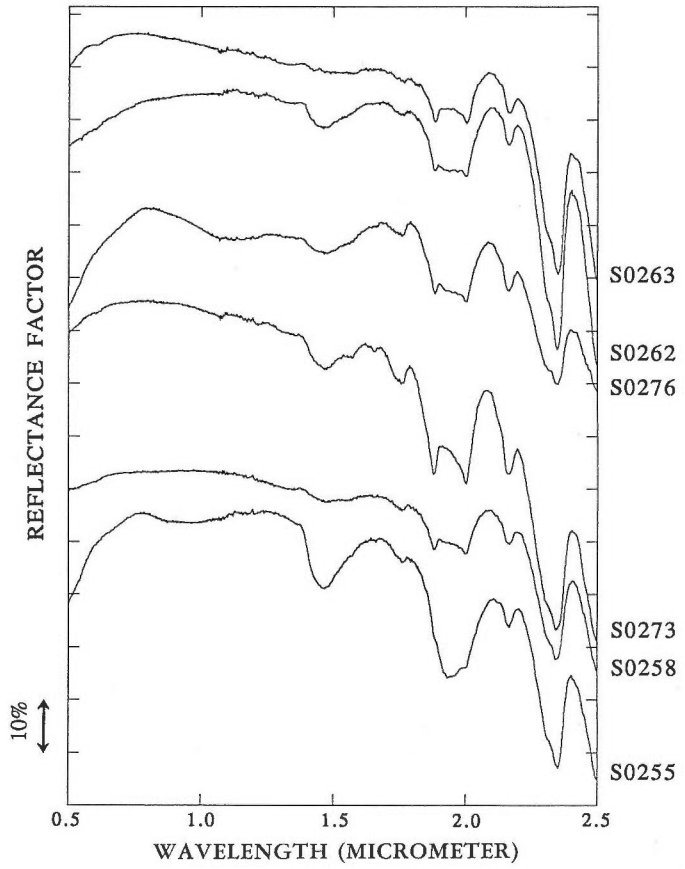

Sample-ID	Spectrum No.	Locality	Calcite contents (%)	Reflectance at 1.0μm	Reflectance at 1.7μm (%)	H_2O+ (%)
870218-S10	S0263	Tsunemi, Fukuoka, Japan	99	72.1	66.8	0.16
870218-S9	S0262	Kanda, Fukuoka, Japan	98	78.2	76.6	0.12
870219-S8	S0276	Kokura, Fukuoka, Japan	98	56.7	57.5	2.58
870219-S5	S0273	Kokura, Fukuoka, Japan	97	85.8	77.1	0.14
870218-S5	S0258	Kanda, Fukuoka, Japan	97	58.3	52.9	0.14
870218-S2	S0255	Hiraodai, Fukuoka, Japan	97	69.2	65.4	0.20

第 8 図　方解石の反射スペクトル
各反射スペクトルは重なり合わないよう上下にシフトした．鉱物の含有量は五十嵐(1984) で計算した．

Fig. 8　Spectra of calcites.
The spectra are displaced vertically. The mineral contents are calculated with Igarashi (1984)

4. 考　察

4.1 吸収帯位置

実験から検出された粘土鉱物・炭酸塩鉱物のおもな吸収帯の位置は以下のとおりである．これらの吸収帯の多くは，OH 基・H_2O および CO_3 基等の吸収によって起こるが，鉱物の種類によって微妙に吸収帯位置が異なっている．

鉱　物	吸収帯位置 (mm)				
モンモリロナイト	1.91	1.42	2.21		
カオリナイト	2.21	1.40	1.42	2.17	
葉ロウ石	1.40	2.17	1.92	2.09	0.953
絹雲母	2.20	1.41			
明ばん石	2.17	1.48	1.43	2.33	1.77
方解石	2.35	2.55	2.17	2.0	1.88

これらの吸収帯位置は，Hunt (1979) の結果と一致する．

4.2 水分の反射スペクトルにおよぼす影響

鉱物の反射スペクトルは，そのサンプルに含まれる水分量 (構造水をのぞく) に大きく影響されるため，鉱物の反射スペクトルと水分量に関する実験を行なった．まず，絹雲母を含む試料を約1ケ月，室内で自然乾燥させた．次に，これを粉末化して6等分し，1%-50%の水を加え，密封して24時間放置した後，反射スペクトルを測定した．絹雲母は，乾燥状態においては1.41 μm, 2.20 μm 付近に顕著な吸収が見られる．試料に含まれる水分が増えるにしたがって，1.4 μm および 1.9 μm 付近に水の吸収帯が現わ

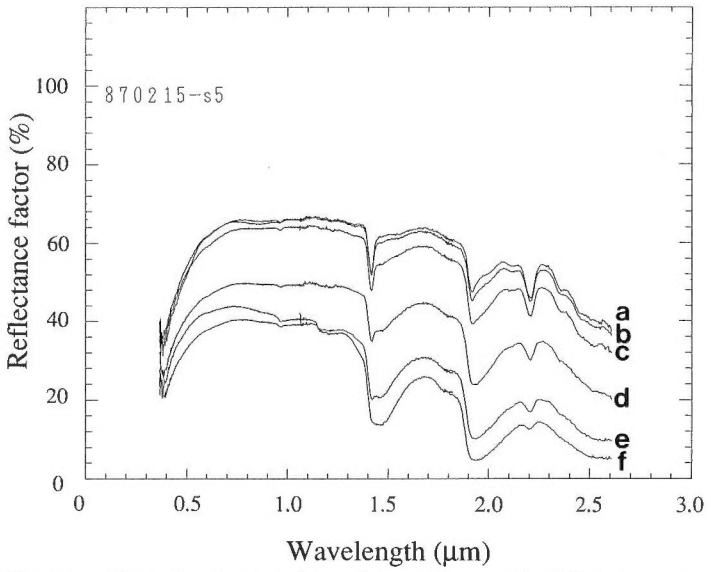

第 9 図　絹雲母を含む試料に 1.0%～50%の水分を加えた場合の反射スペクトル
a: 1%, b: 2%, c: 5%, d: 10%, e: 20%, f: 50%

Fig. 9　Spectra of samples containing sericite added 1.% to 50% humidities.
a: 1%, b: 2%, c: 5%, d: 10%, e: 20%, f: 50%

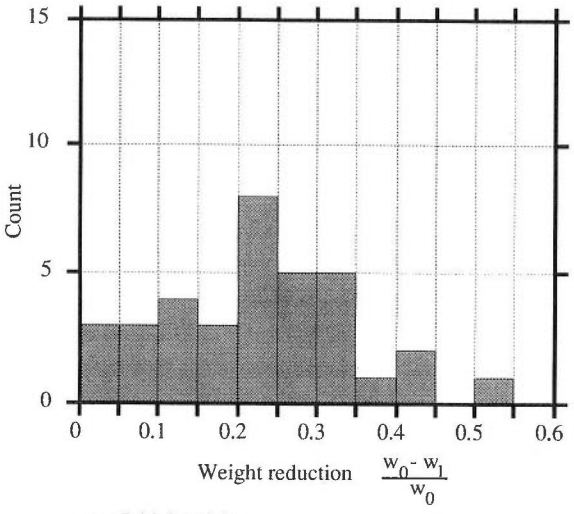

w_0: Initial weight
w_1: Weight after Air dried 68 days
Total nubmer of samples is 35
Average of weight reduction is 22.5%

第10図　室内乾燥による試料の減量
Fig. 10　Weight reduction for Air dry.

れ，これらの波長帯における絹雲母の反射スペクトルの特徴を覆い隠すが，2.20 μm 付近における吸収は検知可能である（第9図）．一方，1.4 μm および 1.9 μm 以外の波長においても，水分量の増加に伴って反射係数が減少し，その減少量は長波長側において大きい（第9図）．粘土試料を約2か月室内乾燥した場合の減少重量の平均は20%以上であり，40%を超える試料もある（第10図）．したがって，湿潤地域における粘土帯の反射係数は，水分の影響によって全体の反射係数が低下すること，1.4 μm および 1.9 μm 付近においては粘土鉱物の反射スペクトルの特徴が覆い隠されることが考えられる．

4.3 X線回折から検出された鉱物と反射スペクトルから検出された鉱物の比較

モンモリロナイト，カオリナイト，葉ロウ石，絹雲母，明ばん石および方解石を対象にして，X線回折で検出された鉱物と反射スペクトルで検出された鉱物を試料毎に比較した．まず，全試料について，X線チャートから対象となる鉱物が含まれるかどうか判定した．次に，反射スペクトルから，以下の基準で対象となる鉱物が含まれるかどうか判定した．

1) 1.91 μm，1.42 μm および 2.21 μm 付近に鋭い吸収があるものはモンモリロナイト
2) 2.21 μm および 2.17 μm に同程度の鋭い吸収があるものはカオリナイト
3) 1.40 μm 付近に非常に強く鋭い吸収があり 2.17 μm，1.92 μm，2.09 μm および 0.95 μm に吸収があるものは葉ロウ石
4) 2.20 μm および 1.41 μm に鋭い吸収があり，1.9 μm 付近には鋭い吸収がないものまたは 2.20 μm に鋭い吸収がありその他には鋭い吸収がないものは絹雲母
5) 1.48 μm，1.43 μm，1.77 μm および 2.33 μm に鋭い吸収があるものは明ばん石
6) 2.35 μm および 2.55 μm に鋭い吸収があるものは方解石

第4表にX線回折からモンモリロナイト，カオリナイト，葉ロウ石，絹雲母，明ばん石および方解石が検出された試料数X，反射スペクトルから同鉱物が検出された試料数R，X線回折および反射スペクトルの両方で同鉱物が検出された試料数X&R およびX&R/X，X&R/R を示す．

葉ロウ石および方解石についてはX線回折の結果と反射スペクトルによる結果が95%以上の高い確

率で一致した．これは，葉ロウ石および方解石が特徴的スペクトルを示すことと，水の反射スペクトルの影響をあまりうけなかったため，スペクトルの判定が容易であったことが考えられる．カオリナイトについては，X線回折の結果と反射スペクトルの結果は64%および89%の割合で一致した．これは，カオリナイトの反射スペクトルが試料に含まれる水分の反射スペクトルなどによって覆い隠されるものの，カオリナイトが2.2 μm 帯に特徴的スペクトルを示すことから比較的高い一致を示すと考えられる．モンモリロナイトについては，X線回折の結果と反射スペクトルの結果は54%および37%の割合で一致した．これはモンモリロナイトの反射スペクトルが試料に含まれる水分の反射スペクトルなどによって覆い隠されために，比較的低い一致を示すと考えられる．特に，水による1.4 μm および1.9 μm 付近の幅の広い吸収のために，1.91 μm および1.42 μm の鋭い吸収が検出できなくなり，絹雲母に誤認された試料も多い．絹雲母については，X線回折の結果と反射スペクトルの結果は69%および73%の割合で一致した．水分を多く含む使用においては，モンモリロナイトと絹雲母の反射スペクトルを判別することは難しいと考えられる．明ばん石については，試料数が少なく，意味のある結果は出ていない．

5. まとめ

リモートセンシングによる資源探査の基礎資料として，可視-短波長赤外域 (0.5-2.5 μm) における粘土・炭酸塩岩の反射スペクトルを測定し，さらに，化学分析やX線回折法による鉱物の同定を行った．これを基にして，可視-短波長赤外域における粘土・炭酸塩岩の反射スペクトルとその特徴について考察した．

この結果，試料を加工することなく測定した反射スペクトルの吸収帯の位置は既存の粉末試料を用いたスペクトル測定の結果と一致した．しかし，試料に含まれる水分が多い場合は全体の反射係数が低下し，1.4 μm および1.9 μm 付近においては鉱物本来の反射スペクトルの特徴を覆い隠すことがわかった．この場合でも，2.2 μm 帯の反射スペクトルの特徴は1.4 μm 帯および1.9 μm 帯の特徴に比較して検出が容易であることがわかった．

謝 辞

地質調査所の神谷雅晴氏・金原啓司氏・須藤定久氏・丸茂克美氏には貴重な試料および分析データの一部を提供していただきました．ここに感謝の意を表します．

文 献

Hunt, G.R. (1979) Near-infrared (1.3-2.4 μm) spectra of alteration minerals - potential for use in remotesensing. *Geophysics*, vol.44, p.1974-1986.

————and J.W. Salisbury (1970) Visible and near-infrared spectra of minerals and rocks: I. Silicate minerals. *Modern Geology*, vol.1, p.283-300.

————and———— (1971) Visible and near-infrared spectra of minerals and rocks: II.Carbonates. *Modern Geology*, vol.2, p.23-30.

五十嵐俊雄 (1984) 粘土質試料のノルム計算．地質ニュース，vol.353, p.37-47.

Van Olphen, H. and J.J. Fripiat (1979) Data handbook for clay materials and other non-metallic minerals. *Pegamon Press*, 345p.

浦井 稔 (1989) 岩石・鉱物の反射スペクトルデータとその表示ソフトウエア (PCSPEC). 地質調査所研究資料集，1989-139, 16p.

————・佐藤 功・二宮芳樹・古宇田亮一・宮崎芳徳・山口 靖 (1989) 可視～短波長赤外域における岩石・鉱物の反射スペクトル・カタログ．地質調査所，369p.

地質調査所報告第278号，p.27-38, 1992
Rept. Geol. Surv. Japan, No.278

地質調査所岩石標準試料“火成岩シリーズ”の中間赤外領域反射スペクトル

二宮芳樹* ・ 佐藤　功*

Mid-infrared reflectance spectra of GSJ rock reference samples "igneous rock series"

By

Yoshiki NINOMIYA and Isao SATO

Abstract: High resolution laboratory spectral measurements of thermal emissions show that reststraulen bands in the thermal infrared region observed for igneous rocks have a trend of systematic shift related to SiO_2 content. Multiband satellite sensors of the thermal emission from the earth's surface with much higher spatial resolution than the existing ones will start to operate in this decade, and should be able to detect these bands. Quantitative estimation of SiO_2 contents of the igneous rocks on the surface of the earth or the other planets by remote sensing technique will be possible. The authors present mid-infrared reflectance spectra of Geological Survey of Japan (GSJ) "igneous rock series" reference samples as the basic data in order to understand the variation of surface's SiO_2 content measured from space. These spectra are measured with a Fourier transform infrared (FTIR) spectrometer equipped with a "diffuse reflectance" accessory.

The results from this study are as follows:

(1) Reststraulen bands are observed in the spectral region from 8 to 14 μm for all samples. These bands systematically shift to longer wavelengths as the composition of the sample changes from acidic to ultrabasic. The correlation between the wavelength at the reststraulen maximum and SiO_2 content is very weak. This suggests that the value of the wavelength at the maximum alone is insufficient for the estimation of the SiO_2 content. Some nonlinear analytical approaches, for example, an approach applying an artificial neural network to the multiband data in this spectral region, can determine the spectral estimation of SiO_2 content with moderately high accuracy.

(2) Christiansen spectral minima are observed at the wavelength just shorter than the reststraulen region for all reflectance spectra of GSJ "igneous rock series" reference samples. The systematic shift of the spectral minima related to the compositional changes are recognized for the samples with the SiO_2 content of 60 % or lower, however, the correlation is not strong. The Christiansen spectral minima for the samples with the SiO_2 content of 60 % or higher seem not to correlate to the SiO_2 contents.

*地殻物理部

Keywords: remote sensing, thermal infrared, reflectance spectra, igneous rocks, silicate minerals, SiO_2 content, reststraulen bands, Christiansen frequency, FTIR, diffuse reflectance, TIMS, ASTER, Kirchhoff's law

要 旨

地球表面の熱放射を高空間分解能・複数バンドで観測する衛星搭載型センサーは，1990年代の稼働を目標に，現在開発が進められている．そのデータを有効に活用するための基礎データとして，地質調査所岩石標準試料“火成岩シリーズ”の中間赤外領域反射スペクトルを測定した．測定スペクトルに認められる残留線バンド・クリスチャンセン周波数はシリカ含有量と相関を示すが，その関係は単純なものではない．スペクトルから実用的な精度でシリカ含有量を定量的に推定するためには，複数バンドデータに対してある種の非線形アルゴリズムを適用する必要があるだろう．

1. はじめに

地質リモートセンシングにおいて，これまで主に用いられてきた波長領域は，可視・近赤外領域 (0.4～2.5 μm) である．この波長領域で観測されるスペクトル特徴は，鉱物中に存在する遷移元素の電子遷移や，鉱物に含まれる水酸基イオン・炭酸イオンの分子結合の倍音振動に起因するものである (G. R. Hunt, 1977)．それに対して，可視・近赤外領域と同様に地球大気の窓にあたる波長領域である熱赤外領域 (8～14 μm) を用いる地質リモートセンシングは，その有用性が度々指摘されてきたものの，地質応用に適した空間分解能 (100m 程度以下) を有する衛星搭載型熱赤外センサーとしては，このスペクトル領域を単一バンドで観測する LANDSAT Thematic Mapper の第6バンドが唯一のものであった．現在，高空間分解能 (100m 前後) でかつ複数バンドで観測する熱赤外リモートセンシングは，様々な科学技術分野で注目を集めている新技術である．航空機搭載型のセンサーとしては，これまでに，TIMS (Thermal Infrared Multispectral Scanner の略；Kahle and Goetz, 1983) をはじめいくつか開発されており，その地質応用への高い有効性が示されている．衛星搭載型のセンサーは，たとえば，1998年に NASA によって打ち上げられる予定の極軌道プラットフォームへの搭載が決定し，現在我が国で開発中である ASTER (Advanced Spaceborne Thermal Emission and Reflection Radiometerの略；津，1991) があり，その利用を想定した多くの基礎的な研究が行われている．地質分野においては，珪酸塩鉱物や主として珪酸塩鉱物で構成される火成岩において，熱赤外領域のスペクトルは，シリカ含有量と相関が高いということが，定性的に明らかにされている (たとえば，Lyon, 1963)．

熱赤外領域を含む中間赤外領域 (2.5～25 μm) の透過スペクトルは，有機化合物の構造解析に多く利用されており，その測定技術は確立されている．無機物・鉱物の透過スペクトルについても，分析を目的として多くの測定が行われており，スペクトルに観測される吸収バンドと構造の関係が明らかにされている (たとえば，J. M. Hunt *et al.*, 1950；Miller and Wilkins, 1952). Sadtler (1973) は，その集大成と言えるスペクトルカタログを発行した．Lyon *et al.* (1959) は，酸性の火成岩の透過スペクトルから，石英含有量・長石のタイプと含有量を定量する手法を開発した．J. M. Hunt and Turner (1953) は，石油探査への応用を目的として，堆積岩の透過スペクトルから鉱物組成を解析する手法について検討した．ただし，透過スペクトルをリモートセンシングで測定する事は不可能であるので，本報告での透過スペクトルに関するレビューは，この程度にとどめておく．

岩石・鉱物について，リモートセンシング手法を用いて観測できる放射スペクトルや反射スペクトルの測定・研究は，いくつかの例外 (例えば，Coblentz, 1905；Simon and MacMahon, 1953) を除けば，1960年代のアポロ計画を契機に活発になった．Lyon (1963) は，火成岩の組成が酸性から超塩基性に変化するのに従って，熱赤外領域の透過スペクトルや反射スペクトルに観測される，Si-O 伸縮基本振動に起因するブロードなピーク (残留線バンド) の波長が長波長側にシフトする事を示した．Lyon (1965) はまた，数種類の岩石について放射スペクトルを直接的に測定し，透過スペクトルや反射スペクトルにおいて認められたのと同様に，組成の変化に伴って残留線バンドがシフトすることを示した．Hovis and Callahan (1966) は，いくつかの火成岩・鉱物から用意した様々な粒子サイズのサンプルについて，熱赤

外を含む赤外領域の反射スペクトルを測定し，残留線バンドに認められる特徴を用いることにより，月やその他の天体の表面の性質をリモートセンシングによってマッピングできる可能性を示した．Aronson *et al.* (1967) は，いくつかの鉱物について，中間・遠赤外領域 (15～200 μm) の反射スペクトルを測定し，天体の組成マッピングへの応用の可能性を考察した．Conel (1969) は，粉末化した珪酸塩鉱物の透過あるいは放射スペクトルにおいて，残留線バンドのすぐ短波長側に観測されるピーク（クリスチャンセンピーク）の波長は，鉱物の同定における重要な特徴量となることを示した．Murcray *et al.* (1970) は，飛行船で月の表面の放射スペクトルを測定するシステムを開発し，6点でデータを取得した．Salisbury *et al.* (1970) は，そのデータの解釈を行った．Logan *et al.* (1973) は，粒子サイズ，背景温度，圧力，加熱の均質性などの様々な測定パラメータが熱赤外領域のスペクトルに与える効果について検討し，クリスチャンセン周波数は岩種の同定における有用な情報となることを示した．Vincent *et al.* (1975) は，いくつかの火成岩について測定した熱赤外領域の反射スペクトルとキルヒホッフの法則から導いた放射スペクトルを報告し，化学分析から得られる16ノルムとスペクトルの間には非常に高い相関関係があることを示した．Salisbury *et al.* (1987) は，珪酸塩鉱物を中心とする多くの鉱物の反射スペクトルを測定し，そのデータをディジタル形式で公表した．Salisbury *et al.* (1988) は，積分球を用いて，多くの火成岩の全球反射スペクトルを測定し，ディジタル形式で公表した．Walter and Salisbury (1989) は，化学分析結果から求められる SCFM 値は火成岩の種別の変化に関連したスペクトルの変化と高い相関を示すことを報告した．Bartholomew *et al.* (1989) は，風化の影響を考慮するために，自然状態の火成岩を中心とするいくつかの岩石について，野外用スペクトロメータを用いて放射スペクトルを測定した．

以上のような実験室内を中心とする測定から得られた研究成果を受けて，いくつかの熱赤外リモートセンシングシステムが開発された．これらのシステムによって取得されたデータは，風化の影響や温度・大気の効果が雑音として含まれているにも関わらず，岩石組成に関する情報を検出することができた．たとえば，Vincent *et al.* (1972 a), (1972b) は，熱赤外領域に2バンドを有するスキャナーを航空機に搭載して，珪岩分布地域と非珪酸塩岩地域を分類することができた．Lyon (1972) は，熱赤外分光計を航空機に搭載して地表のスペクトルを測定し，化学・鉱物組成との関係を示した．Prabhakara and Dalu (1976) は，Nimbus-4地球観測衛星に搭載された熱赤外分光計で取得されたデータを用いて，9 μm 帯における地球表面の放射率の全球マップを作成した．取得されたデータは非常に粗い空間分解能（約100km) であったにも関わらず，得られたマップは特に乾燥・半乾燥地帯において石英の分布密度と強い相関を示した．Kahle and Rowan (1980) は，熱赤外領域に6チャンネルを持つ航空機搭載型のスキャナーによって取得された画像データを用いて岩相マッピングを行い，珪酸塩岩と非珪酸塩岩の分類のみならず，珪酸塩岩の細分ができることを示した．Kahle and Goetz (1983) は，先の研究成果を受けて開発された TIMS で取得した画像データを解析し，シリカ含有量の変化にともなって残留線バンドの波長がシフトするという性質を利用して岩相分類を行い，マルチバンド熱赤外リモートセンシングの高いポテンシャルを示した．その後も，TIMS で取得された画像データを用いて多くの研究がなされ，その高い岩相識別能力が示されている（たとえば，Kahle, 1987; Lahren *et al.*, 1988; Kahle *et al.*,1988)．TIMS の成功を受けて，衛星搭載型の高空間分解能マルチバンド熱赤外スキャナーである ASTER の開発が，現在進められている（津，1991)．

筆者らは，G. R. Hunt and Salisbury (1974, 1975, 1976) が公表した一連の中間赤外スペクトルライブラリに含まれる火成岩の反射スペクトルと，Salisbury *et al.* (1988) が公表した火成岩の中間赤外反射スペクトルライブラリのディジタルデータを用いて，人工ニューラルネットワーク技術を応用することにより，火成岩の熱赤外領域における反射スペクトルからシリカ含有量を予測するシステムを開発した (Ninomiya and Sato, 1990)．また筆者らは，室内において岩石・鉱物の反射スペクトルを測定し，この測定データを上記のシリカ含有量予測システムに適応して，リモートセンシングデータからシリカ含有量を予測するための研究を進めている．本報告では，GSJ 岩石標準試料 “火成岩シリーズ” (Ando *et al.*, 1987) について測定した中間赤外領域反射スペクトルを示し，測定結果について考察を加える．

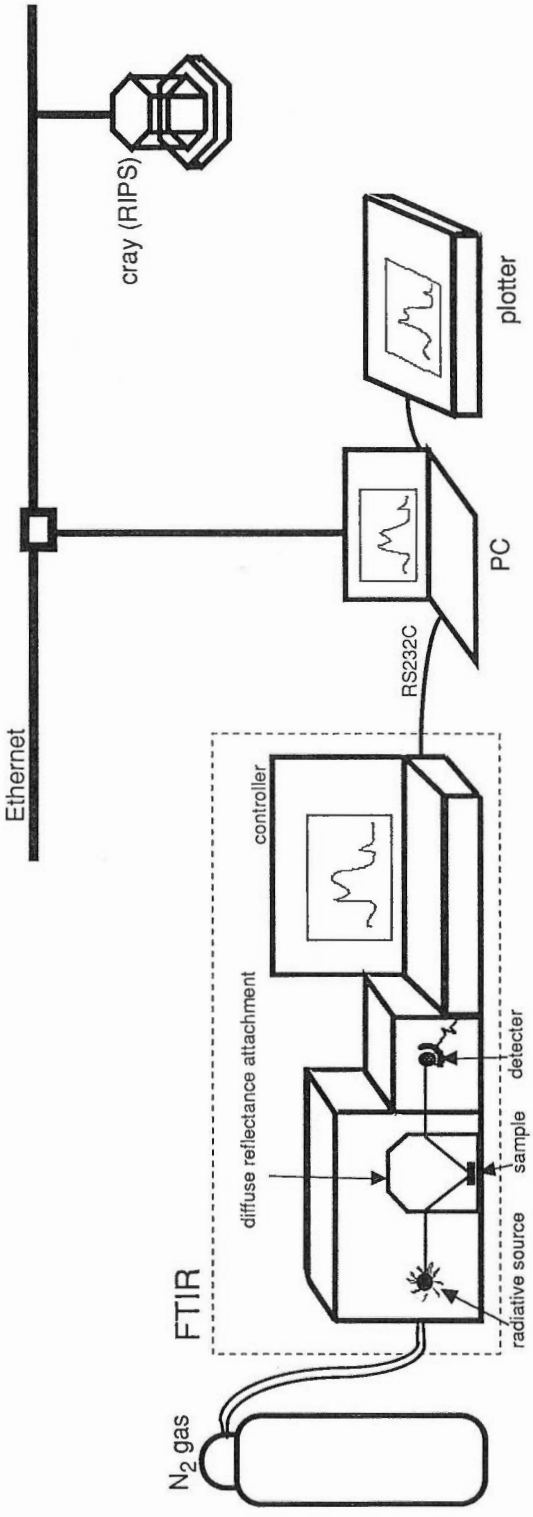

第1図 熱赤外リモートセンシングの基礎データとして岩石の中間赤外領域反射スペクトルを測定するための実験装置の概略図

Fig. 1 Illustration of equipment to measure mid-infrared reflectance spectra of rocks as the basic data for multiband thermal infrared remote sensing.

2. キルヒホッフの法則

受動的な方法による熱赤外リモートセンシングで観測されるスペクトルは，ターゲットの温度に相当するプランク曲線に沿った熱放射スペクトルである．地表の温度が正確に与えられれば，熱放射スペクトルから放射率スペクトルを正確に計算することができる．従って，マルチバンド熱赤外リモートセンシングの基礎データとして測定することが必要なデータは放射率である．しかしながら実験室における常温での放射率測定では，岩石試料からの放射強度は非常に弱いので，雑音となる背景からの放射強度が相対的に強くなってしまい，試料の放射率を求めることは難しい．また，試料を高温にして測定する場合においても，岩石試料と参照黒体の温度を正確に同一温度に保つことは困難である．以上の理由により，直接的に放射率を精度よく測定することは難しい．

さて，吸光率を a，放射率を e，反射率を r，透過率を t と表記した場合，熱平衡の状態におけるキルヒホッフの法則は，次式で与えられる．

$$a+r+t=1. \qquad (1)$$

地表または十分に厚い測定試料においては透過成分は存在しないので，

$$t=0. \qquad (2)$$

また，熱平衡状態においては，

$$a=e. \qquad (3)$$

(1)，(2)，(3) 式より，

$$e+r=1 \qquad (4)$$

が得られる．

(4) 式は，地表において仮定できる条件のもとに，放射率と反射率は互いに補完できる関係にあることを意味する．

反射率の測定方法は能動的であるので，直接的な放射率の測定と比較して，ずっと良好な信号対雑音比でデータを得ることができる．ただし，熱赤外域の反射率測定には光源部が必要となるので，装置が複雑になる．従って，実験室内において質の高いスペクトルを測定する場合には反射率の測定が，野外の自然状態にある試料を測定する場合には放射率の測定が適している．そのどちらも，マルチバンド熱赤外リモートセンシングの基礎データとして重要である．ここでは，実験室内において岩石・鉱物の反射率スペクトルを測定した結果を報告する．

3. 装　　置

第１図に，熱赤外領域を含む中間赤外領域の反射率スペクトルを測定するための実験装置の概略図を示す．

分光光度測定器として，マイケルソン型フーリエ変換赤外干渉計 (FTIR) を用いる．この分光器に拡散反射測定用付属装置を装着する．測定に用いた分光器では，測定の波数分解能は，離散的に 0.5 から 16cm^{-1}の範囲内で設定することができる．この分光器には，２種類の検知器が装着されている．１つが

TGS (硫酸三グリシン) 検知器で，もう1つが MCT (水銀カドミウムテルル) 検知器である．TGS 検知器は常温で動作し，2.17 から 25 μm (4600 から 400cm^{-1}) の波長領域に感度を持つ．MCT 検知器の有効感度波長領域は 2.17 から 16 μm (4600から625cm^{-1}) である．また，MCT 検知器は，液体窒素温度に冷却して使用する必要があるが，TGS 検知器と比較して，ずっと高感度である．

拡散反射測定用付属装置の光学系は，双円錐型である．すなわち，照射・集光それぞれを目的とした2枚の楕円鏡を用いることにより，試料表面で拡散反射した光を，大きな立体角で効率的に集光する．光源からの光は，試料表面において，約 1mm の直径に絞られる．一般に，このスケールにおいて岩石は均質ではない．従って，測定されるスペクトルは，対象岩石試料を代表するものとはいえない．この問題を解決するため，各岩石試料から数片の試料を用意し，それらのスペクトルの平均を，その岩石試料のスペクトルとして代表させる．

測定スペクトルには，大気中の水蒸気や二酸化炭素の吸収バンドが雑音として影響する．この影響をできるだけ取り除くため，乾燥窒素ガスによる試料室のパージを行う．測定したスペクトルは，RS232C 通信ポートを介して，パーソナルコンピュータに転送し，解析を行う．また，このパーソナルコンピュータに接続されたプロッタに解析結果を出力する．さらに高度な解析を行うために，格納したデータを，イーサネットを介して，工業技術院情報計算センター (RIPS) に接続された CRAY スーパーコンピュータに転送する．

4. データ取得

これまでの多くの研究により，珪酸塩鉱物や，主として珪酸塩鉱物で構成される火成岩において，熱赤外領域の反射スペクトルは，シリカ含有量と相関が高いことが，定性的に明らかにされている (たとえば，Lyon, 1963)．ここでは，GSJ 岩石標準試料 "火成岩シリーズ" (安藤，1986；Ando *et al.*, 1987) の熱赤外反射スペクトルを示す．

15種類の火成岩で構成されている，GSJ 岩石標準試料 "火成岩シリーズ" は，Ando *et al.*, (1987) による主成分・微量成分の分析をはじめ，国内外の関連研究機関において，様々な分析・測定が行われている．第1表に，GSJ 岩石標準試料 "火成岩シリーズ" の試料コード，岩石名，シリカ含有量をまとめ

第 1 表　地質調査所岩石標準試料 "火成岩シリーズ" の試料コード，岩石分類名とシリカ含有量(Ando *et al.*, 1987より)

Table 1　A list of sample code, petrographic description and SiO_2 content of GSJ rock reference samples, "igneous rock series" (Ando *et al.*, 1987).

試料コード	岩石名	シリカ含有量 (%)
JG-1a	花こうせん緑岩	72.19
JG-2	花こう岩	76.95
JG-3	花こうせん緑岩	67.10
JR-1	流紋岩 (黒曜石)	75.41
JR-2	流紋岩 (黒曜石)	75.65
JA-1	安山岩	64.06
JA-2	安山岩	56.18
JA-3	安山岩	62.26
JB-1	玄武岩	52.17
JB-2	玄武岩	53.20
JB-3	玄武岩	51.04
JGb-1	はんれい岩	43.44
JP-1	かんらん岩	42.39
JF-1	長石	66.64
JF-2	長石	65.20

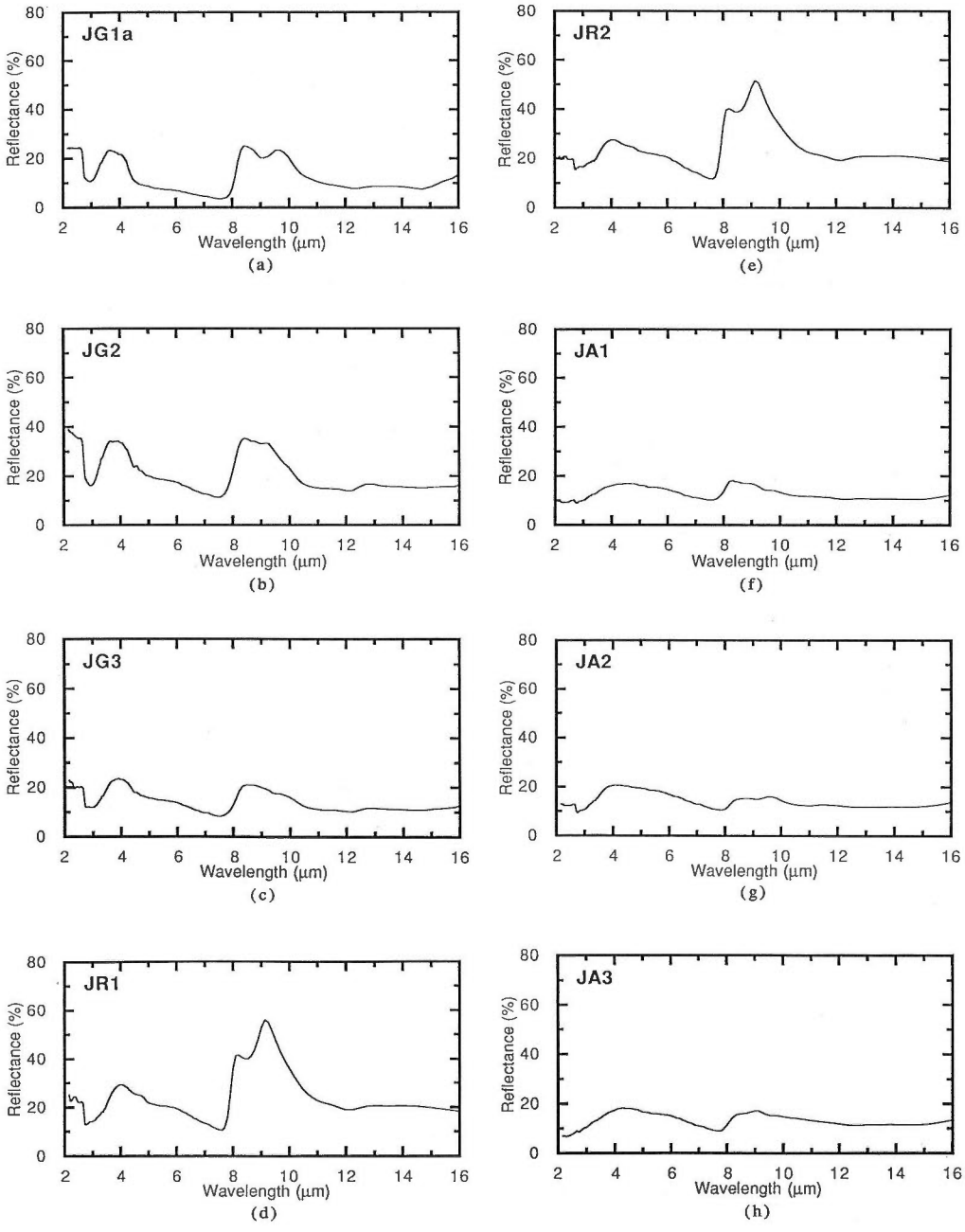

第 2 図　地質調査所岩石標準試料 “火成岩シリーズ” の中間赤外領域反射スペクトル
(a): JG-1a, (b): JG-2, (c): JG-3, (d): JR-1, (e): JR-2, (f): JA-1, (g): JA-2, (h): JA-3, (i): JB-1, (j): JB-2, (k): JB-3, (l): JGb-1, (m): JP-1, (n): JF-2.　試料コードは第 1 表にまとめた.

Fig. 2　Mid-infrared reflectance spectra of GSJ rock reference samples, “igneous rock series”.
(a): JG-1a, (b): JG-2, (c): JG-3, (d): JR-1, (e): JR-2, (f): JA-1, (g): JA-2, (h): JA-3, (i): JB-1, (j): JB-2, (k): JB-3, (l): JGb-1, (m): JP-1, (n): JF-2. These sample codes are listed in Table 1.

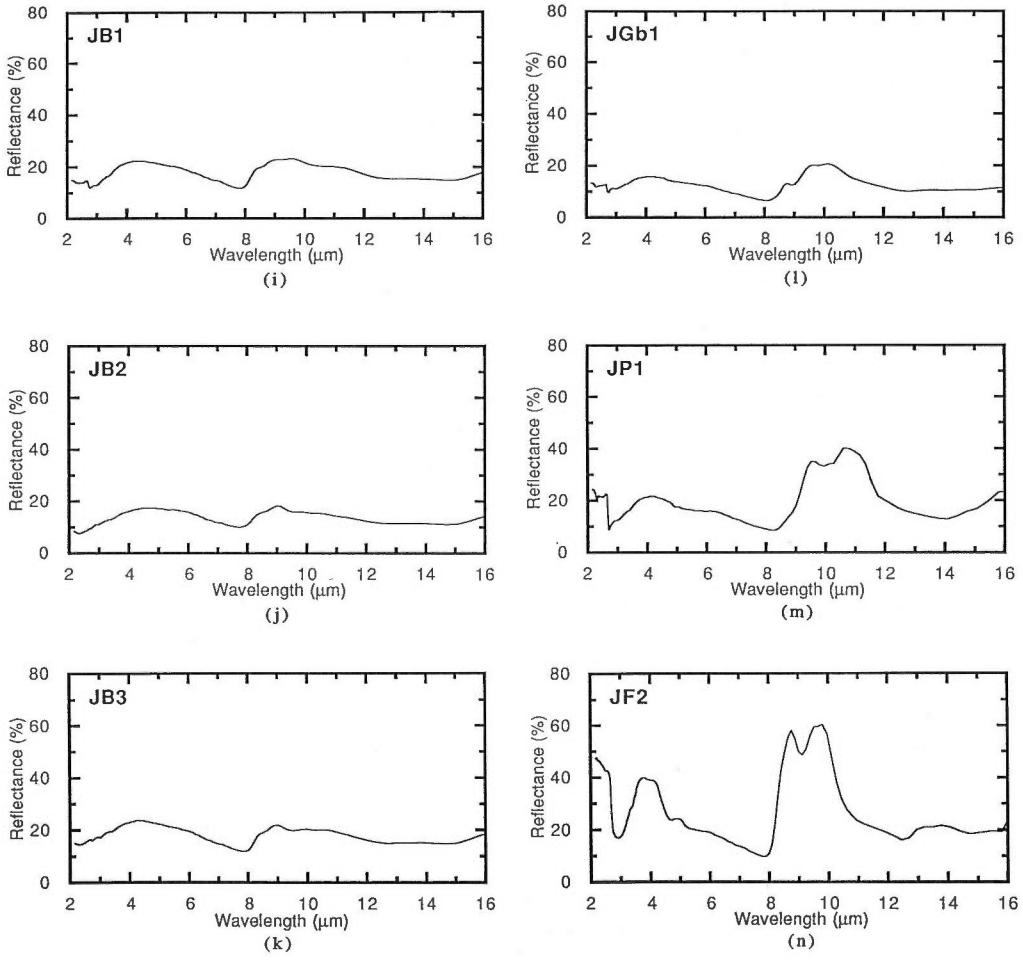

第 2 図 (続き)
Fig. 2 (continued)

る．ただし，JF-1 については，試料を入手できなかった．

ここでは，測定波長領域や波数分解能を犠牲にしても，良好な信号対雑音比を実現することを第一に優先して測定を行った．従って，TGS 検知器よりも高感度である MCT 検知器を用いた．測定波長領域は，2.17 から 16 μm である．また，波数分解能は，設定可能範囲で最も低い 16cm^{-1} に設定して測定した．波長分解能に換算すると，波長によって変化するが，10 μm において約 0.16 μm である．参照物質として，高純度臭化カリウム (KBr) をめのう乳鉢で細かくすりつぶした粉末を用いた．各岩石試料から 20 個の小片を用意し，それらのスペクトルの平均を試料のスペクトルとして代表させた．各小片の反射率スペクトルは，試料からの 32 走査回の反射光の平均スペクトルと参照物質からの 32 走査回の反射光の平均スペクトルの比で求める．

第 2 図に，GSJ 岩石標準試料“火成岩シリーズ”の中間赤外領域反射スペクトルを示す (ただし，JF-1 を除く)．

5. 考　察

測定したスペクトルから，以下のことがわかった．

(1) すべての試料の測定スペクトルにおいて，8から14 μm領域に，残留線バンドが観測された．また，残留線バンドは，シリカ含有量が少なくなるに従って，すなわち，組成が酸性から塩基性に変化するに従って，規則的に長波長側にシフトする事が確認された．この波長領域は，地球大気の窓に相当するので，この性質は，リモートセンシングに応用するうえで，非常に重要である．

第3図に，本稿に提示したスペクトルおよび，G. R. Hunt and Salisbury (1974) によるスペクトル，Salisbury *et al.* (1988) によるスペクトルから求めた，残留線バンド領域で反射率が最大となる波長とシリカ含有量の関係を示す．この図から，両者の間に明らかな逆相関が認められるものの，その相関は非常に弱いことがわかる．従って，反射率が最大となる一波長だけを情報として，精度よくシリカ含有量を予測することはできない．複数バンドデータを非線形アルゴリズムを用いて解析する手法を用いれば，適度な精度でシリカ含有量を予測することができる．たとえば，Ninomiya and Sato (1990) は，人工ニューラルネットワークを応用した手法の検討を行っている．

(2) すべての試料の測定スペクトルにおいて，残留線バンドのすぐ短波長側に，反射率が最小となる波数（クリスチャンセン周波数）が観測された．

第4図に，第3図と同じスペクトルデータセットから求めた，クリスチャンセン周波数に対応する波長とシリカ含有量の関係を示す．この図より，シリカ含有量が60%より小さいサンプルについては，シリカ含有量が小さいほどクリスチャンセン周波数が長波長側にシフトする事が認められる．両者の相関は，あまり強くはないが明瞭である．シリカ含有量が60%より大きいサンプルについては，シリカ含有量とクリスチャンセン周波数の間に相関は認められない．

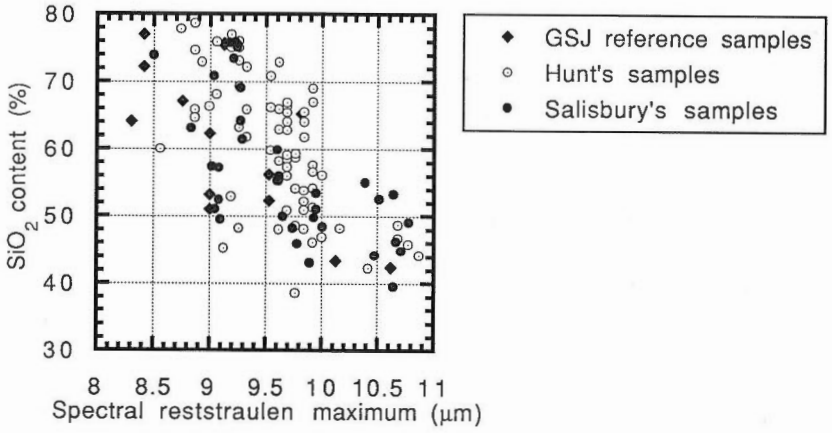

第 3 図　残留線バンド領域で最大値を示す波長とシリカ含有量の関係
図中 "GSJ reference samples" と示したデータは本報告で測定したスペクトルから得た．"Hunt's samples" と示したデータは Hunt and Salisbury (1972) で測定されたスペクトルから得た．"Salisbury's samples" と示したデータは Salisbury *et al.* (1988) で測定されたスペクトルから得た．

Fig. 3　Relationship between spectral reststraulen maximum and SiO_2 content of igneous rocks.
The data marked as "GSJ reference samples" are derived from the spectra measured in this report. The data marked as "Hunt's samples" are derived from the spectra measured by Hunt and Salisbury (1972). The data marked as "Salisbury's samples" are derived from the spectra measured by Salisbury *et al.* (1988).

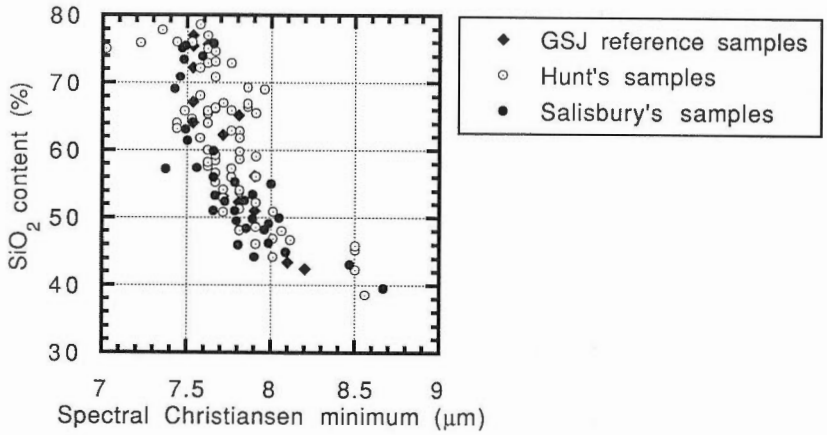

第 4 図　クリスチャンセン周波数とシリカ含有量の関係

図中 "GSJ reference samples" と示したデータは本報告で測定したスペクトルから得た．"Hunt's samples" と示したデータは Hunt and Salisbury (1972) で測定されたスペクトルから得た．"Salisbury's samples" と示したデータは Salisbury *et al.* (1988) で測定されたスペクトルから得た．

Fig. 4　Relationship between spectral Christiansen minimum and SiO_2 content of igneous rocks.

The data marked as "GSJ reference samples" are derived from the spectra measured in this report. The data marked as "Hunt's samples" are derived from the spectra measured by Hunt and Salisbury (1972). The data marked as "Salisbury's samples" are derived from the spectra measured by Salisbury *et al.* (1988).

ここで示した測定データには，以下のような問題点がある．すなわち，本報告で示した反射率測定のジェオメトリーは双円錐型であり，試料面で拡散反射した光のうち，鏡面反射成分を中心とする一部の立体角成分のみを観測する．従って，ここで示した測定データは，放射率のスペクトル形状を予測できるという意味ではたいへん重要なデータであるが，放射率の絶対値を予測することはできない．絶対放射率を予測するためには，積分球を用いて全球反射測定を行い，絶対反射率を測定する必要がある (Salisbury *et al.*, 1988)．絶対放射率が予測できれば，地表モデル・大気モデルやセンサーの性能等のパラメータを与えることによって，センサーで観測される信号をシミュレートすることが可能である．従って，絶対反射率の測定は，リモートセンシングの基礎データとして不可欠である．

6. おわりに

将来実用化が期待されている，高空間分解能マルチバンド熱赤外衛星リモートセンシングデータを有効に利用するためのの基礎データとして，GSJ 岩石標準試料 "火成岩シリーズ" の熱赤外反射スペクトルを測定した結果を報告した．はじめに，これまでの背景について概説を行った．次に，リモートセンシングの基礎データとして必要な放射率は，キルヒホッフの法則により，実験室内で高い信号対雑音比で測定できる反射率から推定できることを示した．第 3 節では，測定に用いた装置の説明を行った．第 4 節では，測定条件と測定結果を示した．最後に，測定したスペクトルについて考察を加え，本測定の問題点を挙げた．

この研究は，昭和 63 年度に終了した大型プロジェクト「資源探査用観測システムの研究開発」のサブテーマ「地質リモートセンシングシステムの研究」の一環として行ったものである．当時地殻化学部の安藤　厚氏には，標準試料の提供をしていただいた．測定にあたっては，地殻物理部の金谷　弘氏に有益な助言をしていただいた．また，ジョンホプキンス大学の John Salisbury 教授には，貴重なデータを提供していただくとともに，有益な議論をしていただいた．米国地質調査所の Carol Finn 博士には，アブストラクトについて助言をいただいた．以上の方々に深く謝意を表します．

文　献

安藤 厚 (1986) GSJ 岩石標準試料“火成岩シリーズ”．ぶんせき，p. 593.

Ando, A., Mita, N. and Terashima, S. (1987) 1986 values for fifteen GSJ rock reference samples, "igneous rock series". *Geostandards Newsletter*, vol. 11, p. 159-166.

Aronson, J. R., Emslie, A. G., Allen, R. V. and McLinden, H. G. (1967) Studies of the middle- and far-Infrared spectra of mineral surfaces for application in remote compositional mapping of the moon and planets. *Jour. Geophys. Res.*, vol. 72, p. 687-703.

Bartholomew, M. J., Kahle, A. B. and Hoover, G. (1989) Infrared spectroscopy (2.3 - 20 μm) for the geological interpretation of remotely-sensed multispectral thermal infrared data. *Int. Jour. Remote Sens.*, vol. 10, p. 529-544.

Coblentz, W. W. (1905) Investigations of infra-red spectra part 5. Carnegie Institution of Washington, Washington, D. C., 38 p.

Conel, J. E. (1969) Infrared emissivities of silicates: experimental results and a cloudy atmosphere model of spectral emission from condensed particulate mediums. *Jour. Geophys. Res.*, vol. 74, p. 1614-1634.

Hovis, W. A. and Callahan, W. R. (1966) Infrared reflectance spectra of igneous rocks, tuffs, and red sandstone from 0.5 to 22 μm. *Jour. Optical Soc. Am*,, vol. 56, p. 639-643.

Hunt, G. R. (1977) Spectral signatures of particulate minerals in visible and near infrared. *Geophysics*, vol. 42, p. 501-513.

——— and Salisbury, J. W. (1974) Mid-infrared spectral behavior of igneous rocks. *Air Force Cambridge Research Laboratories Technical Report* TR-74-0625, 142 p.

——— and ——— (1975) Mid-infrared spectral behavior of Sedimentary rocks. *Air Force Cambridge Research Laboratories Technical Report* TR-75-0356, 49 p.

——— and ——— (1976) Mid-infrared spectral behavior of Metamorphic rocks. *Air Force Cambridge Research Laboratories Technical Report* TR-76-0003, 67 p.

Hunt, J. M., Wisherd, M. P. and Bonham, L. C. (1950) Infrared absorption spectra of minerals and other inorganic compounds. *Anal. Chem.*, vol. 22, p. 1478-1497.

——— and Turner, D. S. (1953) Determination of mineral constituents of rocks by infrared spectroscopy. *Anal. Chem.*, vol. 25, p. 1169-1174.

Kahle, A. B. (1987) Surface emittance, temperature, and thermal inertia derived from Thermal Infrared Multispectral Scanner (TIMS) data for Death Valley, California. *Geophysics*, vol. 52, p. 858-874.

——— and Rowan, L. C. (1980) Evaluation of multispectral middle infrared aircraft images for lithologic mapping in the East Titanic Mountains, Utah. *Geology*, vol. 8, p. 234-239.

——— and Goetz, A. F. H. (1983) Mineralogic information from a new thermal infrared multispectral scanner. *Science*, vol. 222, p. 24-27.

——— Gillespie, A. R., Abbott, E. A., Abrams, M. J., Walker, R. E., Hoover, G. and Lockwood, J. P. (1988) Relative dating of Hawaiian lava flows using multispectral thermal infrared images: A new tool for geologic mapping of young volcanic terranes. *Jour. Geophys. Res.*, vol. 93, p. 15239-15251.

Lahren, M. M., Schweickert, R. A. and Taranik, J. V. (1988) Analysis of the northern Sierra accreted terrane, California, with airborne thermal infrared multispectral scanner data. *Geology*, vol. 16, p. 525-528.

Logan, L .M., Hunt, G .R., Salisbury, J. W. and Balsamo, S. R. (1973) Compositional implications of Christiansen frequency maximums for infrared remote sensing applications. *Jour. Geophys. Res.*, vol. 78, p. 4983-5003.

Lyon, R. J. P., (1963) Evaluation of infrared spectroscopy for compositional analysis of lunar and planetary soils. *Final Report Contract NASA* 49(04), 139 p.

———(1965) Analysis of rocks by spectral infrared emission (8 to 25 microns). *Econ. Geol.*, vol. 60, p. 715-736.

———(1972) Infrared spectral emittance in geological mapping: Airborne spectrometer data from Pisgah Crater, California. *Science*, vol. 175, p. 983-986.

———, Tuddenham, W. M. and Thompson, C. S. (1959) Quantitative mineralogy in 30 minutes. *Econ. Geol.*, vol. 54, p. 1047-1055.

Miller, F. A. and Wilkins, C. H. (1952) Infrared spectra and characteristic frequencies of inorganic ions -their use in qualitative analysis. *Anal. Chem.*, vol. 24, p. 1253-1294.

Murcray, F. H., Murcray, D. G. and Williams, W. J. (1970) Infrared emissivity of lunar surface features 1. Balloon-borne observation. *Jour. Geophys. Res.*, vol. 75, p. 2662-2669.

Ninomiya, Y. and Sato, I. (1990) Estimation of SiO_2 content using thermal infrared reflectance spectra of rocks. *IGARSS '90 proceedings* IEEE-90CH2825-8, p. 979-982.

Prabhakara, C. and Dalu, G. (1976) Remote sensing of the surface emissivity at 9 μm over the globe. *Jour. Geophys. Res.*, vol. 81, p. 3719-3724

Sadtler (1973) Minerals: Infrared grating spectra. Sadtler Research Laboratories, Pennsylvania.

Salisbury, J. W. , Vincent, R. K., Logan, L. M. and Hunt, G. R. (1970) Infrared emissivity of lunar surface features 2. Interpretation. *Jour. Geophys. Res.*, vol. 75, p. 2671-2682.

———, Walter, L. S. and Vergo, N. (1987) Midinfrared (2.1 to 25 μm) spectra of Minerals. *U.S. Geol. Surv. Open File Report* 87-263, 24 p.

———, ——— and D'Aria, D. (1988) Midinfrared (2.5 to 13 μm) spectra of igneous rocks. *U.S. Geol. Surv. Open File Report* 88-686, 17 p.

Simon, I. and McMahon, H. O. (1953) Study of the structure of quartz, cristobalite, and viteous silica by reflection in infrared. *Jour. Chem. Phys.*, vol. 21, p. 23-30.

津 宏治 (1991) EOS 計画とASTERプロジェクト. 日本リモートセンシング学会第 11 回学術講演会論文集, p. 1-4

Vincent, R. K., Thomson, F. J. and Watson, K. (1972a) Recognition of exposed quartz sand and sandstone by two-channel infrared imagery. *Jour. Geophys. Res.*, vol. 77, p. 2473-2477.

——— and ———(1972b) Rock-type discrimination from ratioed infrared scanner images of pisgah crater, California. *Science*, vol. 175, p. 986-988.

———, Rowan, L. C., Gillespie, R. E. and Knapp, C. (1975) Thermal-infrared spectra and chemical analyses of twenty-six igneous rock samples. *Remote Sens. Environ.*, vol. 4, p. 199-209.

Walter, L. S. and Salisbury, J. W. (1989) Spectral characterization of igneous rocks in the 8- to 12-μm region. *Jour. Geophys. Res.*, vol. 94, p. 9203-9213.

Rept. Geol. Surv. Japan, No.278, p.39-132, 1992

Discrimination of lithology using remote sensing data in the visible and near-infrared regions

By

Yasushi YAMAGUCHI*

Abstract: The author investigated possible techniques for discrimination of lithology using remote sensing data.

Reflectance spectra of typical rocks and minerals measured by a spectroradiometer were used in the examination to simulate hypothetical sensor response patterns. As a result of a comparison between two different types of spectroradiometers in terms of their spectral resolution to resolve characteristic spectral features, the author decided to use the spectroradiometer with spectral resolution of 2-4 nm using gratings as dispersion elements.

Reflectance spectra of some minerals exhibit characteristic absorption features in the visible and near-infrared regions. Particularly, phyllosilicate and carbonate minerals have diagnostic absorptions in the 2.2 and 2.35 μm regions respectively. Typical rock types lacking significant amount of these minerals show flat featureless spectra. The author has developed an expert system for mineral identification from reflectance spectra in order to facilitate spectral measurements. Feature coding was employed as a manner of patter recognition of the spectra.

Calibration techniques to convert digital numbers to reflectance of surface materials were compared using the Airborne Imaging Spectrometer data, because remote sensing data are usually provided to us as digital numbers on magnetic tapes. Calibration using field spectra is the best technique, if we can find good field calibration targets. Lacking field spectral measurements, the Log Residual would produce superior results in areas which are not dominantly composed of one cover type. In areas containing one dominant cover type, the Least Upper Bound Residual would probably be the best. For the purpose to collect field spectra in order to perform reflectance calibration, the author has developed a new field radiometer, which has two motor-driven filter wheels and can contain up to eight filters in each wheel.

Using hypothetical sensor response patterns simulated from the reflectance spectra of rocks and minerals, possible techniques for discrimination of lithology using the optical sensor data of the Japanese ERS-1 (Earth Resources Satellite) were examined prior to its operation. The author has proposed two spectral indices, linear combination of three SWIR bands, as to be useful for lithologic mapping, i.e., Alunite Index and Calcite Index. Spectral indices to estimate the proportion of vegetation and phyllosilicate and/or carbonate minerals within a single pixel have been also proposed. The HSI color transform applied to the three SWIR bands is another possible way to express sensor response patterns.

The author applied these techniques to the real data of a test site in Queensland, Australia, obtained by an airborne multispectral scanner, whose bandpasses are quite similar to those of the ERS-1. The reflectance calibration using field spectra was failed due to the difficulty to find good

*Geothermal Research Department

Keywords: ERS-1, image processing, infrared, multispectral scanner, Nevada, Queensland, radiometer, reflectance, remote sensing, satellite, spectral index, spectroradiometer, spectrum, SWIR, VNIR

calibration targets. The Log Residual, on the other hand, succeeded in normalizing the original data, and thus was employed as a calibration technique instead. The spectral indices images successfully showed the epidote-rich zone, hydrothermally-altered areas, and distribution of vegetation. The HSI color transform image also successfully displayed colors corresponding to the SWIR band response patterns. As a result, the proposed techniques with an appropriate calibration method can create images which are useful for lithologic discrimination and easy to interpret geologically.

1. INTRODUCTION

1.1 Previous Studies

Remote sensing has been widely utilized in various application fields including geology, geography, cartography, agriculture, forestry, oceanography, climatology, environmental studies, urban planing, and so on. The term remote sensing was just invented in early 1960's when the conventional terms such as "photograph" or "aerial" appeared to be too limited to cover newly developed fields, e.g., multispectral cameras, infrared films, nonphotographic scanners, and opportunities to observe the Earth from the space. Conceptually, remote sensing is a valuable technique used within both science and technology (Curran, 1987). For a comprehensive definition of remote sensing, some or perhaps all of the following elements need to be considered: (1) the noncontact acquiring, collecting, or recording, (2) from regions of the electromagnetic spectrum that include but exceed the visible region, (3) through the use of instruments, (4) located on mobile platforms, (5) and the symbolic transformation of collected data, (6) by means of interpretive techniques and/or computer-aided pattern recognition (Fussell and Rundquist, 1986).

Geologic application of remote sensing in the above sense was given a big boost by launching of Landsat (called ERTS at that time), which was the first Earth observation satellite, in 1972 by the United States. The Landsat carried an Earth observation sensor called MSS (MultiSpectral Scanner), which provided a synoptic view of the Earth surface. Conventional photogeologic interpretation of the MSS images still occupied a major part of geologic application, but a new approach which utilized spectral information for lithologic mapping was also introduced. One of the most successful results in the early studies was provided by Rowan *et al.* (1974). They employed MSS band ratios to enhance sensor response patterns and successfully demonstrated that a color composite image of the band ratios could delineate distribution of iron -oxide minerals associated with hydrothermally altered areas in Goldfield, Nevada, U.S.A.

Many studies using the MSS data were carried out while Landsat 1, 2, and 3 provided the data of the Earth surface. Band ratios have been the most widely employed technique in many application fields. Another popular method is the principal components analysis, which transforms original data into a new orthogonal coordinate system by choosing the axes mathematically to maximize variance of all the data. The principal components analysis can reduce dimensionalitiy of the original data, and thus is believed to be useful for data compression.

An important new approach was proposed in agricultural application. Namely, Kauth and Thomas (1976) developed four spectral indices using the four MSS bands to assess vegetation, i.e., "brightness", "greenness", "yellowness", and "nonsuch". Richardson and Wiegand (1977) also developed a two-dimensional perpendicular vegetation index using the two MSS bands. Jackson (1983) showed that these indices are special cases of a class of spectral indices, formed by linear combination of n spectral bands, in n-dimensional space. The spectral indices in n-space are similar to the principal components analysis, but chooses the transformation axes to represent specific spectral features.

As the spectral coverage of the MSS was only in the 0.5-1.1 μm wavelength region, spectral

approaches in geologic application were limited to mapping of iron-oxide minerals (Rowan *et al.*, 1974) and discrimination of rock types using total brightness in this spectral region (Goetz and Rowan, 1981). In 1982, Landsat 4 equipped with TM (Thematic Mapper), a new Earth observation sensor, was launched. The TM has seven spectral bands, two of which are in the short-wave-infrared (SWIR; 1.3-2.5 μm) region. The importance of the SWIR region has been stressed in geologic remote sensing since Hunt (1977, 1979) proposed its potential. He measured reflectance spectra of many different types of rocks and minerals using a high-resolution spectroradiometer in laboratory (e.g., Hunt and Salisbury, 1970; Hunt *et al.*, 1971a, 1971b, and 1973). As phyllosilicate and carbonate minerals have characteristic absorptions in the 2.2 μm and 2.35 μm regions respectively, sensors including the SWIR bands should be useful for discriminating certain rock types. For instance, the band ratio between TM Band 5 centered at 1.65 μm and Band 7 centered at 2.22 μm was reported to be sensitive to the existence of clay minerals, and thus useful to detect hydrothermally altered areas (Abrams *et al.*, 1977, 1983; Prost, 1980; Goetz and Rowan, 1981; Podowysocki *et al.*, 1983).

Application of the spectral indices had been restricted to vegetation analysis until Elvidge and Lyon (1984) developed the Mineral Absorption Index using TM data. Elvidge (1985) and Miller and Elvidge (1985) proposed new spectral indices for lithologic discrimination using the TM data. They also made a comparison of ratio-based and baseline-based techniques, and concluded that the latter was more useful.

Recently, rapid technological advances have made it possible to build sensors with more and more spectral bands (e.g., Collins *et al.*, 1981; Marsh and McKeon, 1983; Goetz *et al.*, 1985). The Airborne Imaging Spectrometer developed by NASA can provide almost a continuous spectrum of a surface material and allow us to identify some mineral species that used to be possible only in laboratory. Some calibration and data processing techniques have been proposed for the AIS data (e.g., Goetz *et al.*, 1985; Green and Craig, 1985; Roberts *et al.*, 1985 and 1986). On the other hand, new field spectroradiometers have been also developed in early 1980's. Efforts to develop expert systems, which will be installed in a field spectroradiometer and can tell us the minerals in real time, are being made in these days (e.g., Yamaguchi and Lyon, 1986; Horsfall *et al.*, 1987).

1.2 Context of Investigation

The goal of this study is to develop techniques for lithologic discrimination using remote sensing data in the visible and near-infrared regions. The author places special emphasis on the SWIR region, which has been considered one of the most important ranges in the electromagnetic spectrum for use in geologic remote sensing (Hunt, 1979).

A recent notable trend in remote sensing activities is that the countries other than the United States have started developing Earth observation systems. The Japanese ERS-1 (Earth Resources Satellite) is one of the satellites planned by these countries, and is scheduled to be launched in early 1992. The ERS-1 will be equipped with both an eight-band optical sensor and an L-band SAR (Synthetic Aperture Radar). The SAR is expected to provide the Earth surface images even for cloud-covered areas and will be useful for structural mapping such as faults and foldings. The optical sensor, on the other hand, includes four bands in the SWIR region and is expected to be able to distinguish clay from carbonate rocks that is very difficult by the Landsat TM (Yamaguchi, 1987; 1988).

Many techniques have been developed for lithologic discrimination using the Landsat MSS and TM data. As mentioned in the previous section, the TM has two bands in the SWIR region and has already proven its potential for discriminating certain kinds of rock types. However, due to the increase of the SWIR bands in the new sensors, the techniques developed for the MSS and TM might not be applicable. Therefore, development of new techniques for lithologic discrimina-

tion using the new sensors is indispensable at the moment.

Another major problem of the current image processing techniques is that the images created by these methods are beautiful mathematically but are often difficult to interpret geologically. It is necessary to develop a technique which can provide an image whose geologic meanings can be easily interpreted by a geologist. This dissertation is directed towards development of such techniques for lithologic discrimination using the visible and near-infrared data obtained by a spaceborne or airborne sensor.

In Chapter 2, the author descibes characteristics of reflectance spectra of typical rocks and minerals along with terminology and equipments used in this study. An attempt to build an expert system for mineral identification with reflectance spectra is also shown. In Chapter 3, the author makes a comparison of some calibration techniques from digital numbers recorded on a magnetic tape to reflectance of surface materials. In Chapter 4, development of a new field radiometer, which will be used for reflectance calibration, is described. In Chapter 5, the author discusses possible techniques for lithologic discrimination using reflectance data of rocks and minerals obtained by a spectroradiometer. The techniques proposed are applied to the airborne multispectral scanner data in Chapter 6 in order to evaluate their usefulness in the real data.

2. SPECTRAL FEATURES OF ROCKS AND MINERALS

2.1 Electromagnetic Radiation

Electromagnetic theory had been established since Maxwell's theory and modern quantum theory succeeded in explaining the dual nature of electromagnetic energy, which sometimes behaves as waves, whereas in the other situations displays the properties of particles. Maxwell's theory deals primary with the propagation and macroscopic optical effects, i.e., all electromagnetic radiation is energy in transit and can be regarded as a wave motion. It consists of inseparable oscillating electric and magnetic fields that are always mutually perpendicular to each other and to the direction of propagation whose rate is constant in a vacuum. On the other hand, quantum theory is concerned with the atomic-molecular absorption and emission aspects of electromagnetic radiation, and gives us an important idea that each different material has discrete energy levels with different values and arrangements (Hunt, 1980).

As a result of understanding the nature of electromagnetic energy, many different phenomena that had previously been regarded to be independent were realized as just one form of electromagnetic radiation forming the continuum of energy. The electromagnetic spectrum may be defined as the ordering of the radiation according to wavelength, frequency, or energy, and has been divided into some regions. The name and extent of each region were made somewhat arbitrarily. Figure 1 shows the names for these regions along with their extent of wavelength, frequency, and energy. At the short wavelength end of the spectrum, the types of radiation are named cosmic ray, gamma ray, and X-ray. Microwave and radiowaves are at the long end. Ultraviolet, visible, and infrared rays are located between them. Notice that the visible region, which human eyes can detect, occupies only a small portion of the spectrum.

The infrared region is subdivided into near infrared (NIR; 0.7-3.0 μm, sometimes called as VNIR including the visible region), mid infrared (MIR; 3.0-15 μm), and far infrared (FIR; 15 -1000 μm) ranges respectively. Recently, the name of short-wavelength-infrared (SWIR) range is often used for the region between 1.3 and 2.5 μm, and its importance has been stressed in geologic remote sensing (Hunt, 1977; 1979). The atmospheric window between 8 and 14 μm corresponds to the maximum radiation from the Earth surface as described in the following section, and thus this region is called thermal infrared (TIR) range showing surface temperature.

There are two well-known important laws indicating nature of electromagnetic radiation,

both of which can be led mathematically from the Plank's law, although historically they had been found earlier than the Plank's law. First one is the Stefan-Boltzmann law. All matter whose temperature is above absolute zero degrees K (-273.15 degrees Celsius) emits some form of electromagnetic radiation. Here, we introduce the concept of a blackbody, which is ideal matter capable of absorbing and re-emitting all electromagnetic energy that the matter receives. The total energy (H) emitted from a blackbody is a function of its absolute temperature (T):

$$H = A \times T^4, \tag{1}$$

where A is the Stefan-Boltzmann constant (5.7×10^{-8} $Wm^{-2}K^{-4}$). Therefore, the total radiant energy emitted from an object rises rapidly as its temperature increases.

The second law known as the Wien's displacement law gives the dominant wavelength (R_m) at which a blackbody emits the maximum amount of the electromagnetic radiation:

$$R_m = 2898/T, \tag{2}$$

where T is the absolute temperature of a blackbody. Thus, the sun which can be regarded as a blackbody at 6,000 degrees K has the maximum radiation at about 0.5 μm in the visible region. As temperatures of most of the Earth surface materials fall in the range between 0 to 30 degrees

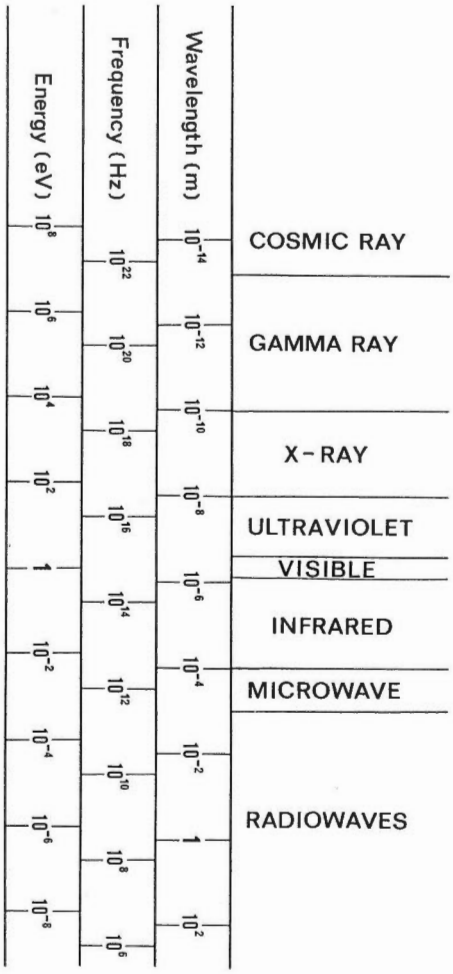

Fig. 1 The electromagnetic spectrum. The nomenclature for different parts of the spectrum, and relationship between wavelength, frequency, and energy.

Celsius (273 to 303 degrees K), their maximum radiation occurs at about 10 μm. This is the reason why the region between 8 to 14 μm corresponding to an atmospheric window is called as thermal infrared (TIR).

In 1990, M.Plank succeded in mathematically describing the spectral distribution of radiation emitted from a blackbody. This important rule is well-known as Plank's law of radiation, in which the spectral radiant exitance can be expressed as a function of wavelength and absolute temperature of a blackbody. The two laws mentioned above, the Stefan-Boltzmann law and the Wien's displacement law, can be mathematically led from the Plank's law, although they had been known ealier historically.

Remote sensing is a technique to measure electromagnetic radiation as defined above, but the electromagnetic region used for remote sensing has been limited to visible to microwave, because radiation generators and/or detectors with practical intensity and sensitivity for regional studies are available only in these regions at present. In this paper, discussions focus on the visible and near infrared regions whose wavelength ranges from 0.4 to 2.5 μm.

2.2 Measurements of Reflectance Spectra

2.2.1 Terminology

By measuring electromagnetic radiation from an object, we can know some physical properties of the object. In some cases, it is possible to identify material forming the object from characteristic patterns of electromagnetic radiation in terms of wavelength. Remote sensing is a technique to measure such electromagnetic radiation in a regional scale. In the VNIR to SWIR regions, most of radiant energy from an object on the Earth consists of reflection of the sun light at the surface of the object. A sensor on an aircraft or a satellite measures intensity of such radiation. The followings are definitions for radiometric terms after Slater (1980).

Radiant energy, Q, is energy traveling in the form of electromagnetic waves, measured in joule.

Radiant flux, $\Phi = dQ/dt$, is the rate at which radiant energy is transferred from a point or a surface to another surface, measured in watts (joule/sec).

Radiant intensity, $I = d\Phi/d\Omega$, of a source is the radiant flux proceeding from the source per unit solid angle in the direction considered, measured in watts per steradian.

Radiance, $L = d^2\Phi/d\Omega\, dA \cos\theta$, in a given direction at a point on the surface being sensed, is the radiant flux leaving an element of the surface surrounding the point and propagated in directions defined by an elementary cone containing the given direction, divided by the product of the solid angle of the cone and the area of the orthogonal projection of the element of the surface on a plane perpendicular to the given direction. Radiance is measured in watts per square meter and steradian.

Irradiance is the sum of the direct solar flux incident on the surface, per unit area of the surface. Thus, irradiance is measured in watts per square meter.

Reflectance is the ratio of reflected radiant flux to incident radiant flux at a surface or a point. The incident and reflected radiant flux must be measured in all directions. Thus, it is not easy to measure reflectance unless a sophisticated laboratory equipment is available.

Reflectance factor is the ratio of reflected radiant flux leaving an element of the surface in directions defined by a cone with an arbitrary solid angle containing the given direction, divided by the reflected radiant flux leaving a perfectly diffuse surface (commonly designated as a Lambertian surface) in the same direction defined by the same cone. Therefore, the reflectance factor measured by the cone with the solid angle of two pai means reflectance.

Bidirectional reflectance factor is the special case of the reflectance factor, that is, geometric relation to an illumination source is taken into account. As shown in Fig. 2, the bidirectional

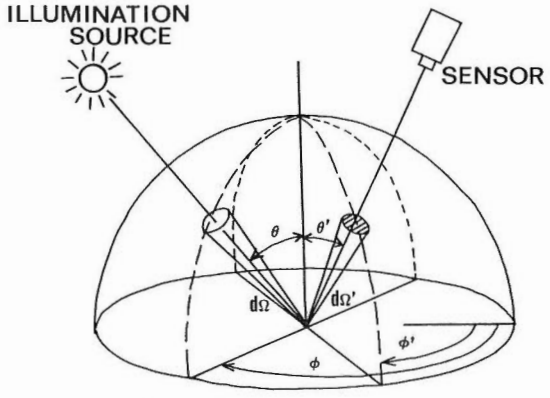

Fig. 2 Geometrical quantities referred to in the bidirectional reflectance factor.

reflectance factor depends on (1) the angle of incidence, θ, of the flux at the surface, (2) the azimuthal angle ϕ of the plane of incidence with respect to a direction across the surface, (3) the angle to the surface normal from which the flux is detected, θ', (4) the azimuthal angle ϕ' of the plane of reflection, (5) the solid angle subtended by the source at a point on the surface, and (6) the solid angle subtended by the entrance pupil of the sensor at the surface.

In most cases to measure "reflectance" of geologic targets such as rocks and minerals using a spectroradiometer or radiometer, the bidirectional reflectance factor is actually measured instead of the reflectance as defined above. In this paper, the term reflectance will be often used instead of the bidirectional reflectance factor just for convenience. Usually, a "white" standard plate is used for reference. The bidirectional reflectance factor can be obtained by rationing radiant flux from a target and radiant flux from the reference. Materials used as reference are magnesium oxide, barium sulfate, fiberflux, or halon, all of which have almost 100 % reflectance over the spectral range of the VNIR and SWIR regions. In this paper, barium sulfate coated on an aluminum plate was used as the reference standard.

2.2.2 Description of Spectroradiometers

Field spectroradiometers have been recently developed, which can be used to facilitate geologic mapping (Yamaguchi and Lyon, 1985). In addition, these spectroradiometers are also used to provide ground truth data for airborne or spaceborne imaging systems. However, when we discuss and compare spectra, we have to take into account some of the problems which arise with use of different equipments with varying specifications. The difference in spectral resolution is the major problem to be discussed.

Before comparing the spectra measured by two different spectroradiometers in the next section, specifications of the spectroradiometers tested are described in this section (Table 1). One is US-based Geophysical Environmental Research (GER) Inc's IRIS (InfraRed Intelligent Spectroradiometer). It has three gratings as dispersion elements, which are rotated by a stepping -motor. Its spectral range of a measurement covers 0.35 to 2.5 μm with 820 channels (in normal scan mode) and spectral resolution is 2 nm in the 0.35 to 1.0 μm region and 4 nm in the 1.0 to 2.5 μm region. It is a dual beam system that looks at two targets (reference + sample) simultaneously, so that it can avoid the effect of illumination changes on reflectance calculation. According to the manual, it can take from 1.5 minutes to over 10 minutes to obtain a spectrum depending on the scan rate factor and light level. As it took from 4 to 7 minutes in the measurements, the author mounted the optical head on a tripod to look down at targets. Spectrum data are dumped onto a cassette tape after each measurement. Data in the memory

Table 1 Specifications of the two spectroradiometers.

	IRIS	PFS
Dispersion Element	grating	circular variable filter (CVF)
Channel	820	256
Range	0.35-2.5 (3.0) μm	0.4-2.5 μm
Spectral Bandwidth	a) 2 nm (0.35-1.0 μm) b) 4 nm (1.0 -3.0 μm)	12-37.5 nm a) 3.0 % (0.4-1.2 μm) b) 1.5 % (1.2-2.5 μm)
Measurement Time	1.5 - 10 min.	4 sec.
Data Record	casette tape	bubble memory
Display	chart recorder	liquid crystal display

can be plotted on the strip chart.

The other spectroradiometer is Australian-based Geoscan Pty. Ltd.'s PFS (Portable Field Spectroradiometer), which obtains a spectrum using a circular variable filter (CVF) as the dispersion element. Its spectral range is from 0.4 to 2.5 μm with 256 channels, and spectral resolution is 12 to 37.5 nm (3.0 % in the 0.4 to 1.2 μm region and 1.5 % in the 1.2 to 2.5 μm region), which is not as good as that taken by the IRIS (Fig.3). The PFS is a single-beam system, and thus we need to measure a standard target first (which is stored in memory), and then direct it to other targets in the reflectance mode. It takes 4 seconds for a measurement, much faster than the IRIS. A large number of spectra can be averaged automatically, if we move the field of view over a wide target area. This function helps to obtain good groundtruth data for inhomogeneous ground targets. The internal "bubble" memory can store about 200 spectra, which can be downloaded with a serial port to a portable computer. Any spectrum taken is immediately shown on the liquid crystal display (LCD) and also any spectrum in the bubble memory can be recalled and plotted on the display at anytime.

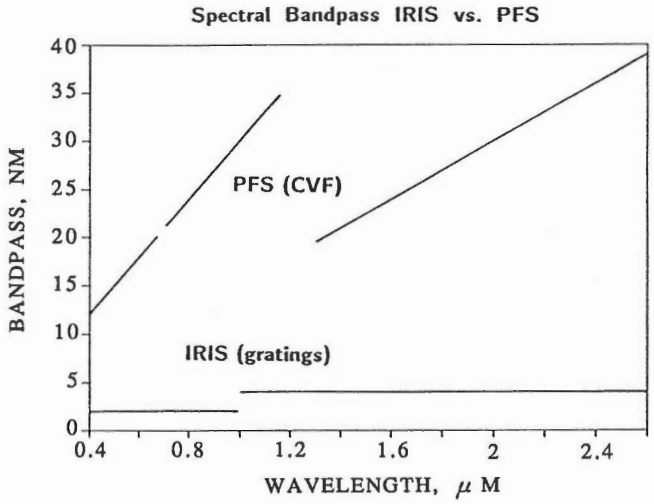

Fig. 3 Spectral bandpass of the two spectroradiometers; the IRIS and the PFS.

2.2.3 Effect of Spectral Resolution

Over 500 field and laboratory spectra have been obtained by using both the IRIS and the PFS, and some of the more interesting spectra of standard minerals and hydrothermally altered rocks of Singatse Range, Nevada, U.S.A. (Section 3.2.2), are shown here. The IRIS spectra were convolved to the equivalent resolution of the PFS in order to make a comparison.

In reflectance (actually bidirectional reflectance factor as shown in the previous section) measurements using a barium sulfate plate as a reference standard, a two-beam spectroradiometer measures the radiance from a target material and the standard, and takes a ratio between them. A single-beam unit performs the two spectra consecutively. Consider that a spectroradiometer obtains an output S in the channel centered at wavelength $\lambda 0$. $S_{\lambda 0}$ is given by:

$$S_{\lambda 0} = L_{\lambda 0}/Ls_{\lambda 0} = \frac{\int_0^\infty R(\lambda) \times E(\lambda) \times F(\lambda) \times G(\lambda)\, d\lambda}{\int_0^\infty Rs(\lambda) \times E(\lambda) \times F(\lambda) \times G(\lambda)\, d\lambda}, \quad (3)$$

where $L_{\lambda 0}$ and $Ls_{\lambda 0}$ are the radiance of the target and the standard, $R(\lambda)$ and $Rs(\lambda)$ are the reflectance of the target and the standard respectively, $E(\lambda)$ is the irradiance from the illumination source, $F(\lambda)$ is the spectral responsivity of the spectroradiometer, and $G(\lambda)$ is the goniometric factor in the measurements.

If we assume that $Rs(\lambda) = 1$, $F(\lambda) = 0$ when $\lambda < \lambda_1$ or $\lambda > \lambda_2$ ($\lambda_1 < \lambda_2$, $\lambda_0 - \lambda_1 = \lambda_2 - \lambda_0$) and $E(\lambda)$ and $G(\lambda)$ are constant when $\lambda_1 < \lambda < \lambda_2$, the above equation can be simplified as:

$$S_{\lambda 0} = \int_{\lambda_1}^{\lambda_2} R(\lambda) \times Fn(\lambda)\, d\lambda, \quad (4)$$

where $Fn(\lambda)$ is the normalized spectral responsivity of the equipment. There is no way to know the "intrinsic" reflectance $R(\lambda)$, because the responsivity $Fn(\lambda)$ of the equipment always smoothes out the $R(\lambda)$. This is a convolution process and we can express it for whole range of the measurement by using a superposition integral:

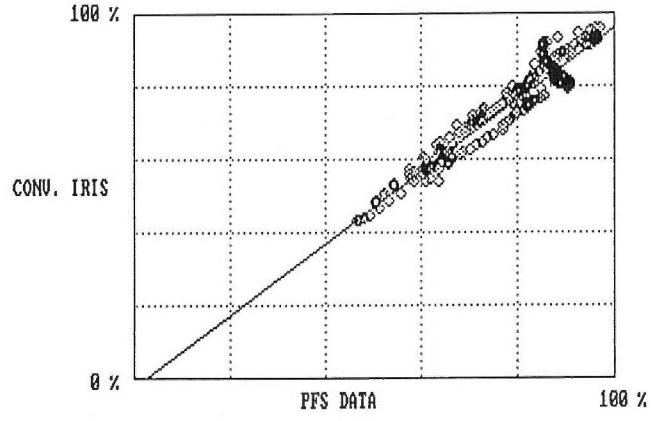

Fig. 4 Correlation between the PFS spectrum and convolved data from the IRIS spectrum. Spectra are of the hydrothermally altered rock, including alunite (Fig. 6). The linear regression line is:
$Y = 0.986 \times X - 2.36$, $R^2 = 0.958$.

$$S(\lambda) = \int_{-\infty}^{\infty} T(v-\lambda) \times R(v)\, dv = T(\lambda) \times R(\lambda), \quad (5)$$

where $S(\lambda)$ is the output and $T(\lambda)$ is the transfer function of the spectroradiometer, which is equivalent to $Fn(\lambda)$, and v is the integration variable. The narrower the bandwidth of $T(\lambda)$ and the sampling interval, the closer the output $S(\lambda)$ becomes to the "intrinsic" reflectance $R(\lambda)$.

To compare the spectra taken by the IRIS and the PFS, this relationship was applied by convolving the IRIS spectra. It was presumed that the IRIS spectra could be used as $R(\lambda)$ and the transfer function $T(\lambda)$ of the PFS had a Gaussian shape. The output for each PFS channel was calculated from the IRIS data and compared with the output of measurement by the PFS. Figure 4 shows scatter plot between data of the convolved spectrum and data of the "real" spectrum, which seems to be good enough.

In Figs. 5 to 8, three spectra for each sample are shown; an IRIS spectrum, a convolved spectrum from the IRIS spectrum and a PFS spectrum. All the spectra were taken indoors under

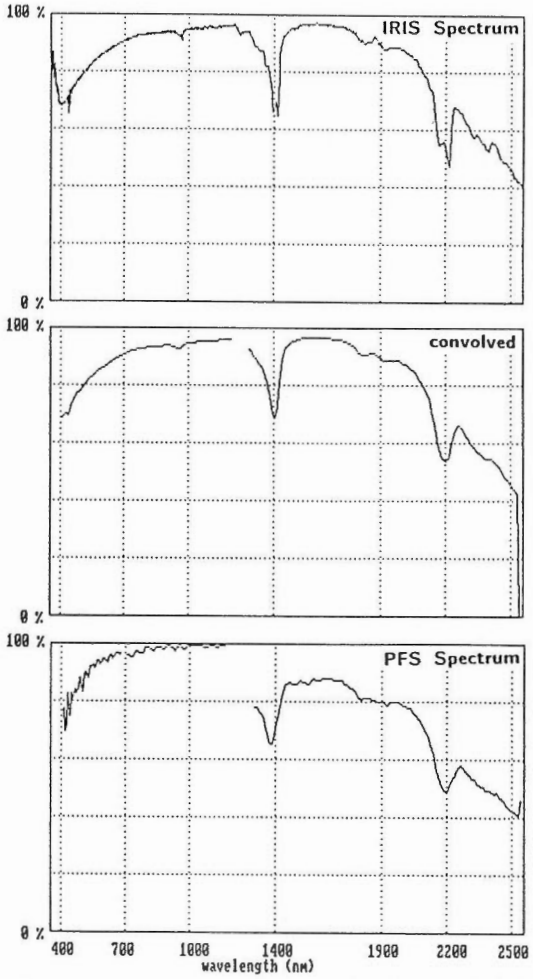

Fig. 5 Spectra of well-crystallized kaolinite. Comparison between the IRIS spectrum (top), a convolved spectrum from the IRIS spectrum (middle), and the PFS spectrum (bottom).

quartz-halogen illumination. We get spectra with almost same quality in the field except for "noisy" data in the atmospheric absorption bands (1.4 and 1.9 μm) when we used the sun as a source. We eliminate this problem by using artificial illumination (a portable quartz-halogen lamp) even outdoors in daylight.

1) Kaolinite (Fig. 5)

This sample is a well-crystallized kaolinite from the Clay Mineral Society standard collection. Kaolinite has very strong hydroxyl (O-H) bands centered near 1.4 and 2.2 μm as discussed in the next section. The IRIS can resolve O-H doublets in the 1.4 and 2.2 μm absorptions. Although the PFS spectra cannot show the doublets, these spectra can be identified as kaolinite by their absorption peak wavelengths and spectral shape. The convolved spectra and the PFS spectra now look very similar.

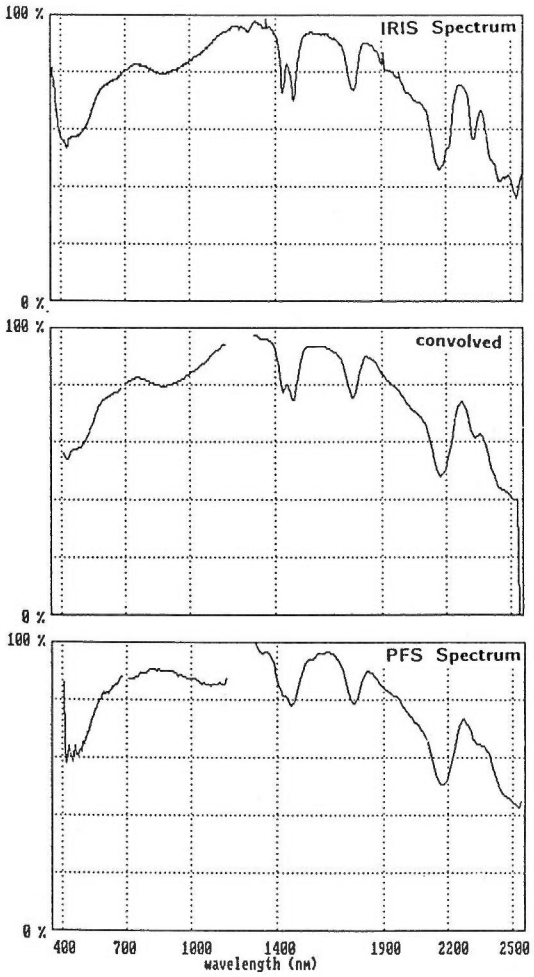

Fig. 6 Spectra of a hydrothermally altered rock, including alunite. Comparison between the IRIS spectrum (top), a convolved spectrum from the IRIS spectrum (middle), and the PFS spectrum (bottom).

2) Hydrothermally altered rock, including alunite (Fig. 6)

These spectra of the hydrothermally altered rock sample, which is collected in an argillic alteration zone in Geiger Hill, three miles north of Virginia City, Nevada, clearly indicate alunite. A doublet in the 1.4–1.5 μm region and a small absorption at 2.3 μm are obvious in the IRIS spectrum, while they are not clear in the PFS spectrum. In the above case, deconvolution techniques (roughly opposite to smoothing) have been successfully applied to recover this doublet from the relatively "low-resolution" PFS data (Zhu and Lyon, unpublished data). As alunite has a characteristic absorption at 1.76 μm (Hunt, 1979), even the PFS can identify it in the field despite the relatively low resolution.

The scatter plot (Fig. 4) shows a good correlation wavelength-by-wavelength between the convolved spectrum from the IRIS data and the PFS spectrum. Both now have 256 data points.

3) Gray clay, including montmorillonite (Fig. 7)

This gray clay sample is strongly altered Tertiary dacitic ash-flow tuff in the Singatse Range. Strong absorptions at 1.4, 1.9, and 2.2 μm suggest montmorillonite (Hunt and Salisbury,

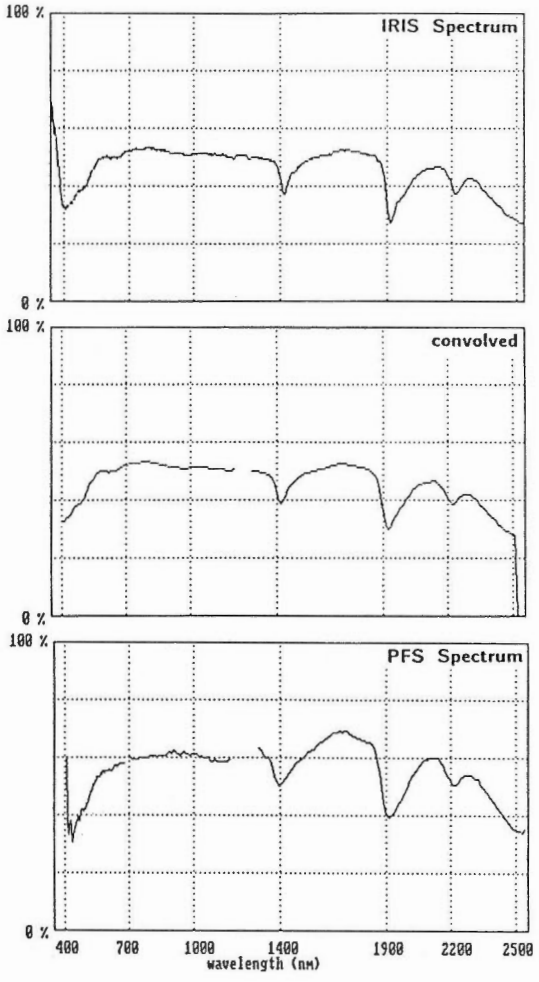

Fig. 7 Spectra of a hydrothermally altered rock, including montmorillonite. Comparison between the IRIS spectrum (top), a convolved spectrum from the IRIS spectrum (middle), and the PFS spectrum (bottom).

1970). As these absorption features are very broad, the PFS spectrum is as good as the IRIS spectrum.

4) Hydrothermally altered rock, including sericite (Fig. 8)

This rock sample is hydrothermally altered quartz monzonite porphyry, which is located in a quartz-pyrite-sericite alteration zone in the porphyry copper system at Yerington, Nevada. Sharp absorptions at 1.4 and 2.2 μm and a broad absorption at 2.35 to 2.4 μm indicate sericite (Hunt and Salisbury, 1970). The absorption at the 1.4 μm in the PFS spectrum is not as sharp as in the IRIS spectrum due to the smoothing effect of the CVF. However, the spectral shapes of the PFS data is similar to the IRIS data and may be enough to identify it as sericite.

Spectra taken by the two different spectroradiometers show good correlation. The IRIS with its higher spectral resolution can provide detailed spectral features such as the O-H doublets of kaolinite and alunite. However, the PFS with a relatively lower resolution has a much shorter scan time, and can give spectra with enough quality to indicate certain kinds of minerals whose

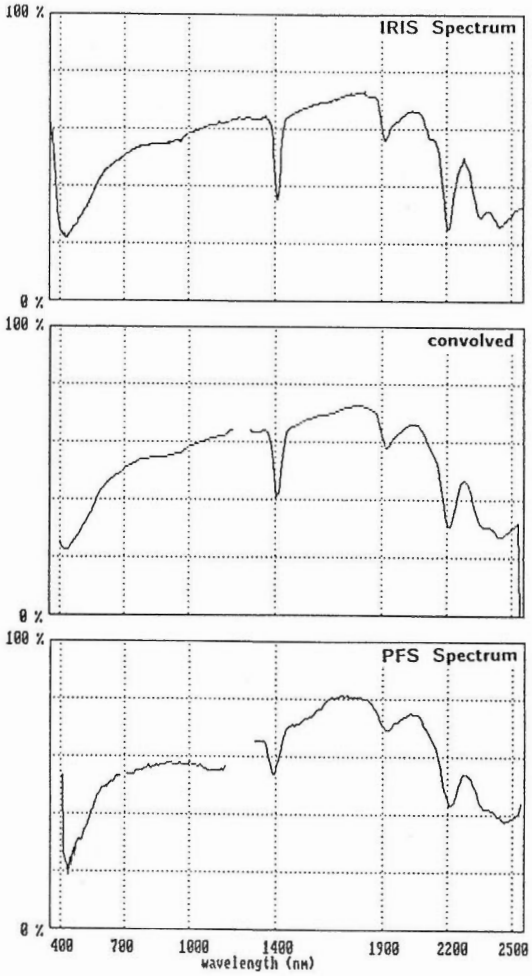

Fig. 8 Spectra of a hydrothermally altered rock, including sericite. Comparison between the IRIS spectrum (top), a convolved spectrum from the IRIS spectrum (middle), and the PFS spectrum (bottom).

spectra have broad absorption features or characteristic bands. For example, alunite, montmorillonite, and sericite could be identified by the PFS spectra, with sufficient accuracy or to permit real time field identification.

The use of both spectroradiometers in the field results in the maximum efficiency of effort. The faster, less specific PFS can be used to pinpoint areas of interest for more detailed, higher -resolution work by the IRIS. In the measurements of the reflectance spectra shown in the next section, the IRIS was used in laboratory under quartz-halogen illumination.

2.3 Reflectance Spectra of Rocks and Minerals

2.3.1 Introduction

Some of the minerals which commonly exist at the Earth surface exhibit characteristic spectral features in the VNIR and SWIR regions. For instance, human eyes can detect spectral patterns of some minerals in the visible range as diagnostic colors that often help us identify mineral species. A rock as an assemblage of minerals shows a composite of the individual spectra of its constituent minerals. Spectral signatures of minerals are produced as a consequence of either electronic or vibrational processes and can be explained by the crystal field theory. Evidence for electronic processes appears primarily in the visible range, whereas evidence for fundamental vibrational processes is evident in the MIR and FIR regions. In the VNIR and SWIR regions, there is an overlap of features due to electronic transitions, and excitation of overtone and combination tone vibrations (Hunt, 1980).

One of the most significant and important spectral signatures in 0.9 to 2.5 μm concerning application to geologic remote sensing is vibrational features due to Al-O-H, Mg-O-H, Fe-O -H, H-O-H, and Si-O-H, which are commonly observable in the spectra of phyllosilicate minerals including hydroxyls. Another characteristic vibrational feature is an absorption due to CO_3 in the SWIR range. Electronic features in 0.4 to 1.7 μm region due to Fe^{2+}, Fe^{3+}, and Mn^{3+} are also important and applicable to remote sensing particularly for detection of iron oxides. On the other hand, vegetation indicates diagnostic spectral patterns in the VNIR and SWIR regions due to chlorophyll and water, and often obscures spectral signatures of rocks and minerals within the same field of view observed by a remote sensor.

Reflectance spectra of typical minerals, rocks, and vegetation were obtained using the IRIS spectroradiometer (Collins *et al.*, 1981). As described in Section 2.2.2, the spectral range of the IRIS is 0.35 to 2.5 μm, with 820 channels in the normal scan mode. Spectral resolution (bandwidth) is 2 nm in the 0.35 to 1.0 μm region and 4 nm in the 1.0 to 2.5 μm region. The measured samples of typical clay minerals were provided by the American Clay Mineral Society and the American Petroleum Institute. Rock samples are mainly of the Singatse Range and Carlin District, Nevada, U.S.A.

2.3.2 Phyllosilicates

1) Kaolinite; $Al_4Si_4O_{10}(OH)_8$

Figures 9 and 10 show reflectance spectra of kaolinite from various localities. Kaolinite has very strong hydroxyl (O-H) bands in the near-infrared, centered near 1.4 and 2.2 μm (Hunt and Salisbury, 1970). There are diagnostic O-H doublets in the 1.4 and 2.2 μm absorptions. Usually, the 2.2 μm doublet is asymmetric and the right minimum is deeper than the left one. If a kaolinite sample is poorly-crystallized such as (f) in Fig. 9 or impure due to the other minerals, these doublets become less clear and finally appear as a single absorption. The reflectance curves show a sloping background from 2.2 μm region toward a longer wavelength due to a strong O-H absorption at 2.6 μm. As kaolinite does not contain constitutional water, the absorption band near 1.9 μm shown in (c), (e), (f) in Fig. 9 and (b), (c) in Fig. 10 is due to

adsorbed water.

2) Dickite; $Al_4Si_4O_{10}(OH)_8$

Dickite is a chemically identical monoclinic form of the triclinic kaolinite. Reflectance spectra of dickite (Fig. 11) look quite similar to those of kaolinite. However, the interval width and the peak height between two minima in the 1.4 μm doublet are larger than those of kaolinite. Moreover, the 2.2 μm doublet is symmetric and clearer than that of kaolinite.

3) Halloysite; $Al_2Si_2O_5(OH)_4\ 2H_2O$

Halloysite has a two layer dioctahedral structure and exists in two forms; one (metahalloysite) with the kaolinite structure and the other a hydrated form. Thus, halloysites may contain constitutional interlayered water molecules unlike kaolinite and dickite (Hunt *et al.*, 1973). Although reflectance spectra of halloysite (Fig. 12) are somewhat similar to those of kaolinite, they show significant fall-off in reflectance toward 2.6-2.7 μm due to presence of molecular water. The 1.4 μm doublet is clear and similar to that of kaolinite. The 2.2 μm doublet is asymmetric and not as clear as that of kaolinite.

4) Montmorillonite; $(Na, Ca)_{0.33}(Al, Mg)_2Si_4O_{10}(OH)_2\ nH_2O$

The montmorillonite group can absorb water molecules between the sheets. Thus, there are characteristic absorption bands at 1.41-1.45 and 1.90-1.94 μm due to presence of molecular

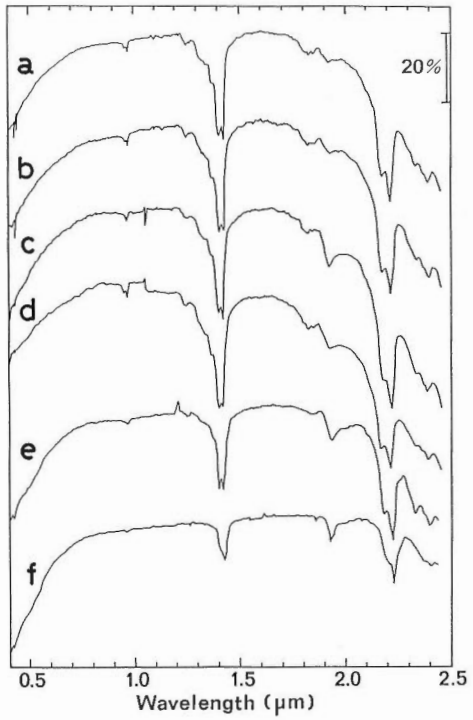

Fig. 9 Reflectance spectra of kaolinite (1). Localities are as follows: a) Washington County, Georgia, b) Warren County, Georgia, c) Dry Branch, Twiggs County, Georgia, d) Ione, Amador County, California, e) unknown, f) unknown.

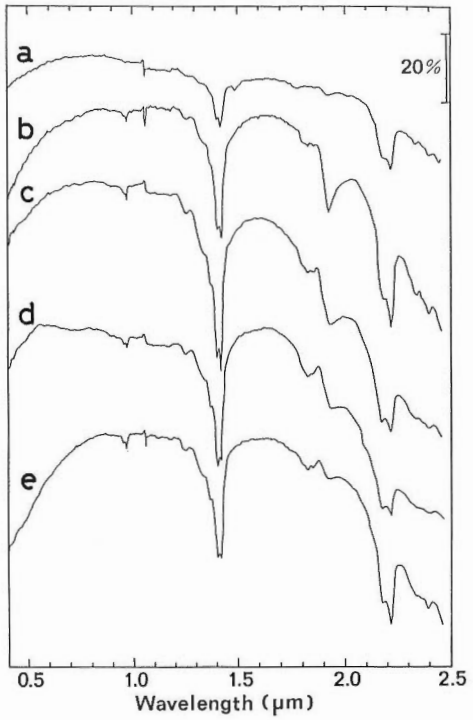

Fig. 10 Reflectance spectra of kaolinite (2). Localities are as follows: a) Riverside, California, b) Macon, Bibb County, Georgia, c) Murfreesboro, Pike County, Arkansas, d) Mesa Alta, New Mexico, e) Bath, Aiken County, South Carolina.

water (Figs. 13, 14, and 15). These features are asymmetric, usually with a steeper slope on the shorter wavelength side. There is another band near 2.25 μm due to Al–OH bending mode (Hunt *et al.*, 1973).

5) Pyrophyllite; $Al_2Si_4O_{10}(OH)_2$

There is a diagnostic very sharp absorption at 1.39 μm (Fig. 16). The 2.17 μm band is also clear. The other weaker absorption features are at 1.0 and 2.3 μm. The 1.9 μm absorption indicates absorbed water in the sample.

6) Talc; $Mg_3Si_4O_{10}(OH)_2$

There is a sharp absorption at 1.39 μm (Fig. 17) similarly to pyrophyllite. Another diagnostic absorptions at 2.32 and 2.39 μm make it possible to distinguish talc from pyrophyllite.

7) Muscovite; $K_2(Al, Fe^{3+}, Fe^{2+}, Mg)_4(Si, Al)_8O_{20}(OH, F)_4$

The strongest band is at 1.4 μm, and the next one is at 2.2 μm (Fig. 18). A broad absorption at 2.35–2.36 μm is also characteristic to muscovite (or sericite).

8) Illite; $KAl_2(OH)_2AlSi_3(O,OH)_{10}$

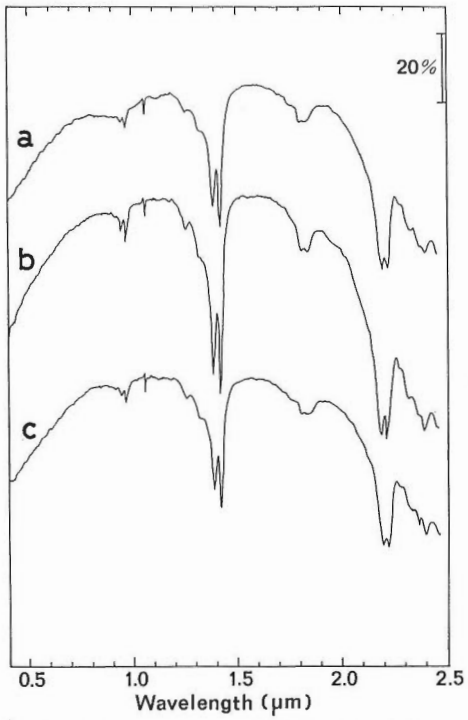

Fig. 11 Reflectance spectra of dickite. Localities are as follows: a) Cusihuriachi, Mexico, b) Red Mountain, Colorado, c) San Juanito, Mexico.

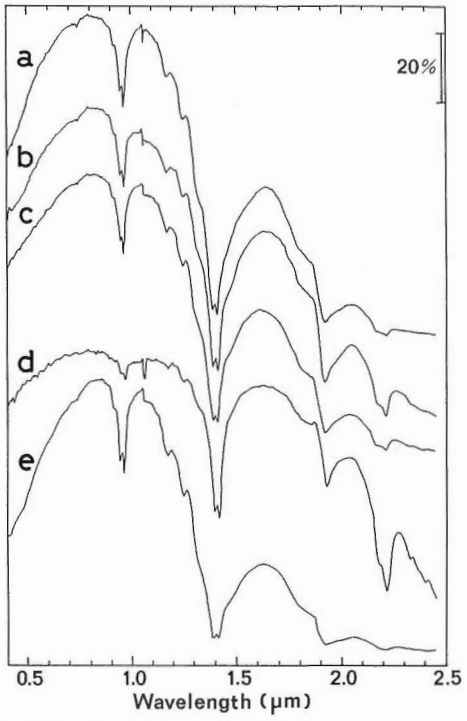

Fig. 12 Reflectance spectra of halloysite. Localities are as follows: a) Huntington, Emery County, Utah, b) Bedford, Lawrence County, Indiana, c) Utah, d) Sparuce Pine, Mitchell County, North Carolina, e) Huron, Lawrence County, Indiana.

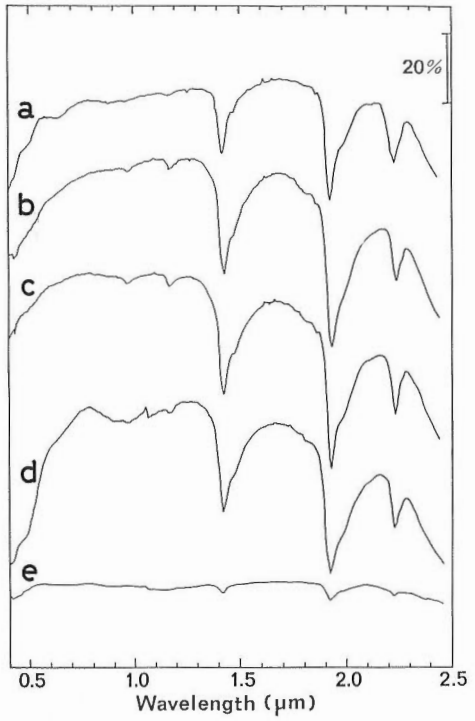

Fig. 13 Reflectance spectra of montmorillonite (1). Localities are as follows: a) Crook County, Wyoming, b) and c) Gonzales County, Texas, d) Palos Verdes, Los Angels County, California, e) Pioche, Lincoln County, Nevada.

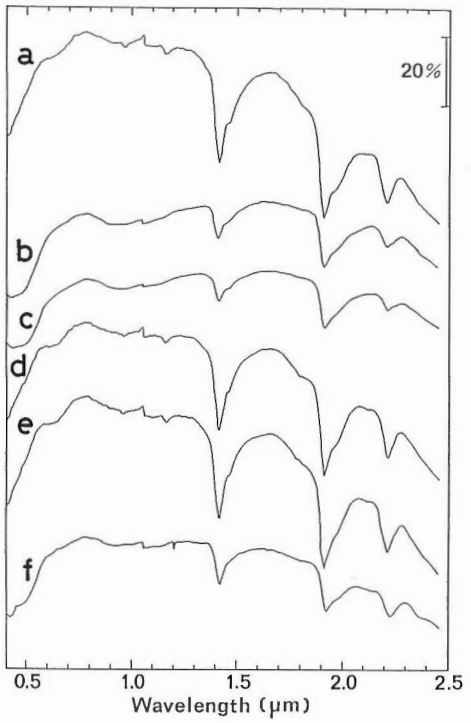

Fig. 14 Reflectance spectra of montmorillonite (2). Localities are as follows: a) Upton, Weston County, Wyoming, b) and c) Amory, Monroe County, Mississippi, d) and e) Clay Spur, Wyoming, f) Catawba, Roanoke County, Virginia.

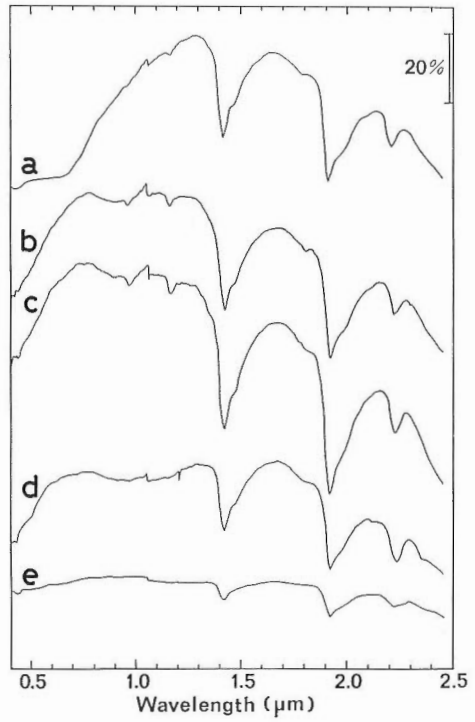

15 Reflectance spectra of montmorillonite (3). Localities are as follows: a) Little Rock, Pulaski County, Arkansas, b) and c) Chambers, Apache County, Arizona, d) High Bridge, Kentucky, e) Cameron, Coconino County, Arizona.

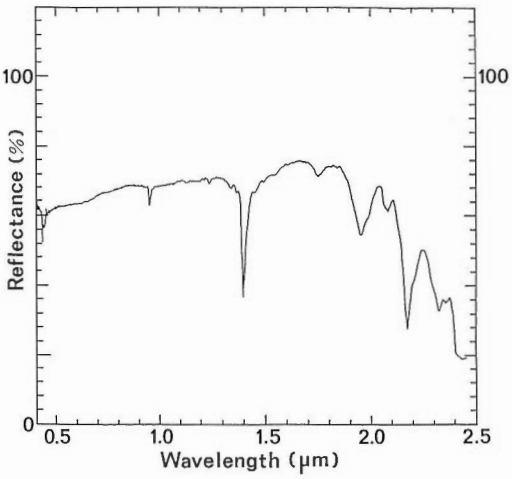

Fig. 16 A reflectance spectrum of pyrophyllite.

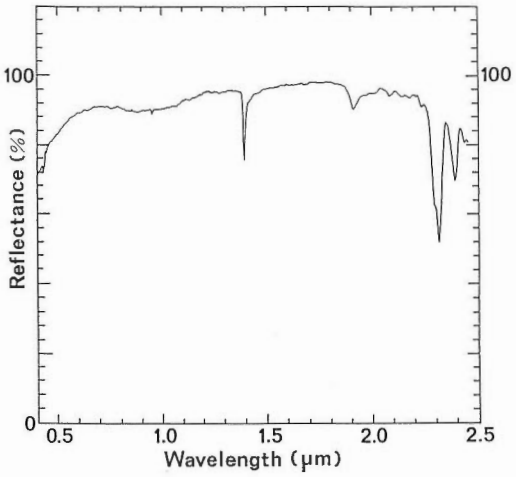

Fig. 17 A reflectance spectrum of talc.

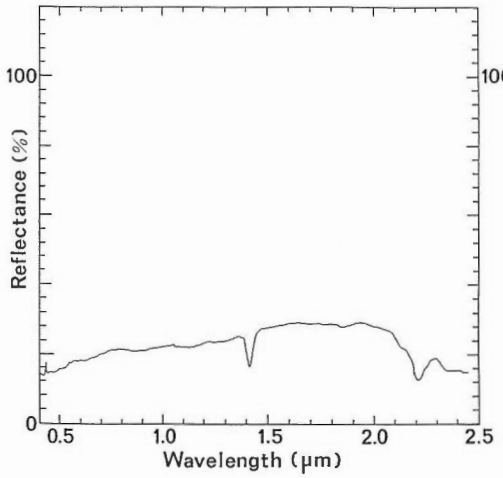

Fig. 18 A reflectance spectrum of muscovite.

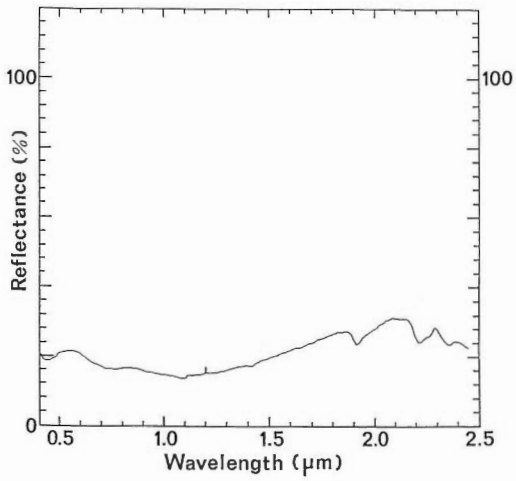

Fig. 19 A reflectance spectrum of illite, whose locality is Silver Hill, Montana.

There are strong absorptions at 1.9 and 2.2 μm, and a weak one at 2.36 μm (Fig. 19).

2.3.3 Carbonates

1) Calcite; $CaCO_3$

The strong absorption at 2.35 μm due to CO_3 is diagnostic to calcite (Fig. 20). There are also less significant bands at 1.88, 2.0, and 2.16 μm. The absorption at 1.4 μm in Fig. 20 (e) and (f) might indicate water as fluid inclusions in the crystal.

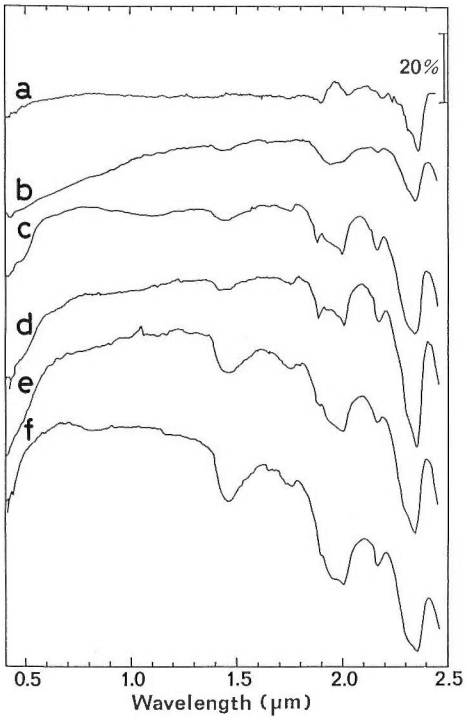

Fig. 20 Reflectance spectra of calcite. Localities are as follows: a) calcium carbonate powder for chemical analysis, b) Jerritt Canyon, Elko County, Nevada, c) Yerington, Lyon County, Nevada, d) Carlin Mine, Eureka County, Nevada, e) and f) Jerritt Canyon, Elko County, Nevada.

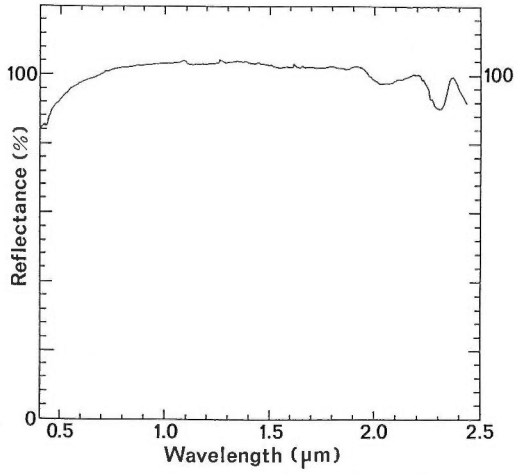

Fig. 21 A reflectance spectrum of magnesite (magnesium carbonate powder for chemical analysis).

2) Magnesite; $MgCO_3$

The reflectance spectrum (Fig. 21) was measured for pure magnesium carbonate powder. It looks quite similar to the spectrum of calcite. However, the absorption minimum due to CO_3 is located at 2.298 μm, which is slightly shorter than that of calcite.

2.3.4 Sulfates

1) Alunite; $KAl_3(SO_4)_2(OH)_6$

Alunite is one of the minerals easily identifiable from its reflectance spectrum. There are a diagnostic doublet at 1.42–1.50 μm, and absorptions at 1.76–1.78, 2.16–2.18, and 2.32–2.34 μm due to Al–O–H (Fig. 22). The absorption at 1.9 μm in Fig. 22 (b) is due to absorbed water.

2) Gypsum; $CaSO_4\ 2H_2O$

There are strong absorption bands at 1.45 and 1.96 μm, and less strong ones at 1.75 and 2.23 μm (Fig. 23). On the right (longer wavelength) slope of the 1.45 μm band, two weak absorption features can be recognized in 1.48–1.55 μm. The other weaker absorption features are at 1.0 and 1.2 μm.

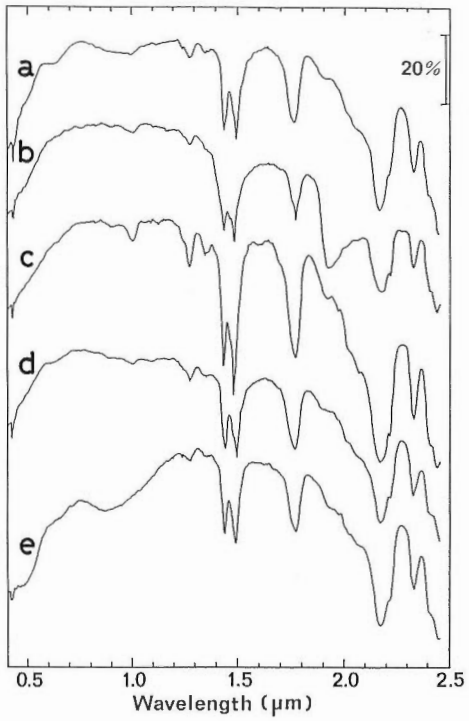

Fig. 22 Reflectance spectra of alunite. Localities are as follows: a), b), c), and d) Nevada, e) Geiger Hill, Washoe County, Nevada.

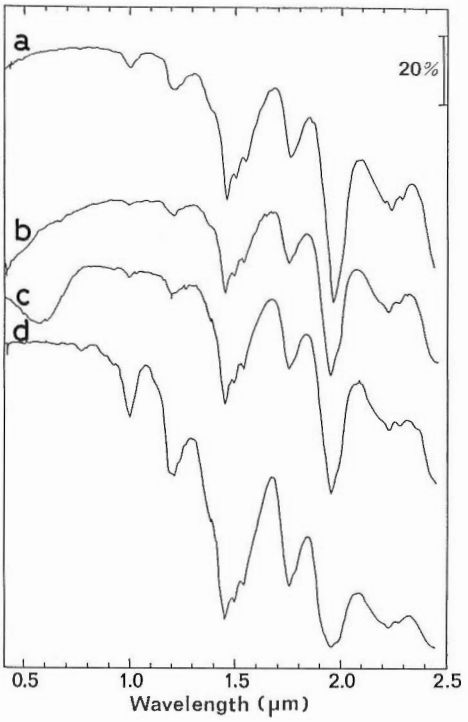

Fig. 23 Reflectance spectra of gypsum. Localities are as follows: a) moistened powder of calcium sulfate for chemical analysis, b) Yerington, Lyon County, Nevada, c) and d) Gypsum Mine, Lyon County, Nevada.

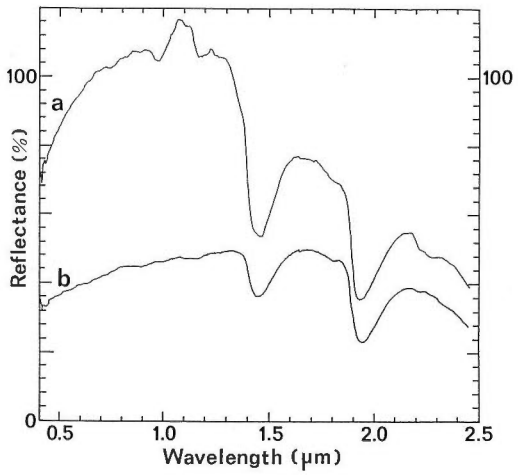

Fig. 24 Reflectance spectra of quartz. a) white milky quartz, b) quartz crystal.

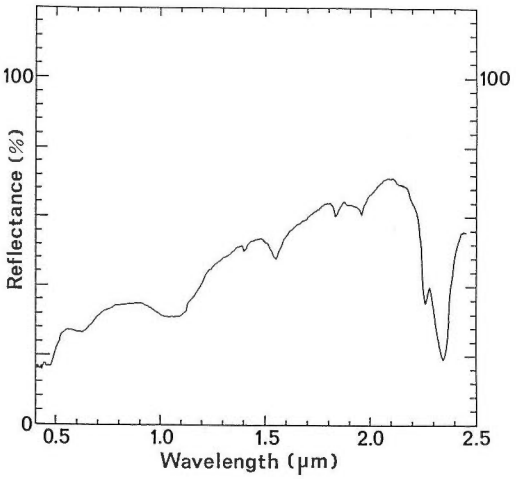

Fig. 25 A reflectance spectrum of epidote, whose locality is Yerington, Lyon County, Nevada.

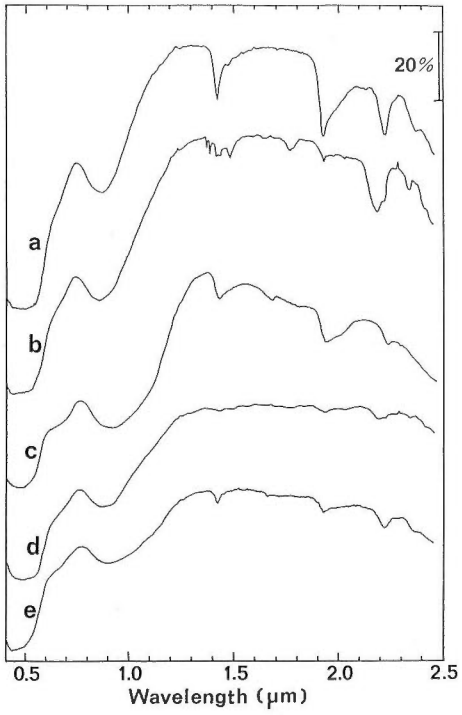

Fig. 26 Reflectance spectra of hematite (a and b), and goethite (c, d, and e). Localities are as follows: a), c), and e) Carlin, Elko County, Nevada, b) and d) Goldfield, Esmeralda County, Nevada.

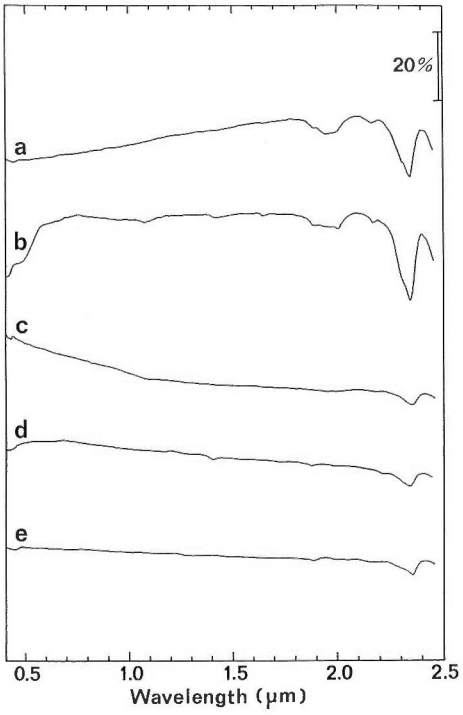

Fig. 27 Reflectance spectra of limestone. Localities are as follows: a), b), and c) Carlin, Elko County, Nevada, d) and e) Yerington, Lyon County, Nevada.

2.3.5 Other Minerals

1) Quartz; SiO_2

Pure quartz is spectrally featureless in the VNIR and SWIR regions. However, quartz crystal often contains fluid inclusion, which exhibits absorption features of water or hydroxyls. The spectra of quartz crystal (Fig. 24) clearly show absorption features at 1.4 and 1.9 μm due to presence of molecular water, and a broad shoulder at about 2.25 μm due to Si-O-H.

2) Epidote; $Ca_2(Al, Fe^{3+})_3Si_3O_{12}(OH)$

The strongest and characteristic absorption feature is at 2.35 μm (Fig. 25). There is a small absorption at 2.26 μm on the left slope of this absorption. The other weaker features are at 1.55, 1.84, and 1.95 μm. There are broad absorptions at 0.6 and 1.0-1.1 μm due to iron.

3) Iron oxides and iron hydroxides

Iron oxide minerals in this case include hematite (Fe_2O_3) and goethite (FeOOH). They have broad absorption features at 0.8 to 1.0 μm (Fig. 26). The absorption minimum of hematite exhibits a shorter wavelength than that of goethite. Spectra of goethite show shoulders at about 0.6 μm on the slope toward the ultraviolet range where a charge transfer band creates a strong absorption (Hunt *et al.*, 1971a). The other features in the region whose wavelength is longer than 1.0 μm are due to hydroxyls and/or water in the samples.

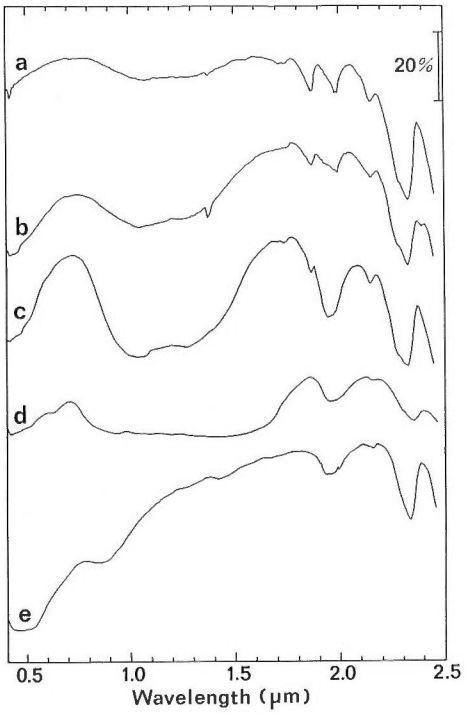

Fig. 28 Reflectance spectra of dolomite (a, b, and c) and ankerite (d and e). Localities are as follows: a) Lee, Massachusetts, b) Ossining, New York, c) Joplin, Missouri, d) Cumberland, England, e) Quijotoa, Arizona.

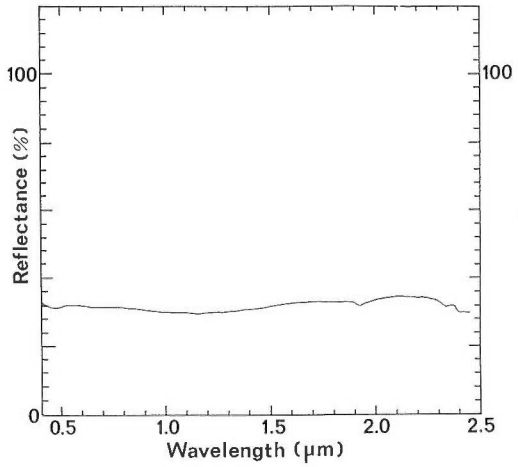

Fig. 29 A reflectance spectrum of a fresh surface of granite, which was collected near Lake Tahoe, California.

2.3.6 Various Rock Types

1) Limestone

The definition of limestone is a sedimentary rock containing at least 50 weight percent of calcite, so that reflectance spectra of limestone (Fig. 27) are similar to those of calcite. But limestone often contain non-carbonate elements such as silt and clay, which obscure diagnostic spectral features of calcite. Although the 2.35 μm absorptions of limestone samples are still recognizable, they are less clear than those of pure calcite (Fig. 20).

2) Dolomite and ankerite; $Ca(Mg, Fe, Mn)(CO_3)_2$

In the above formula, if Mg > Fe, the rock is called dolomite. Whereas, if Mg < Fe, the rock is called ankerite. Spectra of dolomite and ankerite (Fig. 28) indicate the absorption minima at 2.324 to 2.329 μm, which is slightly shorter than that of calcite or limestone at 2.35 μm.

3) Granite

The spectrum of a granite sample (Fig. 29) is almost featureless, because quartz and feldspar, which are major rock forming minerals of granite, are spectrally featureless in the VNIR and SWIR regions. The broad absorption at 2.35 μm might be due to biotite.

4) Basalt, andesite, and tuff

Most of the spectra of these volcanic rocks (Fig. 30) are also featureless like that of granite

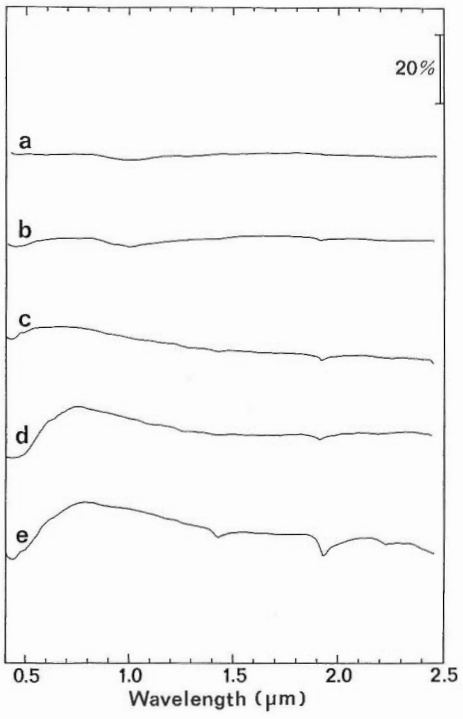

Fig. 30 Reflectance spectra of volcanic rocks. a) and b) basalt, (Carlin, Elko County, Nevada), c) andesite (Yerington, Lyon County, Nevada), d) and e) rhyodacitic tuff (Yerington, Lyon County, Nevada).

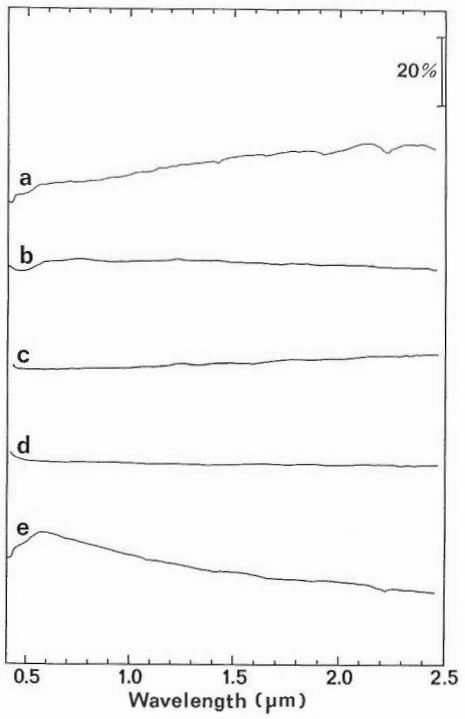

Fig. 31 Reflectance spectra of sandstone (a) and shale (b, c, d, and e). All samples were collected in Carlin, Elko County, Nevada.

because of the same reason described in the explanation of the granite spectrum. However, if the sample is weakly weathered [Fig. 30(e)], there are hydroxyl and water bands at 1.4, 1.9, and 2.2 μm.

5) Sandstone and shale

A spectrum of sandstone reflects the type of sand grains. In this particular case, most of the sand grains consist of quartz, thus the spectrum [Fig. 31(a)] is almost featureless except a weak absorption at 2.35 μm, probably due to mica. Shale is a fine-grained sedimentary rock, and often contains phyllosilicates. In this case, the spectra of shale [Fig. 31(b-e)] exhibit very weak absorption bands at 2.2 and 2.35 μm due to a small amount of phyllosilicates.

6) Chert

The spectra of chert (Fig. 32) look like those of quartz (Fig. 24), i.e., absorption bands due to molecular water at 1.4 and 1.9 μm, and a broad band due to Si-O-H at about 2.25 μm.

2.3.7 Vegetation

1) Green leaves

Vegetation shows a quite different spectral pattern compared with those of rocks and minerals. Fig. 33 shows a reflectance spectrum of green leaves. The most significant feature is a high plateau in the near infrared region with a steep slope from 0.6 to 0.7 μm so called "red edge". There is a small peak in the green region of the visible range due to strong absorptions of chlorophyll in the blue and red regions. Broad and strong absorptions at 1.4 and 1.9 μm in the SWIR range are due to molecular water in plant cells.

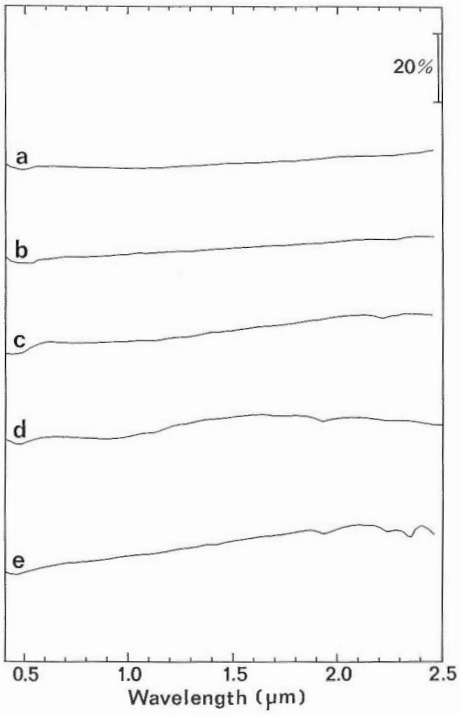

Fig. 32 Reflectance spectra of chert. Localities are as follows: a), b), c), and e) Carlin, Nevada, d) Waterloo, Colorado.

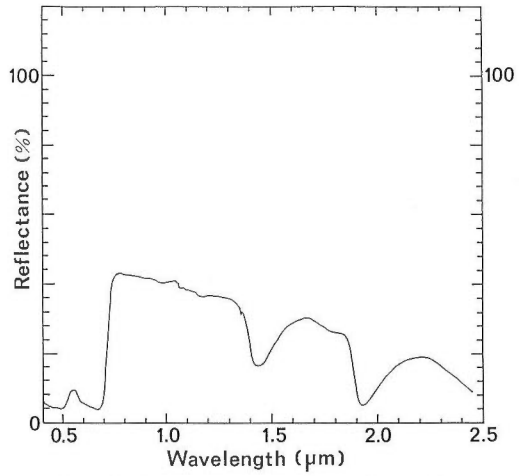

Fig. 33 A reflectance spectrum of green leaves.

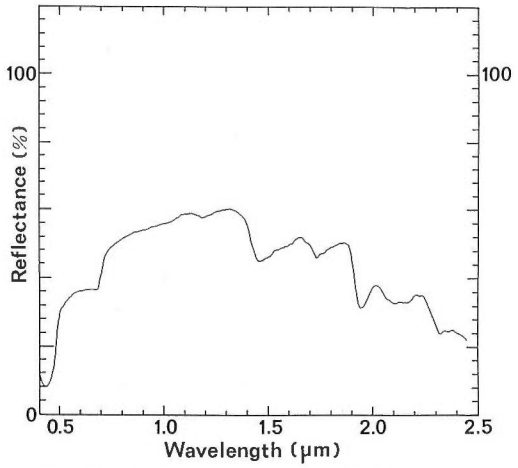

Fig. 34 A reflectance spectrum of lichen.

2) Lichen

Lichen often covers rock surface and makes it impossible to obtain information on the rocks beneath. The reflectance spectrum of lichen (Fig. 34) exhibits a more up and down pattern than that of the green leaves. This pattern indicates a reflectance spectrum of cellulose, which is obscured in the spectrum of the green leaves due to higher concentration of water.

2.4 Identification of Minerals by Spectral Features

2.4.1 Feature Extraction

We can identify most of the important clay minerals from their VNIR and SWIR reflectance spectra, because they have some characteristic absorption features as shown in the previous chapter. The advantage of the spectral method is its quick and easy field operation compared with the X-ray diffraction method, more widely used in mineralogy and petrology. However, similar to the X-ray method, sufficient prior knowledge of spectral features is necessary to tell mineral species apart. This section shows an example of an "expert system" by which we can determine the possible minerals in measured samples without needing "expert" knowledge of mineral spectroscopy. The system consists of four portions: a feature-extraction program, a feature-coding program, a code-matching program and a data file of the codes.

The process of mineral identification from spectra by eye is a type of pattern recognition, employing diagnostic spectral features in their reflectance curves. The wavelength position of an absorption minimum and strength of an absorption are fundamentally important items to characterize each absorption, and represent the styles and strengths of the O-H bondings in the clays.

In order to compare strength of absorptions, we need to define their relative strengths, usually considered to be the depth from the shoulder to the bottom. However, it is not easy to find precisely where the shoulders are, thus the depth determination can be subjective. Moreover, the depth, which is a percentage of the reflectance values, can depend in turn upon the average reflectance of a spectrum. If the average reflectance is low, then the depth of an important absorption can be too small to be detected. For the purpose of identifying these important absorption wavelengths, the shape of their absorptions is often more important than

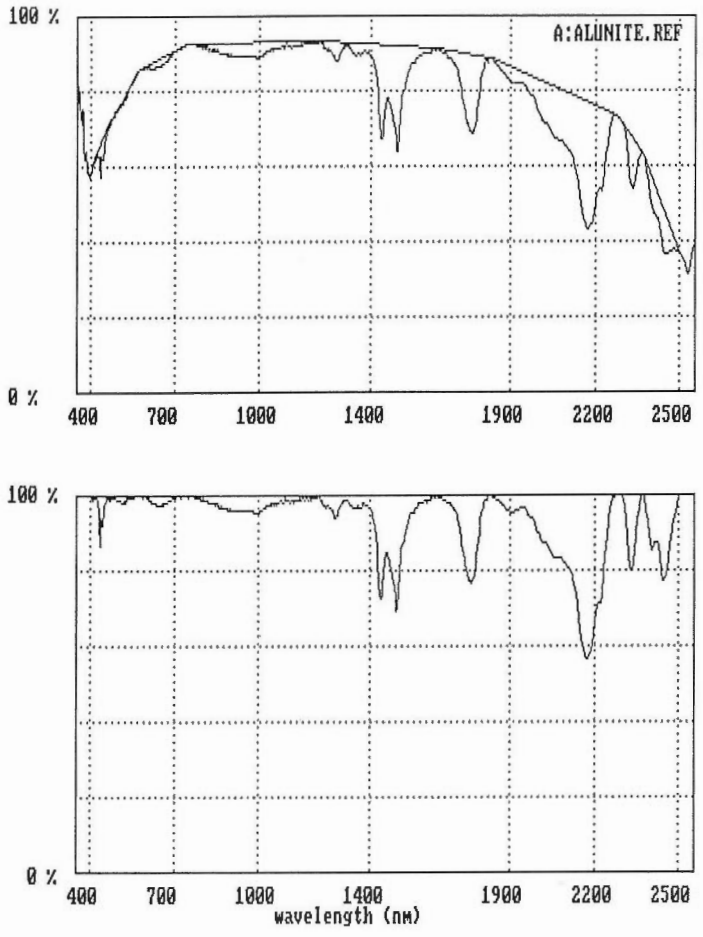

Fig. 35 Upper: A reflectance spectrum of alunite and a hull. Lower: A hull-quotient curve derived from the upper. Note that the common sloping background in the raw reflectance is removed in the hull-quotient curve, thus the absorption features are enhanced. The hull-quotient is calculated only in the range from 0.4 to 2.5 μm.

the absolute measured value. This is a factor which we must introduce next in the systems.

The concept of "hull-quotient" (Green and Craig, 1985) was applied to help avoid these problems. A hull is defined as the lowest convex curve lying above the given spectrum, and hull -quotient is given by taking the ratio between raw reflectance and hull values (Fig. 35). The algorithm is as follows:

Step 1: Find the maximum reflectance value in a spectrum.

Step 2: Calculate a slope of a line from the maximum to each data point whose wavelength is longer than the maximum. Choose the point with the largest slope. Substitute this point to the maximum, and repeat to choose the next point with the largest slope until the last point. Do the same procedure for the data points of shorter wavelength than the maximum, but choose sequentially the point with the smallest slope.

Step 3: Link the maximum and the data points chosen in Step 2. The line drawn represents the hull (Fig. 35).

Step 4: Take ratio between raw reflectance and the hull value for each channel. The result plotted is the hull-quotient curve (Fig. 35).

This method can remove the common sloping background (due to water at 2.7 μm), thus enhancing the absorption features with significant shapes regardless of their raw reflectance values. Notice the effect beyond 2.2 μm shown in Fig. 35.

Next step is to pick up absorption minima in the hull-quotient curve based upon reasonable criteria. Meaningful absorption features (in a typically-noisy spectrum) are regarded as those with sufficient depth and width. We can use following algorithm to detect them.

Step 1: Pick all local minima. All the data points with a negative slope to the left and a positive slope to the right are chosen and marked.

Step 2: Assign the widdh of a window, e.g., four data points. Look at the reflectance of data points, which are a "half-window" width, left and right from the data points marked in Step 1. If both the left and right points have larger reflectance than the center point does, mark the center point again.

Step 3: Assign the threshold depth, e.g., five percent. Check the depth of the data points marked in Step 2. If the depth is larger than the threshold, pick up the data point as the minimum of an absorption.

This algorithm can detect absorptions from reflectance data without smoothing even if the data have small noise fluctuations. The smaller the window width and threshold depth are, the more numbers of shallow minima are picked up, which then may include meaningless noise. On the other hand, large window widths and threshold depths allow us to pick only major absorptions. Empirically the window width and threshold depth were set at four data points (out of 820) and five percent respectively. The number of minima detected usually ranges from two to ten, and rarely more than twenty. The absorptions are automatically arranged in order of depth.

2.4.2 Feature Coding and Matching

Pattern recognition criteria could be described in computer programs by using "IF -THEN" statements. However, it is not easy to make a description of these criteria perfectly by "IF-THEN" statements, because of complexity and diversity of possible patterns of absorptions. Moreover, if we need to add new minerals to be identified, we have to modify the program.

The author proposes a new method, feature coding and matching, for quick and efficient pattern recognition of reflectance spectra. Coding of absorption features can relieve such difficulty in describing criteria for mineral identification. Coding is a manner of expressing the sequence of pattern of absorption features in a spectrum, by their wavelengths and order of strength with a single string of symbols.

Due to the variety of possible chemical substitutions and the degree of crystallization of samples, and/or accuracy of an equipment, each absorption position for a mineral has some variable wavelength extent. For instance, Alunite is expected to have a diagnostic absorption at 1.762 μm (Hunt *et al.*, 1971b), but the wavelength of this absorption had the range of 1.762 to 1.774 μm in our measurements. Therefore, it is more appropriate to use a window with a certain range of wavelengths than an exact wavelength of an absorption.

Sixteen windows were selected over the wavelengths where diagnostic absorptions may occur (Fig. 36). Each window has a hexadecimal-type symbol (0, 1, 2, 3 ... E) listed in Table 2. The range of the windows used is from 1.3 to 2.5 μm, where most of important absorptions of clay minerals appear. The location of windows was chosen so that different patterns of absorptions could be discriminated effectively. These will vary with spectrometer type (e.g., CVF or grating) and also with its wavelength calibration. For example, if there are Al-O-OH absorption doublets at about 1.4 μm (Hunt and Salisbury, 1970), minima may occur in both window "1" and "2".

A code is given to each spectrum according to the following rules.

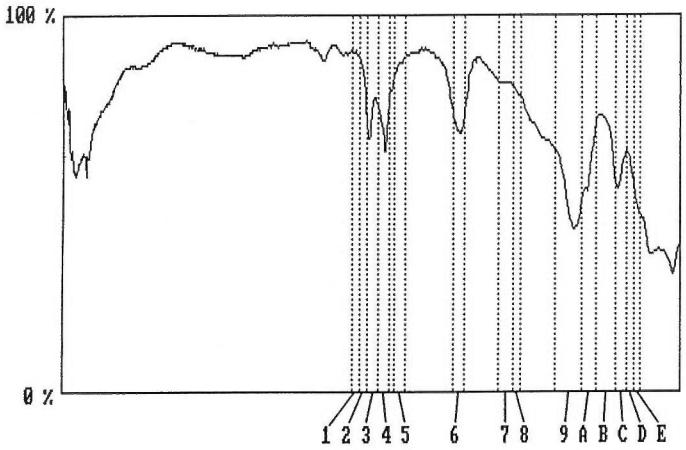

Fig. 36 Locations of fourteen windows (Table 2), in which diagnostic absorption features may occur. A reflectance spectrum of alunite is also shown.

1) The symbol of a window in which each absorption is located is given in order of absorption depth.

2) An absorption which belongs to no windows is ignored.

3) One code for absorptions in one window. If we have more than two absorptions in one window, only the strongest absorption is coded.

4) The number of symbols for one spectrum is set arbitrarily at six. This could easily be enlarged.

Table 3 shows examples how coding is performed. As sample-1 has absorptions at 2.210, 2.197, 1.397, 1.415, and 2.380 μm in order of depth, it can be coded as "A912D". Sample-2 has absorptions at 1.930, 1.415, 1.423, 2.220, and 1.625 μm. As the second and the third ones are in the same window, and the fifth one belongs to no window, this spectrum is expressed as "72A".

Table 4 shows a list of codes of clay minerals to be identified. Because of chemical and physical variability, any mineral can have more than two codes. In a few cases, different minerals can have the same code, that means we cannot discriminate them from the spectra data processed in this manner. As this list is stored as a data base file separately from the identification program, we can modify it easily whenever required. It is easy to add a new mineral or to edit a correction to the codes. Mixtures of "end-member" minerals will show

Tabel 2 Wavelength positions of selected windows.

Window	Wavelength (μm)
1	1.380 - 1.405
2	1.405 - 1.430
3	1.430 - 1.470
4	1.470 - 1.510
5	1.530 - 1.570
6	1.740 - 1.780
7	1.900 - 1.950
8	1.950 - 1.980
9	2.100 - 2.200
A	2.200 - 2.250
B	2.250 - 2.320
C	2.320 - 2.360
D	2.360 - 2.390
E	2.390 - 2.410

progressive changes in their codes.

Alunite (Fig. 22) has diagnostic absorptions at 1.76–1.78, 2.16–2.18, and 2.32–2.34 μm and characteristic doublets at 1.42–1.50 μm, but all their depths are very similar. In order to identify alunite, it is necessary to have the 2.16–2.18 μm band, 1.76–1.78 μm band, and the 1.42–1.50 μm doublets. And if alunite is moistened, it can have a molecular water band at about 1.9 μm. Thus, the many codes for alunite consist of "9", two symbols among "2", "3", and "4", followed by "6" and/or "C", and the symbol "7" can be inserted at any position between them.

Calcite (Fig. 20) has a characteristic strong absorption at about 2.35 μm and is coded as "C". The absorption of magnesite (Fig. 21) is at slightly shorter wavelength than that of calcite and is coded as "B". Talc (Fig. 17) has an absorption at 2.31–2.32 μm, which is very close to those of calcite and magnesite. However, as talc also has another diagnostic strong absorption at 1.39 μm, it is coded as "B1" or "C1". Similarly, epidote (Fig. 25) has the strongest absorption at 2.35 μm and weaker ones at 1.55, 1.95, and 2.26 μm, among which the absorption at 1.55 μm is considered to be diagnostic of epidote. Thus, epidote is coded by "C" first and followed by one or two symbols among "5", "7", "8", and "B", including at least "5".

Gypsum (Fig. 23) has strong absorptions at 1.45 and 1.96 μm and relatively small ones at 1.75 and 2.23 μm. Sometimes small two absorptions at 1.48–1.55 μm on the slope of the 1.45 μm absorption can be picked up. Among them, the 1.45, 1.96, and 1.75 μm bands are diagnostic. If a sample with gypsum is moistened, the absorption at 1.96 μm can shift toward 1.9 μm.Thus, the symbols "3", "8", and "6" must be in the codes, "4", "5", and "A" can be in the codes, and "8" can be substituted by "7".

Kaolinite (Figs. 9 and 10) has diagnostic doublets at 1.4 and 2.2 μm regions if well-crystallized, but only one absorption for each region is resolvable if poorly-crystallized. In the 2.2 μm doublets, the absorption with longer wavelength is always deeper and survives in spectra of poorly-crystallized samples. So the code of kaolinite must have "A" and at least one symbol from "1" or "2", and can have "9". If the sample with kaolinite is moistened, there is a molecular water band at 1.9 μm. In case that the 1.9 μm absorption is the deepest, it is very difficult to discriminate kaolinite from montmorillonite unless there are doublets at 1.4 or 2.2 μm.

Table 3 Examples of spectral coding and code matching.

(a) Sample-1

absorptions			
wavelength(μm)	depth(%)	order	window
1.397	67.5	3	1
1.415	65.2	4	2
2.197	70.3	2	9
2.210	81.7	1	A
2.380	43.8	5	D

=====> Code is "A912D".

(b) Sample-2

absorptions			
wavelength(μm)	depth(%)	order	window
1.415	51.5	2	2
1.423	48.7	3	2
1.625	7.9	5	
1.930	73.9	1	7
2.220	33.0	4	A

=====> Code is "72A".

Table 4 List of spectral codes of typical minerals.

Mineral	Codes
Alunite	9236, 9326, 9246, 9426, 9346, 9436, 2396, 3296, 3496, 4396, 2496, 4296, 2936, 3926, 3946, 4936, 2946, 4926, 79236, 97236, 92736, 92376, 79326, 97326, 93726, 93276, 79246, 97246, 92746, 92476, 79426, 97426, 94726, 94276, 79346, 97346, 93746, 93476, 79436, 97436, 94736, 94376, 72396, 27396, 23796, 23976, 73296, 37296, 32796, 32976, 73496, 37496, 34796, 34976, 74396, 47396, 43796, 43976, 72496, 27496, 24796, 24976, 74296, 47296, 42796, 42976, 72936, 27936, 29736, 29376, 73926, 37926, 39726, 39276, 73946, 37946, 39746, 39476, 74936, 47936, 49736, 49376, 72946, 27946, 29746, 29476, 74926, 47926, 49726, 49276, 923C6, 932C6, 924C6, 942C6, 934C6, 943C6, 239C6, 329C6, 349C6, 439C6, 249C6, 429C6, 293C6, 392C6, 394C6, 493C6, 294C6, 492C6, 7923C6, 9723C6, 9273C6, 9237C6, 7932C6, 9732C6, 9372C6, 9327C6, 7924C6, 9724C6, 9274C6, 9247C6, 7942C6, 9742C6, 9472C6, 9427C6, 7934C6, 9734C6, 9374C6, 9347C6, 7943C6, 9743C6, 9473C6, 9437C6, 7239C6, 2739C6, 2379C6, 2397C6, 7329C6, 3729C6, 3279C6, 3297C6, 7349C6, 3749C6, 3479C6, 3497C6, 7439C6, 4739C6, 4379C6, 4397C6, 7249C6, 2749C6, 2479C6, 2497C6, 7429C6, 4729C6, 4279C6, 4297C6, 7293C6, 2793C6, 2973C6, 2937C6, 7392C6, 3792C6, 3972C6, 3927C6, 7394C6, 3794C6, 3974C6, 3947C6, 7493C6, 4793C6, 4973C6, 4937C6, 7294C6, 2794C6, 2974C6, 2947C6, 7492C6, 4792C6, 4972C6, 4927C6, 923C76, 932C76, 924C76, 942C76, 934C76, 943C76, 239C76, 329C76, 349C76, 439C76, 249C76, 429C76, 293C76, 392C76, 394C76, 493C76, 294C76, 492C76
Calcite	C
Epidote	C5, C57, C58, C5B, C75, C85, CB5, C785, C875, C7B5, CB75, C8B5, CB85

(continues)

Thus, the code "7" of the 1.9 μm window should not be the first symbol of the kaolinite codes, unless there is at least one pair of doublets. Dickite (Fig. 11) has a different code of "29AED", halloysite is often "A217" ; if dried out it becomes "21A97C".

Montmorillonite (Figs. 13, 14, and 15) has three major absorptions at about 1.90–1.94, 1.41–1.45, and 2.2–2.23 μm in order of depth, and its codes can be given as "72A", "73A", "723A", or "732A". Code "A72" is also commonly found. Nontronite is a Fe^{2+} type of the smectite group minerals and has very similar looking spectra as montmorillonite. But its absorption at 2.29 μm is slightly longer than that of montmorillonite at 2.2–2.23 μm, and is located in the different window "B". So the codes of nontronite can be given by substituting "A" by "B" in the codes of montmorillonite.

Pyrophyllite (Fig. 16) has strong absorptions at 1.39 and 2.17 μm, so that it is coded as "91" or "19". Other codes of "198C" and "19C" may occur.

Muscovite or sericite (Fig. 18) has sharp absorptions at about 1.4 and 2.2 μm and a less sharp one at 2.35–2.36 μm. If the sample is moistened, it may have a molecular water band at

Table 4 (continued)

Mineral	Codes
Gypsum	386, 836, 376, 736, 38A6, 3486, 3586, 3846, 3856, 83A6, 8346, 8356, 37A6, 3476, 3576, 3746, 3756, 73A6, 7346, 7356, 34586, 38456, 348A6, 358A6, 83456, 834A6, 835A6, 384A6, 385A6, 34856, 34576, 37456, 347A6, 357A6, 73456, 734A6, 735A6, 374A6, 375A6, 34756
Kaolinite	1A, 2A, A1, A2, 12A, 1A2, 21A, 2A1, A12, A21, 1A9, 2A9, A91, A92, A19, A29, 712A, 172A, 127A, 71A2, 17A2, 1A72, 721A, 271A, 217A, 72A1, 27A1, 2A71, 7A12, A712, A172, 7A21, A721, A271, 71A9, 17A9, 1A79, 72A9, 27A9, 2A79, 7A91, A791, A971, 7A92, A792, A972, 7A19, A719, A179, 7A29, A729, A279
Magnesite	B
Montmorillonite	72A, 73A, 723A, 732A
Nontronite	72B, 73B, 723B, 732B
Pyrophyllite	91, 19
Sericite	2A, A2, 2AC, A2C, 2AD, A2D, 2A7C, A27C, 72AC, 27AC, 7A2C, A72C, 2A7D, A27D, 72AD, 27AD, 7A2D, A72D
Talc	B1, C1

1.9 μm. Thus, the codes of sericite consist of "2", "7", "A", and "C" or "D". And "7" should not be ahead of "2" or "A", if there is not "C" or "D". Surface weathering in field samples shows as a code modification towards that of montmorillonite (illitic).

Identification of minerals can be done by matching the spectral code of measured sample with the spectral codes of important index minerals in the data file. Even if a code of a measured sample has six symbols, it is not necessary that the sequence of symbols matches the codes in the data file. It is possible that only the first two symbols match one of the codes in the data file. In the data file, the codes are stored in order of symbol numbers. Therefore, matching of the code of the measured sample is started with the codes of the same number of symbols in the data file. If we cannot match them, the code of the measured sample is truncated by removing the last symbol. Then code matching is carried out again with the codes in the data file. This process is repeated until the matched code is found, or "no-match" is indicated. The name of that index mineral whose code is same will be displayed on screen. If there is no mineral with the same code as that of the sample, we have two options. One is to leave the sample unclassified, and the other is to add the code of the sample to the data file as a new data. Presently there are about 400 codes in the data base.

Here are two examples of code matching. Sample-1 in Table 3 was coded as "A912D". There are no such codes composed of five symbols in the data file. So let us truncate the last two symbols, and we will get the code "A91". We can find the same code in the data file, and

it is the code of kaolinite. Thus, sample-1 is identified as kaolinite. Sample-2 in Table 3 has the code of "72A". Look for the same code composed of three symbols in the data file, and we can find that montmorillonite has the same code.

2.4.3 Discussion

The mineral identification system described above has been tested for laboratory spectra of about 300 rock samples from Virginia City, Singatse Range, and Carlin districts, Nevada, U.S. A. For the minerals with diagnostic absorptions such as alunite and gypsum, the program could determine them without any problems. The minerals with the strongest absorption at the wavelength longer than 2.2 μm, such as calcite and epidote, could be easily identified as far as the absorption is sufficiently prominent (deeper than the threshold value). However, discrimination between calcite and epidote became difficult, if the diagnostic absorption of epidote at 1.55 μm was not clear (because of mixing with the other minerals).

It was sometimes difficult to discriminate kaolinite, sericite, and montmorillonite especially when the samples were naturally moistened, because the wavelengths of the absorptions are almost same. Only the strength of absorptions can be the key to be used in this system. But it is basically impossible to discriminate them in some cases, because the same codes are given to different minerals. One possible solution is to employ a description of absorption shapes along with its wavelength. For instance, absorptions of montmorillonite are relatively broader and asymmetric-right (Figs. 13, 14, and 15), whereas kaolinite and sericite have relatively narrower and symmetric absorptions (Figs. 9, 10, and 18). But discrimination between kaolinite and sericite is still difficult unless the diagnostic doublets of kaolinite or the absorption at 2.35 μm of sericite is clearly observable. It is even hard by visual observation. Thus, it is the limit of the spectral method, which might be determined by physical properties of these minerals in this NIR range and/or the spectral resolution of the equipment.

Lastly, the problem of mixtures has to be considered, as most of rock samples consist of a mixture of minerals. If two minerals are mixed, their joint spectrum shows the spectral features of two minerals according to the mixture (Hunt, 1979). In one test case, one spectrum showed a mixture of alunite and kaolinite, but was identified as kaolinite. In order to apply the spectral coding method to identify minerals in a mixture, we have to create spectral codes of possible mixtures of minerals.

Spectral coding is a very efficient data compression tool (from 820 data points to 5-6 codes). Although the number of minerals to be identified is limited to fifteen at present, the concept of spectral coding would be useful in a more sophisticated and complete expert system. An advantage of the coding method is its flexibility, in that we can readily change the identification criteria and can add new minerals by modifying the data file. In future, field spectroradiometers with expert systems would tell us the minerals in real time operation.

3. REFLECTANCE CALIBRATION OF MULTISPECTRAL SCANNER DATA

3.1 Significance of Reflectance Calibration

The author discussed diagnostic features in reflectance spectra of rocks and minerals in the previous chapter. Theoretically, reflectance is independent of illumination conditions, and thus indicates physical or chemical properties of the material measured. Reflectance measurements can be performed by ratioing radiance from a target and a reference standard, both of which are measured simultaneously or sequentially with a short interval assuming constant illumination conditions.

However, an airborne or spaceborne remote sensor measures radiance only from a target, which is then transformed into quantitized integer numbers through electronic processes in each spectral band. Eventually, we obtain digital number (DN) values recorded on a magnetic tape, e.g., integers with 6 bits or 8 bits dynamic range. People rarely care about the meanings of the DN values that often leads an image processing result which looks beautiful "mathematically" but is difficult to interpret geologically due to the lack of "physical calibration" of the DN values. It is obvious that calibration of the DN values into the numbers with physical units will allow us to obtain more meaningful results geologically from remote sensing data. Usually, calibration factors to convert DN values into radiance are available from a data book published by the agency which is responsible to build and calibrate a remote sensor prior to launching. To use such calibration factors is one possible way to perform "physical calibration" of DN values into radiance, but further transformation from radiance to reflectance is still needed in some cases.

The purpose of this chapter is to investigate the use of field spectral measurements and laboratory-based techniques as a means of calibrating DN values to percent reflectance. Airborne Imaging Spectrometer (AIS) data provided by NASA were used to make a comparison of the techniques. The author evaluated effectiveness of each method by comparing the calibrated inter-band patterns, as the AIS has enough spectral bands to draw a reflectance spectrum of the target.

3.2 A Test Case Using AIS Data

3.2.1 Description of the AIS System

The Airborne Imaging Spectrometer (AIS) is an instrument built by NASA in 1983 to test the imaging spectrometer concept with two-dimensional infrared area arrays of the type which will be used on the Shuttle Imaging Spectrometer Experiment (SISEX) planned for 1991 and High Resolution Imaging Spectrometer (HIRIS) planned for 1995. The AIS employs a 32 by 32 element mercury telluride array to sample the spectral region from approximately 0.9 to 2.4 μm. Five grating positions are available. Four sequential grating positions can be collected, sampling data either in the "tree mode" (0.9 to 2.1 μm) or the "rock mode" (1.2 to 2.4 μm). Stepping through the four grating positions produces 128 channels of continuous spectral data sampled at wavelength intervals of approximately 9.6 nm. As shown in Fig. 37, a 32 pixel wide swath, approximately 300 meters wide, is collected perpendicular to the flight direction (Jet Propulsion Laboratory, 1985; Goetz *et al.*, 1985).

The data collected by the AIS are severely affected by wavelength specific atmospheric

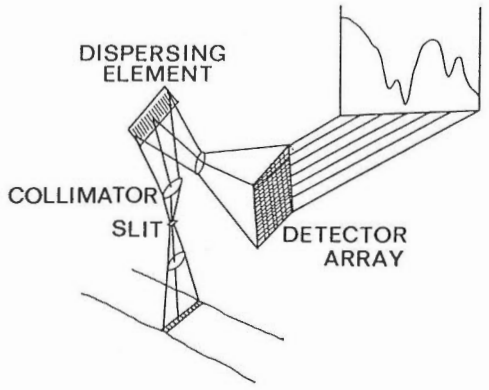

Fig. 37 Concept of the Airborne Imaging Spectrometer.

absorptions and decreased incoming solar irradiance at longer wavelengths (Fig. 38). These factors result in a reduction of the overall brightness and dynamic range of the data in the atmospheric absorption regions and at longer wavelengths. In the next section, techniques are tested to perform solar normalization and atmospheric correction.

Four flight line of data in the "rock mode" were acquired in the vicinity of the town of Yerington, Nevada, and adjacent Singatse Range on July 25th, 1984. The four flights, flight 407, 409, 410, and 411 covered a variety of targets ranging from mine dumps and clay altered areas to alfalfa fields. The data collected along each flight line were processed through a number of steps. First, the data were screened for bad data or line drop-outs. Line drop-outs were located by comparing digital numbers in one cross-track line to digital numbers in the previous cross -track line. An appropriate threshold value was selected empirically, and if the difference between the first line and the previous line was greater than this value, the running average for that channel was assigned to the present pixel. Second, screened data were selectively processed using one of the four calibration techniques tested. Finally, the processed data were destriped by equalizing the downflight sum of each channels for each of the 32 cross-track pixels in a flight.

3.2.2 Geology of the Test Site (Singatse Range, Nevada, U.S.A.)

The studied area is located in the Singatse Range at Yerington and Ann Mason, western Nevada, U.S.A. The Singatse Range is at the western edge of the Basin and Range Province and encompasses an area of 12 km N-S by 6 km E-W. Proffett and Dilles (1984) published a detailed geologic map of this area, and Dilles (1983) reported a detailed study on the hydrothermal rock alteration. Figure 39 is a simplified geologic map. Major lithologic units in the Singatse Range are Triassic-Jurassic metavolcanic and metasedimentary rocks, Jurassic intrusive rocks, and Tertiary volcanic rocks.

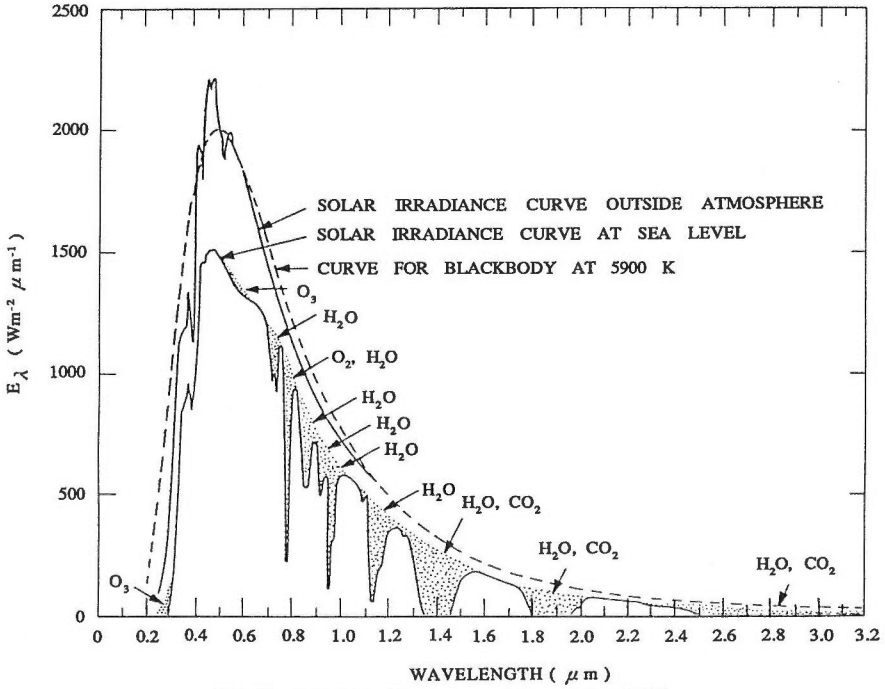

Fig. 38 Solar irradiance curve (after Slater, 1980).

The Triassic-Jurassic metavolcanic and metasedimentary rocks are distributed in the southern Singatse Range forming an overturned syncline with the E-W trending folding axis. Lithologically, they consist of andesitic volcanics, quartzitic sandstone, evaporite (gypsum and anhydrite), limestone and volcanic siltstone, andesitic to dacitic tuff and tuff-breccia, volcanic sandstone and limestone, calcareous argillite, dolomitic limestone, and andesitic volcanics from lower to upper. These rock units are intruded and metamorphosed by the Middle Jurrasic

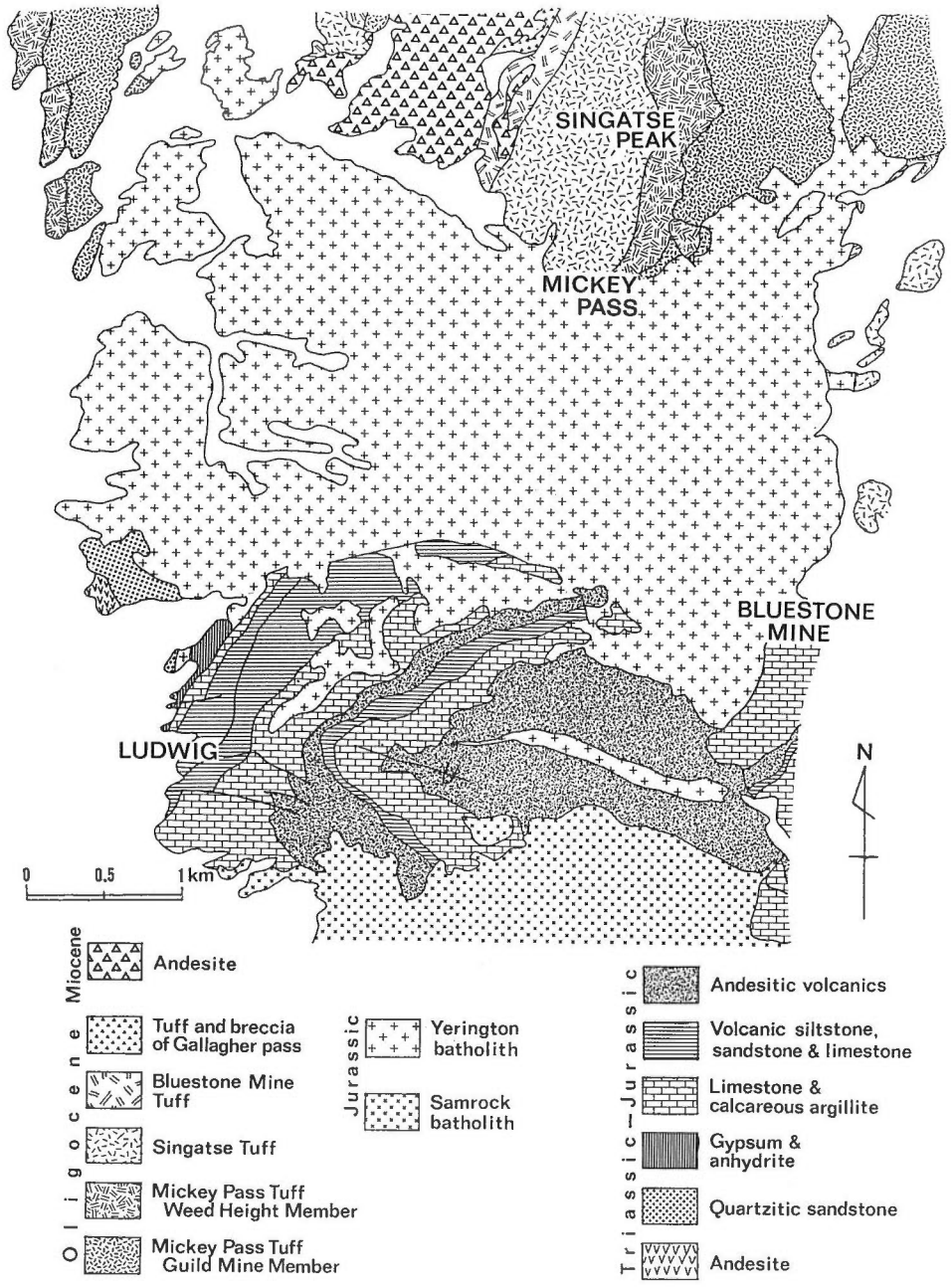

Fig. 39 Geologic map of Singatse Range after Proffett and Dilles (1984).

intrusive rocks.

The Middle Jurrasic intrusive rocks compose the widest distribution in the central portion and are named Yerington Batholith. The Yerington Batholith is composite and strongly differentiated from early granodiorite to quartz monzonite to porphyritic quartz monzonite and finally to quartz monzonite porphyry, with a successive decrease in the volumes of intrusions. The entire batholith was emplaced within one million years at 169 Ma. Quartz monzonite porphry dykes which originate from the porphyritic quartz monzonite below form major swarms with NW-SE trend and cut the older rock units. Porphyry copper mineralization formed contemporaneously with the emplacement of the porphyries. Large areas of the Yerington Batholith are hydrothermally altered that provide good targets of extensive remote sensing studies (Lyon, 1986).

After structural tilting and erosion of the Mesozoic formations, a series of ash-flow tuff sheets was deposited. Five major Oligocene tuffs were recognized; the Guild Mine Member and the Weed Height Member of the Mickey Pass Tuff, the Singatse Tuff, the Bluestone Mine Tuff, and the tuff and breccia of Gallagher Pass, from the oldest to the youngest. Lithologically, the first three are quartz latites, the Bluestone Mine Tuff is rhyolitic, and the last one is dacitic. In early to middle Miocene, basin-and-range normal faulting began. Movement along the faults resulted in steep (average 60 degrees) westward tilting of all older rocks (Proffett, 1977; Proffett and Dilles, 1984).

3.2.3 Linear Regression Using Field Measurements

All four flights were calibrated to spectra measured in the field. Four homogeneous, unvegetated targets were located in the AIS imagery. These targets consisted of two mine dumps, a paved road, and an outcrop of Tertiary tuff. Six to thirteen spectral measurements were made at each site using the IRIS Spectroradiometer described in Section 2.2.2. The spectral data were collected between 10:00 A.M. and 3:00 P.M. in May, 1985. All spectra were standardized to a barium sulfate plate. The number of spectra collected varied depending upon the homogeneity of the target which was assessed visually at the time of collection. Six spectra were collected over the pavement and the Bluestone Mine dumps which showed little spectral variability. Nine were collected over the Yerington Mine dumps. Thirteen were collected over the tuff. In all cases, spectra were collected randomly in an effort to best characterize the target.

Field spectra were despiked in the laboratory to remove artifacts generated by the spectroradiometer in the atmospheric absorption regions. Spikes were removed by interpolation across the spike, usually a region 4 to 8 nm wide. Despiked field spectra were averaged in order to produce one spectrum for each target, and to model the pixel response for that target. Finally the modeled spectra were convolved to the 9.6 nm AIS spectral equivalent using a Gaussian filter transfer function.

Raw data values were extracted from the AIS imagery over the four calibration targets. Between 5 and 19 pixels were extracted for each target and averaged. Next, the averaged pixel value was plotted against the averaged and convolved field spectrum. Least squares regression was used to produce a best fit line. The R^2 values ranged from a low of 0.849 to a high of 0.992. The average R^2 value was approximately 0.95. The slopes and intercepts of the regression equations (Table 5) were used to convert each AIS digital number to percent reflectance.

Several assumptions were made regarding the data analysis. First, the field spectra were collected 8 months after the flight. It was assumed that the target conditions had hot changed markedly during this time. Secondly, the four targets were located on three flight lines. It was assumed that atmospheric and solar conditions had not changed markedly from one flight to the next.

Tabel 5 Wavelength of the AIS channels and regression coefficients for reflectance calibration. Reflectance is given by the following equation: (Reflectance)=**A**×(DN)+**B**.

CHANNEL	WAVELENGTH (μm)	REGRESSION COEFFICIENTS A	B	R^2
1	1.155	0.0197	-7.23	0.972
2	1.644	0.0165	-6.17	0.968
3	1.736	0.0152	-5.11	0.973
4	1.828	0.0156	-6.91	0.975
5	1.192	0.0151	-5.23	0.975
6	1.201	0.0148	-4.43	0.974
7	1.211	0.0146	-3.82	0.974
8	1.220	0.0141	-3.75	0.976
9	1.229	0.0137	-2.99	0.976
10	1.238	0.0141	-3.95	0.963
11	1.247	0.0151	-4.54	0.969
12	1.257	0.0166	-5.34	0.971
13	1.266	0.0167	-4.52	0.970
14	1.275	0.0167	-4.40	0.969
15	1.284	0.0168	-4.82	0.968
16	1.293	0.0182	-5.35	0.977
17	1.303	0.0193	-5.33	0.970
18	1.312	0.0228	-7.04	0.966
19	1.321	0.0272	-8.43	0.964
20	1.330	0.0368	-12.88	0.973
21	1.340	0.0583	-20.06	0.961
22	1.349	0.1035	-29.70	0.951
23	1.358	0.1775	-48.03	0.951
24	1.367	0.2264	-60.33	0.907
25	1.376	0.2089	-53.96	0.890
26	1.386	0.2032	-47.82	0.849
27	1.395	0.2292	-58.80	0.909
28	1.404	0.2112	-52.10	0.922
29	1.413	0.1781	-41.25	0.886
30	1.422	0.1474	-32.06	0.954
31	1.432	0.1180	-24.75	0.935
32	1.441	0.0918	-20.36	0.959
33	1.453	0.0792	-14.17	0.939
34	1.462	0.0732	-14.60	0.946
35	1.471	0.0617	-11.24	0.950
36	1.481	0.0541	-10.59	0.959
37	1.490	0.0401	-6.05	0.951
38	1.499	0.0305	-4.59	0.952
39	1.508	0.0291	-3.91	0.958
40	1.518	0.0279	-4.74	0.963
41	1.527	0.0275	-5.40	0.968
42	1.536	0.0282	-7.08	0.968
43	1.545	0.0280	-6.27	0.968
44	1.555	0.0296	-7.52	0.967
45	1.564	0.0305	-7.94	0.965
46	1.573	0.0307	-7.17	0.960
47	1.583	0.0309	-6.52	0.968
48	1.592	0.0324	-7.82	0.969
49	1.601	0.0317	-6.88	0.970
50	1.610	0.0334	-8.70	0.968
51	1.620	0.0331	-8.56	0.975
52	1.629	0.0336	-9.06	0.976
53	1.638	0.0351	-9.82	0.975
54	1.647	0.0354	-10.12	0.980
55	1.657	0.0365	-11.15	0.978
56	1.666	0.0370	-11.70	0.979
57	1.675	0.0368	-11.59	0.979
58	1.684	0.0374	-11.71	0.980
59	1.694	0.0386	-13.15	0.984
60	1.703	0.0395	-13.40	0.985
61	1.712	0.0414	-14.40	0.985
62	1.722	0.0439	-15.52	0.990
63	1.731	0.0450	-15.24	0.988
64	1.74	0.0482	-16.42	0.992

(continues)

Table 5 (continued)

CHANNEL	WAVELENGTH (μm)	REGRESSION COEFFICIENTS A	B	R^2
65	1.748	0.0448	-13.32	0.980
66	1.757	0.0457	-11.85	0.979
67	1.767	0.0480	-10.56	0.976
68	1.776	0.0571	-12.27	0.968
69	1.785	0.0700	-13.66	0.970
70	1.795	0.0975	-18.93	0.970
71	1.804	0.1495	-28.83	0.970
72	1.813	0.1780	-29.68	0.957
73	1.822	0.1855	-26.48	0.945
74	1.832	0.2024	-31.91	0.977
75	1.841	0.2071	-31.43	0.963
76	1.850	0.2122	-28.63	0.948
77	1.860	0.2604	-33.95	0.929
78	1.869	0.3018	-37.35	0.925
79	1.878	0.3076	-35.22	0.923
80	1.887	0.2908	-32.58	0.932
81	1.897	0.2402	-24.08	0.918
82	1.906	0.2500	-29.50	0.925
83	1.915	0.1884	-17.84	0.883
84	1.925	0.1831	-19.36	0.920
85	1.934	0.1332	-10.64	0.871
86	1.943	0.1272	-11.33	0.894
87	1.952	0.1111	-7.82	0.905
88	1.962	0.0954	-4.30	0.892
89	1.971	0.0853	-4.65	0.912
90	1.980	0.0806	-5.23	0.920
91	1.990	0.0897	-8.05	0.934
92	1.999	0.1040	-8.68	0.917
93	2.008	0.1039	-6.38	0.915
94	2.017	0.0909	-5.46	0.940
95	2.027	0.0815	-6.82	0.948
96	2.036	0.0806	-8.32	0.958
97	2.048	0.0847	-6.04	0.951
98	2.057	0.0857	-6.06	0.948
99	2.067	0.0849	-5.59	0.958
100	2.076	0.0874	-7.85	0.963
101	2.085	0.0800	-5.57	0.964
102	2.095	0.0784	-5.67	0.967
103	2.104	0.0792	-6.34	0.965
104	2.113	0.0786	-6.34	0.967
105	2.123	0.0787	-6.44	0.965
106	2.132	0.0793	-6.59	0.969
107	2.141	0.0814	-6.35	0.968
108	2.151	0.0853	-7.05	0.965
109	2.160	0.0892	-8.25	0.967
110	2.169	0.0910	-8.49	0.964
111	2.178	0.0930	-8.45	0.968
112	2.188	0.0931	-7.80	0.952
113	2.197	0.0921	-8.37	0.957
114	2.206	0.0980	-10.74	0.963
115	2.216	0.0921	-8.51	0.942
116	2.225	0.0963	-8.88	0.941
117	2.234	0.1091	-9.86	0.925
118	2.244	0.1144	-9.13	0.951
119	2.253	0.1211	-9.83	0.950
120	2.262	0.1226	-9.56	0.947
121	2.272	0.1243	-10.19	0.937
122	2.281	0.1269	-9.59	0.943
123	2.290	0.1324	-10.86	0.962
124	2.300	0.1346	-10.86	0.954
125	2.309	0.1408	-12.50	0.949
126	2.318	0.1424	-12.15	0.969
127	2.328	0.1515	-14.04	0.960
128	2.337	0.1601	-13.78	0.960

3.2.4 Calibration Techniques Without Ggoundtruth

Three laboratory-based techniques without groundtruth were also tested. These were the Flat Field correction as defined by the Jet Propulsion Laboratory (Goetz *et al.*, 1985), the Least Upper Bound Residual and the Log Residual proposed by Green and Craig (1985).

The Flat Field correction was applied by dividing the raw data value for a flat, non-absorbing spectrum into every pixel along a flight. Geologic background and field spectra were utilized in selecting the optimal Flat Field spectrum. A pixel located on an alluvial fan was selected as the best Flat Field spectrum along the four flight lines.

The Least Upper Bound Residual and Log Residual processing techniques rely on the theoretical relationship between irradiance, topography, reflectance, and radiance. The relationship can be modeled multiplicatively as follows:

$$X_{i\lambda} = T_i \, R_{i\lambda} \, I_\lambda, \tag{6}$$

where $X_{i\lambda}$ = The radiance of a sample i, at wavelength λ.
T_i = A topographic factor, which accounts for topographic variation in illumination and is assumed constant for all wavelengths.
$R_{i\lambda}$ = Reflectance for a sample i, at wavelength λ.
I_λ = Irradiance for a specific wavelength interval.

Rearranging this formula and transforming it into log space results in the following:

$$\log(R_{i\lambda}) = \log(X_{i\lambda}) - \log(T_i) - \log(I_\lambda) \tag{7}$$

The value X is equal to the digital number value for a sample at each wavelength. The topographic factor T is estimated by calculating the average of the 128 channels for each sample. The value for I varies depending upon whether a Least Upper Bound Residual or a Log Residual is being applied. For the Least Upper Bound Residual, the value I equals the highest real digital number value throughout the image. For the Log Residual, the value I is calculated as the average digital number value for a channel throughout the entire image. Thus, for both techniques, there will be 128 values of I.

Finally, a fourth value, the image average, is added to each calculated value of reflectance. This value, which equals the average brightness for all samples at all wavelengths (one value per image), is used to standardize each processed flight. In addition, it should also be noted that the averages used in the calculations are equal to the average of the logarithms, and not the logarithms of the averages.

3.3 Discussion

Figure 40 shows AIS spectra extracted from the same pixel on flight 407 which have been interpreted as containing kaolinite. Figure 41(a-e) shows AIS spectra of an alfalfa field extracted from flight 411. Figure 41(f) is an AIS spectrum extracted from flight 411 over stubble. The true merits of the four techniques can be best evaluated in terms of noise, the number of processing artifacts, the effective removal of atmospheric absorption features, normalization of solar irradiance and spectral interpretability. Table 6 contains a summary of the results for the four processing techniques over the two targets.

A number of improvements can be made with regard to the level of noise in the Flat Field spectra and Least Upper Bound Residuals. The Flat Field spectrum, which was divided into each pixel, was derived from one pixel over an alluvial fan. According to Conel (verbal communication, Jet Propulsion Laboratory, 1985), an increase in the number of spectra averaged to produce the Flat Field spectrum will raise the signal to noise ratio within it. This should reduce the amount of noise in the resulting Flat Field processed data.

The Least Upper Bound Residual data may be improved by better screening for anomalous data values in the raw AIS data.The algorithm used to remove bad cross-track lines did not remove all of the anomalous data. Anomalously bright data, which are not removed from the raw data, result in an erroneously low calculation for the Least Upper Bound Residual. This phenomenon was particularly severe in the atmospheric absorption regions where the highest real data value tended to be very low. A second screening process, based upon the upper percentiles, may greatly improve the calculated result. Instead of using the maximum value as the Least Upper Bound, the 99.5th brightest value could be used. If all of the anomalously bright data were restricted to the 0.5 percent highest values, this technique would effectively solve this problem.

The Log Residual technique worked very well over the sparsely vegetated kaolinite [Fig.

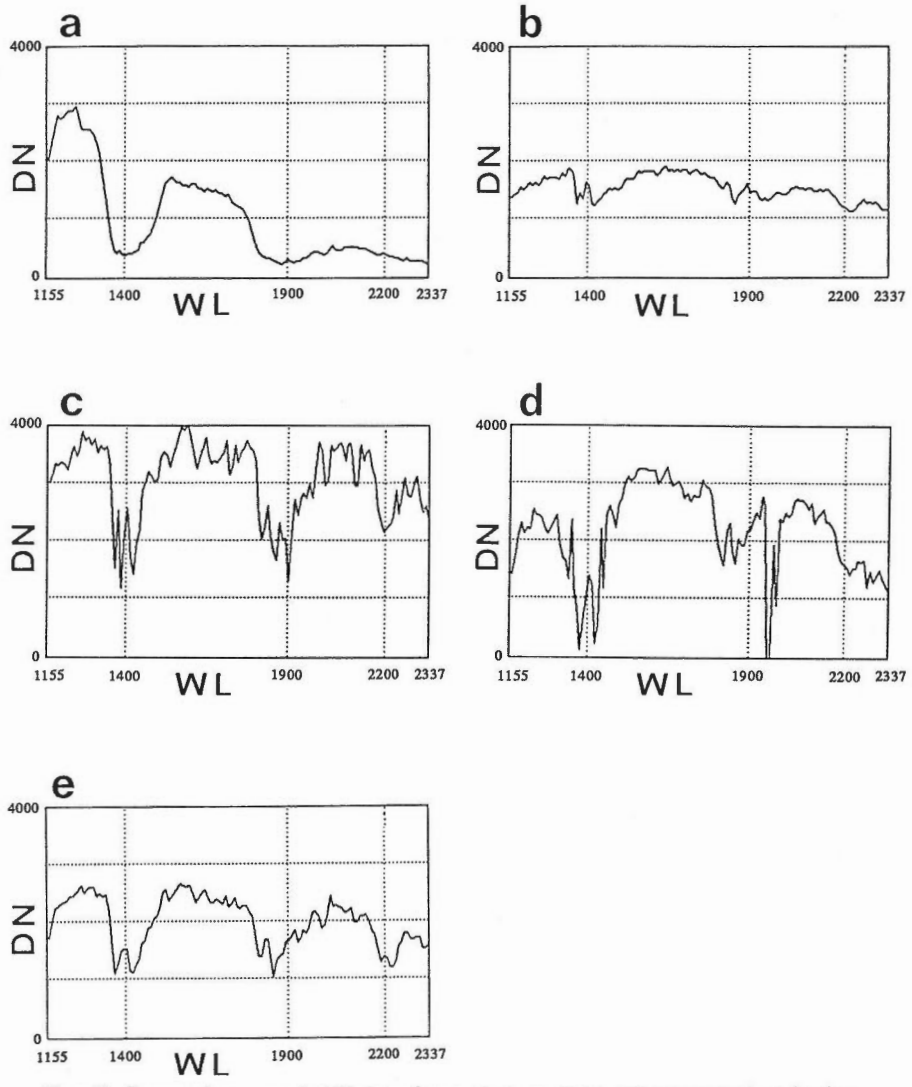

Fig. 40 Raw and processed AIS data for a pixel on flight 407 interpreted as having kaolinite. Plots of digital numbers (DN) vs. wavelength (WL) in nanometer. a) unprocessed data, b) calibrated by field spectra, c) calibrated by the Flat Field, d) calibrated by the Least Upper Bound Residual, e) calibrated by the Log Residual.

40(e)]. However, over the alfalfa field [Fig. 41(e)], the technique performed very poorly. Figure 41(f) shows the Log Residual spectrum for a stubble field adjacent to the alfalfa fields on flight 411. Comparing Fig. 41(e) to Fig. 41(f), it becomes evident that the former is the mirror image of the latter. This is caused by the average spectrum used in the calculations. The average spectrum along flight 411 is an alfalfa spectrum. Any ground target which is not dominantly composed of this cover type will show absorption features where alfalfa has peak brightness and peaks where alfalfa absorbs. This problem may be solved by substituting the average spectrum from another flight line into the calculations for this flight.

The calibrated result may have problems in the atmospheric absorption regions. The most evident problem is in the 1.8 to 2.0 μm region. The alfalfa spectrum [Fig. 41(b-e)] has an

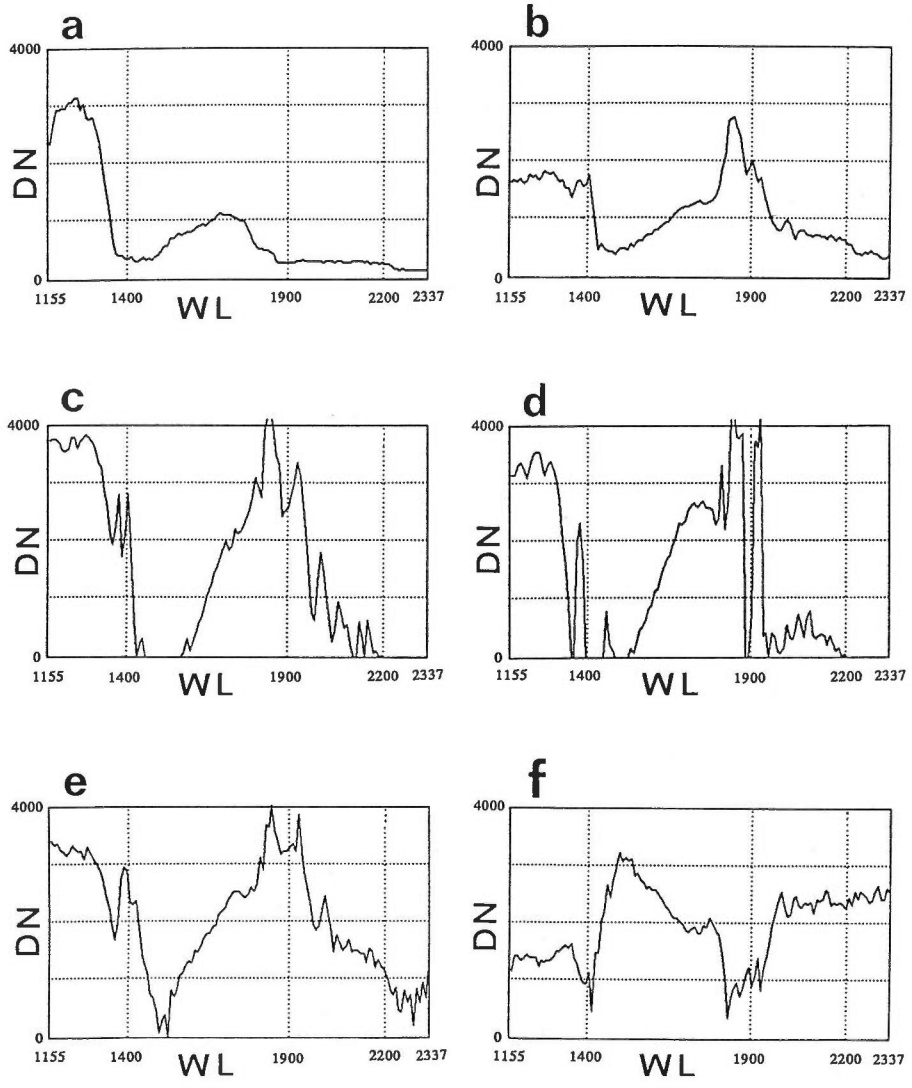

Fig. 41 Raw and processed AIS data for a pixel on flight 411 made up of green alfalfa (a-e). Plots of digital numbers (DN) vs. wavelength (WL) in nanometer. a) unprocessed data, b) calibrated by field spectra, c) calibrated by the Flat Field, d) calibrated by the Least Upper Bound Residual, e) calibrated by the Log Residual. f) shows a Log Residual spectrum for stubble on flight 411. Note that e) is a mirror image of f).

anomalous peak in this region. The fact that this spectral shape is present in all four processed spectra suggests that the problem may be in the unprocessed AIS data. Actually, the alfalfa had raw data values which were nearly twice as large as the pavement in the 1800 to 2000 nm region. A typical vegetation spectrum should be darker than pavement in this region. Thus, it was concluded that the problem was in the original AIS data.

In light of recent findings at the Jet Propulsion Laboratory, the most likely explanation is second order overlap from the shorter 800 to 1200 nm regions (G. Vane, verbal communication). The AIS contains a blocking filter designed to block all wavelengths of light shorter than 800 nm. Thus, light in the 800 to 1200 nm range may add to the 1600 to 2400 nm regions in the form of a second order contribution. This phenomenon would be particularly bad for vegetated areas because vegetation is strongly reflective in the 800 to 1200 nm region and vegetation is strongly

Table 6 A comparison of the calibration techniques.

1) Sparsely vegetated area

PROCESSING TECHNIQUE	SOLAR CORRECTION	ATMOSPHERIC CORRECTION	NOISE	ARTIFACTS	SPECTRAL INTERPRETABILITY
Flat Field	good	moderate	high	numerous	moderate
Least Upper Bound Residual	good	improved*	very high*	numerous*	moderate/ good
Log Residual	good	good	moderate	moderate number	excellent
Field spectra calibrated	very good	very good	low	few	good

2) Heavily vegetated area

PROCESSING TECHNIQUE	SOLAR CORRECTION	ATMOSPHERIC CORRECTION	NOISE	ARTIFACTS	SPECTRAL INTERPRETABILITY
Flat Field	good	moderate	very high	numerous	moderate/ good
Least Upper Bound Residual	good	improved*	very high*	very numerous*	moderate/ good
Log Residual	good	moderate	high	very high	very poor
Field spectra calibrated	very good	very good	low	few**	good/ excellent**

* Line drop outs and anomalous data influenced this result-removing these data may produce a marked improvement.

** An anomalous peak occurs in the 1.8-1.9 μm region. The peak is present in the raw data (compare Figs. 40 and 41)

absorbent in the 1800 to 1900 nm region. Based upon the results obtained in the unvegetated area, this is not a marked problem where vegetation cover is low. Furthermore, second order overlap is not a problem in unvegetated pixels located in heavily vegetated flight lines if the data is calibrated using field reflectance measurements; the second order contribution is incorporated into the best-fit line established between percent reflectance measurements and uncorrected AIS digital numbers.

The results of this study suggest a number of strategies for image processing of data with a large number of spectral dimensions. Of the techniques used in this study, calibration using field spectra is the best. In addition to the advantages shown in this study, the standardized result may be compared to standardized data collected on different dates or with different sensors. However, difficulties in selecting calibration sites, special instrumental requirements and the number of hours required to measure the spectra make the technique very difficult to employ. In addition, it is not always possible, or desired, to collect field measurements prior to analyzing the data. Therefore, effective laboratory-based techniques are important as a means of analyzing this data.

As a result, this study showed that AIS data calibrated to field spectra were less noisy, contained the least number of artifacts and were easier to interpret than AIS processed using the Flat Field correction, Least Upper Bound Residual or Log Residual. All four techniques normalized the decrease in brightness due to a reduction in solar irradiance at longer wavelengths. In addition, all four techniques reduced atmospheric absorption features in the atmospheric absorption regions. Lacking field spectral measurements, the results suggest that the Log Residual technique would be the most effective of the three laboratory based techniques in areas which do not contain a dominant cover type. In areas which contain one dominant cover type, the Least Upper Bound Residual would probably be the best.

4. DEVELOPMENT OF A FIELD RADIOMETER

4.1 A Field Radiometer as a Groundtruth Equipment

Field reflectance measurements are indispensable for the "ground-based" reflectance calibration of imagery as discussed in the previous chapter. If we can assume linear nature of the relationship between the recorded digital numbers in a magnetic tape and ground reflectance, it is easy to convert the digital numbers into reflectance using field targets with enough spatial distribution (Marsh and Lyon, 1980; Conel and Alley, 1985; Roberts *et al.*, 1985 and 1986). Kepper *et al.* (1986) reported that a reflectance calibrated image was composed of fewer image units than an uncalibrated image and these units corresponded more closely to the mapped geologic formations.

In the case of the AIS data, the IRIS spectroradiometer with spectral resolution of 2 to 4 nm (Section 2.2.2) was used to provide ground reflectance, because the AIS has high spectral resolution of 9.6 nm. However, spectral resolutions of the other airborne and spaceborne multispectral scanners are not as high as that of the AIS. For instance, the bandpasses of the Landsat TM range from 60 to 210 nm in the VNIR region, and those of the optical sensor of the Japanese ERS-1, which is planned to be launched in 1992, are 60 to 130 nm (Table 7). In these cases, we do not have to use a high spectral-resolution spectroradiometer as a tool to obtain ground reflectance data, because it takes longer time for data acquisition and subsequent convolution processes. Instead, a field radiometer with the equivalent bandpasses to the airborne or spaceborne sensor should greatly help collect field reflectance data.

It has been also required to evaluate capability of the ERS-1 sensor prior to its operation. Spectral measurements using a field radiometer with the ERS-1 bandpasses will be the most

Table 7 Bandpasses of the Japanese ERS-1 optical sensor.

Band	Bandcenter (nm)	Bandwidth (nm)	
1	560	80	
2	660	60	
3	810	100	stereo
4	810	100	stereo
5	1650	110	
6	2060	110	
7	2190	120	
8	2340	130	

efficient way to get enough hypothetical sensor responses for statistical investigation. After the satellite becomes operational, the field radiometer will be able to provide groundtruth data in various applications. Some field radiometers have already been developed as groundtruth tools for the Landsat remote sensors, but some modifications have been desired in their specifications. For these reasons, the author has developed a new field portable radiometer as a part of the ERS -1 project (Yamaguchi *et al.*, 1988).

4.2 Development of a New Field Radiometer

4.2.1 Specification of the Radiometer

There are some user requirements for a field radiometer. First of all, it has to be portable, i.e., it has to be operated in field by batteries and its weight should not be too great. The newly developed radiometer consists of the optical head and the control unit as shown in Pl. 1.1. The radiometer can be operated by the DC 12V battery, which is rechargeable from AC 100V or 200V power supply and lasts about 3.5 hours in case of continuous measurements. Voltage of the battery can be checked by the analog-meter on the control unit. A lap-top personal computer (NEC PC-98LT) is used for control of the radiometer and can work about 4 hours in field with its internal battery. As the total weight of the radiometer including the control unit and the computer is about 15 kilograms, two persons are needed to carry and operate it in field.

This radiometer has two filter wheels in the optical head as shown in Fig. 42. Each wheel

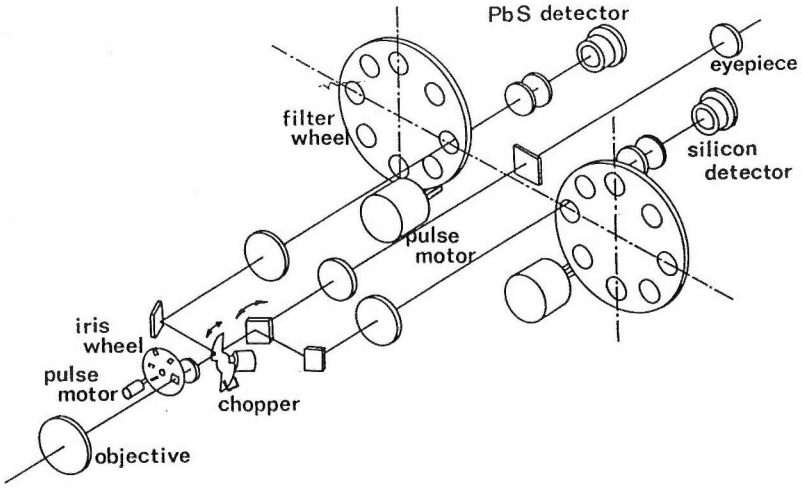

Fig. 42 The optical system in the optical head of the radiometer. Notice two filter wheels and only one aperture for observation.

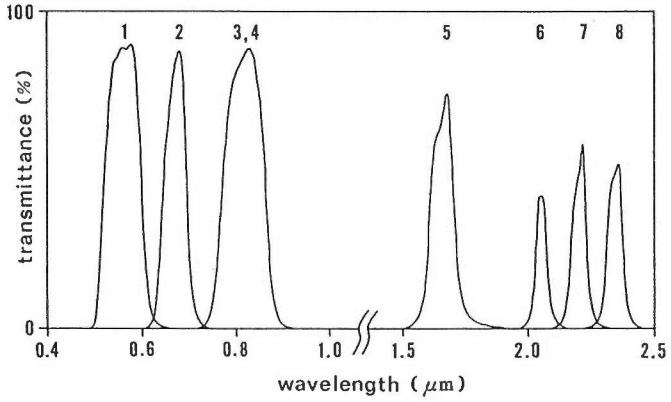

Fig. 43 Transmittance curves of the filters installed.

can contain up to eight interference filters and corresponds to the silicon and lead-sulfide detectors respectively. Therefore, up to eight spectral bands in the VNIR region and another eight bands in the SWIR region are available. At present, three filters in the VNIR region and four filters in the SWIR region whose bandpasses are similar to those of the ERS-1 optical sensor (Fig. 43) have been installed. The filter wheels are automatically rotated by pulse motors in order to accomplish shorter measurement time. During field operations, illumination conditions are always changing. Thus, the shorter the time necessary for a measurement, the less influence from fluctuations of the illumination conditions. It takes about twenty seconds to perform one continuous measurement for the seven spectral bands.

Other requirements for a field equipment are easy operation and a reliable recording medium. It is also desired that a measured result can be checked immediately in field. Otherwise, we can not recognize a failure of measurements until returning to a laboratory from a field survey. For these reasons, it was decided to use a lap-top personal computer for control of the radiometer. The optical head is connected to the computer through the control unit by RS232C interface (Pl. 1.1). We can easily operate the radiometer using the computer keyboard and can check the result immediately on the liquid-crystal display. Measured data can be recorded on a 3.5-inch floppy disc.

An important advantage of this radiometer is that there is only one observation aperture in the optical head. Generally speaking, geologic targets such as surface rocks or soil are quite inhomogeneous even within a field of view of a radiometer. Thus, it is important to carry out a spectral measurement in the same field of view exactly for the different spectral bands when we discuss a spectral response pattern of a particular target. Many of the previously developed radiometers measure a target with different fields of view using multiple apertures. If there is significant inhomogeneity in the target, such systems might cause a problem that each spectral band measures different areas with different spectral properties. In order to avoid it, the optical head of the newly developed radiometer has only one objective aperture and sector mirror (Fig. 42) as to guarantee the same field of view to all the spectral bands. The field of view can be checked through the sighting telescope. When we start a measurement, the light path to the telescope is closed automatically and the incident rays is directed to the filters and detectors. The radiometer also has four different types of irises as shown in Table 8. The most appropriate iris for the measurement is chosen by rotating the iris wheel.

4.2.2 Calibration Using a Standard Lamp

An optical bench (Pl. 1.2) has been prepared for the purpose of performing absolute energy

Table 8 Shape and size of the irises in the radiometer.

iris no.	shape	size (mm)	field of view (degrees)
1	square	8 * 8	4.6
2	square	4 * 4	2.3
3	square	2 * 2	1.15
4	circle	1.5	0.86
5	rectangle	1.5 * 8	0.86 * 4.6
6	(closed)	-	-

calibration of the radiometer. An officially-calibrated irradiation standard lamp is mounted on the optical bench, a distance of fifty centimeters from a standard reflection plate (Fig. 44). This is the same material as the reference plate being used in field measurements, i.e., an aluminum plate with thin coating of barium sulfate on the surface.

Using this optical bench, we can easily get calibration factors to convert readings obtained by the radiometer into absolute energy values. Calibration factors are stored on a floppy disc as a data file and are called when energy conversion is required. An integrating sphere with barium sulfate coating on its internal surface is also prepared. It will be possible to monitor irradiance from the sun using the calibration factors and the integrating sphere equipped at the objective aperture of the radiometer. This capability will allow us to evaluate the satellite data and correct atmospheric effects after the satellite sensor becomes operational.

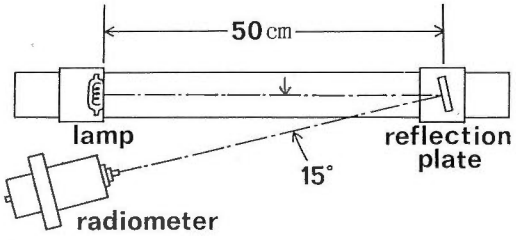

Fig. 44 The arrangement for calibration of the radiometer using the optical bench.

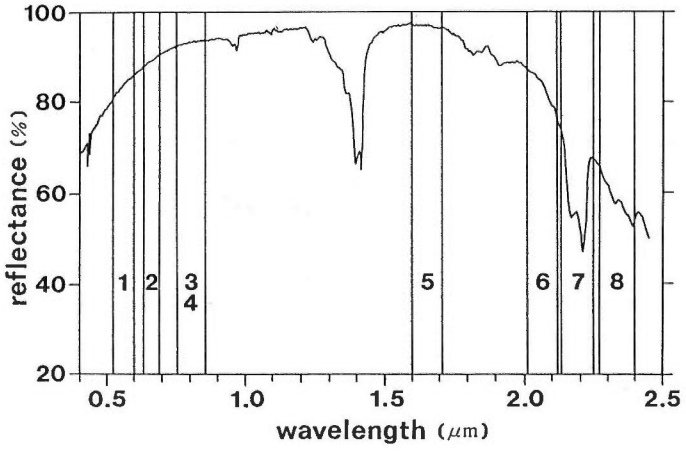

Fig. 45 A reflectance spectrum of kaolinite powder obtained by a high-resolution spectro-radiometer and the bandpasses of the optical sensor of the Japanese ERS-1.

Table 9 Comparison of the response to kaolinite powder. Notice that these measurement results coincide well each other.
(a) Measurement results obtained by the new field radiometer. An average of ten measurements.
(b) Hypothetical response patterns convolved from the reflectance data obtained by the high-resolution spectroradiometer. An average of four spectra.

	Band 1	Band 2	Band 3	Band 5	Band 6	Band 7	Band 8
(a)	79.99	86.00	86.78	89.39	79.92	54.34	54.59
(b)	82.27	88.02	91.60	95.03	83.00	54.04	56.10

4.2.3 Reliability of the Radiometer

Some measurements have been carried out as a test of the radiometer. Firstly, the repeatability of measurements and the effect of temperature were examined by changing the temperature at 0, 25, and 40 degrees Celsius. The dark current did not exceed 0 ± 1 percent of readings in any cases. It was also shown that the fluctuation of the measurements was not more than two percents of the readings when measured over the white reference plate in any cases of the three temperatures tested.

Next, reliability of the radiometer was tested by comparing the measurement results to the spectra obtained by the high-resolution spectroradiometer over the same targets. Fig. 45 shows the typical reflectance spectrum of kaolinite; an important clay mineral in hydrothermally -altered areas. This spectrum was then convolved into the hypothetical response pattern through the filters installed in the radiometer by multiplying the filter transmittance curves (Fig. 43). The same target was also measured by the new radiometer. As shown in Table 9, these two response patterns coincided sufficiently well. Namely, kaolinite shows high responses except the Bands 7 and 8 in the SWIR region because of the characteristic absorption at 2.2 μm due to the existence of hydroxyl. Many other measurements have also shown good coincidence between the response patterns obtained by these two methods. Consequently, it can be concluded that the newly developed radiometer would provide reliable spectral data as the ground truth to the ERS-1 optical sensor, probably also to the other remote sensors.

4.3 Discussion

A new field portable radiometer has been developed as a groundtruth equipment for the optical sensor of the Japanese ERS-1. As a result of the preliminary investigation, it has been shown that the radiometer worked sufficiently well with enough reliability in spectral measurements. It will be possible to get enough sensor response patterns for statistical investigation of the ERS-1 sensor prior to its launching. After the satellite becomes operational, this radiometer will be used to collect groundtruth data in various applications.

The filter wheels in the radiometer can contain up to sixteen filters, more than the seven spectral bands of the ERS-1 sensor. So, such usage as identification of clay minerals using filters with the specific bandpasses around 2.2 μm might be possible in future. This is another possible application of the radiometer as an useful field tool for exploration geology (e.g., Gladwell *et al.*, 1983).

5. COMPARISON OF VARIOUS TECHNIQUES FOR DISCRIMINATION OF LITHOLOGY

5.1 Introduction

In this chapter, the author examines possible techniques for discrimination of lithology using multiband data taken by an airborne or a spaceborne system. We will deal with the optical sensor of the Japanese ERS-1 (Earth Resources Satellite) for examination because of its expected capability of lithologic discrimination by the SWIR bands (Fig. 46). Reflectance data of typical-minerals and rocks obtained using the IRIS spectroradiometer (Section 2.2.2) and stored in a spectral data base were used prior to actual measurements by the satellite sensor, because the ERS-1 sensor is currently being manufactured. The reflectance spectra were converted into hypothetical sensor responses following Jackson (1983). Namely, the reflectance for a particular ERS-1 band was obtained by summing the product of the spectra and a response function at each spectroradiometer channel of a spectrum and dividing this sum by the response function values. The response function of the sensor was assumed to be rectangular in shape, i.e., 100% spectral response within each bandpass shown in Fig. 46 and Table 7 and no response for the rest of the spectral ranges.

This is, of course, a crude assumption, and it will have to be substituted by the real response function as soon as it becomes available. Moreover, atmospheric effects and other sensor parameters, such as the signal/noise ratio, are not considered in this paper, because many of them have not been available yet. These parameters do affect the capability of the sensor and are expected to decrease the separability in discriminating different materials, but are assumed not to change the result of this chapter, whose purpose is to develop an approach for the ERS -1 sensor data. Consequently, the hypothetical sensor responses of each band are given by simply averaging reflectance values within each bandpass. By using the simulated SWIR bands data, three typical techniques; band ratios, spectral indices and HSI color transform, were compared in terms of the capability to discriminate different rocks and minerals.

Another assumption made is that the recorded digital numbers (DN) are linearly related to the ground reflectance. Conel and Alley (1985) deduced linear nature of the relationship between the DN values of aircraft scanner image data and the ground reflectance. Marsh and Lyon (1980) showed that the surface and satellite data are highly correlated within defined contrast constraints after the satellite DN values are corrected for between-band gain differences and compensation is made for atmospheric attenuation and scattering. If we assume the linear relationship, it will be possible to calculate coefficients in the linear regression between the DN values and the ground reflectance using field reflectance measurements over spatially uniform targets. Therefore, the results derived from consideration in reflectance will be applicable to the "reflectance calibrated" DN values.

Figure 47 shows simulated sensor response patterns of typical minerals, rocks, and vegetation. Vegetation has a quite different pattern from the others, especially in the visible to near -infrared bands, i.e., low in Bands 1 and 2, and high in Band 3 (and 4). As the bandpasses of the visible to near-infrared bands are almost equivalent to Landsat TM Bands 2, 3, and 4, we can apply data processing techniques developed for the TM data, particularly for the purpose to discriminate vegetation from rock and soil (e.g., Crist and Cicone, 1984; Elvidge and Lyon, 1985a). Note that the patterns of the minerals and rocks in the visible to near-infrared bands are similar, whereas those in the last three SWIR bands are significantly different. This fact confirms the importance of the SWIR bands as expected (Hunt, 1979), so that our discussions will focus on the SWIR bands.

In the SWIR bands, andesite and granite in Fig. 47 have flat reflectance patterns, whereas

the minerals show right-sloping patterns, except alunite in Band 8. The minerals have characteristic absorptions in the 2.1–2.35 μm region due to hydroxyls and/or carbonates, and their SWIR spectra generally have background reflectance that decrease toward longer wavelengths (Fig. 46) due to existence of absorbed water and/or hydroxyls at 2.7 μm in the all minerals as shown in Section 2.3.

In such data with a sufficient sampling rate and high spectral resolution (Fig. 46), pattern recognition of a spectral shape is a powerful and practical method to identify a mineral as discussed in Section 2.4. Wavelength position and relative strength of diagnostic absorption minima in a spectrum are the keys to identify a mineral. However, due to the limited number of bands in the ERS-1 sensor, such a pattern recognition technique cannot be employed. Moreover, we must take into account the fact that DN of a pixel obtained by a satellite sensor is a result of mixed reflection from different materials within an instantaneous field of view. Even in a bare rock and soil area without vegetation cover, the Earth surface observed by a satellite

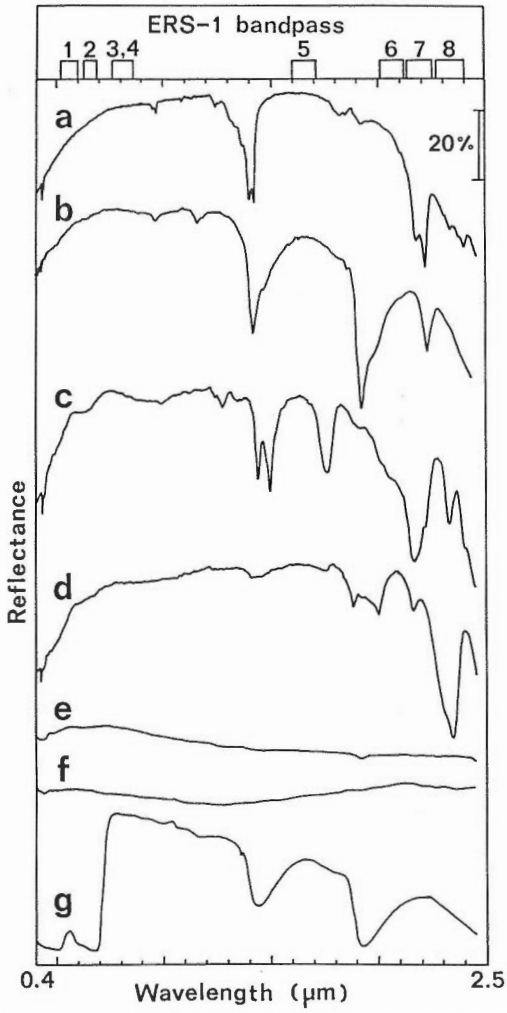

Fig. 46 Reflectance spectra of typical minerals, rocks, and vegetation from 0.4 to 2.5 μm. The top column shows the bandpasses of the Japanese ERS-1 optical sensor. (a) kaolinite; (b) montmorillonite; (c) alunite; (d) calcite; (e) andesite; (f) granite; (g) green leaves.

is usually composed of a mixture of different minerals. In the next section, we will discuss possible data processing techniques that enable us not only to discriminate among different rocks and minerals but also to quantify to some degree the concentration of a component in a mixture. The technique to separate vegetation using the ERS-1 data will be discussed in Section 5.3.

5.2 Comparison of the Techniques for Multiband Data

5.2.1 Band Ratios

Band ratios are the most widely employed and computationally simple method of data processing to evaluate multiband data. Previous authors have described many ratio-based image processing techniques (e.g., Rowan *et al.*, 1974; Goetz and Rowan, 1981). The ratio between TM Band 5 centered at 1.6 μm to TM Band 7 centered at 2.2 μm was reported to be sensitive to the existence of clay minerals, and thus useful to detect hydrothermally altered areas (Abrams *et al.*, 1977 and 1983; Prost, 1980; Podwysocki *et al.*, 1983). As the center of the ERS -1 Band 5 is located at almost the same wavelength as that of the TM Band 5, and the Bands 6, 7, and 8 of the ERS-1 are three, nearly-equal subdivisions of the TM Band 7, this technique may be applicable to the ERS-1 data.

Figure 48 is a cluster plot of ERS-1 Band 5 vs. ERS-1 Band 7 for the sensor responses of typical minerals and "unaltered rocks". In this particular case, the word "unaltered rocks" is

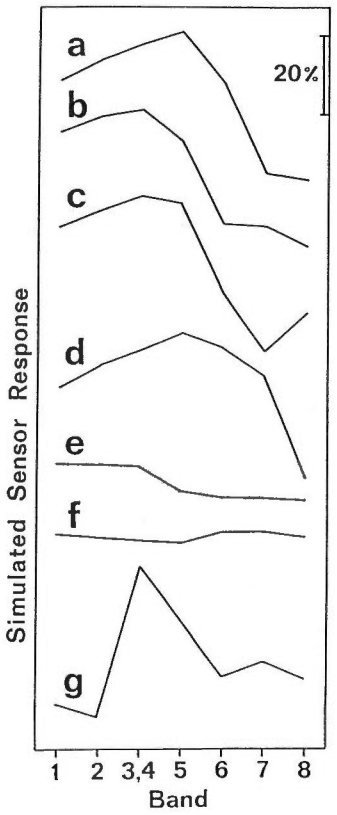

Fig. 47 Simulated response patterns of typical minerals, rocks, and vegetation to the ERS-1 optical sensor in reflectance: (a) kaolinite; (b) montmorillonite; (c) alunite; (d) calcite; (e) andesite; (f) granite; (g) green leaves.

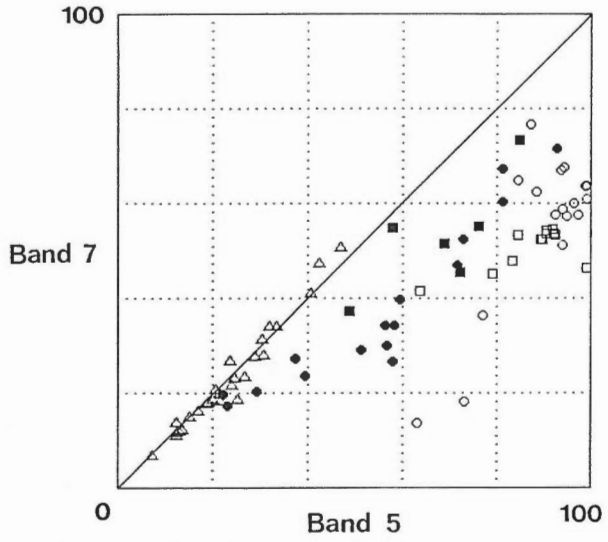

Fig. 48 A cluster plot of Band 5 vs. Band 7 for the sensor response patterns of typical minerals and unaltered rocks: (○) kaolinite; (●) montmorillonite; (□) alunite; (■) calcite; (△) unaltered rocks (andesite, granite, etc.).

used for the rock samples lacking a significant amount of phyllosilicate and carbonate minerals which have characteristic absorption features in the SWIR region, i.e., including fresh basalt, andesite, dacite, rhyolite, welded tuff, granite, sandstone, shale, and chert. The typical minerals analyzed are powder or fresh surfaces of rocks provided by the American Clay Mineral Society and the American Petroleum Institute. Spectral measurements of the unaltered rocks are done on fresh or weathered surfaces of the rock samples.

Generally, data points with a certain band-ratio plot on a straight line with a zero y -intercept. In Fig. 48, most of the unaltered rocks plot on or above the $Y = X$ line, whereas the others plot below it. Therefore, it is obvious that we can easily separate these minerals from these unaltered rocks by means of the band ratios. However, it is also clear from Fig. 48 that the ratio values of the minerals overlap each other. The plot of Band 5 vs. Band 6 or 8 also shows similar relationships. This fact suggests that the band ratios including the Band 5 may not be useful for discriminating among clay minerals nor separating hydrothermally altered areas from carbonate rocks.

Figure 49 shows cluster plots of Bands 6, 7, and 8 for the minerals and the unaltered rocks shown in Fig. 48. For instance, kaolinite and montmorillonite plot around the $Y = X$ line in Fig. 49(b), having band ratio values of nearly 1.0. On the other hand, alunite and calcite plot above and below this line, respectively, because they have higher and lower Band 8/7 ratio values than 1.0, respectively. Three ratios are available among the three SWIR bands (Bands 6, 7, and 8), but the combination of any two ratios is enough to describe all the possible patterns in the case of the three bands. Figure 50 shows a cluster plot of the two band ratios of 7/6 and 8/6 for the typical minerals and the unaltered rocks. Most of the data points have values below 1.0 for both band ratios, because of the general negative slope of the SWIR spectra toward longer wavelengths.

The ratio-based data processing techniques should be adequate for discriminating these minerals, because the clusters of alunite, kaolinite, and calcite are separated by this process. Even a simple strategy such asparallelepiped classification (Lillesand and Kiefer, 1979) should be able to separate these minerals. However, there is a basic problem if we apply the band ratios

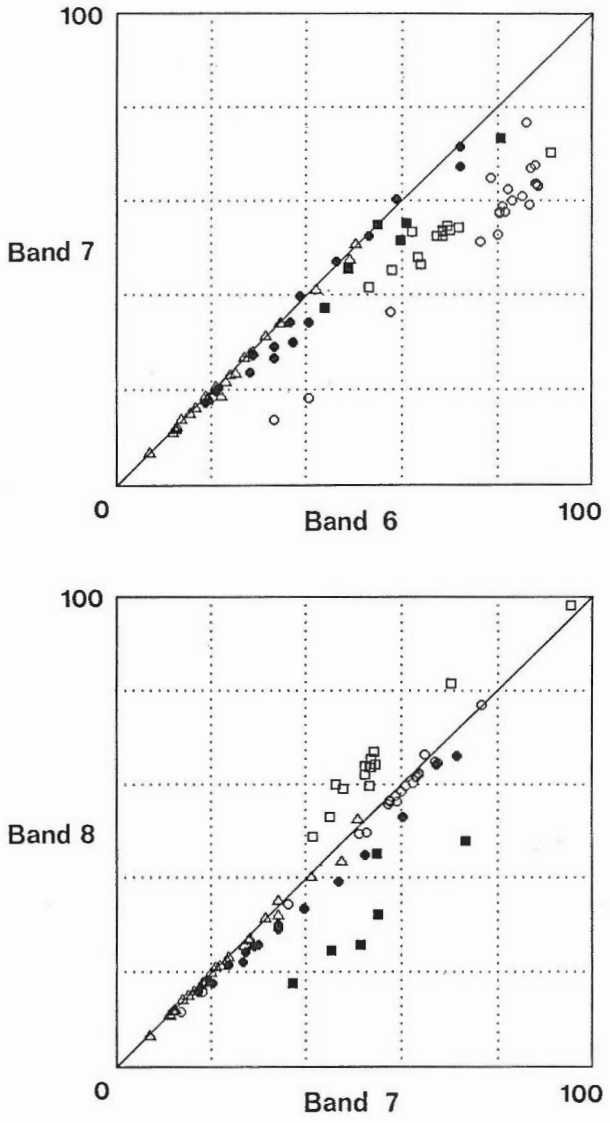

Fig. 49 Cluster plots of Band 6 vs. Band 7 and Band 7 vs. Band 8 for the sensor response patterns of typical minerals and unaltered rocks. See Fig. 48 caption for symbols.

to a mixture (Elvidge, 1985; Miller and Elvidge, 1985). Miller and Elvidge (1985) pointed out, at mapping limonite stain in TM imagery, that the use of the TM Band 3/1 ratio in raw TM data may result in the overestimation of limonite stain on bright rock and soil materials and the underestimation of limonite stain on dark rock and soil. Atmospherically corrected TM data may exhibit the reverse condition, overestimation of ratio values on dark substrates and underestimation of ratio values on bright substrates. As our discussions are based upon the reflectance data, they correspond to the atmospherically corrected case in Miller and Elvidge (1985). Therefore, it is clear that we have the same problem that the mixing of pure minerals will result ratio values not proportional to the concentration of a component in a mixture. In order to avoid this problem, the author proposes the application of a "base-line" data processing technique, a kind of the n-space spectral indices (Jackson, 1983), which are discussed in the

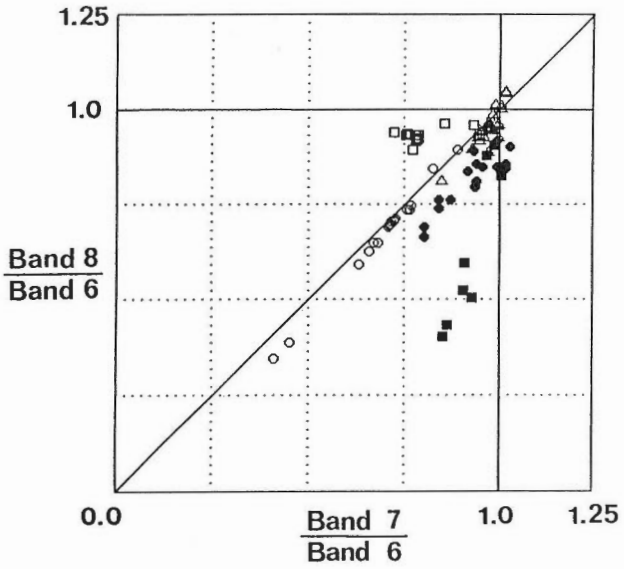

Fig. 50 A cluster plot of the band ratios of 7/6 and 8/6 for typical minerals and unaltered rocks. See Fig. 48 caption for symbols.

next section, to be used instead of a ratio-based technique, as was proposed by Elvidge (1985) and Miller and Elvidge (1985).

5.2.2 Spectral Indices and Principal Components Analysis

The concept of the spectral indices was initiated by Kauth and Thomas (1976), who proposed four indices called "Brightness", "Greenness", "Yellowness", and "Nonsuch" using the four Landsat MSS bands. Richardson and Wiegand (1977) developed a two-dimensional perpendicular vegetation index (PVI) using two bands of the Landsat MSS. Jackson (1983) showed that these indices are special cases of a class of spectral indices, formed by linear combinations of n spectral bands, in n-dimensional space. Application of n-space indices had been restricted to vegetation analysis until Elvidge and Lyon (1984) developed the Mineral Absorption Index (MAI) for assessment of hydroxyl-bearing minerals, and Miller and Elvidge (1985) proposed the Iron Absorption Index (IAI) for iron-oxide staining. Both groups successfully showed that the n-space indices allowed quantitative interpretation of many spectral features that were analyzed previously through the use of the band ratios.

A spectral index can be defined as a value measured by projecting a data point onto an axis with an appropriate unit vector direction. In a three-dimensional case, the second and third indices are deviations of each data point from the previously established baseline which represents a background (Jackson, 1983). Thus, it is essential to choose an appropriate baseline when we apply this technique to multispectral data. In this paper, reflectance values are used to calculate the indices instead of DN values of real satellite data.

In order to establish such a baseline, let us look at the three-dimensional shape of the data structure in Bands 6, 7, and 8. Figure 51 shows cluster plots of Band 6 vs. Band 7, and Band 7 vs. Band 8 for approximately 600 spectra of rocks and minerals. About 100 of them are of pure minerals including kaolinite, montmorillonite, alunite, calcite, halloysite, dickite, illite, epidote, muscovite, and pyrophyllite as shown in Section 2.3. Most of the others are various rock types collected in Nevada, U.S.A., including hydrothermally altered rocks, unaltered volcanic and sedimentary rocks, and carbonate rocks. Note that the data points are highly correlated in

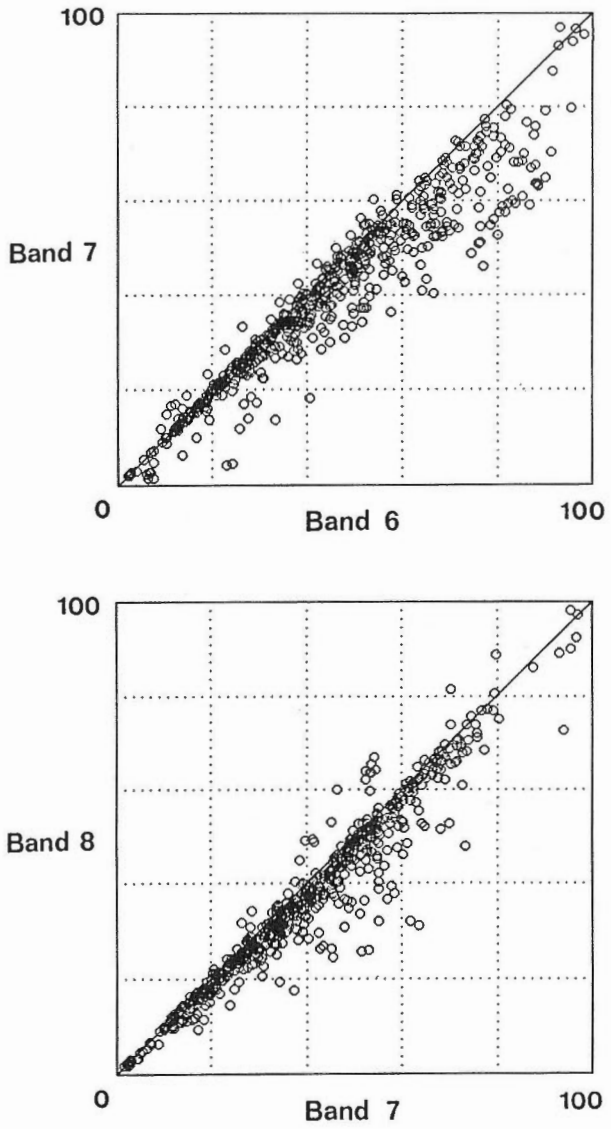

Fig. 51 Cluster plots of Band 6 vs. Band 7 and Band 7 vs. Band 8 for the sensor response patterns calculated from the approximately 600 spectra of rocks and minerals.

these plots. The three-dimensional shapes of the data structure is like a "raccoon tail", with decreasing point density outwards from its axis. The "best fit" line to the axis has a slope slightly less than 1.0, because many of the measured samples include clay minerals, which have the negative slope for the SWIR bands. A sample with a constant reflectance in the three bands would plot on the line:

$$\text{Band } 6 = \text{Band } 7 = \text{Band } 8. \qquad (8)$$

Data points which plot apart from this line represent the spectra with unequal reflectance in the three bands, presumably showing the samples with characteristic absorption features. Therefore, the (1:1:1) line given by Eq.(8) is defined as a baseline, from which we can calculate deviations

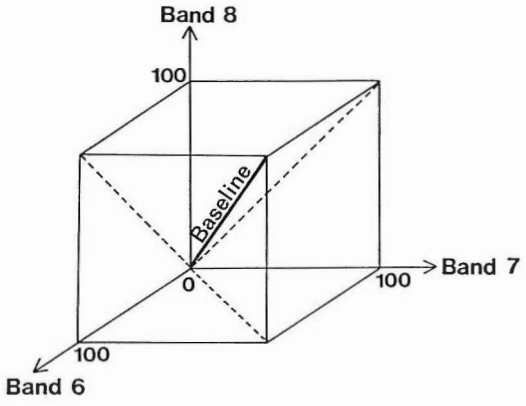

Fig. 52 Three-dimensional concept of the (1:1:1) baseline in Bands 6, 7, and 8.

of each data point as the spectral indices. Figure 52 shows the three-dimensional concept of the (1:1:1) baseline. The first index measured along the baseline is comparable to the soil brightness of Kauth and Thomas (1976), and is the average brightness of a target measured in the three SWIR bands.

If we apply principal components analysis to the data in Fig. 51, the first axis (the best fit line) is very close to the baseline defined by Eq.(8). A fundamental difference is that the baseline -based technique chooses the axes to represent specific spectral features (i.e., to indicate specific targets of interest), whereas the principal components analysis chooses the axes mathematically by maximizing variance of all the data. The axes chosen by these two techniques do not necessarily coincide with each other.

To compute the second and third indices, we assign the second and third axes with appropriate directions. In Kauth and Thomas (1976), the second axis was chosen to indicate a cluster of green vegetation, and the third axis was fixed automatically to be orthogonal to both the first and second axes. In our case to discriminate rock types, the second axis should be chosen on the basis of the data points representing a characteristic mineral, and will be perpendicular to the baseline.

Figure 53 is a schematic diagram of a plot viewed along the direction of the baseline toward the origin for the possible sensor response patterns. Each three-bar diagram represents a certain band pattern in a subarea or on a boundary of two subareas, and the hexagon indicates the possible data limit corresponding to the outer surfaces of a cube defined in the reflectance space (Fig. 52). A data point on the baseline would plot at the center of the hexagon. This plot suggests that the view from the baseline direction may be a very efficient way to discriminate different response patterns in the three-dimensional space. Figure 54 shows the same view for the data points of the typical minerals, i.e., projection of the data points onto a plane perpendicular to the baseline. (This view is very similar to the projection onto the plane including the second and third axes chosen by the principal components analysis as mentioned before.)

The second and third axes should be parallel to the plane shown in Fig. 54. If we abandon orthogonality of these axes and intend to choose them to indicate characteristic minerals, they are not necessarily orthogonal each other, nor is the number of the axes limited to two. However, only a "two-index" content of information excluding the first index (brightness) is meaningful in the three-band case, and selection of two orthogonal axes is the most efficient way to extract available information. Here, two axes indicating the averages of the clusters of alunite and calcite were chosen for computing the spectral indices, because these two axes cross at about 90

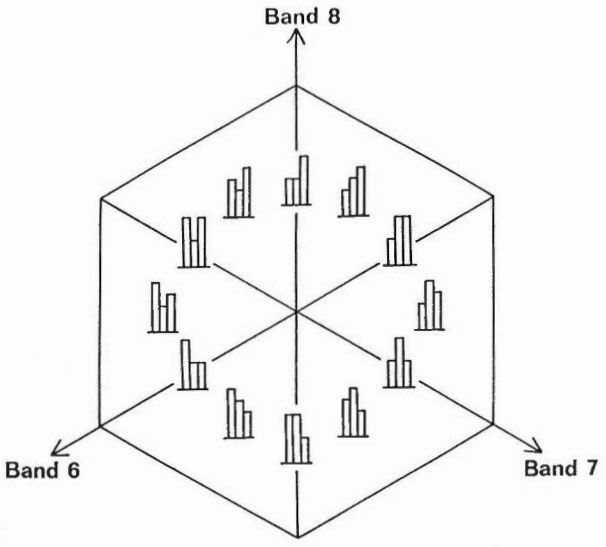

Fig. 53 Sensor response patterns in the plane orthogonal to the baseline shown in Fig. 52. Each three-bar diagram represents a possible pattern of Bands 6, 7, and 8 from left to right, in a subarea or on a boundary between two subareas. The hexagon indicates the data limit defined by the outer surface of a cube in reflectance space shown in Fig. 52.

degrees (Fig. 54). As explained in the next section, hue values in Table 11 are measured around the baseline for the average of each mineral cluster. Thus, the angle between these two axes is given by subtracting the hue value of alunite from that of calcite, and we get 93 degrees, which is assumed to be close enough to 90 degrees to assure the orthogonality. The author names these two indices Alunite Index (ALI) and Calcite Index (CLI).

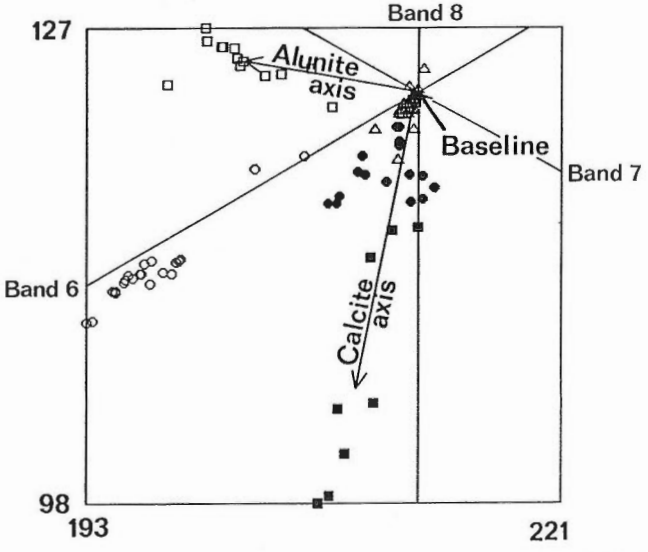

Fig. 54 A cluster plot in the same plane as Fig. 53 including the point (100,100,100) for typical minerals and unaltered rocks. Arrows indicate the axes of the Alunite Index and the Calcite Index. Numbers are the x and y coordinate values on the projected plane. See Fig. 48 caption for symbols.

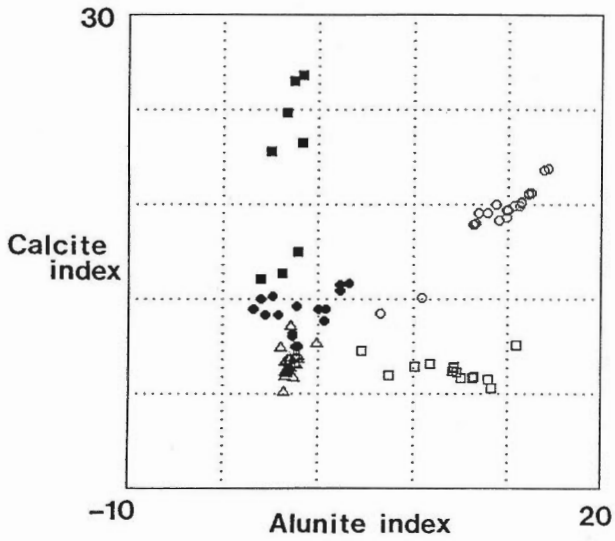

Fig. 55 A cluster plot of the Alunite Index and the Calcite Index for typical minerals and unaltered rocks. See Fig. 48 caption for symbols.

Figure 55 shows a cluster plot of the proposed two indices for the typical minerals and the unaltered rocks. As shown by Jackson (1983), an index can be formed by a linear combination of the three bands, whose coefficients are given in Table 10. Namely, the i-th index value A(i) for each data point is given by

$$A(i) = \sum_{j=1}^{3} C(i, j) \times R(j), \qquad (9)$$

where C(i,j) is the coefficient of the i-th index for the j-th band, and R(j) is a sensor response in the j-th band. The data points of alunite and calcite have large values in their indices, whereas those of kaolinite and the unaltered rocks show large and small values in the both indices, respectively.

The data points of montmorillonite plot close to those of the unaltered rocks, because the response pattern of montmorillonite in these three bands is similar to that of the unaltered rocks (Fig. 47). Spectral indices in four-dimensional space, constructed by using the Band 5 along with the Bands 6, 7, and 8, might be better for discriminating montmorillonite from the unaltered rocks. This will be discussed in Section 5.4.

These preliminary results indicate that spectral indices are more useful than band ratios for

Table 10 Transform coefficients of the three SWIR bands for the spectral indices.

	Coefficients		
Index	Band 6	Band 7	Band 8
Brightness	0.58	0.58	0.58
Alunite Index	0.62	-0.77	0.16
Calcite Index	0.54	0.26	-0.80

analyzing simulated ERS-1 data recorded in Bands 6, 7, and 8. An important advantage in utilizing the spectral indices is that the indices are proportional to concentration of certain components in a mixture, if the spectrum of the mixture can be formed by linear mixing of each component's spectrum. Moreover, it may be possible to determine a fixed linear transformation to aid in viewing the data regardless of scenes (Kauth and Thomas, 1976). A black-and-white image showing intensities of the spectral index proposed in this paper or a color composite image made by assigning the spectral indices to color primitives will greatly help the detection of spectral features, and thus will be quite useful for lithologic mapping.

5.2.3 HSI Color Transform

The "raccoon tail-like" shape of the data structure with a hexagonal data limit (Figs. 51 and 53) reminds us of HSI or HSV color models (Gillespie, 1980; Foley and Van Dam, 1982), which describe color using three physiological parameters; H (hue), S (saturation), and I (intensity) or V (value). We employ the HSI model [Fig. 56(a)] here.

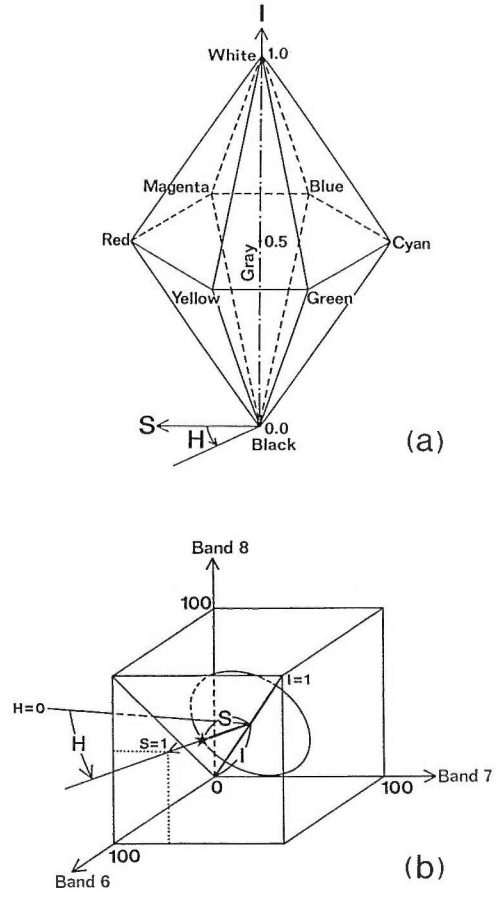

Fig. 56 (a) HSI color model after Foley and Van Dam (1982). (b) Perspective drawing to show relation between the three parameters of the HSI model and the three SWIR bands in reflectance space.

Table 11 Three parameters of the HSI color transform for the averages of the typical minerals and the "unaltered rocks".

Mineral	Hue(degree)	Saturation	Intensity
Kaolinite	63	0.50	0.63
Montmorillonite	99	0.10	0.37
Alunite	16	0.18	0.63
Calcite	109	0.24	0.63
Unaltered rock	275	0.02	0.23

Figure 56(b) is a perspective drawing to show the proposed correlation of the band response in reflectance space to the three parameters of the HSI color model. It is natural to assign the baseline to the axis of intensity, namely the brightness corresponds to the intensity, normalized to range from 0 to 1. For instance, the response with the maximum reflectance in the three bands:

$$(\text{Band 6, Band 7, Band 8}) = (100, 100, 100), \tag{10}$$

corresponds to I = 1, the top of the hexagonal bipyramid in the HSI model [Fig. 56(a)], which contains the maximum-value color (white). Hues are often described by a "color wheel", and thus directly correspond to the angle around the baseline, ranging from 0 to 360 degrees. Usually, color starts with red at 0 degree of the hue. In this case, let us assign the direction indicating the band response pattern of

$$(\text{Band 6, Band 7, Band 8}) = (100, 0, 100), \tag{11}$$

which is close to the direction showing the cluster of alunite, to 0 degree of the hue (red), so that the clusters of kaolinite and calcite are located roughly in the directions of yellow and green, respectively. Finally, saturation is defined as a normalized deviation of a data point from the baseline, ranging from 0 on the baseline (I-axis) to 1 on the outer surfaces of the cube defined by the possible data limit in reflectance space (Fig. 52). Table 11 shows the H, S, and I parameters for the average of the clusters of alunite, calcite, kaolinite, montmorillonite, and unaltered rocks.

Once the values of the three parameters are determined, we can transform them into appropriate DN values in red, green, and blue (RGB) space to create a color image. The transform function can be either linear or nonlinear. It is also possible to enhance different band response patterns by setting intensities constant.

The HSI color transform will enable us to display different minerals or rock types by easily interpretable colors. For instance, hydrothermally altered areas including alunite, kaolinite, or montmorillonite will be shown by red to yellow color. Carbonate rocks including calcite will be greenish in an image. The more concentration of the minerals, the purer (or more vivid) color will be displayed. On the other hand, unaltered rocks with a nearly constant reflectance would be gray, because they plot on the baseline in reflectance space and have almost 0 saturation values. As a result, we can conclude that the HSI color transform will be able to provide a color image which geologists can easily interpret for the purpose of lithologic mapping.

5.3 Effect of Vegetation

5.3.1 Vegetation Contribution to the Total Absorption

As clay and carbonate minerals have characteristic absorption features at around 2.2 μm in the SWIR region due to existence of hydroxyls or carbonates as shown in Section 2.3, their sensor responses to Bands 6, 7, and 8 of the ERS-1 are significantly lower than those to Band

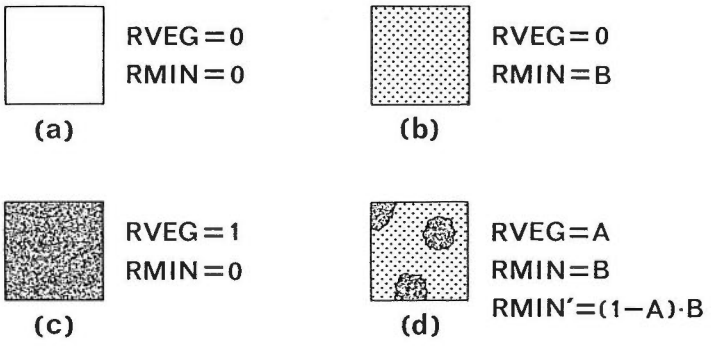

Fig. 57 A spectral mixing model for a single pixel: (a) No vegetation and no clay or carbonate minerals; (b) No vegetation and B×100 % concentration of clay and/or carbonate minerals; (c) 100 % vegetation cover; (d) A×100 % vegetation cover and B×100 % concentration of clay and/or carbonate minerals in the substrate. Relative proportion of the minerals in this pixel (RMIN') is given by (1−A)×B.

5 centered at 1.65 μm. Vegetation also shows the similar response pattern, because its spectra has back ground reflectance that decreases toward longer wavelengths due to the presence of water in plant cells. If reflection from vegetation and minerals are optically mixed within an instantaneous field of view corresponding to a single pixel, the total absorption in the SWIR bands should consist of the two components:

$$\text{Total absorption} = \text{Vegetation component} + \text{Mineral component} \quad (12)$$

This problem was recognized in processing of TM data. For instance, Elvidge and Lyon (1985a) succeeded in filtering out the vegetation contribution to the total absorption for the purpose of delineating argillic alteration areas using the 1.65/2.22 μm (TM Bands 5/7) and the 0.83/0.66 μm (TM Bands 3/2) ratios. Subsequently, they used baseline-based indices instead of band ratios (Elvidge, 1985; Elvidge and Lyon, 1985b), i.e., the total absorption index (TABS), the perpendicular vegetation index (PVI), and the mineral absorption index (MAI).

These indices measure the "total" absorption due to each component in a pixel. As shown in Fig. 57, if we introduce the proportion of each element in a single pixel, Eq. (12) is modified to:

$$\text{TABS} = \text{RVEG} \times \text{MVABS} + (1 - \text{RVEG}) \times \text{RMIN} \times \text{MMABS}, \quad (13)$$

where TABS is the total absorption index, RVEG is the proportion of vegetation in a single pixel, and RMIN shows the concentration of the clay and/or carbonate minerals in the substrate. Both of the RVEG and RMIN range from 0.0 to 1.0. MVABS stands for the maximum vegetation absorption indicating the maximum TABS value for a pixel with 100% cover of vegetation,whereas MMABS represents the maximum mineral absorption indicating the maximum TABS value for a pixel with 100% concentration of clay and/or carbonate minerals. We assume that there are pixels showing the MVABS and MMABS in the area of interest. In order to know the RMIN, rewrite the Eq. (13) to:

$$\text{RMIN} = (\text{TABS} - \text{RVEG} \times \text{MVABS}) / ((1 - \text{RVEG}) \times \text{MMABS}). \quad (14)$$

Let us also assume that the RVEG can be estimated by the following equation using a vegetation index:

$$\text{RVEG} = \text{Vegetation index of the pixel} / \text{Maximum vegetation index}. \quad (15)$$

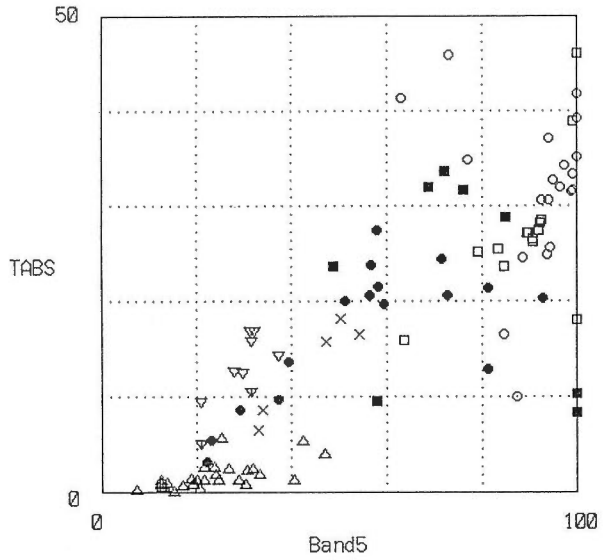

Fig. 58 A cluster plot of Band 5 vs. TABS defined in the four-dimensional space including Bands 5, 6, 7, and 8 for the simulated ERS-1 sensor response patterns of typical minerals, rocks, and vegetation:
(○)kaolinite; (●)montmorillonite; (□)alunite; (■) calcite; (△) unaltered rocks; (▽) green leaves; (▽) sagebrush; (×) lichen.

Combining Eqs. (14) and (15), the RMIN for each pixel can be calculated. So, it is important to choose an appropriate vegetation index and the other spectral indices for estimating the RVEG, RMIN, and TABS.

5.3.2 Estimation of Total Absorption

The band ratio of Band 5 over the average or minimum value of Bands 6, 7, and 8 is equivalent to the band ratio of Landsat TM Band 5/7, which is widely accepted for assessing argillic alteration areas or carbonate rocks. However, as discussed in Section 5.2.1, the mixing of two components will result in ratio values not proportional to the concentration of a component, if we assume a linear spectral mixing model that a spectrum of mixture can be formed by linear mixing of each component's spectrum. Therefore, spectral indices, linear combination of spectral bands, should be more appropriate than band ratios.

A spectral index can be defined as a value measured by projecting a data point onto an axis with an appropriate unit vector direction. Usually, the first index in n-space spectral data indicates the average brightness measured along the previously established "baseline" which represents a background (Jackson, 1983). In this case, let us use the equal reflectance line as the baseline (Band 5 = Band 6 = Band 7 = Band 8) in the four-dimensional space of the four SWIR bands. The total absorption (TABS) of each data point is defined as the deviation from this baseline following Jackson(1983):

$$\mathrm{TABS} = \sum_{i=5}^{8} (G(i) \times \mathrm{Band}\ (i)) \ / \ \sum_{i=5}^{8} G(i)^2, \tag{16}$$

$$\text{where } G(i) = \mathrm{Band}\ (i) \ - \ 0.25 \times \sum_{j=5}^{8} \mathrm{Band}\ (j). \tag{16'}$$

Figure 58 shows a plot of the TABS vs. Band 5. It is clear that vegetation and the clay/

carbonate minerals indicate higher TABS values than unaltered rocks. A simpler substitutional way is to calculate the TABS in the two-dimensional space using Band 5 and the minimum value among the Bands 6, 7, and 8 responses:

$$\text{TABS} = 0.7071 \times [\text{Band } 5 - \text{Minimum (Bands } 6,7,8)]. \quad (17)$$

As the TABS values given by these two equations were very close, we might be able to use Eq. (17) instead of Eq. (16) for practical use.

5.3.3 Comparison of Vegetation Indices

Many spectral indices have been developed to reduce multi-dimensional data to a single number for assessing vegetation. Perry and Lautenschlager (1984) reviewed various vegetation indices and concluded that for practical purposes several widely used indices were equivalent. If so, we should employ a simple vegetation index. Here, the author discusses the "greenness indices", which can be defined by choosing an appropriate axis direction and formed by linear combination of spectral bands following Jackson (1983). In the case of seven spectral bands, it is possible to define 127 different greenness indices with different band combinations out of the seven spectral bands including seven cases for each band.

The effectiveness of the greenness indices has been accomplished by evaluating the statistical separation of the vegetation cluster from the rock cluster for each index. The vegetation cluster includes 7 green leaf samples, 2 sagebrush samples, and 5 lichen samples, whereas the rock cluster includes 21 kaolinite samples, 14 alunite samples, 16 montmorillonite samples, 8 calcite samples, and 28 unaltered rock samples (such as fresh granite and andesite). The separability employed here is defined as follows:

$$\text{Separability} = (\text{AVE}_1 - \text{AVE}_2) / (\text{STD}_1 + \text{STD}_2), \quad (18)$$

where AVE and STD represent an average and a standard deviation respectively, and the suffix numbers correspond to the two clusters.

Figure 59 shows computed separabilities for the 127 cases. Notice that those cases with more spectral bands did not necessarily give higher separabilities, and the two band case showed the highest separability. This indicates that the spectral bands with similar band responses to both the vegetation and rock groups might decrease the separability, and thus such bands should

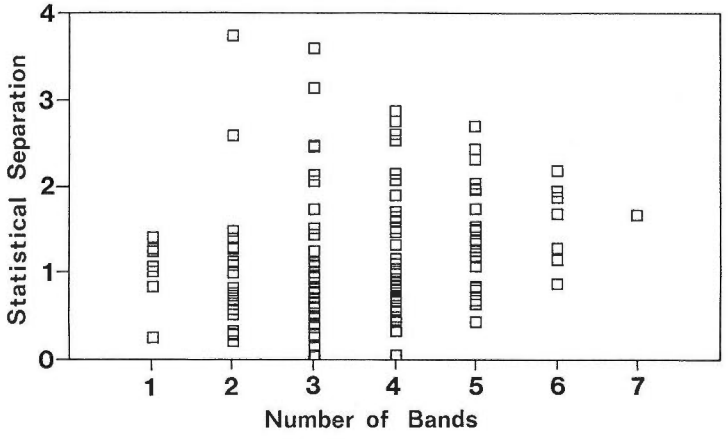

Fig. 59 Statistical separations between various greenness indices calculated for the green vegetation cluster and those for the rock-mineral cluster. The x-axis represents band numbers used in the calculation of the greenness indices. A total of 127 cases is plotted.

Table 12 Ten cases with the highest statistical separations between greenness indices calculated for the green vegetation cluster and those for the rock-mineral cluster. The rock-mineral cluster includes clay minerals, carbonate minerals, and unaltered rocks.

ORDER	TOTAL BANDS	BANDS USED	SEPARABILITY
1	2	2, 3	3.74
2	3	2, 3, 5	3.59
3	3	1, 2, 3	3.14
4	4	1, 2, 3, 5	2.87
5	4	1, 2, 3, 6	2.75
6	5	1, 2, 3, 5, 6	2.69
7	4	1, 2, 3, 7	2.60
8	2	1, 3	2.59
9	4	2, 3, 5, 6	2.52
10	3	2, 3, 6	2.47

not be included to form the greenness index for vegetation discrimination. Table 12 shows the ten cases with the highest statistical separations. It can be concluded that the spectral index using only Bands 2 and 3 is the most appropriate for assessing vegetation (Fig. 60). This result is in harmony with Elvidge and Lyon (1985b) where the typical vegetation indices were compared using the concept of signal-to-noise values. This two-dimensional index is well known as the perpendicular vegetation index (PVI), which was originally developed for Landsat MSS by Richardson and Wiegand (1977) and has been shown to be applicable to TM by Crist and Cicone (1984). In this particular case using reflectance values, the PVI is defined as:

$$\mathrm{PVI} = 0.7071 \times (\mathrm{Band\ 3} - \mathrm{Band\ 2}). \tag{19}$$

Consequently, the PVI given by Eq. (19) was chosen to give the RVEG for each pixel and thus to estimate RMIN using Eq. (14):

$$\mathrm{RVEG} = \mathrm{PVI} / \mathrm{MPVI}, \tag{15'}$$

where MPVI indicates the maximum perpendicular vegetation index.

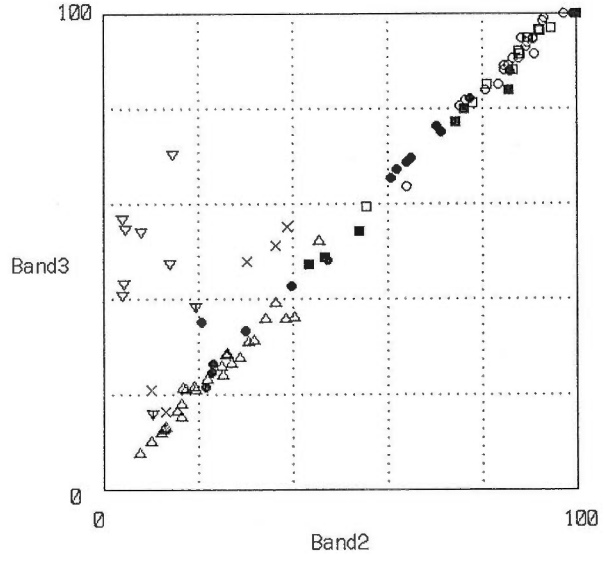

Fig. 60 A cluster plot of Band 2 vs. Band 3 for typical minerals, rocks, and vegetation. See Fig. 58 caption for symbols.

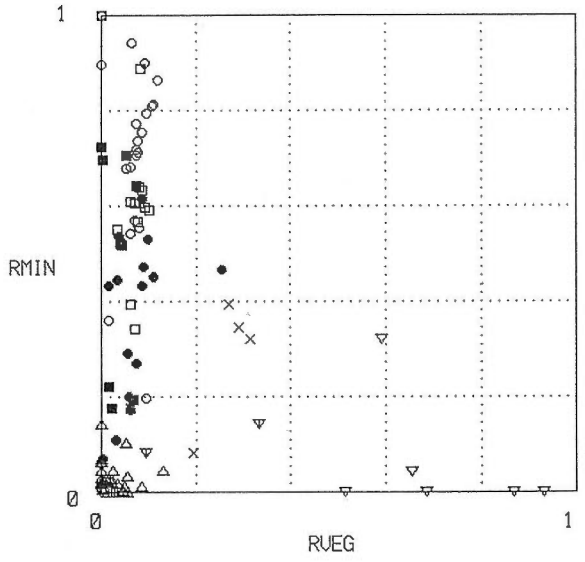

Fig. 61 A cluster plot of RVEG vs. RMIN for typical minerals, rocks, and vegetation. The MPVI, MVTABS, and MMTABS are 39.6, 18.2, and 46.0, respectively. See Fig. 58 caption for symbols.

5.3.4 Evaluation of the Newly Developed Indices

Using the TABS given by Eq. (16) and the PVI given by Eq. (19), we can estimate the RMIN and RVEG in Eqs. (14) and (15'). The MVABS in Eq. (13) can be given by choosing the maximum TABS among the pixels with high PVI, whereas the MMABS is assigned to the maximum TABS among the pixels with low PVI. Figure 61 is a cluster plot of the calculated RVEG vs. RMIN. The typical minerals show low RVEG and a wide range of RMIN values. Unaltered rocks have low RVEG and RMIN (less than 0.2 for each). On the other hand, vegetation exhibits low RMIN and a wide range of RVEG values, especially, green leaves show high RVEG. In this particular case, the MPVI, MVABS, and MMABS are 39.6, 18.2, and 46.0 respectively.

The range of RVEG and RMIN is between 0.0 and 1.0. In cases where RVEG and RMIN are smaller than 0.0, they are automatically reset to 0.0. In cases where they are larger than 1.0, they are reset to 1.0. Figure 62 shows the equal RMIN lines in the cluster plot of PVI vs. TABS. The possible extent of the RMIN satisfying the condition is the triangle defined by the lines of RMIN = 1.0, RMIN = 0.0, and the Y-axis. Coordinates of the three corners of this triangle are as follows:

$$(0, 0), (0, \mathrm{MMABS}), (\mathrm{MPVI}, \mathrm{MVABS}). \tag{20}$$

It is expected that the RMIN values depends upon estimates of the MMABS, MVABS, and MPVI. In Fig. 62, the relation between PVI and TABS for vegetation looks non-linear, i.e., the TABS is saturated for the green leaves with high PVI values. Such saturation in TABS might result in the underestimation of RVEG and the overestimation of RMIN for each pixel, so that it is necessary to assign a threshold PVI value, which is used as the MPVI instead of the real maximum among the PVI values. Figure 63 shows another RVEG vs. RMIN plot with the different MPVI value of 20.0, visually estimated from Fig. 62. It seems more reasonable in Fig. 63 than Fig. 61 that almost all of the vegetation except lichens plot on the X-axis. Anyhow, we have to pay special attention to selecting appropriate MPVI, MVABS, and MMABS in order

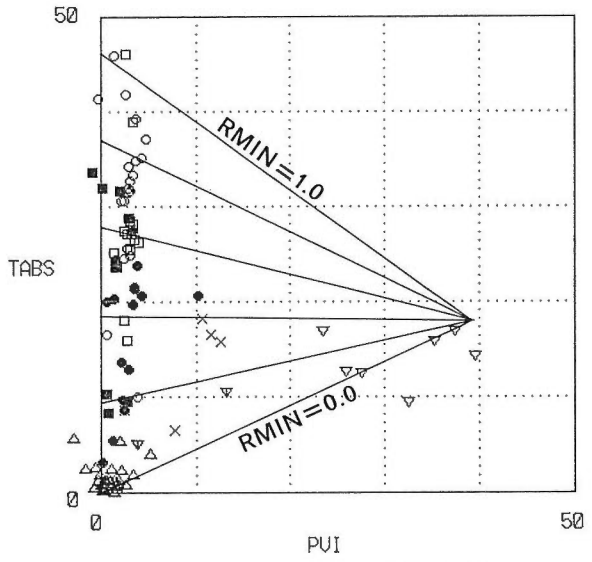

Fig. 62 Equal RMIN lines in a cluster plot of PVI vs. TABS with the same conditions as in Fig. 61. The possible extent of RVEG is in a triangle defined by the lines of RMIN=1.0, RMIN=0.0, and the Y-axis. See Fig. 58 caption for symbols.

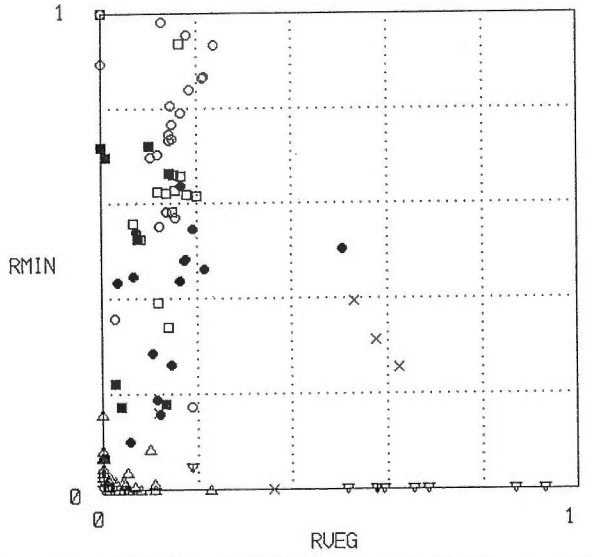

Fig. 63 A cluster plot of RVEG vs. RMIN with the threshold PVI value of 20.0, which is used as the MPVI. The MVTABS and MMTABS are the same as those in Fig. 61. See Fig. 58 caption for symbols.

to get accurate estimates of RVEG and RMIN when we employ the method developed in this paper.

5.4 Discussion

In Section 5.2.2, the author have developed two spectral indices for lithologic discrimination using the three SWIR bands of the ERS-1, i.e., the Alunite Index (ALI) and Calcite Index (CLI). These indices calculate deviation of each data point from the 1:1:1 baseline in the three

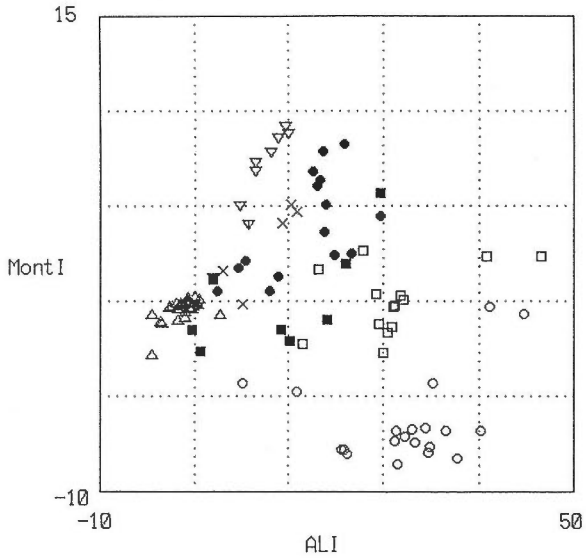

Fig. 64 A cluster plot of ALI and "montmorillonite index" in the four-dimensional space including Band 5 along with Bands 6, 7, and 8. See Fig. 58 caption for symbols.

-dimensional space defined by Bands 6, 7, and 8. Figure 64 shows these indices for typical minerals and vegetation. As pointed out in Section 5.2.2, it is difficult to discriminate montmorillonite from unaltered rocks and vegetation. The author also mentioned the possibility of including Band 5 in the calculation of the ALI and CLI. However, as shown in Fig. 64, recalculated indices including Band 5 exhibit worse separabilities among the minerals than those without the use of Band 5 (Fig. 55). As discussed in Section 5.3.3, only two bands were necessary for the vegetation index. In both cases, additional bands only result in decreased separability. Montmorillonite can easily be distinguished from vegetation using the PVI, and from unaltered rocks using the TABS developed in this paper. As a conclusion, Band 5 is used to give the TABS, but should not be involved in discrimination among different rock types.

One of the other possible indices using the spectral bands of the ERS-1 is the iron absorption index (IAI) developed by Miller and Elvidge (1985). However, as the ERS-1 does not have a band equivalent to the TM Band 1, we have to use the ERS-1 Band 1 equivalent to the TM Band 2 instead. Therefore, the usefulness of the IAI using the ERS-1 Bands 1 and 2 is not as good as that of the IAI developed for TM.

Figure 65 is a flow diagram showing the possible sequence of data processing for surface mapping using the spectral bands of the ERS-1. First, the TABS and PVI are calculated by the Eqs. (16) and (19). Then, RVEG and RMIN in a single pixel are given by using the Eqs. (14) and (15). Finally, the pixels with high RMIN are subdivided for further lithologic discrimination using the ALI and CLI by using the Eq. (10). Such combinations of the spectral indices should help us to perform surface mapping using the ERS-1 data. The HSI color transform applied to the three-dimensional data structure is another possible way to express the sensor response patterns in the SWIR bands, and will be able to create a color image useful for visual interpretation.

Although these discussions are based upon reflectance data obtained by a spectroradiometer, it can be concluded that the spectral bands of the ERS-1 allow us to discriminate surface materials more effectively than with Landsat TM data. Specifically, the ERS-1 will allow for the separation of clay minerals from carbonate minerals in the 2.0-2.4 μm region. Before we

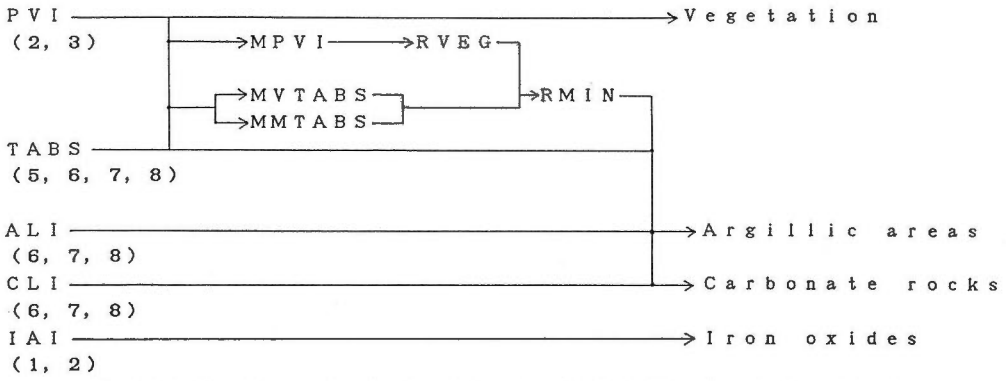

Fig. 65 A flow diagram showing the strategy for discrimination of vegetation and rock types using the spectral indices developed in this paper.

apply these techniques, preprocessing such as reflectance calibration of DN values recorded in a magnetic tape has to be carried out. Calibration techniques discussed in Chapter 3 and/or the field radiometer shown in Chapter 4 would help to perform such calibration.

After the sensor parameters become available, we should take into account of them for more quantitative investigation of the possibility of surface mapping by using the ERS-1 data. Effects of the sensor parameters such as sensitivity, noise level, and calibration factors may be discussed hereafter. Atmospheric effects are another major problems to be considered. Despite these considerations, the result of the investigation indicates that the ERS-1 sensor would be quite promising for lithologic and vegetation discrimination.

6. APPLICATION OF THE CONCEPT TO THE AIRBORNE MSS DATA

6.1 Description of the Geoscan AMSS System

The author applied the image processing techniques discussed in the previous chapter to image data obtained by Geoscan AMSS MkI (Airborne Multi Spectral Scanner Mark One) prior to actual measurements by the Japanese ERS-1 optical sensor, which is currently being manufactured. The AMSS MkI, an airborne scanner built by Geoscan Pty. Ltd. of West Australia (Honey and Daniels, 1985; 1986), has quite similar bandpasses to those of the ERS-1 sensor. As the main concern of the Geoscan is mineral exploration, they determined the bandpasses of this scanner strategically in order to maximize capability of lithologic discrimination and alteration mapping.

The AMSS MkI has 13 spectral bands; 5 in the VNIR, 4 in the SWIR, and 4 in the TIR (Table 13). A big advantage of this scanner is that all spectral bands are coregistered with the same spatial resolution. Thus, we can combine different information obtained by the bands in different spectral regions, i.e., VNIR, SWIR, and TIR, to perform more accurate surface geologic mapping. Of the 13 spectral bands, the VNIR and SWIR bands have similar bandpasses to those of the optical sensor of the Japanese ERS-1, except a point that the AMSS lacks the 1.6 μm band. Roughly, AMSS Bands 2, 3, 4, 6, 7, and 9 correspond to the ERS-1 Bands 1, 2, 3 (or 4), 6, 7, and 8 respectively.

The imaging field of view is 90 degrees, i.e., 45 degrees from nadir on each side of the aircraft, and the instantaneous field of view is 5 milliradian. Therefore, ground resolution is about 10 meters in case of 2,000 meters altitude. Swath width is 512 pixels before panoramic

Table 13 Bandpasses of the Geoscan AMSS MkI.

BAND	BANDPASS
1	0.45 - 0.5
2	0.55 - 0.6
3	0.65 - 0.7
4	0.83 - 0.87
5	0.93 - 0.97
6	1.98 - 2.08
7	2.16 - 2.19
8	2.205 - 2.235
9	2.3 - 2.4
10	8.5 - 8.9
11	9.7 - 10.1
12	10.8 - 11.2
13	11.5 - 12.0

correction. All spectral bands are recorded simultaneously as 8-bit data in a band interleaved by line format on 9 track 1600 bpi CCT's. Real time color display in aircraft is also available. Nominal signal to noise ratio is 10/1. The aircraft as a platform of the sensor is an unpressurized Beechcraft Queenair at altitudes up to 10,000 feet above terrain (Honey and Daniels, 1986).

6.2 Description of the Test Site (Ravenswood, Queensland, Australia)

6.2.1 Topography and Climate

The image data provided by Geoscan Pty. Ltd. were of three test sites in Australia. The author chose the Ravenswood test site as a target of this research, because of interesting geologic setting and accessibility to the area, and carried out a field survey in September, 1987. Approximate center of the studied area is 20°05'S, 146°40'E, in Queensland, Australia (Fig. 66), and is located in the northeast corner of the 1:250,000 Charters Towers topographic sheet, or in the northwest corner of the 1:100,000 Ravenswood topographic sheet. Figure 67 is a map showing the selected area for image processing and locations of the ground calibration targets.

The studied area is gentle hilly terrain with low topographic relief, and the height ranges from 210 to 350 meters. Pandanus Creek, a branch of Burdekin River, cuts the studied area from northwest to southeast, but had no water in September, 1987. There is an abandoned town of Silver Valley, once the center of gold mining in this region. The climate of this area is considered semiarid. Vegetation cover is approximately 10 to 30 percents, mainly of eucalyptus trees about 2 to 5 meters tall (Pl. 1.3). There was only a little shrub in 1987 due to low precipitation in the recent few years.

6.2.2 Geology

The description of geology in and around the studied area follows explanation notes for the 1:250,000 geologic map of Charters Towers (Clarke and Paine, 1970). Figure 68 is a simplified geologic map of the Ravenswood area from the 1:250,000 sheet. The oldest rocks in the Ravenswood region are Cape River Beds of Cambrian or Ordovician age, which crop out in the south and east of the target area. The main rock type is sericite schist, quartzite, phyllite, and metavolcanics. Lenses of acidic and minor intermediate volcanics in the Cape River Beds are called Mount Windsor Volcanics, which thicken eastwards. The Cape River Beds are regarded broadly as Cambrian to Ordovician based upon an Upper Cambrian age for the Mount Windsor Volcanics (Rb/Sr method), and are intruded by Ravenswood Granodiorite Complex.

Ravenswood Granodiorite Complex of Middle Ordovician, and Upper Silurian or Lower Devonian age occurs widely in and around the Charters Tower Sheet. Hornblende-biotite granodiorite and tonalite, which are the initial most widespread phase of the Complex, occupy most of the studied area. Isotopic dating by the Rb/Sr whole rock method has shown two conflicting results; an isochron of 454±30 Ma for most of the specimens collected from the Ravenswood Granodiorite Complex, and an isochron of 394±30 Ma for some of the specimens.

Tuckers Igneous Complex of late Carboniferous or early Permian age intruded into the Ravenswood Granodiorite Complex as stocks and bosses, and has yielded K/Ar ages of 277-282 Ma. In the western portion of the studied area, biotite-hornblende granodiorite of the Tuckers Igneous Complex forms a small rugged hill.

In the south of the studied area, lacustrine and fluviatile deposits of sandstone, minor conglomerate, and siltstone disconformably overlie the Pre-Tertiary rocks. They occurred before the main period of lateritization, probably in the Lower Tertiary, and are overlain by Sellheim Formation.

Sellheim Formation composed of sandstone and conglomerate borders the Burdekin River well above the present flood level. A Pleistocene age is indicated by fossil wood from grits on

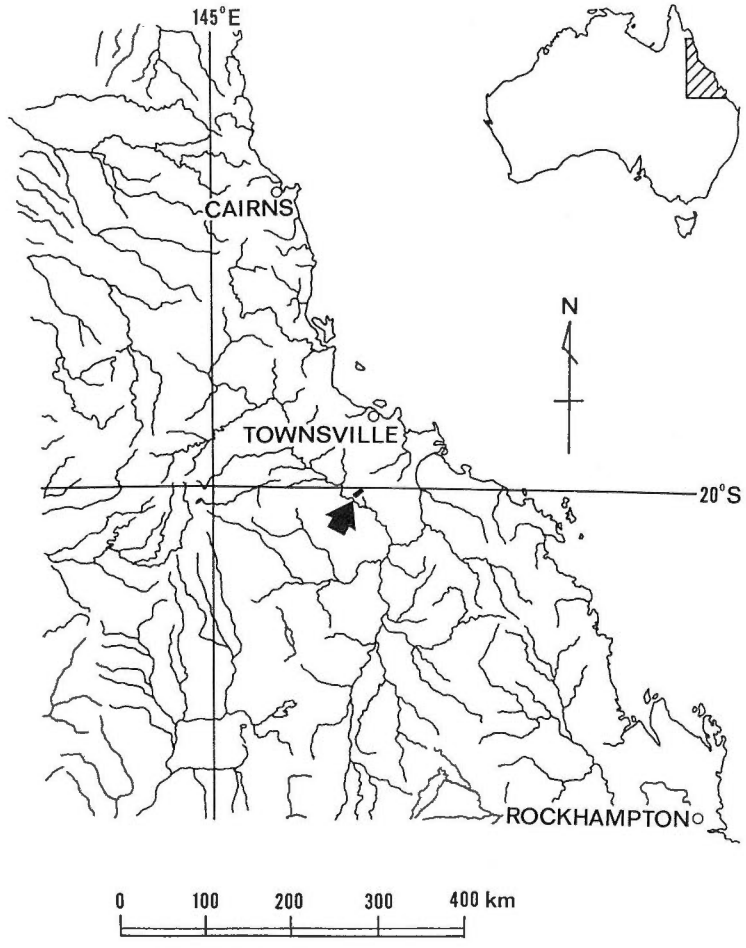

Fig. 66 Location of the studied area in Queensland, Australia.

the right bank of the river.

A large amount of gold has been produced in this area. Although all mining of the main production period had ceased by 1916, there are revivals of gold exploration and mining these days. The lodes occur within the Ravenswood Granodiorite Complex almost without exception. The deposits occur near the roof of the Ravenswood Granodiorite Complex as simple or composite tabular bodies occupying fissures, and have a simple mesothermal mineral assemblage.

6.3 Image Processing

6.3.1 General

The dimension of the original data provided was 512 pixel wide and 2500 line long, and the

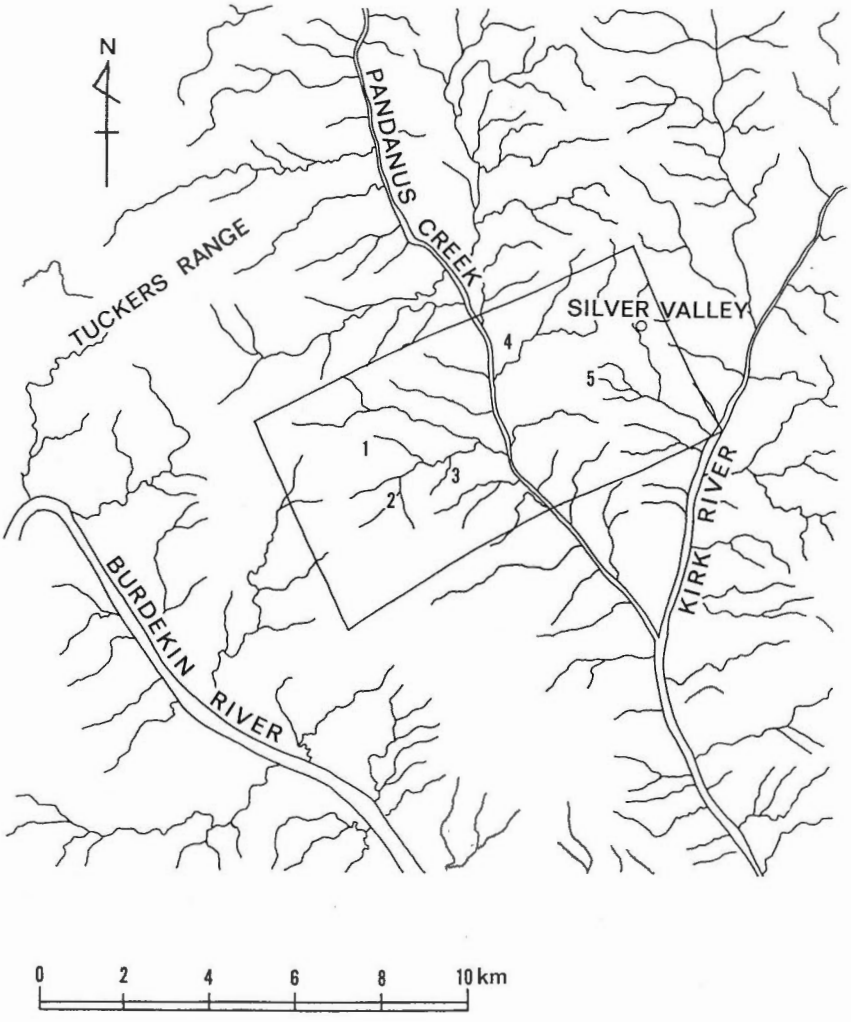

Fig. 67 The test area for image processing. The shape of the area is not complete rectangular due to geometric distortion of the image. Numbers indicate locations of the ground calibration targets.

flight altitude was approximately 6,000 feet, so that the image swath and the ground resolution at nadir are about 4 kilometers and 10 meters respectively. The author selected a subarea for image processing with the dimension of 512 pixel wide and 1024 line long that corresponds to a surface area of approximately 4 by 8 kilometers as shown in Fig. 67.

Radiometric preprocessing had already been done by Geoscan prior to image processing by the author. Generally the raw digital data recorded by the scanner has two major components; the energy reflected and emitted from the target area, and energy either scattered or emitted into the instantaneous field of view by the atmosphere. Thus, it is necessary to correct the raw data for the atmospheric backscatter contribution. It is assumed that the atmospheric contribution is additive. The procedures developed by Geoscan involve determining the mean, down the whole image, of the digital radiance for each pixel, smoothing the profile of the radiance using

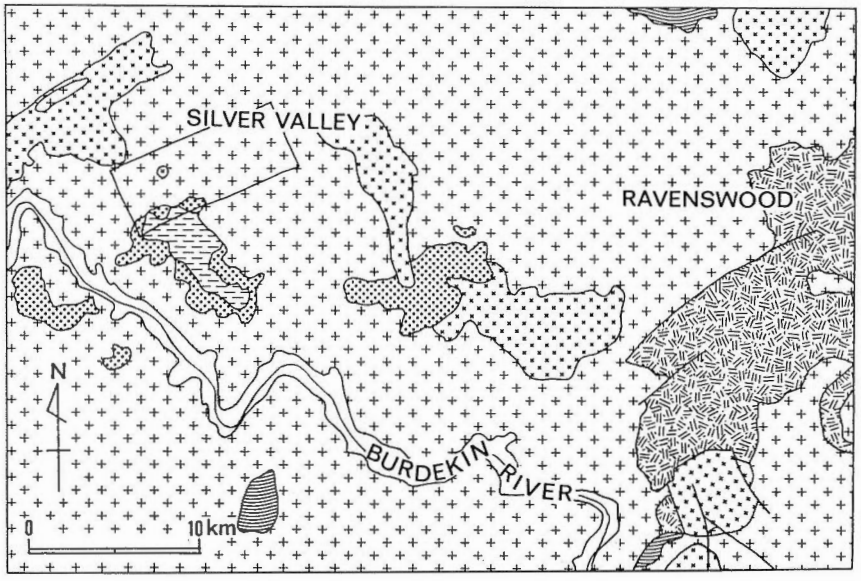

Pleistocene — Sellheim Formation

Tertiary — Lacustrine and fluviatile deposits

Upper Carboniferous to Lower Permian — Tuckers Igneous Complex and Boori Igneous Complex

Middle Ordovician and Upper Silurian or Lower Devonian — Ravenswood Granodiorite Complex

Cambrian to Ordovician — Cape River Beds; Mount Windsor Volcanics

Fig. 68 Geologic map of the Ravenswood area after Clarke and Paine (1970).

a cubic spline, then applying a D.C. offset to each radiance value, for each band, for each pixel (Honey and Daniels, 1986).

The author did not applied geometric correction to the image data in this case. The most significant systematic geometric effects are the tangent theta distortion due to the constant angular rotation rate, which results in a variation in the lateral translation rate of the instantaneous field of view across the surface; and the panoramic distortion which is a combination of the tangent theta effect, and the increased pixel size on the surface away from nadir. These effects can be modeled from the information on altitude, scan rate and instantaneous field of view (Honey and Daniels, 1986). However, such correction is not vital to this particular case, which focuses on a spectral response pattern of each pixel.

Plate 2.1 is a common false color image of the studied area assigning Bands 4, 3, and 2 to red (R), green (G), and blue (B) respectively. Histogram equalization was applied in order to achieve better visual expression (histogram equalization is applied to all images displayed hereafter, except to those created by HSI color transform). In this color assignment, vegetation demonstrates reddish color. Plate 2.2 is a false color image assigning Bands 6, 7, and 9 in the SWIR region to RGB. These bands roughly correspond to the ERS-1 Bands 6, 7, and 8 respectively. This image is not colorful, because data values of these three bands are highly correlated.

6.3.2 Reflectance Calibration by Field Measurements

The author has discussed significance of reflectance calibration in Chapter 3. Roughly, there are two different ways to perform reflectance calibration; one is linear regression using field measurements, and the others are techniques without groundtruth. The former is tested in this section, and the Log Residual technique representing the latter will be discussed in the next section.

As discussed in Chapter 3, there are some restrictions to apply the reflectance calibration using field measurements to image data. In a strict sense, field reflectance measurements have to be done simultaneously to data acquisition by an aircraft or satellite sensor in order to avoid any unexpected changes of surface conditions. However, the author assumed that the targets had not changed markedly during the period between the data acquisition and the field survey, as he visited the test area more than one year after the data acquisition. Moreover, the author measured reflectance spectra of the rock and soil samples in laboratory, because he could not bring a field radiometer to the test site. The next important condition is to choose field targets with enough spatial distribution in terms of the pixel size. However, it was extremely difficult to satisfy this condition in this particular case, because most of the area is more or less covered with vegetation. Five calibration targets, whose locations are shown in Fig. 67, were chosen, but none of them are completely vegetation free.

Figure 69 shows reflectance spectra of the rock and soil samples collected at the calibration targets. These spectra were obtained by the IRIS spectroradiometer after the manner described in Section 2.2. Then, the reflectance spectra were convolved to the AMSS MkI spectral equivalent by the procedure described in Sections 2.2.3 and 5.1 assuming a rectangular filter transfer function for each bandpass shown in Table 13.

Raw data values were extracted from the AMSS imagery over the five calibration targets. Table 14 shows statistics of the extracted pixel values for each target. Next, the averaged pixel values were plotted against the convolved field spectra (Fig. 70). Least squares regression was used to produce best fit lines. Table 15 shows coefficients of the best fit lines and correlation coefficient R^2. Note that the R^2 values for the VNIR bands are not high. The Band 1 showed negative correlation, probably due to Rayleigh scattering in the shorter wavelength and/or spectral inhomogeneity of the targets. The SWIR bands showed higher R^2 values ranging from

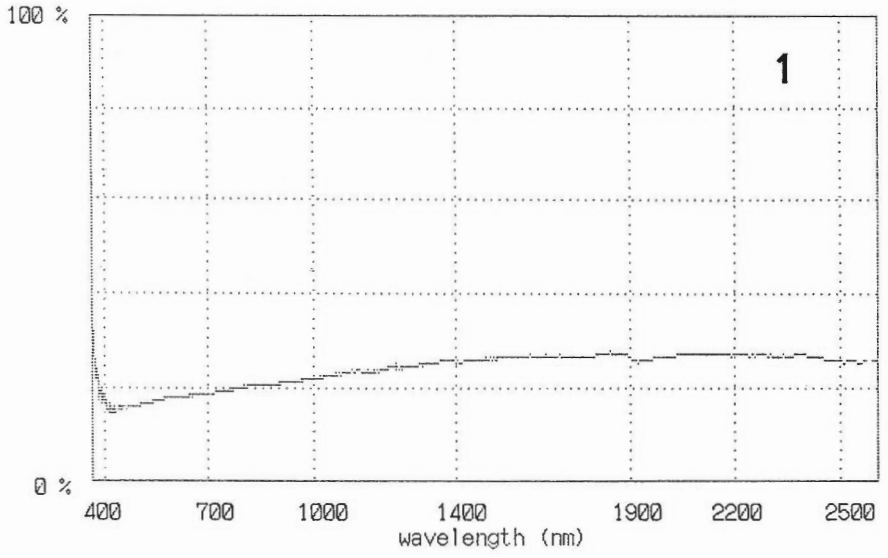

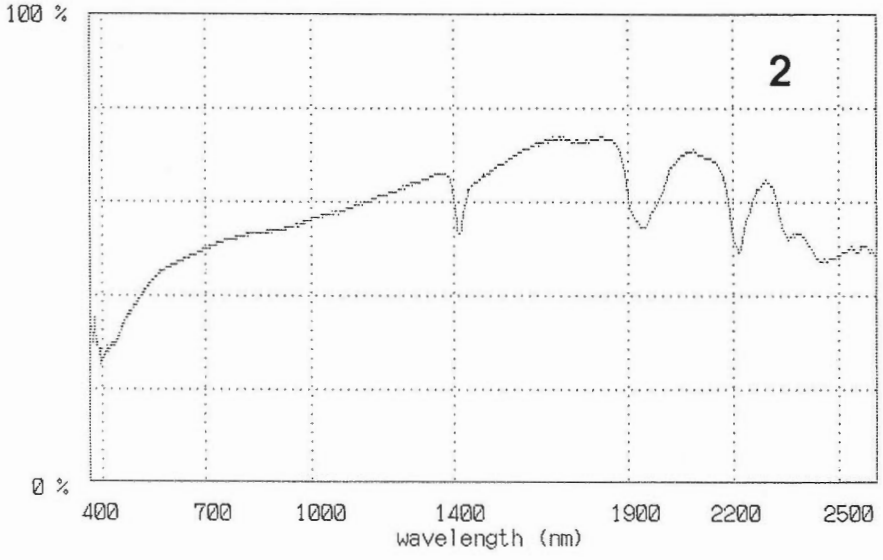

Fig. 69 Reflectance spectra of the ground calibration targets: 1) Granodiorite (Tuckers Igneous Complex); 2) Hydrothermal alteration including sericite; 3) Pale red soil; 4) Red soil; 5) Epidote-rich granodiorite.

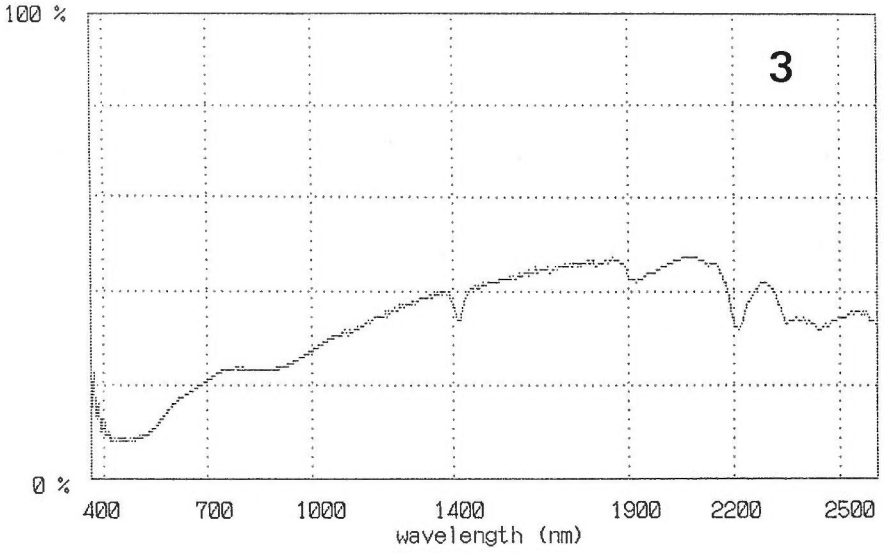

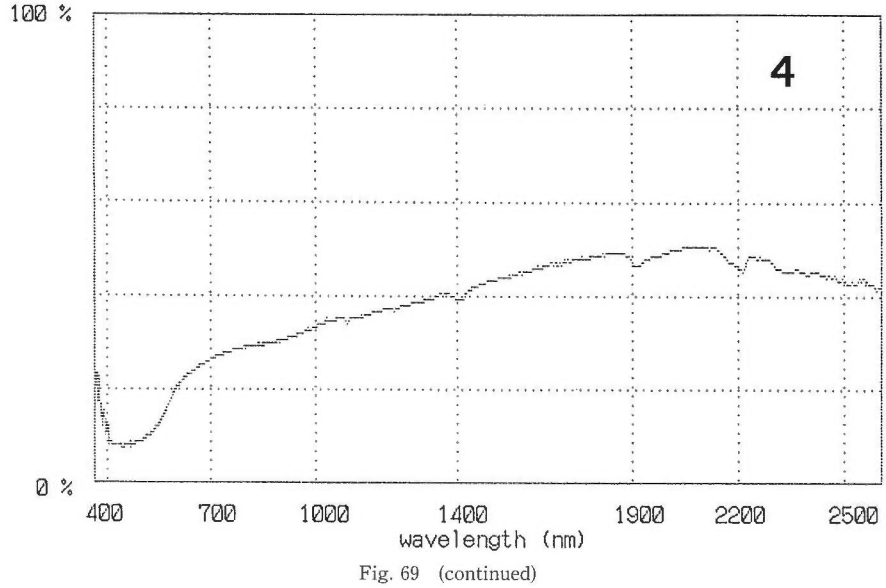

Fig. 69 (continued)

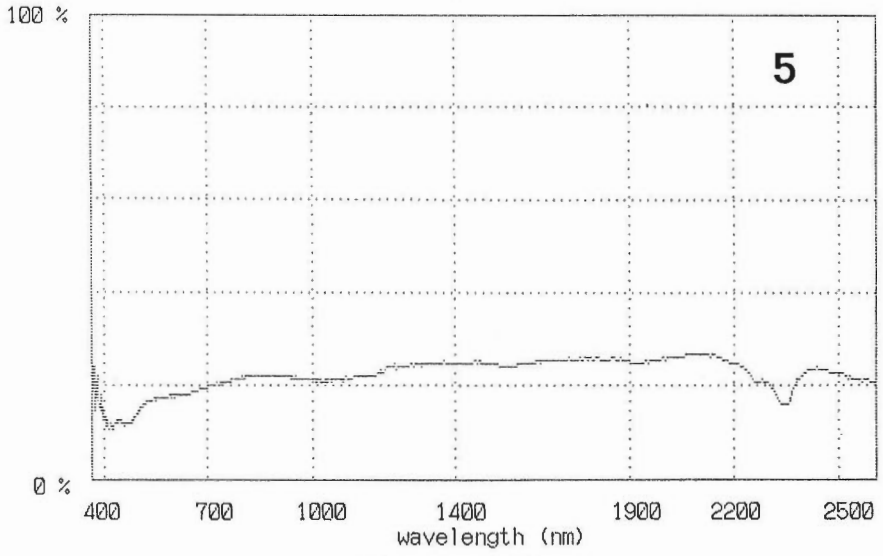

Fig. 69 (continued)

0.893 to 0.985. Finally, the slopes and intercepts of the regression equations were used to convert each AMSS digital number to percent reflectance.

A false color image of reflectance calibrated data looks almost same as that of uncalibrated data, because the reflectance calibration only removes intercepts and linearly stretches the data. In order to check whether the reflectance calibration is appropriately done or not, let us make an assumption that adequately calibrated data should plot around an 1:1 reflectance line in interband plots. In other words, reflectance of the surface materials in the studied area should be highly correlated as a whole, and the slope of the best fit line between responses of two bands should be very close to 1.0 as shown in Section 5.2.2.

Figures 71 and 72 are cluster plots of Band 6 vs. Band 7, and Band 7 vs. Band 8, before and after the reflectance calibration respectively. It is difficult to find a significant improvement as a result of the calibration. Table 16 shows slopes and intercepts of the best fit lines and correlation coefficients among the three SWIR bands before and after the reflectance calibration. The slope between Bands 7 and 9 after reflectance calibration is 1.086, which has been slightly improved from 1.149 for the uncalibrated data. However, in the case of Bands 6 and 7, the slope values became even worse, from 0.7703 to 0.7482, which is not very close to 1.0. This result means that the assumption made should be rejected.

We can conclude that the reflectance calibration was not adequately done in this particular case. A major reason might be spectral inhomogeneity of the calibration targets. As described before, it was difficult to find calibration targets with a spectrally homogeneous material, because most of the area is more or less covered with vegetation, mainly eucalyptus trees in this case. The reflectance measurements were done only for rock and soil samples, so that the spectra do not represent the response of each pixel. Consequently, it was decided that the reflectance calibration using field spectral measurements was not applied to the image data in this study.

6.3.3 Log Residual

As the MkI AMSS is radiometrically uncalibrated, it is not possible to convert the digital values representing radiance in each of the channels to an absolute reflected or emitted radiance value (Honey and Daniels, 1986). Therefore, we need to employ another technique to "cali-

Table 14 Statistics of the pixels extracted as reflectance calibration targets. N indicates

1) Granodiorite (Tuckers Igneous Complex)	N = 208
Band	Mean	Standard deviation
1	102.8	17.5
2	80.2	16.8
3	63.1	14.8
4	55.5	12.8
5	55.4	19.3
6	71.1	14.0
7	78.9	13.6
8	72.6	14.4
9	65.5	15.6

2) Hydrothermal alteration	N = 9
Band	Mean	Standard deviation
1	225.8	11.9
2	215.0	0.0
3	217.1	8.2
4	215.2	13.9
5	213.4	2.6
6	216.4	14.3
7	198.3	30.2
8	204.8	30.6
9	200.8	33.9

3) Pale red soil	N = 88
Band	Mean	Standard deviation
1	124.5	15.5
2	148.7	16.1
3	145.2	16.9
4	114.8	10.0
5	119.4	18.3
6	149.6	19.1
7	147.4	14.8
8	156.7	18.6
9	142.9	18.1

4) Red soil	N = 169
Band	Mean	Standard deviation
1	125.1	17.1
2	146.6	16.1
3	148.7	16.0
4	106.5	11.7
5	106.5	16.7
6	145.1	14.4
7	140.0	14.6
8	148.3	16.4
9	138.3	15.9

(continues)

Table 14 (continued)

5) Epidote-rich zone N = 988

Band	Mean	Standard deviation
1	118.1	20.7
2	110.3	18.2
3	93.4	16.3
4	73.9	10.8
5	67.4	17.3
6	69.9	16.2
7	79.7	14.1
8	70.3	15.1
9	64.6	16.0

Table 15 Coefficients of the best fit lines and correlation coefficients between the pixel value (DN) and ground reflectance (GR). The best fit lines are: (GR)=A×(DN)+B.

BAND	A	B	R^2
1	-0.035	19.4	-0.238
2	0.25	-13.5	0.958
3	0.23	-5.6	0.885
4	0.20	2.6	0.886
5	0.22	6.4	0.984
6	0.26	13.9	0.951
7	0.25	8.1	0.985
8	0.21	9.4	0.893
9	0.24	5.5	0.941

Table 16 Coefficients of the best fit lines between the SWIR bands. A best fit line is: (Band N+1)=A×(Band N)+B.

1) Band 6 vs. Band 7

Before reflectance calibration			/	After reflectance calibration		
A	B	R^2	/	A	B	R^2
0.7703	28.05	0.932	/	0.7482	4.78	0.932

2) Band 7 vs. Band 9

Before reflectance calibration			/	After reflectance calibration		
A	B	R^2	/	A	B	R^2
1.149	-24.94	0.988	/	1.086	-9.27	0.998

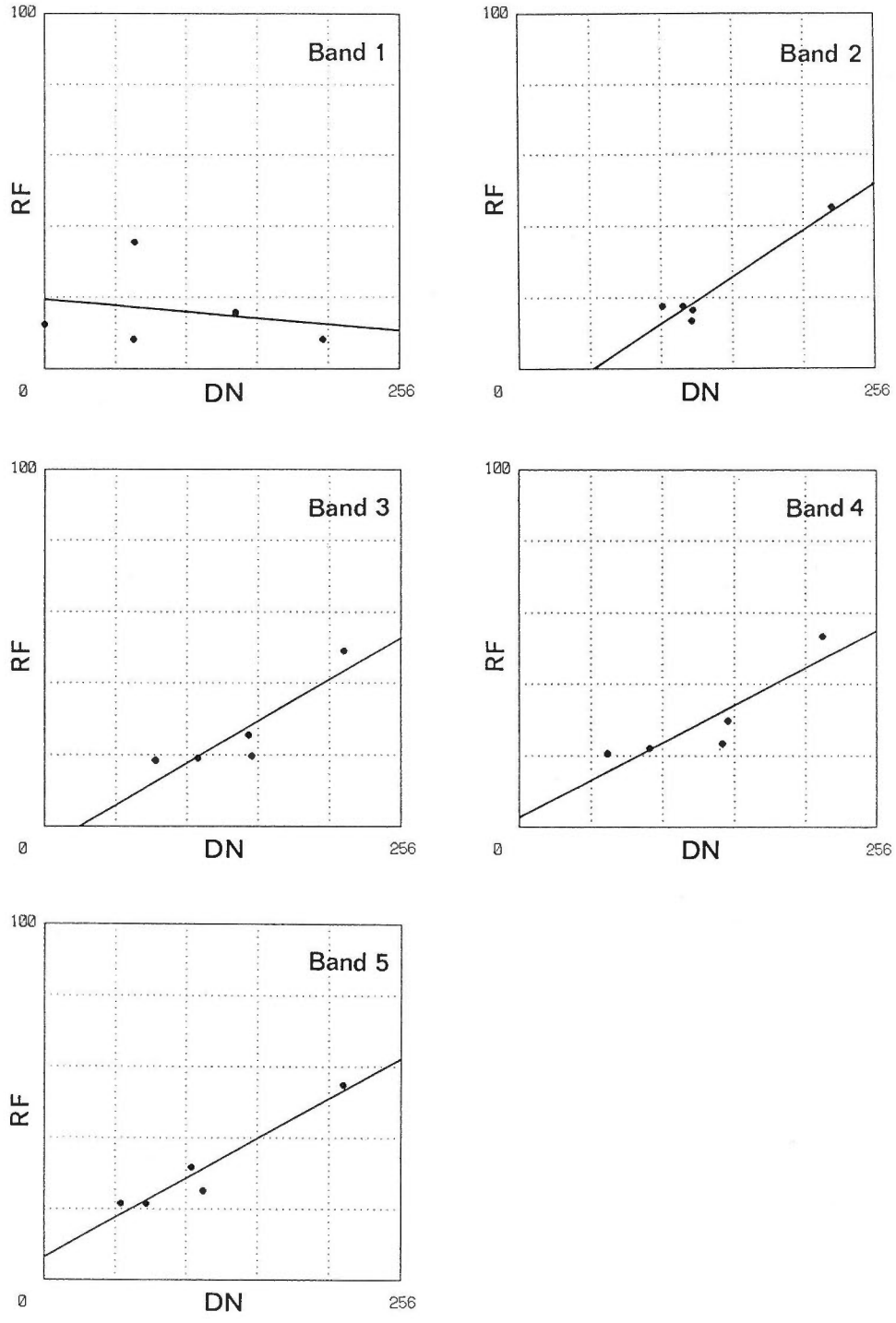

Fig. 70 Digital number (DN) of each spectral band versus reflectance (RF) for five ground targets. Coefficients of the linear regression lines are shown in Table 15.

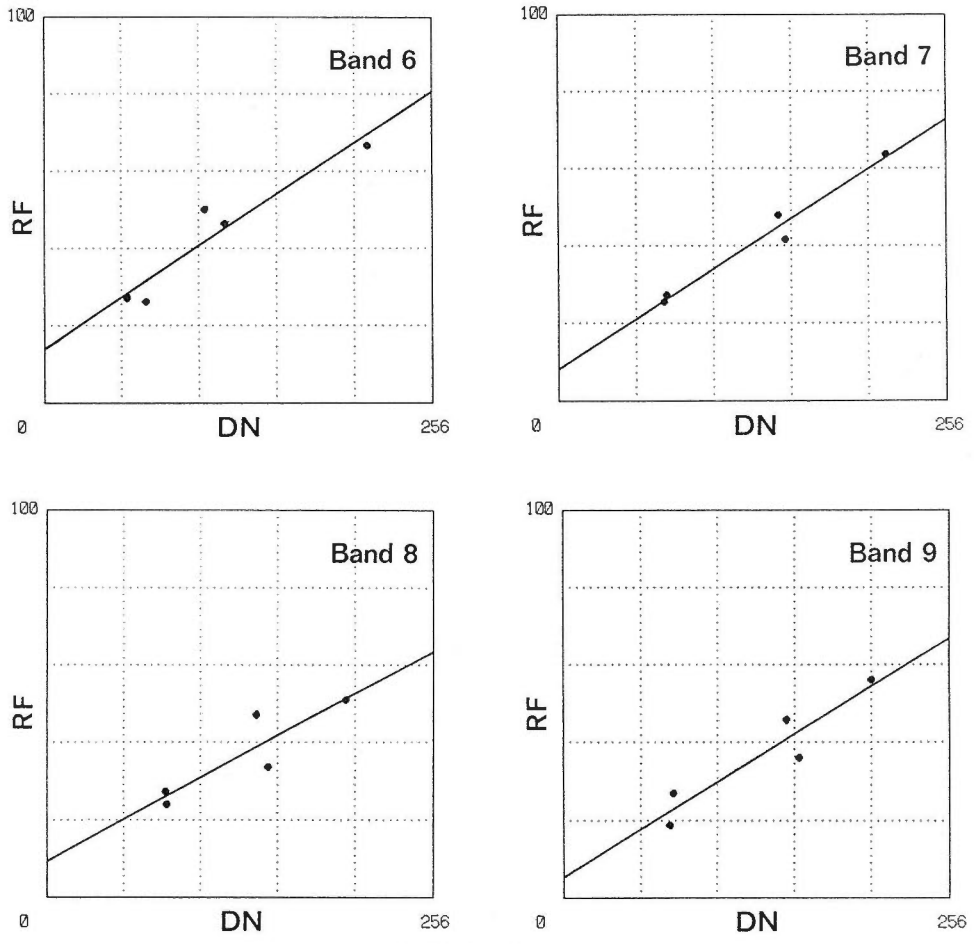

Fig. 70 (continued)

brate" the image data instead of the reflectance calibration discussed in the previous section, if we try to apply the image processing techniques developed for reflectance data in Section 5.2. The Log Residual technique discussed in Section 3.2.4 is applicable to this case, because the studied area is not dominantly composed of one cover type. The Log Residual normalizes each pixel value of each band by using the average of each band in the spatial dimension and the average of each pixel in the spectral dimension.

Figure 73 shows cluster plots of Band 6 vs. Band 7, and Band 7 vs. Band 9 after applying the Log Residual. These plots do not show highly correlated nature of pixel values any more. This means that the normalization process of the Log Residual has removed out not only interband mean differences but also brightness changes due to a topographic effect.

A color composite image of Bands 6, 7, and 9 after the Log Residual processing is shown in Pl. 2.3, which demonstrates more colorful patterns than Pl. 2.1 of the same band combination. For instance, the yellowish area in the northeast of Pandanus Creek indicates the epidote-rich zone in Ravenswood Granodiorite Complex. The area surrounding the epidote-rich zone and the linear reddish anomaly in the southwest of Pandanus Creek suggest hydrothermally altered areas with phyllosilicate minerals such as sericite or kaolinite. Therefore, this image itself is quite useful for discrimination of lithology. However, the author considers the Log Residual as a

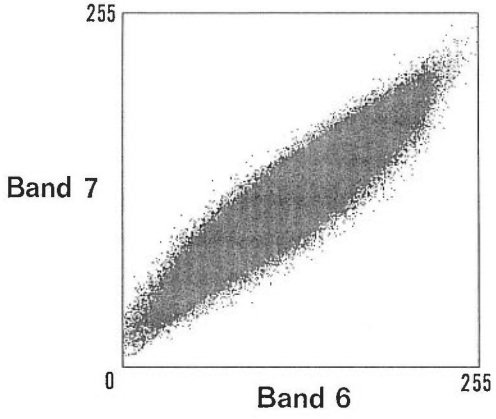

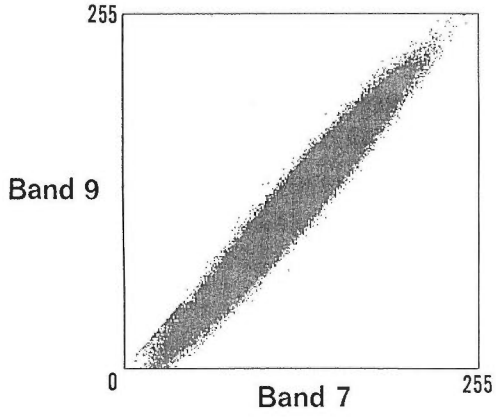

Fig. 71 Cluster plots of Band 6 vs. Band 7, and Band 7 vs. Band 9. Note high correlation among these three bands.

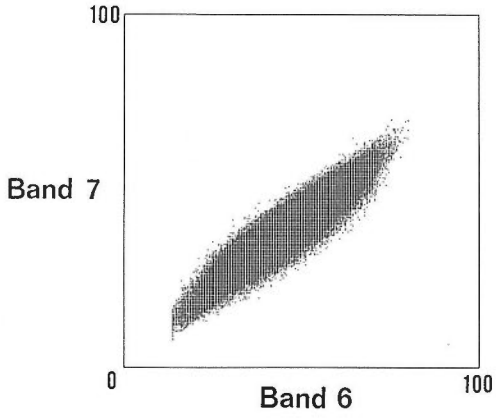

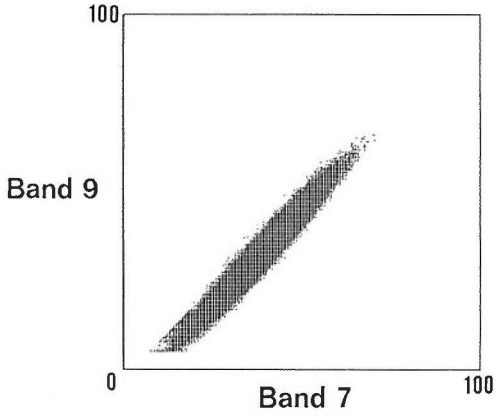

Fig. 72 Cluster plots of Band 6 vs. Band 7, and Band 7 vs. Band 9 after reflectance calibration using ground targets.

preprocessing technique for the reflectance calibration prior to the next procedures; calculation of spectral indices and HSI color transform.

6.3.4 Spectral Indices

The author proposed spectral indices for discrimination of lithology in Sections 5.2.2 and 5.3 using reflectance data. In this section, the author will use the data set normalized by the Log Residual in order to calculate the spectral indices; Alunite Index (ALI) and Calcite Index (CLI). Coefficients for each band to form the indices are the same as those proposed in Section 5.2.2 based upon an assumption that the Log Residual can provide an interband pattern which imitates a reflectance pattern of each pixel in a relative sense. The indices are given by the equations;

$$\text{ALI} = 0.62 \times (\text{Band 6}) - 0.77 \times (\text{Band 7}) + 0.16 \times (\text{Band 9}) \quad (21)$$

$$\text{CLI} = 0.54 \times (\text{Band 6}) + 0.26 \times (\text{Band 7}) - 0.80 \times (\text{Band 9}). \quad (22)$$

Plates 3.1 and 3.2 are black and white images of the ALI and the CLI respectively. The brighter

on the image, the higher index values.

The ALI image indicates a semicircular high anomaly in the southwest of Silver Valley and a linear anomaly in the east of Pandanus Creek. The former surrounds a circular dark area, which is a hill composed of an epidote-rich alteration zone in granodiorite. The latter corresponds to a hydrothermally altered zone in granodiorite. A reflectance spectrum of the sample collected in this zone (Fig. 69) suggests presence of sericite. These anomalies were not shown in the published maps, but were confirmed by the field survey in 1987 by the author.

The CLI image (Pl. 3.2) apparently displays different patterns from the ALI image. There is a broad high anomaly in the east of Pandanus Creek, where the ALI ranges low to high. The western half of this anomaly has low ALI values and coincides well with the epidote-rich zone. The rest of this anomaly and another anomaly in the west of Pandanus Creek are high in the both ALI and CLI. These anomalies might indicate phyllosilicate minerals such as kaolinite or sericite according to the hypothetical response patterns of typical minerals shown in Section 5.2.2.

Perpendicular Vegetation Index (PVI) was also calculated using Bands 3 and 4 in order to assess vegetation. Raw data of Bands 3 and 4 were used, because interband calibration is not necessary in calculation of such a spectral index in two dimensional space. Only selection of an appropriate rock-soil baseline is vital to index values.

Elvidge (1985) chose ground targets without vegetation and extracted pixels for each target from the imagery. Then, linear regression was used to establish rock-soil baselines. However, as explained in Section 6.3.2, it was very difficult to find such calibration targets in this particular case. A rock-soil baseline was, thus, established somewhat arbitrary on a cluster plot for Band 3 vs. Band 4 (Fig. 74). The best fit line in the plot is;

$$(\text{Band } 4) = 0.5633 \times (\text{Band } 3) + 35.29. \tag{23}$$

The slope of this line should be slightly larger than the rock-soil baseline, because pixels representing vegetation plots above the best fit line. Taking into account the fact that vegetation cover ranges approximately from 10 to 30 percents in this area, the following rock-soil line was determined by visual interpretation of Fig. 74;

$$(\text{Band } 4) = 0.678 \times (\text{Band } 3) + 19.6. \tag{24}$$

Coefficients for each spectral band to form the PVI were calculated following Jackson(1983). Consequently, the PVI is given by the equation;

$$\text{PVI} = -0.56 \times (\text{Band } 3) + 0.83 \times (\text{Band } 4). \tag{25}$$

A PVI image is shown in Pl. 3.3. Relatively dense vegetation along Pandanus Creek and its branches indicate high PVI values. On the other hand, the epidote-rich zone with high CLI values has low PVI.

In order to combine information on lithology and vegetation, a color composite image was made (Pl. 4.1). Namely, the PVI, ALI, and CLI are assigned to RGB color primitives respectively. Areas with relatively dense vegetation, which is reddish in the image, are distributed along drainage. Areas with bluish color means high CLI values, and well correspond to the epidote -rich zone in the east of Pandanus Creek. Greenish areas indicate high ALI values, but they seem to be more widespread than expected. This might be caused by the normalizing effect of the Log Residual. As shown in Section 5.2, vegetation has a upper convex reflectance pattern in the three SWIR bands. If there are significant amounts of vegetation pixels in the processed area, the normalization effect of the Log Residual enhances even a flat response pattern to lower convex, which will have a high ALI value. The cyan anomalies, which indicate pixels with high values in both the ALI and CLI, are thus more important. We can find two significant cyan anomalies, which suggest hydrothermally altered areas with phyllosilicate minerals; the area

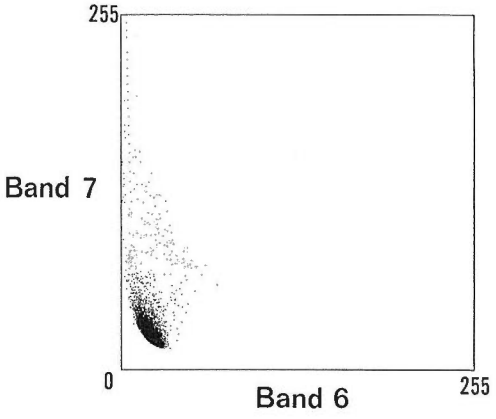

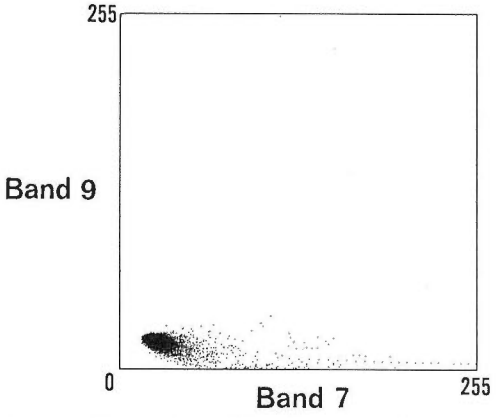

Fig. 73 Cluster plots of Band 6 vs. Band 7, and Band 7 vs. Band 9 after normalization by the Log Residual. Note that the high inter-band correlation has been removed.

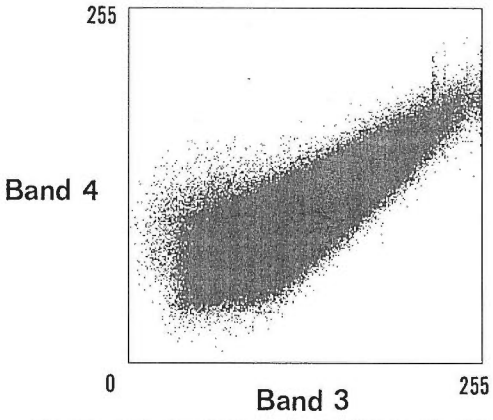

Fig. 74 A cluster plot between Band 3 vs. Band 4.

surrounding the epidote-rich zone in the east of Pandanus Creek and the linear anomaly in the west of Pandanus Creek. The latter has been confirmed by the field survey.

6.3.5 HSI Color Transform

The HSI color transform is another candidate to express characteristic band response patterns for lithologic discrimination. HSI color images were created according to the way proposed in Section 5.2.3. First, raw data of Bands 6, 7, and 8 were used as input. The gray axis was the (1:1:1) equal reflectance line in Section 5.2.3, but the best fit line found by linear regression was used instead because of the failure of the reflectance calibration in this case. Therefore, the concept of the technique is almost equivalent to those of Gillespie *et al.* (1986). The zero hue (red) is assigned to the direction of the band response pattern of

$$(\text{Band 6, Band 7, Band 9}) = (255, 0, 255), \tag{26}$$

which is close to the direction showing the cluster of alunite. Saturation and intensity were fixed to 1.0 and 0.5 respectively for all pixels in order to achieve maximum color enhancements.

Plate 4.2 shows the HSI image created. Some anomalous areas can be found by yellowish color, particularly around the epidote-rich zone. However, it is unreasonable that the vegetation along Pandanus Creek is reddish color. According to the concept discussed in Section 5.2.3, yellowish and reddish colors should indicate alunite and kaolinite type alterations respectively. As the interband correction was not applied in this case, the colors in the image means nothing but differences of relative strength in the raw data. In other words, this image can show some lithologic boundaries by differences of colors, but it is difficult to tell the meanings of the colors displayed on the image.

Next, the Log Residual data of the Bands 6, 7, and 9 were used for the same processing of HSI color transform. The gray axis is again the best fit line obtained by linear regression, and saturation and intensity are constant 1.0 and 0.5 respectively. Plate 4.3 is the HSI image created. In this case, unlike to Pl. 4.2, vegetation is displayed blue. The epidote-rich zone is displayed as greenish color that is reasonable according to the concept proposed in Section 5.2.3. Yellow color corresponds well to the hydrothermally altered areas. One problem is the widespread reddish color. The reason is the same as described in the previous section that the Log Residual technique enhances a flat response pattern due to its normalizing effect in vegetated area. At any rate, the HSI color image of Pl. 4.3 is different from Plate 11 in the point that the meanings of the colors are interpretable geologically.

6.4 Discussion

The author applied the image processing techniques for discrimination of lithology proposed in Chapter 5 to the airborne multispectral scanner data. The reflectance calibration using field measurements was not successful, because the author could not find good calibration targets. Instead, the author employed the Log Residual technique discussed in Section 3.2.4 as an interband calibration method in a relative sense, and successfully normalized the data. It is concluded that the Log Residual can be substituted for reflectance calibration to some degree, particularly in the cases that an image processing result is required before a field survey or calibration targets are difficult to be found.

The spectral indices, the ALI and CLI, have provided reasonable results. This fact means that both the preprocessing by the Log Residual and the calculation of these indices were adequately done to the data in this case. The HSI color transform also gave a sufficient result. The important point is that the color images shown in Pls. 4.1 and 4.3 can be interpreted geologically from the colors displayed. Whereas the HSI color transform from the raw data shown in Pl. 4.2 and the principal component analysis simply provide colorful images which are difficult to interpret geologically. As a result, adequacy of the techniques proposed in Chapter 5 have been proven.

7. CONCLUSION

1. The author compared two spectroradiometers in terms of spectral resolution and efficiency in spectral measurements of rocks and minerals. The spectroradiometer using gratings as dispersion elements can resolve characteristic spectral features such as absorption doublets of kaolinite and alunite. Whereas, the spectroradiometer using a circular variable filter (CVF) can obtain a spectrum in a relatively short time, but can not resolve such doublets due to lower spectral resolution. The author chose the former to be used in this study.

2. The author measured several reflectance spectra of rocks and minerals, some of which exhibit characteristic absorption features in the visible and near-infrared regions. Particularly, phyllosilicate minerals including clay minerals have diagnostic absorptions in the 2.2 μm region.

Carbonate minerals and epidote have a diagnostic absorption in the 2.35 μm region. Typical rock types lacking significant amount of these minerals show flat featureless reflectance spectra in these spectral region.

3. The author developed an expert system for identification of minerals using the visible and near-infrared spectra. Feature coding was employed as a manner of pattern recognition of the spectra. A spectroradiometer with such an expert system will allow us real time identification of minerals in field.

4. The author examined calibration techniques to convert digital numbers recorded on a magnetic tape to reflectance of surface materials. The linear regression method using field spectra is the best way if we can find good field calibration targets. Lacking field measurements, the Log Residual would produce superior results in areas which are not dominantly composed of one cover type. In areas containing one dominant cover type, the Least Upper Bound Residual would probably be the best technique.

5. The author developed a new field radiometer in order to provide groundtruth data for reflectance calibration. This radiometer has two motor-driven filter wheels, each of which can contain up to eight filters and corresponds to the silicon and lead-sulfide detectors respectively. Preliminary investigation has shown that the radiometer provides reliable spectral data.

6. The author proposed possible techniques for discrimination of lithology using the optical sensor data of the Japanese ERS-1. The two spectral indices, linear combination of the three SWIR bands, will be useful for discrimination of lithology, i.e., Alunite Index (ALI) and Calcite Index (CLI). The HSI color transform applied to the three SWIR bands is another possible way to express sensor response patterns, and allows us to create a color image useful for interpretation of different rock types.

7. The author proposed the following equations to estimate the proportion of vegetation (RVEG) and clay and/or carbonate minerals (RMIN) within a single pixel based upon a linear spectral mixing model:

$$\mathrm{RVEG} = \mathrm{PVI} / \mathrm{MPVI}$$

$$\mathrm{RMIN} = (\mathrm{TABS} - \mathrm{RVEG} \times \mathrm{MVABS}) / ((1 - \mathrm{RVEG}) \times \mathrm{MMABS})$$

where PVI indicates the perpendicular vegetation index formed by Bands 2 and 3, and MPVI is the maximum PVI value. TABS is the total absorption index defined in the four-dimensional space of the four SWIR bands, and MVABS and MMABS represent the maximum TABS values for a pixel with 100 percent vegetation cover and that with 100 percent concentration of the minerals respectively.

8. The author applied the proposed techniques to the airborne multispectral scanner data of Queensland, Australia. The reflectance calibration using field spectral measurements was failed due to the difficulty to find good calibration targets in the test area. The Log Residual, on the other hand, succeeded in normalizing the original data, and thus was employed as a calibration technique instead. The images of spectral indices, the ALI and CLI, calculated on the normalized data by the Log Residual successfully showed the epidote-rich zone and hydrothermally-altered areas. The Perpendicular Vegetation Index (PVI) image exhibited a good result for assessment of vegetation. The HSI color transform image created from the three SWIR bands also successfully displayed colors corresponding to the SWIR band response patterns.

9. We will be able to performed discrimination of lithology using the techniques proposed in this study, i.e., the spectral indices and the HSI color transform along with appropriate calibration techniques such as the linear regression using field spectra or the Log Residual. These techniques can create images which can be easily interpreted by geologists.

ACKNOWLEDGMENTS

The author wishes to express his sincere gratitude to Professor Hisao Nakagawa of Tohoku University for his continual encouragement and a critical reading of the manuscript. The author would also like to thank Professors Yokichi Takayanagi and Kei Mori, and Associate Professors Kunihiro Ishizaki, Kenshiro Ogasawara, and Koji Minoura of Tohoku University for their helpful suggestions and guidance. Thanks are due to Emeritus Professor Nobu Kitamura of Tohoku University for his pertinent orientations when the author studied geology in Tohoku University.

The author owes a great deal of gratitude to Dr. Hirokazu Hase of the Geological Survey of Japan for his helpful suggestions and encouragement during the course of this study. The author is also grateful to Professor Ronald J. P. Lyon of Stanford University for teaching fundamentals of geologic remote sensing to the author. Dr. Frank R. Honey of Geoscan Pty. Ltd. kindly provided the AMSS data used in Chapter 6. It would have been impossible to accomplish this research without his offer. Several helpful discussions with Dr. Dar A. Roberts of University of Washington are also gratefully acknowledged. The research described in the Chapter 3 was done as a cooperative study with him. The author also wishes to thank Dr. David A. Mouat of University of Nevada System for his helpful suggestions particularly on the Section 5.3.

The author would also like to thank the following people for their helpful discussions and suggestions: Dr. Daiei Inoue of the Central Research Institute of the Electric Power Industry, Dr. Katsuro Ogawa, Dr. Kenji Okabe, Dr. Hiroji Tsu, Dr. Shiro Tamanyu, Mr.Isao Sato, Mr. Minoru Urai, Dr. Hirofumi Muraoka, and Dr. Yoshinori Miyazaki of the Geological Survey of Japan.

REFERENCES

Abrams, M.J., Ashley, R.P., Rowan, L.C., Goetz, A.F.H. and Kahle, A.B. (1977) Mapping of hydrothermal alteration in the Cuprite mining district, Nevada, using aircraft scanner images for the spectral region 0.46 to 2.36 μm. *Geology*, vol. 5, p. 713-718.

————, Brown, D., Lepley, L. and Sadowski, R. (1983) Remote sensing for porphyry copper deposits in southern Arizona. *Econ. Geol.*, vol. 78, p. 591-604.

Clarke, D.E. and Paine, A.G.L. (1970) *1:250,000 Geological Series with Explanatory Notes, Charters Towers, Queensland, Sheet SF/55-2.* Bureau of Mineral Resources, Geology and Geophysics of Australia, Canberra, 34 p.

Collins, W., Chang, S.H. and Kuo, J.T. (1981) Infrared airborne spectroradiometer survey results in the western Nevada area. *Final Report to NASA, Contract JPL 955832*, Aldrige Laboratory of Applied Geophysics, Columbia University, New York, 61 p.

Conel, J.E. and Alley, R.E. (1985) Lisbon Valley, Utah, Uranium test site report. In: Paley, H.N. (ed.), *The Joint NASA/Geosat Test Case Project, Final Report, Part 2*, AAPG Bookstore, Tulsa, vol.I, sec. 8, p. 1-158.

Crist, E.P. and Cicone, R.C. (1984) A physically-based transformation of Thematic Mapper data—the TM tasseled cap. *IEEE Trans. Geosci. Remote Sens.*, vol. GE-22, p. 256-263.

Curran, P.J. (1987) On defining remote sensing. *Photogram. Eng. Remote Sens.*, vol. 51, p. 305-306.

Dilles, J.H. (1983) The petrology and geochemistry of the Yerington batholith and the Ann-Mason porphyry copper deposit, western Nevada. *Ph. D. thesis, Applied Earth Sciences Department, Stanford University*, Stanford, (MS).

Elvidge, C.D. (1985) Separation of leaf water and mineral absorption in the 2.22 μm Thematic Mapper band. *Ph. D. thesis, Applied Earth Sciences Department, Stanford University*, Stanford, (MS).

————and Lyon, R.J.P. (1984) Mapping clay alteration in the Virginia Range-Comstock Lodge, Nevada with airborne Thematic Mapper imagery. *Proceedings of the Third Thematic Conference on Remote Sensing for Exploration Geology*, Environmental Research Institute of Michigan, Ann

Arbor, p. 161-170.
——— and ——— (1985a) Estimation of the vegetation contribution to the 1.65/2.22 μm ratio in airborne Thematic Mapper imagery of the Virginia Range, Nevada. *Int. Jour. Remote Sens.*, vol. 6, p. 75-88.
——— and ——— (1985b) Influence of rock-soil spectral variation on the assessment of green biomass. *Remote Sens. Environ.*, vol. 17, p. 265-279.
Foley, J.D. and Van Dam, A. (1982) *Fundamentals of Interactive Computer Graphics.* Addison-Wesley, Reading, 664 p.
Fussell, J. and Rundquist, D. (1986) On defining remote sensing. *Photogram. Eng. Remote Sens.*, vol. 52, p. 1507-1511.
Gillespie, A.R. (1980) Digital techniques of image enhancement. In: Siegal, B.S. and Gillespie, A.R. (eds.), *Remote Sensing in Geology*, John Wiley & sons, New York, p. 139-226.
———, Kahle, A.B. and Walker, R.E. (1986) Color enhancement of highly correlated images. I. Decorrelation and HSI contrast stretches. *Remote Sens. Environ.*, vol. 20, p. 209-235.
Gladwell, D.R., Lett, R.E. and Lawrence, P. (1983) Application of reflectance spectrometry to mineral exploration using portable radiometers. *Econ. Geol.*, vol. 78, p. 699-710.
Goetz, A.F.H. and Rowan, L.C. (1981) Geologic remote sensing. *Science*, vol. 211, no. 4484, p. 781-791.
———, Vane, G., Solomon, J.E. and Rock, B.N., (1985) Imaging spectrometry for Earth remote sensing. *Science*, vol. 228, no. 4704, p. 1147-1153.
Green, A.A. and Craig, M.D. (1985) Analysis of aircraft spectrometer data with logarithmic residuals. *Proceedings of the Airborne Imaging Spectrometer Data Analysis Workshop, JPL Publication 85-41*, Jet Propulsion Laboratory, Pasadena, p. 111-119.
Honey, F.R. and Daniels, J.L. (1985) Application of Carr Boyd Minerals Limited airborne multispectral scanner to spectral discrimination of hydrothermally altered areas. *Proceedings of the Fourth Thematic Conference on Remote Sensing for Exploration Geology*, Environmental Research Institute of Michigan, Ann Arbor, p. 227-231.
——— and ——— (1986) Rock discrimination and alteration mapping for mineral exploration using the Carr Boyd/Geoscan airborne multispectral scanner. *Proceedings of the Fifth Thematic Conference on Remote Sensing for Exploration Geology*, Environmental Research Institute of Michigan, Ann Arbor, p. 267-278.
Horsfall, C.L., Lister, R., Buda, R., Green, A.A. and Craig, M.D. (1987) Expert system software for computer identification of minerals from their short-wave infrared spectra. *Proceedings of the 4th Australasian Remote Sensing Conference*, The 4th Australasian Remote Sensing Conference Inc., Adelaide, p. 642-655.
Hunt, G.R. (1977) Spectral signatures of particulate minerals in the visible and near infrared. *Geophysics*, vol. 42, p. 501-513.
——— (1979) Near-infrared (1.3-2.4 microns) spectra of alteration minerals—potential for use in remote sensing. *Geophysics*, vol. 44, p. 1974-1986.
——— (1980) Electromagnetic radiation: the communication link in remote sensing. In: Siegal, B.S. and Gillespie, A.R. (eds.), *Remote Sensing in Geology*, John Wiley and sons, New York, p. 5-45.
——— and Salisbury, J.W. (1970) Visible and near-infrared spectra of minerals and rocks: I. Silicate minerals. *Modern Geol.*, vol. 1, p. 283-300.
———, ——— and Lenhoff, C.J. (1971a) Visible and near-infrared spectra of minerals and rocks: III. Oxides and hydroxides. *Modern Geol.*, vol. 2, p. 195-205.
———, ——— and ——— (1971b) Visible and near-infrared spectra of minerals and rocks: IV. Sulphides and sulphates. *Modern Geol.*, vol. 3, p. 1-14.
———, ——— and ——— (1973) Visible and near-infrared spectra of minerals and rocks: VI. Additional silicates. *Modern Geol.*, vol. 4, p. 85-106.
Jackson, R.D. (1983) Spectral indices in n-space. *Remote Sens. Environ.*, vol. 13, p. 409-421.
Jet Propulsion Laboratory (1985) *Airborne Imaging Spectrometer, Science Investigator's Guide to AIS Data.* Jet Propulsion Laboratory, Pasadena, 46 p.
Kauth, R.J. and Thomas, G.S. (1976) The tasselled cap—A graphic description of the spectral-temporal development of agricultural crops as seen by Landsat. *Proceedings of the Symposium on Machine Processing of Remotely Sensed Data*, Purdue University, West Lafayette, p. 41-51.
Kepper, J.C., Lugaski, T.P. and MacDonald, J.S. (1986) Discrimination of lithologic units, alteration patterns and major structural blocks in the Tonopah, Nevada area using Thematic Mapper data. *Proceedings of the Fifth Thematic Conference on Remote Sensing for Exploration Geology*, Environmental Research Institute of Michigan, Ann Arbor, p. 97-115.
Lillesand, T.M. and Kiefer, R.W. (1979) *Remote Sensing and Image Interpretation.* John Wiley & sons, New

York, 612 p.

Lyon, R.J.P. (1986) Comparison of the 1984 & 1985 AIS data over the Singatse Range (Yerington) Nevada. *Proceedings of the Second Airborne Imaging Spectrometer Data Analysis Workshop, JPL Publication 86-35*, Jet Propulsion Laboratory, Pasadena, p. 86-95.

Marsh, S.E. and Lyon, R.J.P. (1980) Quantitative relationships of near-surface spectra to Landsat radiometric data. *Remote Sens. Environ.*, vol. 10, p. 241-261.

——— and McKeon, J.B. (1983) Integrated analysis of high-resolution field and airborne spectroradiometer data for alteration mapping. *Econ. Geol.*, vol. 78, p. 618-632.

Miller, N.L. and Elvidge, C.D. (1985) The iron absorption index: a comparison of ratio-based and baseline-based techniques for the mapping of iron oxides. *Proceedings of the Fourth Thematic Conference on Remote Sensing for Exploration Geology*, Environmental Research Institute of Michigan, Ann Arbor, p. 405-415.

Perry, C.R. and Lautenschlager, L.F. (1984) Functional equivalence of spectral vegetation indices. *Remote Sens. Environ.*, vol. 14, p. 169-182.

Podwysocki, M.H., Segal, D.B. and Abrams, M.J. (1983) Use of multispectral scanner images for assessment of hydrothermal alteration in the Marysvale, Utah, mining area. *Econ. Geol.*, vol. 78, p. 675-687.

Proffett, J.M., Jr. (1977) Cenozoic geology of the Yerington district, Nevada, and implications for the nature and origin of basin and range faulting. *Geol. Soc. Am. Bull.*, vol. 88, p. 247-266.

——— and Dilles, J.H. (1984) *Geologic Map of the Yerington District, Nevada, Map 77.* Nevada Bureau of Mines and Geology, and Mackay School of Mines, University of Nevada, Reno.

Prost, G.L. (1980) Alteration mapping with airborne multi-spectral scanners. *Econ. Geol.*, vol. 75, p. 894-906.

Richardson, A.J. and Wiegand, C.L. (1977) Distinguishing vegetation from soil background information. *Photogram. Eng. Remote Sens.*, vol. 43, p. 1541-1552.

Roberts, D.A., Yamaguchi, Y. and Lyon, R.J.P. (1985) Calibration of Airborne Imaging Spectrometer data to percent reflectance using field spectral measurements. *Proceedings of the Nineteenth International Symposium on Remote Sensing of Environment*, Environmental Research Institute of Michigan, Ann Arbor, p. 679-688.

———, ——— and ——— (1986) Comparison of various techniques for calibration of AIS data. *Proceedings of the Second Airborne Imaging Spectrometer Data Analysis Workshop, JPL Publication 86-35*, Jet Propulsion Laboratory, Pasadena, p. 21-30.

Rowan, L.C., Wetlaufer, P.H., Goetz, A.F.H., Billingsley, F.C. and Stewart, J.H. (1974) Discrimination of rock types and detection of hydrothermally altered areas in south-central Nevada by use of computer-enhanced ERTS images. *U.S.G.S. Prof. Pap. 883*, 35 p.

Slater, P.N. (1980) *Remote Sensing, Optics and Optical Systems.* Addison-Wesley, Reading, 575 p.

Yamaguchi, Y. (1987) Possible techniques for lithologic discrimination using the short-wavelength-infrared bands of the Japanese ERS-1. *Remote Sens. Environ.*, vol. 23, p. 117-129.

——— (1988) Spectral indices for vegetation and rock type discrimination using the optical sensor of the Japanese ERS-1. *Proceedings of the Sixth Thematic Conference on Remote Sensing for Exploration Geology*, Environmental Research Institute of Michigan, Ann Arbor, p. 159-168.

——— and Lyon, R.J.P. (1985) A comparative field study of spectroradiometers and radiometers as used in geologic mapping of a porphyry copper at Yerington, Nevada. *Proceedings of the Nineteenth International Symposium on Remote Sensing of Environment*, Environmental Research Institute of Michigan, Ann Arbor, p. 523-532.

——— and ——— (1986) Identification of clay minerals by feature coding of near-infrared spectra. *Proceedings of the Fifth Thematic Conference on Remote Sensing for Exploration Geology*, Environmental Research Institute of Michigan, Ann Arbor, p. 627-636.

———, Sato, I. and Ohkura, T. (1988) Development of a field radiometer as a ground truth equipment for the Japanese ERS-1. *Int. Archives Photogram. Remote Sens.*, Int. Soc. Photogram. Remote Sens., vol. 27, part B7, p. 718-727.

可視・近赤外域のリモートセンシングデータによる岩相識別

山口　靖

要　旨

リモートセンシングは，可視域からマイクロ波域の電磁波放射を用いた広域探査手法であり，その広域概観能力などのため，様々な応用分野において用いられている．近年のセンサー技術の進歩により，センサーの多バンド化が進行し，リモートセンシングによって地表物質の分光反射特性が得られるようになってきた．このため，こうしたスペクトル情報を用いた地表物質の識別・同定が可能となりつつあるが，このような多バンドデータからの効率的な岩相識別の手法は，まだ確立されていない．また，従来の多バンドデータの処理手法においては，主成分分析に代表されるように，数学的には意味のある処理結果が得られたとしても，その地質学的解釈がしばしば困難であることが問題点として挙げられる．

本研究では，可視・近赤外域 (0.4-2.5 μm) のリモートセンシングデータを用いて岩相識別を行う方法について検討を行った．まず，代表的な鉱物や岩石の可視・近赤外域における分光反射特性を測定し，それらから仮想的なセンサー応答を作り出した．そして，これらの仮想的センサー応答を用いて，岩相識別を効率的に行うためのデータ処理手法を新たに考察した．さらに，この手法を実際のリモートセンシングデータに適用し，手法の妥当性の評価を行った．従来の研究では，まずデータが存在し，そのデータをどのように処理するかが議論の中心となっている．本研究では，どのようなデータ処理を行うべきかを先に議論し，その結果を実際のデータに適用している．このようなアプローチによって，地質学的に解釈のしやすい結果を与えうるデータ処理手法を開発できることが示された．

まず，議論の基礎となる代表的な鉱物や岩石の分光反射スペクトルを得るために，測定機器である分光放射計の比較検討を行った．その結果，鉱物や岩石の反射スペクトルの詳細な検討のためには，回折格子を用いた高分解能の野外用分光放射計が適することがわかった．この分光放射計の測定波長範囲は 0.35-2.5 μm，スペクトル分解能は 0.35-1.0 μm で 2 nm，1.0-2.5 μm で 4 nm である．代表的な鉱物と岩石の分光反射率を測定し，各々に特徴的なスペクトル特徴を記載した．フィロ珪酸塩鉱物と炭酸塩鉱物は，それぞれ短波長赤外域 (1.3-2.5 μm) の 2.2 μm と 2.35 μm 付近で特徴的な吸収を示す．鉄酸化物鉱物は，0.4 と 1.0 μm 付近にブロードな吸収帯を持つ．これらの鉱物を多く含んだ岩石は，鉱物と同様の吸収特徴を示すが，十分な量を含まない岩石は，平坦で吸収特徴のない分光反射スペクトルを示す．植物は，近赤外域で高い反射率を示し，1.4 および 1.9 μm 付近に水による強い吸収帯を持つ．

こうした分光反射スペクトルのパターンから，試料中に含まれている鉱物の名前を自動的に推定する一種のエキスパートシステムの開発を行った．対象とした鉱物は，地質マッピングや鉱床探査において重要で，出現頻度も大きく，しかも可視・近赤外域において特徴的な吸収を示すフィロ珪酸塩鉱物と炭酸塩鉱物とした．これらの鉱物の標準試料の反射スペクトルから，意味のある吸収特徴を抽出し，波長位置と相対的な吸収強度に応じて16進数様の特徴コード化を行う．こうして得られたコードをデータファイルとして保管しておく．鉱物名の同定は，対象とする試料の反射スペクトルを特徴コード化し，そのコードをデータファイル中のコードと比較することによって行われる．実際のデータでのテスト結果によれば，肉眼によるパターンの認識，同定と同じ程度の結果が得られた．

リモートセンシングのデータとしてユーザに与えられるのは，DN (Digital Number) と呼ばれる値である．しかし，上記のように地表物質の物性値として得られるのは反射率である．従来のデータ処理手法は，DN 値の示す物理的意味を考えないで行うものがほとんどであり，処理結果に物理的（または地質学的）意味を持たせることが困難である原因のひとつとなっている．すなわち，データ処理の前段階として，DN 値を反射率に変換することが必要である．このため，NASAより提供を受けた AIS (Airborne Imaging Spectrometer) のデータを用いて，DN 値を反射率へ変換するための校正手法の検討を行った．対象とする画像範囲内において，十分な空間的広がりを持ち，スペクトル的に均質であるような適当な校正用標的が存在する場合には，その標的の分光反射率測定を現地において実施し，測定結果と DN 値との間の直線回帰を行うことによって，DN 値から反射率への変換係数を求めることができる．このような

反射率測定結果を用いない方法としては，対象範囲内においてひとつの地表タイプが卓越する場合には Least Upper Bound 法が，卓越しない場合には Log Residual 法が最も適している．これら2つの方法は，DN 値が反射率・地形効果・照射効果の3者の積で表されるとの仮定に基づき，各バンドと各ピクセルの幾何平均によって，各ピクセルの各バンドの DN 値をノーマライズするものである．

野外の校正用標的での反射スペクトル測定を効率化するために，新しい野外用分光放射計を開発した．この放射計はパルスモータによって自動的に回転されるフィルタホイールを2つ持ち，各ホイールには8個までのフィルタが装着可能である．各スペクトルバンドについて同一の測定視野を保証するため，測定開口部は1ヶ所のみとし，放射計内部で入射光を分割する方式とした．また，標準照度電球と光学ベンチを使用することにより，放射計の絶対エネルギ校正を行うこともできる．標準試料についての測定結果によれば，本放射計は十分に信頼に足る性能であることがわかった．

日本が1992年に打ち上げを計画している地球資源衛星 (ERS-1) の光学センサーを対象として，そのデータから岩相識別を効率的に行うためのデータ処理手法を考察した．ERS-1 のセンサーは現在製作中であり，実際の測定データは入手できないため，分光放射計で測定した代表的な鉱物や岩石の分光反射スペクトルから仮想的なセンサー応答を作り出し，それらを基にしてデータ処理手法を考察した．岩相識別のためには，短波長赤外域の3つのバンドを組み合わせた2つのスペクトル指標（明バン石指標と方解石指標）が有効である．これらの指標は，バンド間応答パターンの違いを定量化するものであり，各バンドの値の線形結合として計算される．また，同じ3バンドによる HSI カラー変換も，バンド間の応答パターンの違いを強調するのに有効である．

ひとつのピクセル内に植生が混合している場合には，まず 1.6 μm バンドも含めた短波長赤外域の4つのバンドによって，植生とフィロ珪酸塩鉱物または炭酸塩鉱物に由来する総吸収量を算出する．さらに，可視・近赤外域のバンドによって，ピクセル内の植生の占有比率を見積り，それを用いて総吸収量のうちで植生に由来する吸収量を差し引くことができる．植生の占有率の見積りには，2つのバンドの線形結合である直交植生指標が最も有効である．

仮想的なセンサ応答から考察したデータ処理手法について，その妥当性を評価するため，オーストラリア Geoscan 社の航空機 MSS (MultiSpectral Scanner) データに対して各手法を適用した．このスキャナは，ERS-1 の光学センサとよく似たバンド構成となっている．前処理として，DN 値を反射率に変換するために，画像上で選定された校正用標的の岩石を採取し，分光放射計で反射率を測定した．各標的の DN 値と反射率との直線回帰により，DN 値から反射率への変換係数を得た．しかし，変換前後の各バンドの DN 値の比較検討の結果，得られた変換係数は妥当ではないとの結論に達した．これは，校正用標的がスペクトル的に均質ではなく，測定された反射スペクトルが校正用標的のスペクトルを代表していないためである．このため，代わりに Log Residual 法を適用し，各バンドの DN 値を反射率に類似したバンド間応答パターンに変換した．

変換された DN 値を用いて，短波長赤外域の3つのバンドから明バン石指標と方解石指標，可視・近赤外域の2つのバンドから直交植生指標を求め，これらをカラー合成した．いっぽう，短波長赤外域の3つのバンドの DN 値に対する回帰直線を等反射率ラインと見なし，これを HSI 変換の I（明度）軸に割り当て，H（色相）と S（彩度）とを強調したカラー画像も作製した．これら2種類のカラー画像は，画像上に示された色が特定のバンド間応答パターンに対応している．さらに，前処理によって，バンド間応答パターンは分光反射率のパターンと類似したものとなっているため，各々の色の示す意味が明確である．すなわち，本研究によって開発されたデータ処理手法は，岩相識別に有効であり，地質学的に解釈のしやすい画像を提供できると結論される．

1 A field unit of the radiometer. An optical head on the tripod, a control unit (left), and a lap-top computer (bottom right) with a printer (bottom left).

2 The optical bench for calibration of the radiometer. The stabilized power supply (left), the officially calibrated irradiation standard lamp (center), and the standard reflection plate (right).

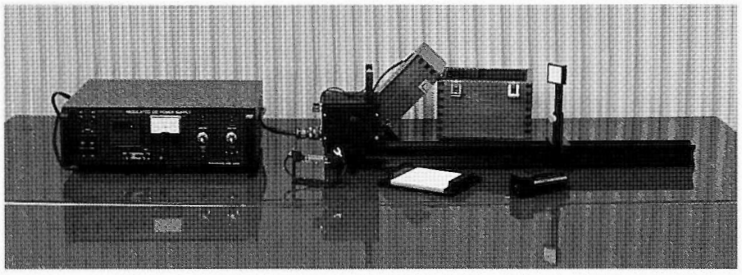

3 Typical landscape in the test area. Eucalyptus trees are the predominant vegetation.

1 A false color image with Band 2 as blue, Band 3 as green, and Band 4 as red. The image direction is NE (top) to SW (bottom) as shown in Fig. 67.

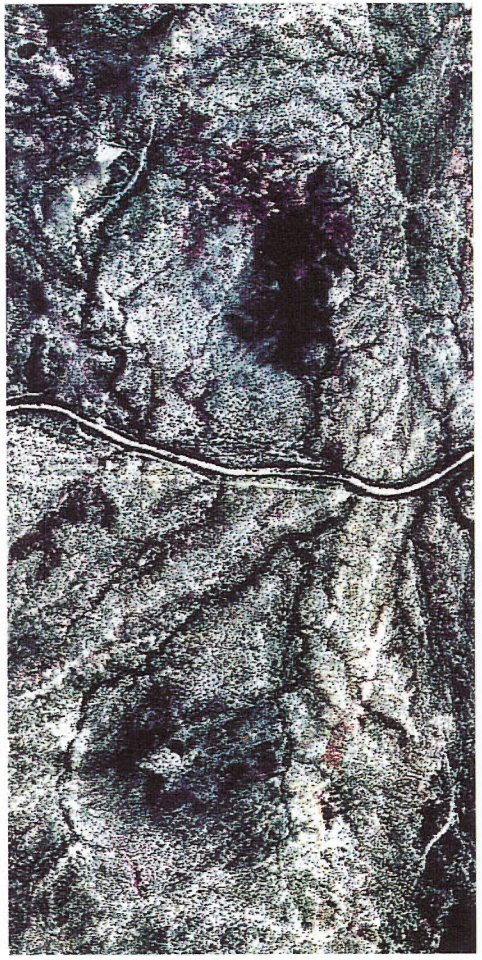

2 A color composite image with Band 6 as red, Band 7 as green, and Band 9 as blue. The image direction is NE (top) to SW (bottom) as shown in Fig. 67.

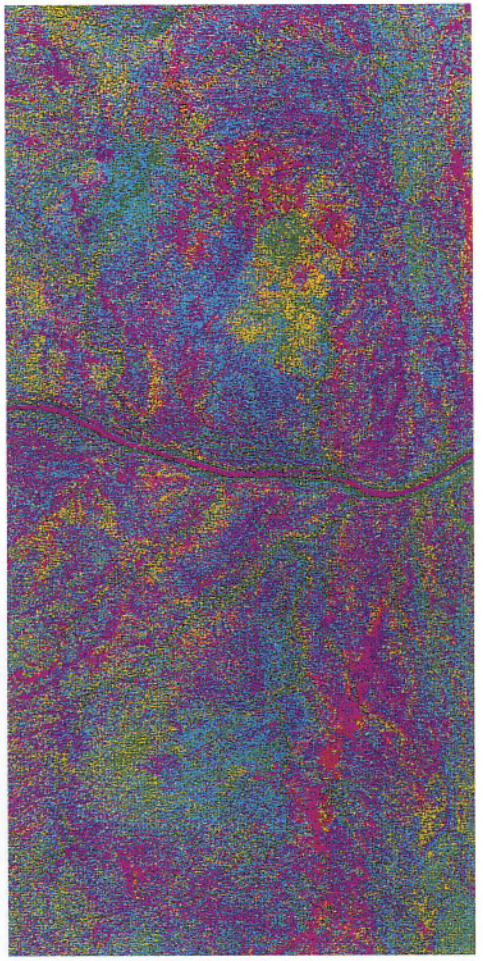

3 A color composite image with the log residual of Band 6 as red, the log residual of Band 7 as green, and the log residual of Band 9 as blue. The image direction is NE (top) to SW (bottom) as shown in Fig. 67.

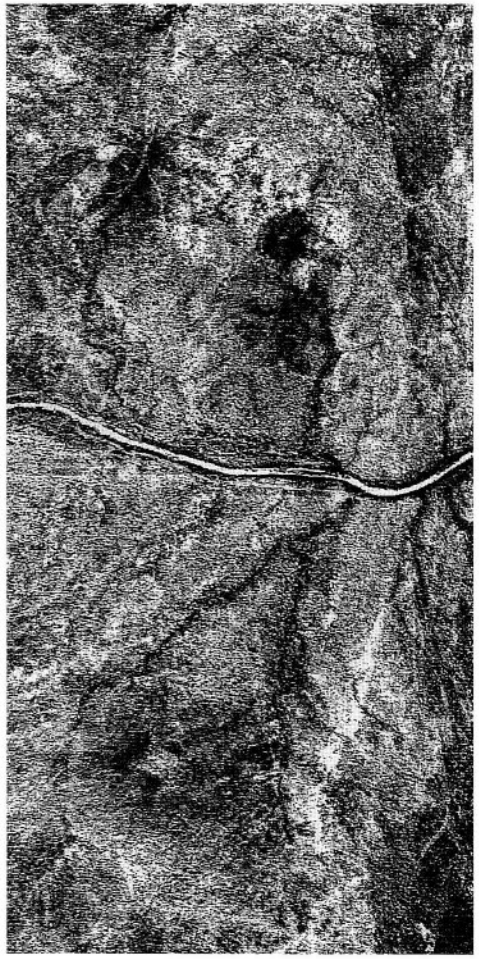

1 The Alunite Index image calculated using Bands 6, 7, and 9. The image direction is NE (top) to SW (bottom) as shown in Fig. 67.

2 The Calcite Index image calculated using Bands 6, 7, and 9. The image direction is NE (top) to SW (bottom) as shown in Fig. 67.

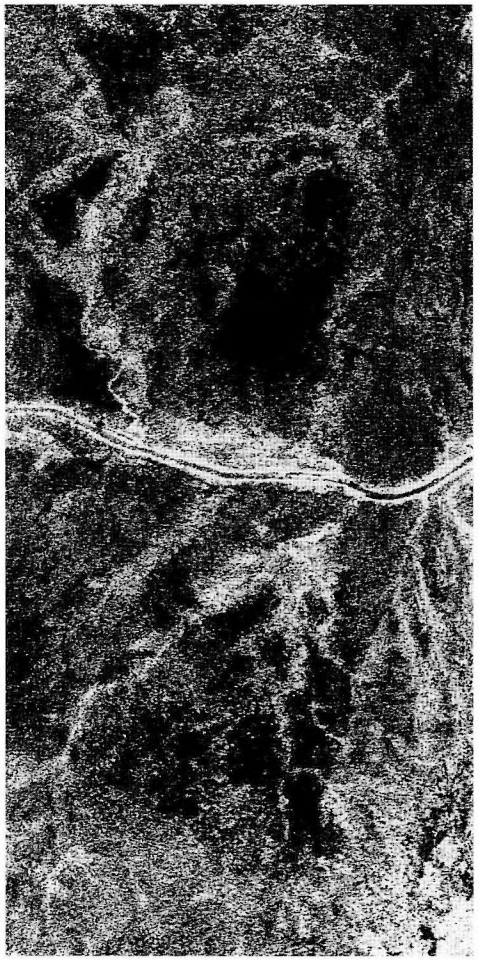

3 The Perpendicular Vegetation Index image calculated using Bands 3 and 4. The image direction is NE (top) to SW (bottom) as shown in Fig. 67.

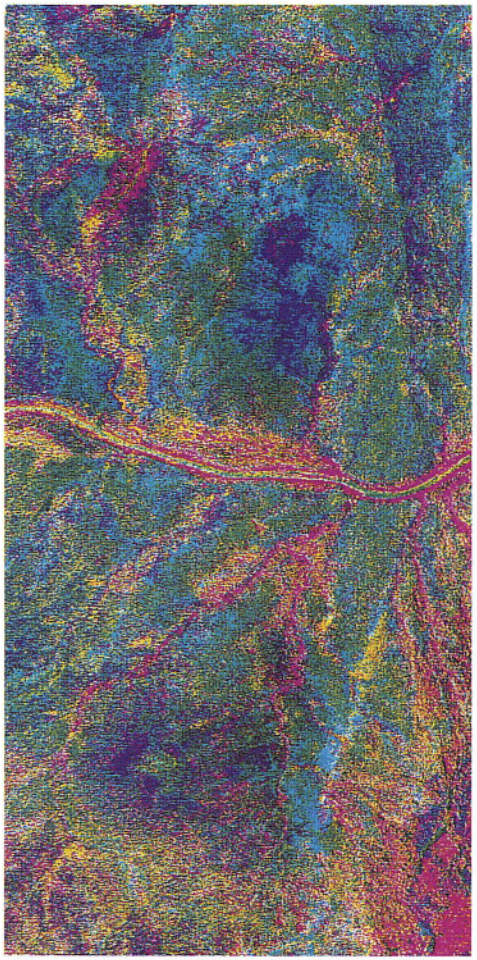

1 A color composite image with the Alunite Index as blue, the Calcite Index as green, the Perpendicular Vegetation Index as red. The image direction is NE (top) to SW (bottom) as shown in Fig. 67.

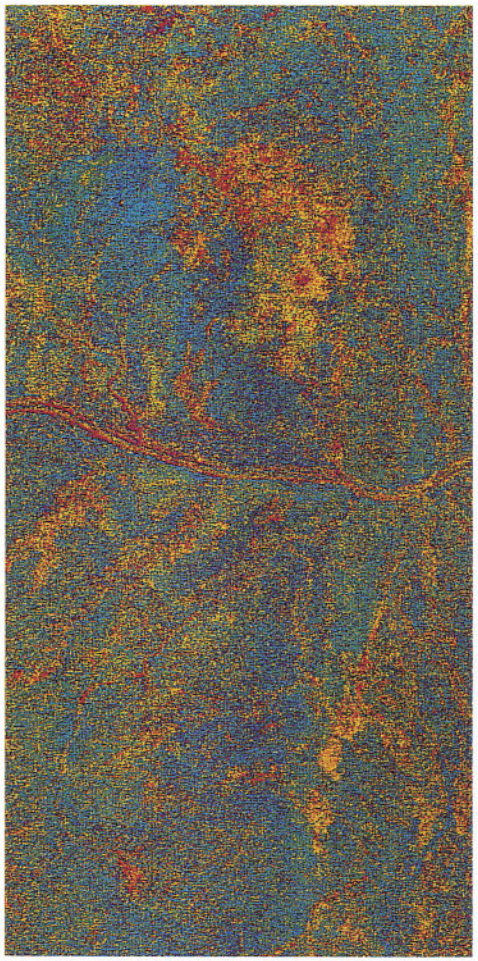

2 The HSI color image calculated using the raw data of Bands 6, 7, and 8. The image direction is NE (top) to SW (bottom) as shown in Fig. 67.

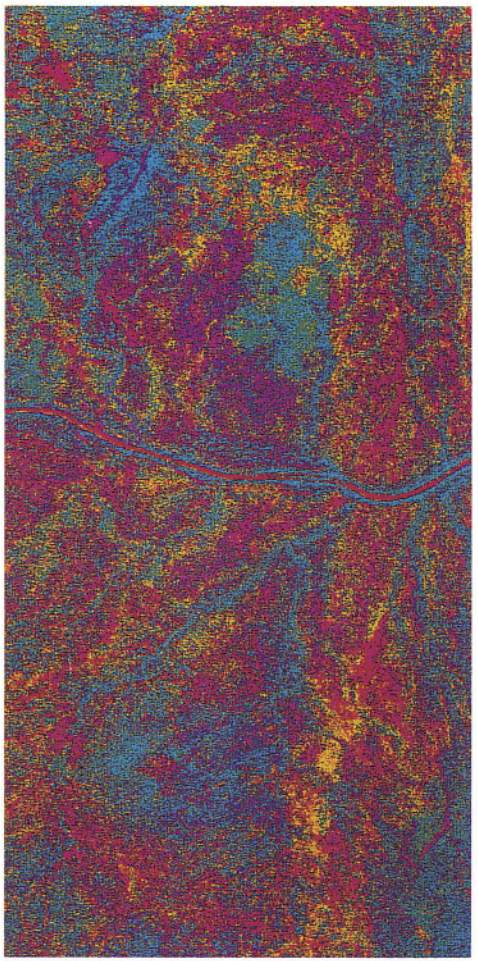

3 The HSI color image calculated using the log residuals of Bands 6, 7, and 8. The image direction is NE (top) to SW (bottom) as shown in Fig. 67.

地質調査所報告第278号，p.133-144, 1992
Rept. Geol. Surv. Japan, No.278

シミュレーションデータによるJERS-1光学センサの岩石識別のためのバンド組合せ

佐　藤　　功*

Band combinations for rock discrimination based on the computer-simulated JERS-1 optical sensor data

By

Isao SATO

Abstract: Computer-simulated data are used to evaluate the band combinations of the optical sensor (OPS) carried on JERS-1 for the purpose of rock discrimination as a pre-launch evaluation. Stepwise discriminant analysis based on the computer simulated data are used to select the optimum band combination for rock and mineral discrimination. The results of the discriminant analysis are as follows:

(1) Bands 2 and 3 of the OPS are effective to delineate vegetated regions.

(2) The short-wavelength infrared bands (bands 7,8,6, and 5 in order) of the OPS effectively contribute to discriminate non-altered rocks, various altered rocks, and carbonate rocks.

(3) The OPS has high capability to extract the carbonates- and alunite-rich rock regions.

The results will be a guidline of the optimum band selection for the purpose of rock discrimination and also should be practically verified by real JERS-1's OPS images acquired during the data verification and/or operational period.

要　旨

JERS-1衛星に搭載される光学センサ(OPS)の各観測バンドについて，岩石識別の立場からどのようなバンド組合せが一般的に適当であるかを，実験室で測定した種々の岩石・鉱物の反射係数データを基に計算機シミュレーションした観測DN値データを用い，段階的判別解析により検討した．この結果から，OPSの観測バンド2および3は植生の抽出に効果的であること，短波長赤外域の全観測バンド5～8が炭酸塩岩，種々の変質鉱物および非変質岩の区別に役立つこと，そして炭酸塩岩と明バン石の識別に高いポテンシャルを有していることを示した．

*地殻物理部

Keywords: Japanese Earth Resources Satellite-1, the Optical Sensor (OPS), band combination, rock discrimination, computer simulation, sensor response, stepwise discriminant analysis, LOWTRAN-5 code, reflectance factor

1. はじめに

わが国が1992年2月に打ち上げ予定の地球資源衛星 (JERS-1: Japanese Earth Resources Satellite-1) に搭載される光学センサ (OPS と呼称) は，可視・近赤外領域および短波長赤外領域での中心波長の異なる7つの観測バンドで地球表面を観測することができる．なお，OPS は立体視用のバンド4 (バンド3と同じ波長域) を含めて，全部で8つの観測バンドを有している．第1表に JERS-1 衛星の主要な諸元を，第2表に OPS の各観測バンドの仕様等を示す．LANDSAT の TM (Thematic Mapper) センサと比較すると，JERS-1 の OPS の特徴は一般に地質応用分野において関心の高い短波長赤外領域のバンド数が，TM の2バンドに対し，4バンドに増えていることである．このため短波長赤外領域の反射係数において特徴的な吸収を示す炭酸塩岩や変質鉱物を含む岩石などの識別能力の向上に期待が寄せられている．一般にセンサ設計段階でその主たる観測目的によって観測バンドの設定が行なわれる．その場合には，過去の類似のセンサにおける利用経験や対象物の反射スペクトル特性などに関する研究結果を参考にしつつ，航空機センサや計算機によるシミュレーションデータの評価によって具体的な観測バンドの仕様が決められることになる．このようなシミュレーションデータとしては航空機センサによるシミュレーションデータが実際的で有効であるが，識別したい岩石等が分布しているなど検討に適切な候補地が見つかっても，かなりのデータ取得費用がかかるという欠点がある．そこで，計算機によるシミュレーションデータが頻繁に利用されることになる．ここでは後者の検討方法を採用した．本報告では OPS の立体視用のバンド4を除く各バンドの事前評価の一環として，実験室で測定した種々の岩石・鉱物などの反射率データを使用して，OPS の各バンドでの観測データである DN値を計算機により

第 1 表　地球資源探査衛星 (JERS-1) の主要な諸元
Table 1　Major specification of the Japanese Earth Resources Satellite-1 (JERS-1).

軌道	太陽同期準回帰軌道
衛星高度	約５７０ｋｍ
軌道傾斜角	約９８度
回帰日数	４４日
降交点通過時刻	午前１０時３０分頃
走査幅	７５ｋｍ
設計寿命	約２年

第 2 表　光学センサ (OPS) の観測バンドの仕様
観測バンドのバンド帯域および中心波長は μm で示す．
Table 2　Observation bands specification of the optical sensor (OPS).
The bandpass and center wavelength of the observation band are shown in micrometer.

バンド番号	バンド帯域	中心波長	バンド幅
1	0.52-0.60	0.56	80ｎｍ
2	0.63-0.69	0.66	60ｎｍ
3	0.76-0.86	0.81	100ｎｍ
4	0.76-0.86	0.81	100ｎｍ
5	1.60-1.71	1.655	110ｎｍ
6	2.01-2.12	2.065	110ｎｍ
7	2.13-2.25	2.19	120ｎｍ
8	2.27-2.40	2.335	130ｎｍ
地表分解能	約１８ｍ・２４ｍ		
量子化ビット数	6 bits		

シミュレーションし，岩石識別のためにどのようなバンド組合せが適切であるかを段階的判別解析によって検討した結果を述べる．

2. センサ応答について

一般に地質応用では衛星画像データを処理し，その処理後のフォールスカラー画像を地質判読することによって地表の岩石識別が行なわれている．その場合異なる3つの観測バンドでの対象物ごとの DN 値のパターンの違いから生じるフォールスカラー画像の色相や色彩の違いを解析者が認識することで対象物を識別している．したがって画像による物質の識別能力を向上させるには，DN値そのものによる物質の識別能力を上げる必要があり，物質の識別が容易になるような複数の波長帯域で物質を観測することになる．これまでに利用されてきている衛星画像ではこのような観点から識別しようとする物質の反射スペクトル特徴を基に観測波長帯域，すなわち観測バンドが適切に選択されてきている．このように

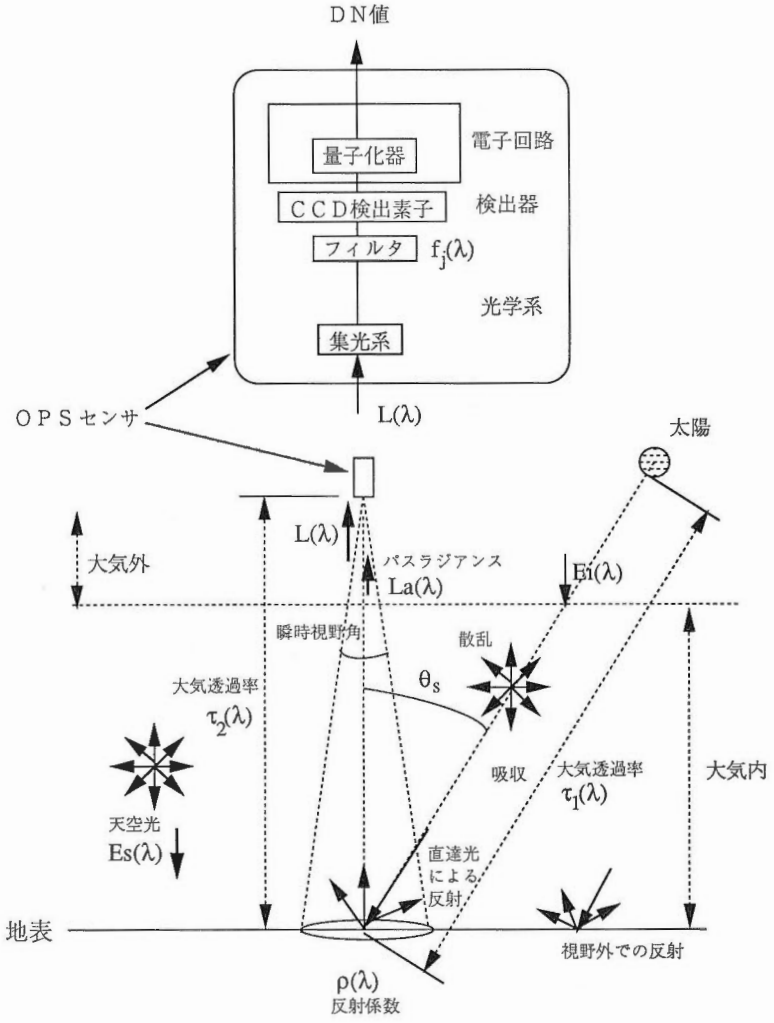

第 1 図　光学センサの DN 値出力が得られるプロセスの概念図
Fig. 1　Conceptual Diagram of the process to output DN values from a optical sensor.

して選んだ観測バンドの数を増やせば，それだけ多くの物質を識別しやすくなると言える．しかしながら，センサの開発技術の制約，衛星の搭載重量や容積等の制約等のために観測バンドを無制限に増やすことは困難である．そこで観測バンドの選択が適切に行なわれなければならない．JERS-1 の OPS の観測バンドについても，過去の様々な物質のスペクトル特性に関する研究やこれまでの他のセンサデータの利用経験を反映して具体的な観測バンドが決められてきたが，その観測バンドの識別能力の評価は様々な観測条件，識別対象に応じて種々の方法によって実施すべきである．本研究では様々な岩石・鉱物の反射スペクトルデータから JERS-1 光学センサの各観測バンドでの DN値を計算機によってシミュレーションし，得られた DN値データのもつ岩石・鉱物の識別能力の検討を行なった．

光学センサのセンサ応答である DN値出力が得られるまでのプロセスは，以下のように考えられる(第1図)．太陽からの光は地球大気を通過して地表へ到達する．この間に太陽光は地球大気中で大気を構成している水蒸気，二酸化炭素，オゾン，微量ガスなどの成分によって，一部のエネルギーが吸収され，また大気分子や大気中に浮遊しているエアロゾル等によって散乱される．大気中で散乱された光のうち地表へ向かう成分 (天空光) および地表へ直接達した太陽光によって地表面の物質が照射されると，物質の組成や表面形状，水分量等で決まる反射率特性に従って，太陽および大気からの照射光はその一部が反射光となって地表上の半球全体に広がる．衛星から直下の地球表面を観測している光学センサは，物質表面で反射され，再び地球大気で吸収および散乱されてセンサまで到達してきた光をセンサの光学系によって定まった立体角で集光し，検出部へと導く．この集光された光には太陽光が地表で反射されずに大気中で散乱されただけのものもあり，また必ずしも視野内にない周辺領域の地表で太陽光が反射されたものが大気中で散乱したものもある．このようにセンサ方向へ向かう大気中で散乱された成分をパスラジアンスという．センサの検出部では CCD (Charge Coupled Device) 検出素子が直線状に配置されており，その素子表面には観測バンドの仕様で決められたフィルタが接着されている．フィルタはセンサの光学系へ入射してきた光のうち観測バンド帯域の光のみを検出素子へ通過させる．そしてフィルタを通過した光は検出素子によって光電変換されてアナログ電気信号となる．この入射フォトンの数と検出素子の変換効率等によって決まるアナログ電気信号はセンサの信号処理部で量子化されて，ディジタル値へ変換され観測データである DN値となる．

以上のようなプロセスを厳密にモデル化することができれば観測される DN値を正確に計算することが可能になる．しかし，大気や地表の状態は非常に変化に富んでいて厳密なモデル作成は困難であるので，それらの標準的なモデルを用い，さらに OPS の DN値シミュレーションを簡便化するためにいくつかの仮定を設けた．

センサの光学系入口での上向き分光放射輝度 $L(\lambda)$ は，地表が完全拡散反射特性をもつとすると，以下のように定式化される．

$$L(\lambda) = (1/\pi) \cdot [Ei(\lambda) \cdot \tau_1(\lambda) \cdot \cos(\theta s) + Es(\lambda)] \cdot \rho(\lambda) \cdot \tau_2(\lambda) + La(\lambda)$$

ただし，

$L(\lambda)$ ：センサの望遠鏡入口での上向き分光放射輝度 ($W/cm^2/sr/\mu m$)
$Ei(\lambda)$ ：大気の外側での太陽からの分光放射照度 ($W/cm^2/\mu m$)
$Es(\lambda)$ ：天空光による分光放射照度 ($W/cm^2/\mu m$)
$La(\lambda)$ ：パスラジアンス ($W/cm^2/sr/\mu m$)
$\tau_1(\lambda)$ ：大気の透過率 (太陽-地表間)
$\tau_2(\lambda)$ ：大気の透過率 (地表-センサ間)
$\rho(\lambda)$ ：地表物質の分光反射係数
θs ：太陽の天頂角

$L(\lambda)$ がセンサ直下の瞬時視野 (IFOV) 内の地表にある物質で太陽直達光の反射した成分のみで決まり，天空光やパスラジアンスによる成分は無視できると仮定すると，上式は

$$L(\lambda) = (1/\pi) \cdot Ei(\lambda) \cdot \tau_T(\lambda) \cdot \rho(\lambda) \cdot \cos(\theta s)$$

ただし，

$\tau_T(\lambda)$：太陽の直達光の全行程（太陽-地表-センサ間）での透過率

すなわち，$\tau_T(\lambda) = \tau_1(\lambda) \cdot \tau_2(\lambda)$

となる．

センサに入射した光が DN値に変換される過程において種々の雑音成分（検出器や電子回路による電子雑音，量子化雑音など）が付加されるが，ここではこれらの雑音は無視する．また検出器の光電変換効率は理想的に 1.0 であるとする．さらに，実フィルタはガウス分布のような形状をして，その半値でバンド帯域が規定されているが，計算を簡単化するためフィルタの形状は観測バンドの帯域での理想的な矩形フィルタであるとする．ただし，フィルタや光学系の透過率によってバンド毎に入射光に対する減衰が異なるので各観測バンド間の相対通過強度は考慮に入れた．そして，検出器のダイナミックレンジ（実際の試験データは未だ利用できないので，第 3 表に示した高入力レベルの場合の最大分光放射輝度の設計値を使用）の範囲内で，検出器出力のアナログ信号を線形に 6bits に量子化する．以上から，あるバンド j でのセンサ応答である DN_j 値は以下のように計算できる．

$$DN_j = F_q(R_j, p)$$

ただし，

$$R_j = \left(\int f_j(\lambda) \cdot Ei(\lambda) \cdot \tau_T(\lambda) \cdot \rho(\lambda) \cdot \cos(\theta s) \cdot d\lambda\right) / \left(\pi \cdot \int H_{0j} \cdot d\lambda\right)$$

ここで，

$f_j(\lambda)$　：OPS センサのバンド j のフィルタ関数

ただし，矩形フィルタと仮定し，その強度はフィルタや光学系の透過率に依存している．

H_{0j}　：OPS センサのバンド j における最大分光放射輝度の設計値

$F_q(x,p)$：量子化関数で，次式のように p ビットで x を量子化する．OPS では p=6 である．

$$F_q(x,p) = \begin{cases} 2^p & x \geqq 1 \\ \mathrm{INT}(x \cdot 2^p) & 0 \leqq x \leqq 1 \\ 0 & x \leqq 0 \end{cases}$$

なお，INT (v) 関数は実数値 v を整数化するものである．

第 3 表　OPS の各観測バンドでの最大分光放射輝度（高入力レベルでの設計値）

Table 3　Maximum spectral radiance (design value in the case of the High Level Input mode) for each observation band of the OPS.

バンド番号	最大分光放射輝度
1	324
2	250
3	248
4	239
5	33.3
6	17.8
7	13.7
8	10.8

単位：W／cm^2／sr／μm

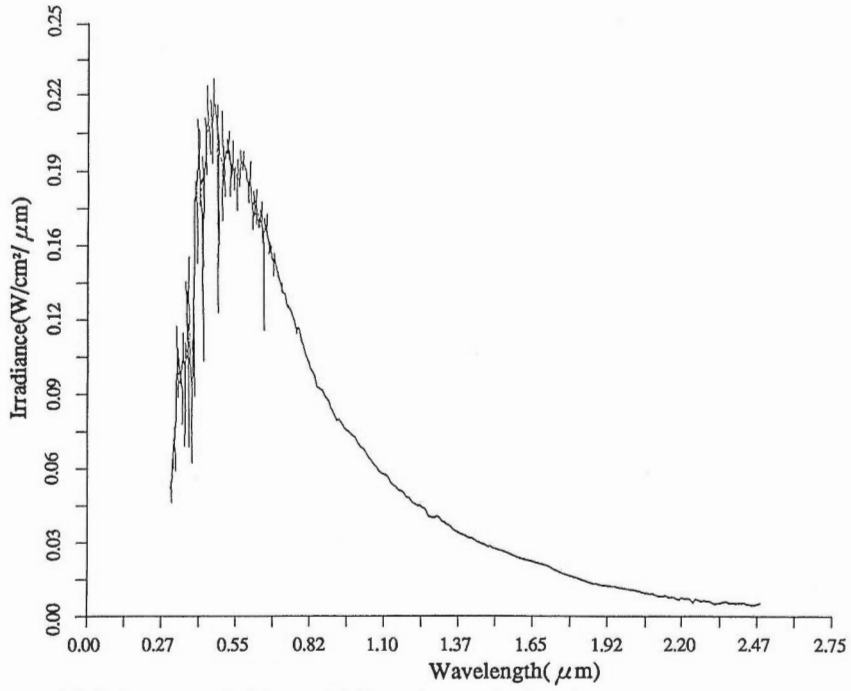

第 2 図　航空機実験データから推定された大気外での太陽の分光放射照度 (Arvesen *et al.*,1969)
Fig. 2　Extraterrestrial solar spectral irradiance, which is estimated by aircraft experimental data (Arvesen *et al.*,1969).

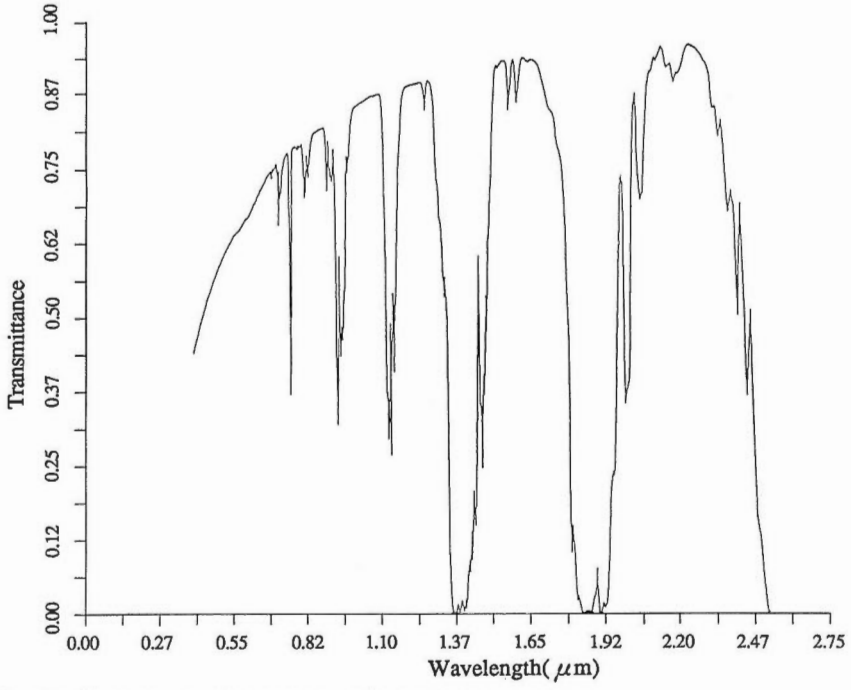

第 3 図　LOWTRAN-5 で模擬した地表-センサ間の行程での大気の透過率
(注：視程 23km での 1962 米国標準大気 (春-夏) モデルを透過率計算に用いた．センサ高度は 570km である．)
Fig. 3　Atmospheric transmittance of the path between the earth surface and the sensor, which is estimated by LOWTRAN-5 code. (Note: 1962 U.S. standard Spring-Summer model atmosphere with 23km visibility is applied in the transmittance calculation. The sensor altitude is 570km.)

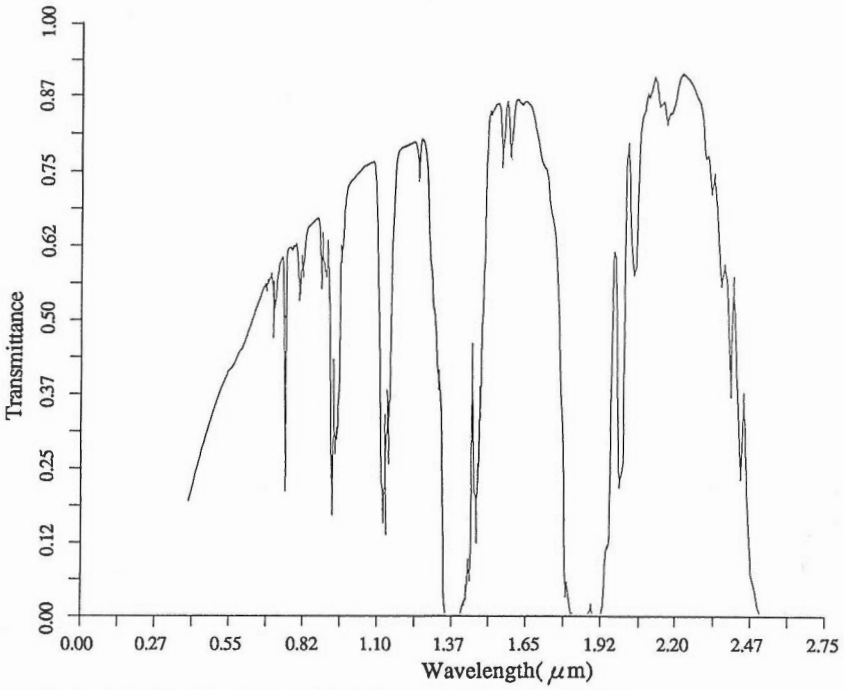

第 4 図　LOWTRAN-5 で模擬した太陽-地表間の行程での大気の透過率
（注：視程 23km での 1962 米国標準大気（春-夏）モデルを透過率計算に用いた．太陽天頂角は 60度とした．）

Fig. 4　Atmospheric transmittance of the path between the sun and the earth surface, which is estimated by LOWTRAN-5 code.
(Note: 1962 U.S. standard Spring-Summer model atmosphere with 23km visibility is applied in the transmittance calculation. The solar zenith angle is assumed to be 60 degrees.)

上記の計算式に基づいて，OPS の 7 つの異なる観測バンドについて，高分解能スペクトロメータで測定した種々の対象物の分光反射係数データを用いて，太陽高度としてはやや低目である太陽天頂角が60度の場合のセンサ応答である DN値を計算した．実際には太陽天頂角としてはもっと小さくなる場合が多く，この時には DN値は大きくなると予想される．同時に地表の僅かな反射係数の違いが量子化した後も区別されるので，識別能力も上がると考えられる．したがって太陽天頂角が 60 度の場合は条件としては少しばかり悪いと言える．なお，観測バンド幅があまり狭くないので，数値積分は 10nm ステップで行なった．また，透過率の計算には LOWTRAN-5 (Kneizys *et al.*, 1980) を用いた．この時の大気モデルは 1962 年米国標準大気モデル（春-夏）で，視程が 23km 以上の晴天時のものとした．第 2 図は計算に用いた大気の外側での太陽による分光放射照度 (Arvesen *et al.*, 1969) を，第 3 図は高度 570km にある OPS センサと地表間での大気の透過率の計算値を，第 4 図は太陽-地表間での大気の透過率の計算値を示す．

3. 対象物質の種類とその分光反射係数と各観測バンドとの関係

地表物質として検討の対象とした岩石および鉱物は，第 4 表に示すようにカテゴリ別に炭酸塩岩類 (CAR; 主に石灰岩，その他として苦灰質石灰岩，苦灰岩，大理石)，変質鉱物であるカオリナイト (KAO)，絹雲母 (SER)，パイロフィライト (PYR)，明バン石 (ALU)，モンモリロナイト (MON)，そして非変質岩 (UAL; 安山岩，玄武岩，砂岩，レキなど) である．炭酸塩岩と変質鉱物を主たる対象にしたのは，OPS の短波長赤外域での観測バンドがこれらの岩石・鉱物における特徴的な吸収波長の存在するところと対応しているためである．また，地表は植生で被覆されていることも考慮して，識別の対象には

第 4 表　段階的判別解析に用いた対象物のカテゴリーコード，その名称およびサンプル数の一覧表

Table 4　The list of category codes, their names and the number of samples for each category used in the stepwise discriminant analysis.

コード	カテゴリ名称	サンプル数
VEG	green vegetation	6
UAL	unaltered rocks	16
CAR	carbonate rocks	39
KAO	kaolinite	36
MON	montmorillonite	10
ALU	alunite	8
SER	sericite	18
PYR	pyrophyllite	13
TOTAL		146

植物 (VEG; 芝など) も加えた．なお，これらの対象を各カテゴリごとに括弧内で記述したコードによって示すことにする．

第 4 表に示したようにサンプル数は各カテゴリ毎に均等にできなかったが，統計的に解析するのでできる限り多くのサンプル数になるようにした．使用したサンプル数は全部で 146 個である．ただし，後述する段階的判別解析における識別対象とするカテゴリの組合せによっては約 100 個程度になっていることもある．

各カテゴリ内の代表的な対象物の分光反射係数データを第 5 図に示す．ここで用いた分光反射係数は硫酸バリウムを塗布した標準白色板に対する相対的な二方向反射係数である．なお，第4図では分光反射係数データを見やすくするためにデータが重ならないように縦軸方向にシフトさせている．分光反射係数データの特徴と OPS の各観測バンドとの概略の関係は次のようになる．炭酸塩岩類では炭酸基 (CO_3^{2-}) を含み，2.34 μm 付近にこの炭酸基による吸収がある．この吸収位置はバンド 8 と対応している．一方，変質鉱物は水酸基 (OH^-) を含み，2.2 μm 付近にその吸収があり，バンド7と対応している．バンド 5 はこれらの岩石や鉱物などで吸収のない波長領域にあり，そのためにレファレンスとしての役割を果たすことが期待される．また，植生は可視から近赤外域へ向けての反射率の急激な立ち上がりに特徴がある．バンド 1 は植生の反射係数データにおける 550nm を中心とする“グリーンヒル”に，バンド 2 は 640nm および 680nm 付近のクロロフィル吸収に，バンド 3 と 4 は 750nm 以上の近赤外域での高反射率領域の肩部に対応している．

4. 岩石識別のためのバンド組合せ

OPS の 7 つの観測バンドにより可能なバンド組合せのうち，種々の地表物質の分布状況によってそれらを識別するための最適なバンド組合せが異なることが予想される．特に，識別対象として植生がある場合と植生がない場合では，3 バンドによるカラー画像表示を考えた時，植生と岩石との区別のためにバンド組合せが異なることは LANDSAT 画像による経験から明らかである．したがって，植生が含まれる場合と植生のない露岩地域の場合を考慮するとともに，さらに炭酸塩岩が含まれない場合や変質鉱物を 1 つのカテゴリにまとめた場合も含めて全部で 6 つの識別対象カテゴリ組合せの場合を想定して，それぞれの場合ごとに 3 つの観測バンドの最適な組合せを検討した．すなわち，各々の場合ごとに OPS の 7 つの観測バンドでの DN値データ群の中から，各対象カテゴリを区分するために最も効果がある観測バンドのものを順次選択して，上位 3 つの観測バンドのものを決めればよい．これには判別解析を用いることができる (井上，1983)．用いた判別解析ソフトウェアとしては，工業技術院研究情報センターにある段階的判別解析 (stepwise discriminant analysis) ソフトウェアである BMDP7M を使用した．

BMDP7M ではマハラノビスの汎距離に基づく線形な分類関数の計算に用いられる判別変数を段階的に選択する．また，判別変数の増減選択も可能で，マハラノビスの汎距離に基づきグループ間の差をテストする量である F値によってその増減をコントロールしている．

第5表は6つの識別対象カテゴリ組合せの各場合での判別解析の結果を示したもので，それぞれの場合に対応する各カテゴリを区分するために優先的に選択された上位3つの観測バンドとその時の各カテゴリの判別正答率を示したものである．なお，判別解析の各カテゴリでの判別正答率は用いたそのサンプルの数に依存し，サンプル数が多いほど判別正答率は細かく把握できる．したがって，各カテゴリごとのサンプル数が n 個であれば，100/n (%) の刻みで判別正答率が計算されるので，判別正答率の値から期待されるカテゴリに適切に区別されたサンプル数も把握できる．

植生を含む場合は，バンド2，3，および7が総合的に各カテゴリの識別能力が高い．この結果から，

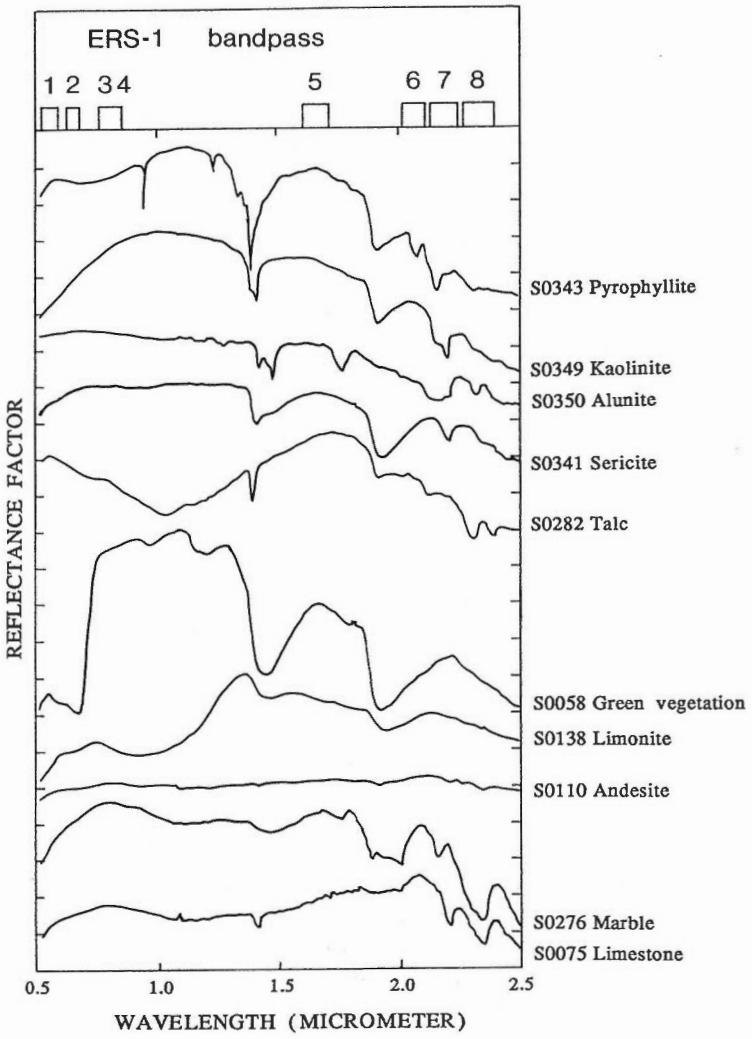

第 5 図　各カテゴリ内の代表的な対象物の分光反射係数データ
(8つの OPS 観測バンドを図の上部に示す.)

Fig. 5　Spectral reflectance factors for typical targets in the categories used.
(The eight OPS's bandpasses are shown in the upper part.)

第 5 表　6つの場合での段階的判別解析の結果(3バンド選択の場合)
第1欄には解析によって順次選択された3つの観測バンドを示す．各カテゴリでの正答率を次の欄に示す．

Table 5　The result of the stepwise discriminant analysis (in the case of three bands selection) in the six cases.
The first coloum shows the selected three observation bands in order by the analysis. The values

SELECTED BANDS IN ORDER	PERCENT CORRECT (%) CATEGORY CODE								
	VEG	UAL	CAR	KAO	MON	ALU	SER	PYR	TOTAL
2,3,7	100.0	100.0	56.4	47.2	20.0	50.0	61.1	69.2	59.6
2,3,7	100.0	100.0	----	47.2	50.0	50.0	38.9	69.2	59.8
2,3,7	100.0	100.0	76.9	<----------		85.9	----------	---->	85.6
2,7,8	-----	100.0	74.4	80.6	50.0	75.0	27.8	61.5	70.0
2,7,8	-----	100.0	----	77.8	60.0	75.0	44.4	61.5	71.3
1,7,8	-----	100.0	84.6	<----------		88.2	----------	---->	88.6

バンド2と3とによってまず植生が岩石と区別され，そしてバンド7で非変質岩とバンド7に吸収のある変質鉱物とを区別するためと考えられる．バンド2および3が植生を識別するのに必要であるという結果はクロロフィル吸収に対応するバンド2と植物特有の近赤外域の急激な反射係数の立ち上がりに対応するバンド3との2つのセンサ応答の傾斜パターンが植生の抽出に寄与しているものと考えられる．これについては岩石では非変質岩や変質鉱物はバンド2と3の DN値は比較的低い時も高い時もあるが，そのバンド比は植物のようには大きくはならないことによると考えられる．

植生がない場合は，バンド2(またはバンド1)，7，そして8が順次選択された．また，非変質岩，炭酸塩岩類そして変質鉱物の3つのカテゴリだけの場合は，バンド1, 7および8となった．非変質岩と種々の変質鉱物だけで，炭酸塩岩類が含まれない場合は，バンド2，7および8となった．この場合のバンド1あるいはバンド2のどちらが選択されるかはその理由は明らかではない．ここで疑問になる点はレファレンスとなるバンド5あるいは変質鉱物の識別のために有効であると考えられるバンド6を含む3つのバンド組み合わせが選択されていないことである．そこで段階的判別解析を途中で終了せずに最後まで進めることにした．第6表に3つの観測バンドに限定しない場合の結果を示す．第6表から植生を含まない場合に注目すると，変質鉱物を細分しない場合には結果が少し違っているが，変質鉱物を細分する場合には，バンド2，7，8，6，5の順に選択され，次のステップではバンド2が除かれた．これは，非変質岩，種々の変質鉱物そして炭酸塩岩類を識別する場合，観測バンドの必要度が高い順にバン

第 6 表　6つの場合での段階的判別解析の詳細な結果
第1欄には解析によって順次選択された3つの観測バンドを示す．各カテゴリでの正答率を次の欄に示す．

Table 6　The detail result of the stepwise discriminant analysis in the six cases.
The first coloum shows the selected observation bands in order by the analysis. The values of percent correct for each category are shown in the next.

SELECTED BANDS IN ORDER	PERCENT CORRECT (%) CATEGORY CODE								
	VEG	UAL	CAR	KAO	MON	ALU	SER	PYR	TOTAL
2,3,7,8,6,5	100.0	100.0	84.6	75.0	80.0	75.0	72.2	69.2	80.8
2,3,7,8,6,5	100.0	100.0	----	72.2	80.0	87.5	77.8	84.6	82.2
2,3,7,8,5,1	100.0	100.0	87.2	<----------		83.5	----------	---->	87.0
2,7,8,6,5,-2	-----	100.0	76.9	72.2	80.0	75.0	50.0	61.5	73.6
2,7,8,6,5,-2	-----	100.0	----	66.7	80.0	87.5	55.6	76.9	74.3
1,7,8,5,6	-----	100.0	89.7	<----------		91.8	----------	---->	92.1

ド7，8，6，5となること，すなわち OPS の短波長赤外領域の全観測バンドが有効であることを示している．このことはこれらの観測バンドの異なる3種類の比を利用することで，バンド比を利用しない場合よりも識別が良くなることをも示唆していると言える．

また判別解析の結果から，明バン石と炭酸塩岩はその他のカテゴリに比較して短波長赤外域の観測バンドによって個別的にかなり良く識別できると予想される．これについては，Yamaguchi (1988) が明バン石および方解石の識別指標としてそれぞれ ALI (Alunite Index) および CLI (Calcite Index) をバンド6，7，8の線形結合式で提案していることと一致する．また，非変質岩と変質鉱物を含む岩石との識別は可能であると判断されるが，変質鉱物のうちのカオリナイト，モンモリロナイト，絹雲母，パイロフィライトについては，これらを個々に識別することは容易ではないと考えられる．

5. おわりに

JERS-1 の光学センサである OPS の各観測バンドについて，岩石識別の立場からどのようなバンド組合せが一般的に適当であるかを，種々の岩石・鉱物および植物の分光反射係数データから計算機シミュレーションした DN値を用い，段階的判別解析により検討した．その結果から，(1) 植生の識別には OPS の観測バンド2および3が有効であること，(2) 非変質岩，個々の変質鉱物，炭酸塩岩の識別には OPS の短波長赤外領域の全観測バンドがバンド7，8，6，そして5の順に効果的に寄与していること，(3) 特に，炭酸塩岩と明バン石の識別には OPS は高いポテンシャルを有していることを示した．

これらの結果は OPS データによる岩石識別において最適な観測バンドを選択する時のガイドラインとして利用可能であると考えられる．しかし，本シミュレーションでは，天空光やパスラジアンス成分およびセンサ雑音などを無視していること，大気の状態が現実には様々であること，特にパスラジアンス成分は大気の状態や観測バンドによる違いもあり，加算的に可視～近赤外領域の DN値に大きく影響することなどの理由から，OPS センサの観測バンドの岩石識別性能の詳細な把握には実観測データによる評価が必要である．

OPS の実観測画像データによる岩石識別では，識別のプロセスを2段階にして，まず植生をバンド2，3により分離し，次に植生以外の露岩領域をバンド7，8および6で非変質岩，変質鉱物，炭酸塩岩類などを区分する手法が適切であると考えられる．

また，本研究では検討していないが，バンド比を組み合わせることにより，これらの相互区分がさらに良くなる（横山ほか，1988）と考えられる．

謝　辞

岩石や鉱物などの反射率データは地質調査所浦井　稔氏および山口　靖氏が測定されたものを主に使用させて頂いた．記して感謝致します．

文　献

Arvesen, J.C., Griffin, R. N. Jr. and Pearson, B.D. Jr. (1969)　Determination of Extraterrestrial Solar Spectral Irradiance from a Research Aircraft. *Applied Optics*, vol.8, no.11, p.2215-2232.

井上大栄 (1983)　リモートセンシングによる岩石分類の試み―可視・近赤外センサーによる変質帯抽出の可能性―．電力中央研究所報告，833032, p.1-28.

Kneizys, F.X. *et al*. (1980)　Atmospheric Transmittance/Radiance: Computer Code LOWTRAN 5, AFGL-TR-800067, 233p.

佐藤　功 (1989)　JERS-1 (OPS) の計算機シミュレーション・データによる岩石区分のためのバンド組合せ．日本リモートセンシング学会第9回講演論文集，p.41-44.

Yamaguchi, Y. (1987)　Possible techniques for lithologic discrimination using the short-wavelength-

infrared bands of the Japanese ERS-1. *Remote Sensing of Environment*, vol.23, p.117-129.
横山威生・岡田和也・駒井二郎 (1988) ERS-1 シミュレーション・データによる変質帯識別. 物理探査学会第 79 回学術講演会講演論文集, p.273-275.

地 質 調 査 所 報 告

第 272 号

Sato, Y. : Paleontological study of molluscan assemblages of the Miocene Moniwa Formation, Northeast Japan and description of their Pectinidae, 1991

第 273 号

須田芳朗・矢野雄策：日本の地熱調査における坑井データ　その 2　検層データおよび地質柱状図データ，1991

第 274 号

鹿野和彦・加藤碵一・柳沢幸夫・吉田史郎：日本の新生界層序と地史，1991

第 275 号

玉生志郎編：日本の地熱資源評価に関する研究，1991

第 276 号

村田泰章・須田芳郎・菊地恒夫：日本の岩石物性値　—密度，磁性，P 波速度，有効空隙率—，1991

第 277 号

Matsuhisa, Y., Aoki, M. and Hedenquist J.W. eds.: High-temperature acid fluids and associated alteration and mineralization, 1991

REPORT, GEOLOGICAL SURVEY OF JAPAN

No. 272

Sato, Y. : Paleontological study of molluscan assemblages of the Miocene Moniwa Formation, Northeast Japan and description of their Pectinidae, 1991 (in English)

No. 273

Suda, Y. and Yano, Y. : Well data compiled from Japanese Nation-Wide geothermal surveys, Part 2 Logging data geologic columnsdata, 1991 (in Japanese with English abstract)

No. 274

Kano, K., Kato H., Yanagisawa, Y. and Yosida, F. : Stratigraphy and geologic history of the Cenozoic of Japan, 1991 (in Japanese with English abstract)

No. 275

Tamanyu, S. ed. : Research on the geothermal resource assessment in Japan, 1991 (in Japanese with English abstract)

No. 276

Murata, Y., Suda, Y. and Kikuchi, T. : Rock Physical Properties of Japan —Density, Magnetism, P-wave Velocity, Porosity, Thermal Conductivity—, 1991 (in Japanese with English abstract)

No. 277

Matsuhisa, Y., Aoki, M. and Hedenquist J.W. eds. : High-temperature acid fluids and associated alteration and mineralization, 1991 (in English)

平成 4 年 3 月27日 印 刷
平成 4 年 3 月31日 発 行

通商産業省工業技術院 地 質 調 査 所

〒305 茨城県つくば市東 1 丁目1—3

印 刷 者 和 田 信 一
印 刷 所 住友出版印刷株式会社
東京都北区西が丘2—9—13

ISSN 0366-5542
CODEN: CCHHAQ

REPORT No. 278

GEOLOGICAL SURVEY OF JAPAN

Katsuro OGAWA, Director

RESEARCH ON GEOLOGIC REMOTE SENSING SYSTEM

GEOLOGICAL SURVEY OF JAPAN

Higashi 1-1-3, Tsukuba-shi, Ibaraki-ken, 305 Japan

1992

地 調 報 告
Rept. Geol. Surv. Japan
No. 278, 1992